

Wenshan Cai
Vladimir Shalaev

Optical Metamaterials

Fundamentals and Applications

 Springer

Optical Metamaterials

Wenshan Cai • Vladimir Shalaev

Optical Metamaterials

Fundamentals and Applications

 Springer

Dr. W. Cai
Stanford University
Stanford, CA
USA
caiw@stanford.edu

Prof. V. Shalaev
Purdue University
West Lafayette, IN
USA
shalaev@purdue.edu

ISBN 978-1-4419-1150-6 e-ISBN 978-1-4419-1151-3
DOI 10.1007/978-1-4419-1151-3
Springer New York Dordrecht Heidelberg London

Library of Congress Control Number: 2009936791

© Springer Science+Business Media, LLC 2010

All rights reserved. This work may not be translated or copied in whole or in part without the written permission of the publisher (Springer Science+Business Media, LLC, 233 Spring Street, New York, NY 10013, USA), except for brief excerpts in connection with reviews or scholarly analysis. Use in connection with any form of information storage and retrieval, electronic adaptation, computer software, or by similar or dissimilar methodology now known or hereafter developed is forbidden.

The use in this publication of trade names, trademarks, service marks, and similar terms, even if they are not identified as such, is not to be taken as an expression of opinion as to whether or not they are subject to proprietary rights.

Printed on acid-free paper

Springer is part of Springer Science+Business Media (www.springer.com)

*To my son Sheling, my wife Yun Tai, and to
the memory of my mother, Shuxin Wang
(1943–2008).*

– Wenshan Cai

*To my family and close friends, who keep
supporting me through my life and career.*

– Vladimir M. Shalaev

Preface

This book deals with optical metamaterials – artificially structured materials with nanoscale inclusions and strikingly unconventional properties at optical frequencies. These materials can be treated as macroscopically homogeneous media and can exhibit a variety of unusual and exciting responses to light. Man-made materials with subwavelength inclusions have been purposely utilized by artists and craftsmen for centuries, as indicated by a number of glass vessels ranging from the late Roman era to the Renaissance period. However, optical metamaterials have flourished only in the present century thanks to combined advances in nanofabrication, numerical modeling, and characterization tools. In only a few years, the field of optical metamaterials has emerged as one of the most exciting topics in the science of light, with stunning and unexpected outcomes that have repeatedly fascinated researchers, scientists, and even the general public.

The philosophy behind the area of optical metamaterials is distinct from most other branches of optical studies in that it does not emphasize the explanation, implementation, or utilization of known phenomena, but rather it focuses on the creation of entirely new stories and new events that no one has even considered. This philosophy is best illustrated by a simple quotation from *Back to Methuselah* by George Bernard Shaw, one of the finest playwrights of the twentieth century. The quote became widespread after its adoption by Robert Kennedy during his presidential campaign:

“Some men see things as they are and say ‘Why?’ I dream things that never were and say, ‘Why not?’”

Indeed, the persistence of asking “why” has been fascinating scientists throughout the history of optics. From ancient scholars like Euclid, Ptolemy and Alhazen to the modern giants who shaped today’s knowledge of optics, the pursuit of answers to observed phenomena has led to major discoveries that have made it possible for us to understand the realities of optics. By combing the knowledge derived from asking “why” and the implementation of available materials, numerous optical components, devices and systems have been developed that have radically altered both the everyday life of people around the globe and the scope of modern science.

With all the advances in optics throughout the ages, now is perhaps the time to focus more on the theme of “why not.” It is time to rethink the limits of optics,

and reconsider the long-established guidelines within which optical scientists often work. With this in mind, we choose to be bold and adventurous, rethinking the answers to questions such as, “Why not refract light the other way?” Or maybe we should ask, “Why not build a microscope to see a DNA strand with the naked eye?” We can even ponder more mysterious and mythical questions, including, “Why not create a cloak that makes an object invisible?” These concepts are not strictly prohibited by any fundamental physical laws, nor are many other equally fascinating possibilities. Perhaps, then, it is indeed time to explore many truly amazing ideas that may be temporarily beyond our vision, but not inherently beyond our reach.

All the questions above, now open for reconsideration by asking “why not,” are the pursuits of optical metamaterials. In this research field, the control of light is not limited by the properties of optical materials that are readily available. Instead, we choose to create materials that never were, by tailoring the elements of artificial structures down to the deeply subwavelength scale. This aspect of optical metamaterials is bound to revolutionarily alter the design strategies and implementation philosophies that people use in building optical devices and systems. The new research field of optical metamaterials opens a whole new world of fundamental studies and practical applications that were quite undreamt of in the realm of conventional optics. Still in its infancy, the optical metamaterials have already offered hope to the seemingly crazy dreams mentioned above, and they have demonstrated potential benefits in various applications including optical sensing, novel waveguides and antennas, sub-diffraction-limited imaging, nanoscale photolithography, photonic nanocircuits, and many more.

The intense development in the evolving field of optical metamaterials has started attracting an increasing number of students and researchers. Although a large and drastically growing number of publications are constantly added to the literature of this field, we feel there remains a lack of a reader-friendly book that helps to make optical metamaterials accessible to a wider audience. In particular, new participants in a highly interdisciplinary field of study like optical metamaterials can easily get lost if they have to wade through many textbooks of different subjects simultaneously. To describe optical metamaterials in a simple, easy-to-understand way was our primary motivation for embarking on this book.

In writing the book, we sought to provide an accessible entrance into the fascinating world of optical metamaterials. In a relatively slim volume, we are trying to provide students and researchers with the basic knowledge that is required to enter this research area, as well as providing the broad perspective that is now needed to understand the latest breakthroughs. It should be stressed that this book is not intended as a thorough treatise and up-to-date review of all research work available in this field. Instead, the book provides a comprehensive, self-contained but digestible introduction to the basic ideas and major topics in optical metamaterials. We hope that it will be useful to the interested reader as a stepping stone towards more advanced research currently underway in the field. We have tried to produce a balanced text from which the reader will be able to gain a perspective of optical metamaterials as a whole as well as a flavor for where the subject is going.

We now would like to take a moment to guide you through the contents of this book. The material in the book is presented in an order that aims to progressively increase the reader's comprehension of the subject. The book starts with a discussion of the definition, emergence, motivation and scope of the research field of optical metamaterials. Then in Chap. 2 we discuss the optical properties of metals, dielectrics and their composites. The delicate arrangement of these materials forms the constituent building blocks for the metamaterials we are truly interested in studying. Chapter 3 covers the fabrication techniques, characterization schemes and data treatment methods for optical metamaterials. Once the basics have been established, from Chap. 4–6 we present three major categories of optical metamaterials, namely electric metamaterials, magnetic metamaterials, and negative-index metamaterials. The principles, advances, and examples for each category will be analyzed in detail. The last three chapters deal with exciting novel opportunities made possible by optical metamaterials. In Chap. 7 we discuss nonlinear effects in optical metamaterials, including the necessary mathematical descriptions. Chapter 8 describes metamaterial-based imaging systems with subwavelength resolution. Most notably, several milestone experiments related to super-resolution in both the near- and far-field regimes are discussed. Finally, in Chap. 9 we provide the principles and applications of transformation optics, which molds the flow of light in an unprecedented manner by specifying the spatial distributions of anisotropic material parameters. In particular, this chapter gives a detailed discussion of the most intriguing outcome of transformation optics – an electromagnetic cloak of invisibility.

We have attempted to introduce most of the major subjects involved in optical metamaterials while at the same time keeping the book within a relatively small compass. Although the frontier in the study of optical metamaterials is developing rapidly, the basic knowledge and ways of thinking presented in this book are expected to be widely adopted in many of the new topics of optical metamaterials that are either ongoing or about to breach the horizon. The book can be used as a reference text by people working in metamaterials, plasmonics, nanophotonics, and other related fields. It can also be used as a course textbook or a book for self-instruction at the senior undergraduate or graduate level, as well as for a short course offered by a professional society. As such, the book presumes that the reader has a general knowledge of basic electrodynamics at the undergraduate level.

This book would not have been completed without the help of many people. In particular, we are deeply grateful to Mark Thoreson for his painstaking review and critical proofreading of the entire manuscript. We are also thankful for the support and helpful suggestions from Professor Mark Brongersma at Stanford University.

In addition, it is a pleasure to acknowledge our debt and gratitude to many colleagues whose expertise, discussions, and collaboration have benefited us over the years. These include Drs. A. V. Kildishev, A. K. Sarychev, V. P. Drachev, A. K. Popov, U. K. Chettiar, H.-K. Yuan, I. R. Gabitov, S. A. Myslivets, N. M. Litchinitser, E. E. Narimanov, A. E. Boltasseva, T. A. Klar, Sir J. B. Pendry, V. G. Veselago,

X. Zhang, D. R. Smith, M. Wegener, N. Engheta, N. I. Zheludev, U. Leonhardt, M. A. Noginov, V. A. Podolskiy, G. W. Milton, D. H. Werner, I. C. Khoo, A. I. Maimistov, R. Z. Sagdeev, D. A. Genov, A. Boardman, and I. I. Smolyaninov. We are also grateful to our families and close friends for their support.

Stanford, CA
West Lafayette, IN

Wenshan Cai
Vladimir M. Shalaev

Contents

1	Introduction	1
1.1	What are Metamaterials?	1
1.2	Macroscopic Effective Parameters	5
	References	8
2	Optical Properties of Metal-Dielectric Composites	11
2.1	Optical Materials and Electronic Structures	11
2.2	Optical Properties of Dielectric Materials	13
2.3	Optical Properties of Metals	19
2.4	Metal-Dielectric Composites and Mixing Rules	25
	References	36
3	Experimental Techniques and Data Treatment	39
3.1	Fabrication of Two-Dimensional Optical Metamaterials	39
3.2	Approaching the Third Dimension	43
3.3	Characterization of Spectral Properties	47
3.4	Extraction of Homogenized Optical Parameters	51
	References	56
4	Electric Metamaterials	59
4.1	A Brief Overview of Artificial Dielectrics	59
4.2	Optical Properties of Stratified Metal-Dielectric Composites	60
4.3	Periodic Array of Metallic Wires	64
4.4	Semicontinuous Metal Films	71
	References	74
5	Magnetic Metamaterials	77
5.1	Negligible Optical Magnetism in Nature	77
5.2	Split-Ring Resonators	78
5.3	Optical Magnetic Elements	82
5.4	Magnetism in the Visible Spectrum	88

5.5	Analytical Model of Magnetic Nanostrips	93
5.6	High-Permittivity Route to Artificial Magnetism	96
	References	98
6	Negative-Index Metamaterials	101
6.1	A Brief Historical Review	101
6.2	Reversed Phenomena in Negative-Index Media	103
6.3	Negative Refraction in Microwave Frequencies	105
6.4	The Debut of Optical Negative-Index Materials	107
6.5	General Recipe for Construction	112
6.6	Alternative Approaches	116
	References	120
7	Nonlinear Optics with Metamaterials	123
7.1	Recent Advances of Nonlinear Effects in Metamaterials	123
7.2	Second-Harmonic Generation and the Manley–Rowe Relations in Negative-Index Materials	126
7.3	Optical Parametric Amplifications in Negative-index Materials	131
	References	134
8	Super Resolution with Meta-Lenses	137
8.1	Perfect Lens with Subwavelength Resolution	137
8.2	Near-Field Superlens	140
8.3	“Tunable” Superlens Using Random Composites	142
8.4	Potential Applications of the Composite Lens	148
8.5	Far-Field Imaging with Super-Resolution	149
	References	155
9	Transformation Optics and Electromagnetic Cloak of Invisibility	159
9.1	Invisibility and Transformation Optics: An Overview	159
9.2	Cloaking by Coordinate Transformation	162
9.3	Towards Experimental Demonstrations	167
9.4	Non-magnetic Optical Cloak	171
9.5	Cloaking with High-Order Transformations	176
9.6	Designs for High-Order Optical Cloaking	180
9.7	Alternative Approaches for Optical Cloaking	187
9.8	Concluding Remarks on Transformation Optics	191
	References	193
	Index	197

Chapter 1

Introduction

1.1 What are Metamaterials?

Almost all electromagnetic phenomena and devices result from interactions between waves and materials. In this sense, the realization of an electromagnetic functionality is meant to manipulate the waves in a desired manner by elaborating structures and geometries with available materials. With the myriad of delicate structures proposed and produced by scientists and engineers around the world, the eventual capability and diversity of electromagnetic devices are largely limited only by the scope of available materials used to build them. Some fundamental constraints do exist that may make a desired property absolutely impossible. For example, no medium allows a chain of optical pulses traveling inside it to travel faster than the free space speed of light because of the causality requirement. However, many desired electromagnetic properties, similar to the case of monopole magnets, seem to be lacking in nature even though there are no physical laws preventing the existence of such phenomena.

Conventionally, novel electromagnetic materials are synthesized at the molecular level. Teflon[®] (polytetrafluoroethylene) is representative of this situation. This synthetic fluoropolymer exhibits many attractive features, such as a very low refractive index, that are not available in most transparent media at room temperature; hence it finds numerous optical applications due to its beneficial properties. Another approach to realize a novel electromagnetic property is to create an artificially structured composite consisting of well-arranged functional inclusions of subwavelength dimensions. Although the unit size of such inclusions is usually several orders beyond the atomic or molecular level of a conventional material, the inhomogeneity scale of these composite structures is still much smaller than the wavelength of interest and their electromagnetic responses can be expressed in terms of homogenized, “effective” material parameters. Such artificial, functional materials engineered to fulfill the prescribed electromagnetic properties, usually referred to as “metamaterials,” are the theme of this book. In particular, we focus our attention on the carefully fashioned structures exhibiting exotic properties at optical frequencies – we will consider optical metamaterials.

The prefix “meta” (μετα in Greek) means “beyond,” and in this sense the name “metamaterials” signifies systems that are beyond conventional materials. The word “metamaterial” first appeared in literature in 2000 when Smith et al. published their seminal paper on a structured material with simultaneously negative permeability and permittivity at microwave frequencies [1]. Other sources suggest that the term “metamaterial” was first coined slightly earlier, by Rodger M. Walser, a physics professor at the University of Texas in 1999 [2–4]. In merely a few years, the field of metamaterials has rapidly grown and blossomed, involving researchers in various disciplines including basic physics, optics, material science, mechanics and electrical engineering.

There has been enormously widespread use of the term “metamaterial” since the beginning of this century, which results in over 2,000 papers in the database of Institute for Scientific Information (ISI) with it as a key word and over 300,000 Google™ search results as of early 2009. However, the exact meaning of metamaterial is still nebulous; a unique and unambiguous definition for metamaterials is still yet to be established. Even some of the most visible definitions for the term do not satisfy all the researchers in the field. For example, the European Union’s Metamorphose Network, the primary sponsor of the Metamaterials Congress, defines a metamaterial as “an arrangement of artificial structural elements, designed to achieve advantageous and unusual electromagnetic properties” [5]. Such a definition, although it addresses the “artificial” nature of metamaterials, is perhaps overly inclusive and fails to recognize the important difference between metamaterials and other man-made structures such as photonic crystals.

Many leading experts in the field prefer to put terms like “properties unlike any naturally occurring substance” or “not observed in nature” in the definition of a metamaterial [6]. These definitions usefully emphasize the major pursuit of metamaterial research – to achieve electromagnetic features not found in conventional materials. However, it might be too glib to exclude any naturally occurring property from the focus of metamaterial research. We are truly humble in the face of Mother Nature, and it would take far too much effort and may not be possible at all to thoroughly examine and determine the *nonexistence* of a property in naturally occurring materials. For example, although materials with negative index of refraction are, incontrovertibly, one of the central topics in metamaterial research, negative refraction has been astonishingly observed in compound eyes of some lobsters [7]. The situation is quite similar to what happened in area of photonic crystals, which are periodic optical structures designed to affect the motion of photons. Although photonic crystals are a brilliant achievement of the work of many researchers, similar structures and phenomena have actually existed for millions of years inside gemstone opals and the wings of Morpho butterflies [8].

After examining the key concepts behind metamaterials, we shall define metamaterials with the following definition for the purposes of our discussions: *A metamaterial is an artificially structured material which attains its properties from the unit structure rather than the constituent materials. A metamaterial has an inhomogeneity scale that is much smaller than the wavelength of interest, and its electromagnetic response is expressed in terms of homogenized material parameters.*

Metamaterials are, above all, man-made materials. The structural units of a metamaterial, known as meta-atoms or meta-molecules, must be substantially smaller than the wavelength being considered, and the average distance between neighboring meta-atoms is also subwavelength in scale. The subwavelength scale of the inhomogeneities in a metamaterial makes the whole material macroscopically uniform, and this fact makes a metamaterial essentially a “material” instead of a device. The scale of the inhomogeneities also distinguishes metamaterials from many other electromagnetic media. Conventional materials and artificial metamaterials share the feature that their lattice constants are much smaller than the wavelength of interest. When the scale of the inhomogeneities is on the order of a wavelength, however, the response of the structure is dominated by diffraction and interference effects. Phenomena in this category occur across nearly the entire electromagnetic spectrum, including crystals in X-ray diffraction, photonic crystals in optics, and phased array radars at microwave frequencies. With even larger inhomogeneity scales, the response of structures is usually described using geometrical optics and ray tracing.

In our metamaterial definition, we don’t demand anything in terms of emergent properties in a metamaterial, because there is no rigorous way to define how “different” the metamaterial properties should be compared to the properties of its constituent materials or other naturally occurring media. Nor do we require any ordering in a metamaterial; although most reported metamaterials do follow a certain periodicity, there are also many random composites with fascinating electromagnetic responses. We do not want to exclude such materials from the scope of metamaterial research.

When tracing the history of metamaterials, it makes little sense to argue who made the first metamaterial. Centuries ago, people started using metamaterials deliberately in art pieces without a full understanding of the physics behind the results they achieved. A famous example is the Lycurgus Cup exhibited in the British Museum; the Roman glass chalice dates from the fourth century AD. The cup was made from probably the first known metamaterial – ruby glass with gold nanoparticles embedded [9]. The scattering property of the metamaterial offered the cup a unique beauty, appearing green when viewed in reflected light such as daylight but reddish with light transmitted through the glass, as depicted in Fig. 1.1 [10, 11].

In modern science, artificial electromagnetic metamaterials were produced and studied long before the term “metamaterial” entered the scientific community. Perhaps one of the first modern metamaterials with engineered, subwavelength meta-atoms was attributed to the “twisted jute” material proposed by Bose in 1898 to produce an artificial chiral effect [12]. Artificial dielectrics, which are usually periodic arrays of metallic wires, spheres or plates, were studied extensively by microwave engineers more than half of a century ago [13–15]. These artificial dielectrics are essentially identical to the electric metamaterials in the current terminology. Other examples of metamaterials or their elements developed before the term metamaterial was coined include the split-ring resonators [16, 17], arrayed frequency filters [18], bianisotropic and chiral materials [19], and others.

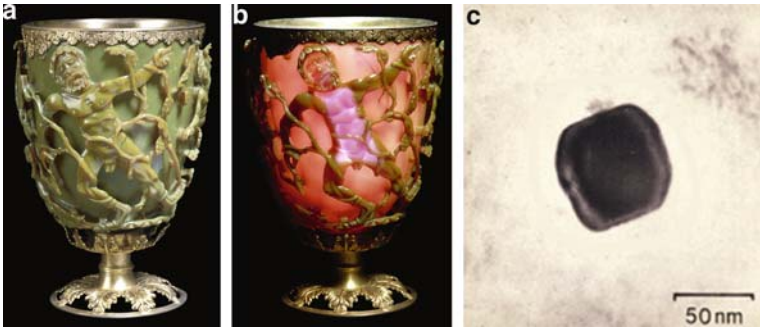


Fig. 1.1 The Lycurgus Cup viewed (a) in reflected light and (b) in transmitted light. A metallic nanoparticle used in the metamaterial is shown in (c). (a, b), Copyright The Trustees of the British Museum. (c), Adapted from [9]. Courtesy of D. J. Barber and I. C. Freestone

When discussing the emergence of metamaterials and the surge of interest in this field, we have to appreciate a few seminal papers that laid the groundwork for research in the area of modern metamaterials. In our opinion, there are three milestone papers that should be mentioned in this regard. The first is Veselago's paper on left-handed materials [20]. This paper studied the strikingly unusual phenomena to be expected in a hypothetical left-handed substance in which the field vectors E , H and the wave vector k form a left-handed system. The paper also explicitly presented the required material parameters to achieve the material – simultaneously negative values of permittivity and permeability. The first experimental demonstration of a Veselago medium by Smith et al. is second in our list [1], which makes the huge leap from a theoretical prediction to experimental validation. The third seminal paper is Pendry's work on a perfect lens [21], which represents the initial attempt to fill the gap between novel metamaterials and exciting applications. Interestingly, all the three papers that inaugurated the field of metamaterials were focused on negative index metamaterials. This fact is the major reason that during the first few years of the surge in metamaterial interest, the word metamaterial was almost synonymous with left-handed material. Today's metamaterial research has expanded far beyond materials with negative refraction. Various artificially engineered metamaterials are now demonstrating unprecedented electromagnetic properties that are not observed in naturally occurring materials and cannot be obtained by conventional synthesis techniques. The structural units of metamaterials can be tailored in shape and size, their composition and morphology can be artificially tuned, and inclusions can be designed and placed in a predetermined manner to achieve prescribed functionalities.

The idea of metamaterials has been quickly adopted in the optics community. Among all the branches of today's metamaterial research, those materials exhibiting tailored electromagnetic responses at light frequencies, known as *optical metamaterials*, are by far the most fascinating and most challenging topic. Light is the ultimate means of sending information to and from the interior structure of materials – it packages data in a signal of zero mass and unmatched speed. The burgeoning

optical metamaterial research activities are a result of the combination of a wealth of nanofabrication techniques with advances in nanoscale imaging and computational electromagnetic design and simulations. Within the rapidly developing and highly multidisciplinary field of optical metamaterials, several key research directions have been emerging, including optical magnetism [22–24], optical negative index materials [25–29], giant artificial chirality [30, 31], nonlinear optics in metamaterials [32–35], super resolution with metamaterials [36–41], and electromagnetic cloaks of invisibility [42–46]. We note that both “optical metamaterials” and “photonic metamaterials” appear in literatures frequently without noticeable difference in their meanings. So in this book, the two terms are used interchangeably.

Photonic metamaterials revolutionarily altered the way that people propose and design functional optical devices. Materials used in conventional optical designs are usually both homogeneous and isotropic; therefore the design of devices is largely an issue of engineering the interfaces between different media. For instance, in the lens-making industry, cascaded lenses of different materials with finely controlled curvatures are often used to minimize multiple types of aberrations. The emergence of photonic metamaterials allows us to tailor optical space and provide new responses that are precluded in the constituent materials. The design strategy of optical devices is radically changed when metamaterials are involved – the desired functionality is achieved not only by configuring the interfaces between different materials, but by the control of essentially every single point in optical space. This enables applications using novel, spatially varying architectures of metamaterials where the electromagnetic properties of every position are carefully prescribed.

The last 6 years have witnessed the birth and development of the new research area of optical metamaterials. Such unconventional electromagnetic media can have numerous and far-reaching implications. These materials bring the promise of creating entirely new prospects for controlling and manipulating photons, and they provide potential benefits in various fields including optical sensing, miniature antennae, novel waveguides, subwavelength imaging, nano-scale photolithography and photonic circuits. We should note that the research field of photonic metamaterials is still in its infancy. Today’s optical metamaterials are still far from perfect. They are usually highly dissipative, dispersive and anisotropic, but they are very real nonetheless. Having confirmed the ability of optical materials to produce unprecedented results, researches are now optimizing their design, exploring the new physics behind these materials and postulating exciting new functional devices.

1.2 Macroscopic Effective Parameters

Most electromagnetic phenomena are governed by Maxwell’s equations, which are a set of equations describing the interrelationship between fields, sources, and material properties. Impinging fields in a system can influence the organization of the electrical charges and magnetic dipoles in a medium, and fields can induce polarization and magnetization to some degree, depending on the particular

material involved. The electromagnetic properties of a material are determined by two material parameters: the permittivity ε and the permeability μ , describing the coupling of a material to the electric and magnetic field components of an electromagnetic wave, respectively. These two parameters, along with another two related values – the refractive index $n = \sqrt{\mu\varepsilon}$ and the impedance $Z = \sqrt{\mu/\varepsilon}$, are essentially macroscopic effective parameters because they are used to describe the overall average response of the material as a whole. Microscopically, a piece of crystal consists of atoms arranged in a periodic manner with a lattice constant of a few angstroms. On the atomic scale, in each atom or molecule, tiny electric dipoles can be excited by the electric component of incident light, and subsequent radiation of the energy in the dipoles occurs with a certain delay in time. The excited dipoles create a periodic local field in the crystal, referred to as Lorentz local field; therefore the field distribution inside the crystal is certainly not uniform. However, the incident light does not really feel the underlying inhomogeneity in the crystal, nor does it feel the processes of absorption and radiation. On the macroscopic scale, the detailed features and responses of the inhomogeneous structure are averaged, and relationships can be established between the macroscopic field vectors in Maxwell's equations, namely the electric field E , the magnetic field H , the electric displacement field D , and the magnetic flux density B . This is the origin of the permittivity and permeability parameters of materials. At optical frequencies, this complicated physics is usually described using the transmittance and reflectance of light with a certain retardation (delay) in addition to the energy absorbed in the material, and a complex value of the refractive index or permittivity is used to describe such phenomena.

Similarly, the scale of inhomogeneities in a metamaterial is much smaller than the wavelength of interest – the metamaterial design ensures this. The inhomogeneity scale corresponds to the lattice constant of the artificial structure for the case of periodic metamaterials. Therefore, though the interaction between electromagnetic fields and meta-atoms is quite complicated at the scale of the inhomogeneities, macroscopically the wave feels a homogeneous medium. Furthermore, similar to the treatment of conventional materials, the electromagnetic responses of the metamaterial to external fields can be homogenized and are described using effective parameters including the permittivity, permeability, refractive index and impedance. This fact explains again why metamaterials made from basic constituents are identified as materials instead of devices. From the point of view of Maxwell's equations, a material is a collection of subwavelength units with global properties described by ε and μ . Through the dedicated design of meta-atoms, which is usually a delicate metal-dielectric structure, metamaterial research allows us to tailor the electromagnetic response of media in an unprecedented manner.

We should note that although the macroscopic material parameters are often treated as single real numbers (for example, we say the refractive index of water is 1.33), the actual situation is much more complicated. Using the permittivity ε as an example, causality forces it to be dispersive, which means that permittivity is a function of wavelength (except for the case of a vacuum). The frequency dependence of permittivity is deeply rooted in the causality requirement – the material's

response to the external field must arise after the field is applied, and there must be a phase delay between the excitation field and the radiated one. Since the permittivity function $\varepsilon(\omega)$ is analytic in the upper half complex plane, it satisfies the Kramers–Kronig relations [47]. Therefore, there is an imaginary part associated with $\varepsilon(\omega)$ that characterizes the dissipation of energy within a medium. In an anisotropic medium, the field vectors E and D are not necessarily parallel to each other; hence the permittivity must be in the form of a tensor rather than a scalar value. Anisotropic and strongly dispersive features generally occur in most of metamaterials studied thus far; for this reason, we should always specify the frequency and direction under consideration when we address any effective parameters in a metamaterial. Finally, there are cases such as bianisotropic media where the electromagnetic response is not sufficiently described with ε and μ tensors because of the complexity of the unit scatterers. Such structures may require additional material parameters like magnetoelectric coefficients, which link the electric field vectors and the magnetic ones. Although some important metamaterial elements like split-ring resonators are bianisotropic to some extent, we shall exclude detailed discussions of such situations in this book.

Since the response of a material to external fields is largely determined only by the two material parameters ε and μ , we can use an electromagnetic parameter space to classify materials based on the two values [48]. As shown in Fig. 1.2, the real part of permittivity ε_r is plotted to the horizontal axis of the parameter space, while the vertical axis corresponds to the real part of permeability μ_r . Therefore materials with all possible combinations of ε_r and μ_r can be placed in the parameter space. Conventional materials known to be transparent are found in the first quadrant, where both ε_r and μ_r have positive values. A negative value of $\varepsilon(\mu)$ indicates that the direction of the electric (magnetic) field induced inside the material is in the opposite direction to the incident field. Noble metals at optical frequencies

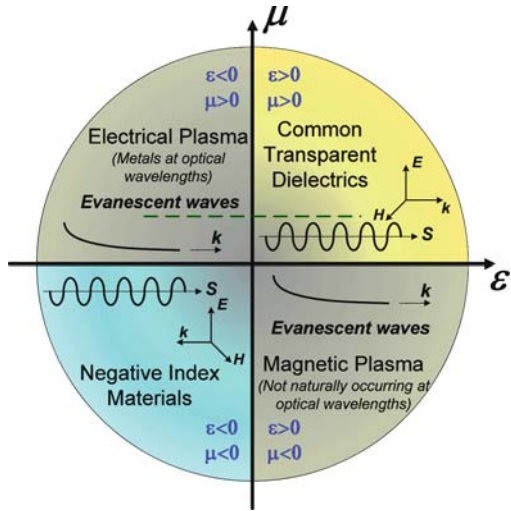


Fig. 1.2 The parameter space for ε and μ . The two axes correspond to the real parts of permittivity and permeability, respectively. The dashed green line represents non-magnetic materials with $\mu = 1$

are good examples for materials with negative ε , and negative μ can be found in ferromagnetic media near a resonance [49]. No propagating waves can be supported in materials represented by the second and fourth quadrants, where one of the two parameters is negative and the index of refraction becomes purely imaginary. In the domain of optics, all conventional materials are confined to an extremely narrow zone around a horizontal line at $\mu = 1$ in the space, as represented by the dashed line in Fig. 1.2.

Metamaterial research, essentially, is related to the innovative exploitation of the electromagnetic parameter space. The major focus of the metamaterial community is to create artificial materials that enter regions of the parameter space that are not forbidden by Maxwell's equations but are not observed in any conventional media, and to take advantage of this expanded parameter space for better control of electromagnetic waves. Progress in optical metamagnetics has allowed researchers to move material properties away from the non-magnetic line, and negative index metamaterials have opened the third quadrant of the parameter space, which was completely inaccessible previously. With the current and foreseeable advances in computational power and fabrication techniques, other territories of the parameter space will be explored in the search for additional and unprecedented electromagnetic properties. It is hard to see any fundamental factors that may limit the eventual capabilities of optical metamaterials in molding the flow of light, except for our own creativity, imagination, and eagerness.

Let us briefly mention the notation conventions that will be used in this book for our discussions. Throughout this book, the permittivity ε is a dimensionless value and represents the *relative* permittivity (also called the dielectric constant), i.e., the permittivity of a material relative to that of a pure vacuum at the same frequency. A similar concept applies for the permeability μ . We also use a frequency-dispersive permittivity $\varepsilon(\omega)$ and permeability $\mu(\omega)$ to characterize the electromagnetic response of a material. There is an alternative description based on the generalized, spatially dispersive permittivity tensor $\tilde{\varepsilon}(\omega, \vec{k})$ to describe both the electric and magnetic responses without using permeability μ [50]. We also mention here that we have selected $\exp(-i\omega t)$ for the time-harmonic factor, which is assumed for all electromagnetic waves in this book. Consequently, a usual passive medium exhibits positive values in the imaginary parts of permittivity, permeability, and refractive index.

References

1. Smith DR, Padilla WJ, Vier DC, Nemat-Nasser SC, Schultz S (2000) Composite medium with simultaneously negative permeability and permittivity. *Phys Rev Lett* 84:4184–4187
2. Wikipedia (2009) Metamaterial. <http://en.wikipedia.org/wiki/Metamaterial>, Accessed April, 2009
3. Walser RM (2001) Electromagnetic metamaterials. In: Lakhtakia A, Weiglhofer WS, Hodgkinson IJ (eds) *Complex mediums II: beyond linear isotropic dielectrics*, Proc. SPIE 4467, SPIE – International Society for Optical Engineering, San Diego, CA, USA, pp. 1–15
4. Lakhtakia A, Mackay TG (2007) Meet the metamaterials. *Opt Photon News* 18:32–39
5. Metamorphose <http://www.metamorphose-eu.org/>. Accessed April, 2009

6. Pendry JB, Smith DR (2006) The quest for the superlens. *Sci Am* 295:60–67
7. Stavennga DG (2006) Invertebrate superposition eyes-structures that behave like metamaterial with negative refractive index. *J Eur Opt Soc* 1:06010
8. Kinoshita S, Yoshioka S, Kawagoe K (2002) Mechanisms of structural colour in the Morpho butterfly: cooperation of regularity and irregularity in an iridescent scale. *Proc R Soc Lond Ser B* 269:1417–1421
9. Barber DJ, Freestone IC (1990) An investigation of the origin of the color of the *Lycurgus* cup by analytical transmission electron-microscopy. *Archaeometry* 32:33–45
10. Wagner FE, Haslbeck S, Stievano L, Calogero S, Pankhurst QA, Martinek P (2000) Before striking gold in gold-ruby glass. *Nature* 407:691–692
11. Leonhardt U (2007) Optical metamaterials – invisibility cup. *Nat Photonics* 1:207–208
12. Bose JC (1898) On the rotation of plane of polarization of electric waves by a twisted structure. *Proc R Soc Lond* 63:146–152
13. Kock WE (1946) Metal-lens antennas. *Proc IRE* 34:828–836
14. Brown J (1953) Artificial dielectrics having refractive indices less than unity. *Proc IEE* 100: 51–62
15. Rotman W (1962) Plasma simulation by artificial dielectrics and parallel-plate media. *IEE Trans Antennas Propag AP*-10:82–95
16. Hardy WN, Whitehead LA (1981) Split-ring resonator for use in magnetic-resonance from 200–2000 Mhz. *Rev Sci Instrum* 52:213–216
17. Froncisz W, Hyde JS (1982) The loop-gap resonator – a new microwave lumped circuit electron-spin-resonance sample structure. *J Magn Reson* 47:515–521
18. Hong JS, Lancaster MJ (1996) Couplings of microstrip square open-loop resonators for cross-coupled planar microwave filters. *IEEE Trans Microw Theory Tech* 44:2099–2109
19. Saadoun MMI, Engheta N (1992) A reciprocal phase-shifter using novel pseudochiral or omega-medium. *Microw Opt Tech Lett* 5:184–188
20. Veselago VG (1968) Electrodynamics of substances with simultaneously negative values of sigma and mu. *Sov Phys Usp* 10:509–514
21. Pendry JB (2000) Negative refraction makes a perfect lens. *Phys Rev Lett* 85:3966–3969
22. Linden S, Enkrich C, Wegener M, Zhou JF, Koschny T, Soukoulis CM (2004) Magnetic response of metamaterials at 100 terahertz. *Science* 306:1351–1353
23. Zhang S, Fan WJ, Minhas BK, Frauenglass A, Malloy KJ, Brueck SRJ (2005) Midinfrared resonant magnetic nanostructures exhibiting a negative permeability. *Phys Rev Lett* 94:037402
24. Cai WS, Chettiar UK, Yuan HK, de Silva VC, Kildishev AV, Drachev VP, Shalaev VM (2007) Metamagnetics with rainbow colors. *Opt Express* 15:3333–3341
25. Shalaev VM, Cai WS, Chettiar UK, Yuan HK, Sarychev AK, Drachev VP, Kildishev AV (2005) Negative index of refraction in optical metamaterials. *Opt Lett* 30:3356–3358
26. Zhang S, Fan WJ, Panoiu NC, Malloy KJ, Osgood RM, Brueck SRJ (2005) Experimental demonstration of near-infrared negative-index metamaterials. *Phys Rev Lett* 95:137404
27. Dolling G, Enkrich C, Wegener M, Soukoulis CM, Linden S (2006) Simultaneous negative phase and group velocity of light in a metamaterial. *Science* 312:892–894
28. Dolling G, Wegener M, Soukoulis CM, Linden S (2007) Negative-index metamaterial at 780 nm wavelength. *Opt Lett* 32:53–55
29. Chettiar UK, Kildishev AV, Yuan HK, Cai WS, Xiao SM, Drachev VP, Shalaev VM (2007) Dual-band negative index metamaterial: double negative at 813 nm and single negative at 772 nm. *Opt Lett* 32:1671–1673
30. Plum E, Fedotov VA, Schwanecke AS, Zheludev NI, Chen Y (2007) Giant optical gyrotropy due to electromagnetic coupling. *Appl Phys Lett* 90:223113
31. Decker M, Klein MW, Wegener M, Linden S (2007) Circular dichroism of planar chiral magnetic metamaterials. *Opt Lett* 32:856–858
32. Klein MW, Enkrich C, Wegener M, Linden S (2006) Second-harmonic generation from magnetic metamaterials. *Science* 313:502–504
33. Klein MW, Wegener M, Feth N, Linden S (2007) Experiments on second- and third-harmonic generation from magnetic metamaterials. *Opt Express* 15:5238–5247

34. Popov AK, Shalaev VM (2006) Negative-index metamaterials: second-harmonic generation, Manley–Rowe relations and parametric amplification. *Appl Phys B* 84:131–137
35. Popov AK, Shalaev VM (2006) Compensating losses in negative-index metamaterials by optical parametric amplification. *Opt Lett* 31:2169–2171
36. Fang N, Lee H, Sun C, Zhang X (2005) Sub-diffraction-limited optical imaging with a silver superlens. *Science* 308:534–537
37. Taubner T, Korobkin D, Urzhumov Y, Shvets G, Hillenbrand R (2006) Near-field microscopy through a SiC superlens. *Science* 313:1595
38. Liu ZW, Lee H, Xiong Y, Sun C, Zhang X (2007) Far-field optical hyperlens magnifying sub-diffraction-limited objects. *Science* 315:1686
39. Liu ZW, Durant S, Lee H, Pikus Y, Fang N, Xiong Y, Sun C, Zhang X (2007) Far-field optical superlens. *Nano Lett* 7:403–408
40. Cai WS, Genov DA, Shalaev VM (2005) Superlens based on metal-dielectric composites. *Phys Rev B* 72:193101
41. Jacob Z, Alekseyev LV, Narimanov E (2006) Optical hyperlens: far-field imaging beyond the diffraction limit. *Opt Express* 14:8247–8256
42. Pendry JB, Schurig D, Smith DR (2006) Controlling electromagnetic fields. *Science* 312:1780–1782
43. Schurig D, Mock JJ, Justice BJ, Cummer SA, Pendry JB, Starr AF, Smith DR (2006) Metamaterial electromagnetic cloak at microwave frequencies. *Science* 314:977–980
44. Cai WS, Chettiar UK, Kildishev AV, Shalaev VM (2007) Optical cloaking with metamaterials. *Nat Photonics* 1:224–227
45. Cai WS, Chettiar UK, Kildishev AV, Shalaev VM, Milton GW (2007) Nonmagnetic cloak with minimized scattering. *Appl Phys Lett* 91:111105
46. Cai WS, Chettiar UK, Kildishev AV, Shalaev VM (2008) Designs for optical cloaking with high-order transformations. *Opt Express* 16:5444–5452
47. Jackson JD (1998) *Classical electrodynamics*. Wiley, New York
48. Pendry JB (2003) Focus issue: negative refraction and metamaterials – introduction. *Opt Express* 11:639
49. Thompson GHB (1955) Unusual waveguide characteristics associated with the apparent negative permeability obtainable in ferrites. *Nature* 175:1135–1136
50. Agranovich VM, Shen YR, Baughman RH, Zakhidov AA (2004) Linear and nonlinear wave propagation in negative refraction metamaterials. *Phys Rev B* 69:165112

Chapter 2

Optical Properties of Metal-Dielectric Composites

2.1 Optical Materials and Electronic Structures

As discussed in the preceding chapter, metamaterials are man-made materials consisting of artificially structured units that are made from naturally occurring substances and usually (but not necessarily) arranged in a periodic fashion. These units, sometimes called “meta-atoms” or “meta-molecules,” are a delicate arrangement of two or more conventional materials with known bulk properties, although the character of the composite architecture can be quite exotic and distinct from all of its constituents. This scenario is quite similar to what we are familiar with in the everyday act of cooking: The taste of the final outcome can be far beyond the simply combined flavors of the individual ingredients, but a good cook must know the nature of each ingredient before putting them together in a prescribed procedure. Similarly, in order to design and implement optical metamaterials, it is essential to study the physical properties of the basic constituent materials, including dielectrics, semiconductors, and metals. It is also necessary to understand the mechanism responsible for their optical behaviors. The purpose of this chapter is to help us understand the optical behavior of the basic constituents of metamaterials.

Although used extensively in optics, the terms “dielectric” and “metals” are actually borrowed from electronics, where different types of bulk materials are classified based on their resistivity. In a dielectric, also called an insulator, the allowed energy bands are either completely filled or completely empty. Consequently, no electrons can move in an electric field, and the flow of electric current is prohibited. On the contrary, a conductor contains free electric charges that will flow when an electric potential difference is applied to the material. Metals are by far the most commonly used conductors due to the fact that they are rich in loosely held free electrons because one or more of their energy bands are partly filled. Another important category in the electronic material classification system is “semiconductors,” which are materials that have all their energy bands entirely filled except for one or two bands that are slightly filled or slightly empty. A classical way to visualize the difference between these different types of electronic materials is to use the Fermi level and energy band theory, which are detailed in most textbooks on solid state physics [1].

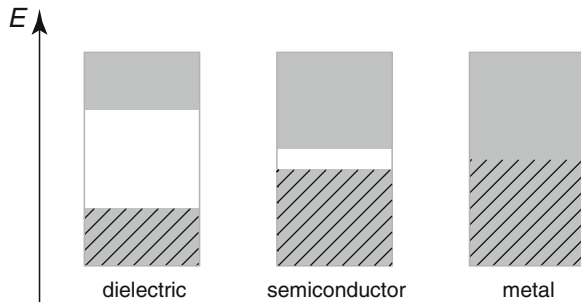


Fig. 2.1 Simplified energy band diagram for a typical dielectric, semiconductor, and metal. The shaded gray and light gray regions represent the valence band and the conduction band, respectively, and the empty region between them indicates the band gap

According to the Pauli exclusion principle, no two electrons in an atom can share one identical quantum state. In fact, this discreteness requirement can be extended beyond an isolated atomic system. In a crystalline solid, for example, discrete energy levels are created due to the covalent bonding of atoms in the crystal lattice. These allowed energy levels are lumped into two energy bands, the conduction band and the valence band. The valence band consists of numerous closely spaced levels which are mostly filled by electrons, while the conduction band represents electronic levels at higher energies that are mostly unoccupied. The two bands are separated by an energy region where no electron states are allowed. The width of this empty energy region, called a band gap or forbidden band, determines whether a substance is a dielectric, semiconductor or conductor. The band gap width represents the energy barrier that must be overcome by a bound electron in the valence band in order to take part in the electric conduction process. The energy band diagrams for typical dielectrics, semiconductors and metals are illustrated in Fig. 2.1.

A dielectric is characterized by a wide energy band gap, usually larger than 5 eV. As a result, a relatively high energy is necessary to promote a valence band electron into the conduction band. This is why thermal generation of free carriers in dielectrics is extremely weak, and a huge amount of energy is required to obtain even a feeble amount of current. The band structure of semiconductors, as depicted in the middle panel of Fig. 2.1, is probably the most familiar band diagram because of the extensive use of semiconductors in today's electronics industry. The moderate forbidden gap makes it possible for electrons in the valence band to be lifted to the conduction band with a small excitation energy and become free to conduct current. In sharp contrast to dielectrics and semiconductors where there are two distinct bands separated by an energy gap, in conductors like metals, the valence band and the conduction band overlap without a forbidden band in between. Consequently, any energy that is added to electrons is sufficient to propel them into the conduction band, and there are always sufficient free electrons moving about in a conductor to form a current flow if an electric field is applied.

When it comes to the optical properties of materials, we should be very careful when applying the concepts from electronics to our optical studies. Many

dielectrics, indeed, have optical properties that are closely correlated with their electronic structure. For example, the photon energy of visible light, which ranges between 1.5 eV and 3 eV, is not sufficient to bridge the gap between the valence band and the conduction band in common insulators. Therefore, such materials are typically transparent in the visible spectrum. As an alternate scheme, it would be quite plausible to classify materials simply based on their electronic properties. Doing so can cause even further confusion, however. One good example to illustrate this point is indium tin oxide (ITO), a solid that is extensively used in transparent electrodes in the display and lighting industries owing to its spectacular feature of combining both electrical conductivity and optical transparency. Electronically, therefore, ITO is a metal-like substance, but optically it acts as a dielectric. This situation is also true for some real metals. For example, tungsten is clearly a metal because it conducts current in the filaments of light bulbs. In the visible light spectrum, however, tungsten looks more like a lossy dielectric and features a positive dielectric constant value.

In most circumstances in the research of optical metamaterials, semiconductors are treated as dielectric materials, which can be either lossless or absorptive depending on the wavelength range being considered. As seen in Fig. 2.1, the electronic structure of insulators and semiconductors are different merely in the width of the forbidden gap. Strictly speaking, there is not a clear dividing line that separates one category from the other. In electronics, the relatively narrow forbidden band in some semiconductors facilitates the manipulation of electrons via various schemes, which was the starting point of semiconductor device technology. In optics, however, it is the photons that excite electrons in the valence band. Therefore, the critical consideration becomes the comparison of photon energy and the bandgap of a crystal, which specifies the shortest wavelength (the “critical” wavelength) at which the dielectric remains transparent. The critical wavelength λ_c is related to the bandgap E_g by

$$\lambda_c = \frac{hc}{E_g} = \frac{1240 \text{ nm}}{E_g (\text{in eV})}, \quad (2.1)$$

where h is Planck’s constant and c is the speed of light in vacuum. The values of band gap and critical wavelength for some common dielectrics are given in Table 2.1 [1,2].

When used as transparent dielectrics, many semiconductors feature a high dielectric constant, which is particularly useful in the design of many metamaterial-based functions. In Chaps. 8 and 9 we will show a few examples of metamaterial devices with high-permittivity semiconductors as the dielectric constituents.

2.2 Optical Properties of Dielectric Materials

Dielectrics are by far the dominant materials used for optical components and devices. In conventional optical systems, almost all functional parts, except for some reflection surfaces, are made from crystalline and glassy materials. The reason is

Table 2.1 Band gap and critical wavelength of common dielectrics at room temperature

Dielectric material	Band gap (eV)	Critical wavelength (μm)
Diamond	5.50	0.23
Si	1.12	1.10
Ge	0.66	1.87
SiC	2.99	0.41
GaN	3.44	0.36
GaP	2.27	0.55
GaAs	1.42	0.87
InP	1.34	0.92
InAs	0.35	3.50
ZnO	3.44	0.36
ZnS	3.68	0.34
ZnSe	2.82	0.44
CdTe	1.48	0.84
PbS	0.41	3.03
SiO ₂	~8.5	~0.15
Al ₂ O ₃	~9	~0.14
TiO ₂	3.0	0.41

simple: light is effectively manipulated only when it can efficiently pass through a medium, meaning that the medium is, at least to some degree, a dielectric

The underlying physical background of light interacting with a dielectric can be analyzed using Maxwell's equations plus the following two constitutive relations:

$$D = \varepsilon_0 E + P = \varepsilon_0(1 + \chi_e)E = \varepsilon_0 \varepsilon_r E \quad (2.2a)$$

$$B = \mu_0(H + M) = \mu_0(1 + \chi_m)H = \mu_0 \mu_r H \quad (2.2b)$$

Equation (2.2a) specifies the relationship between the electric displacement D , the electric field E , the polarization density P and the electric susceptibility χ_e , while (2.2b) is for their magnetic counterparts. The vacuum permittivity and permeability in SI units are $\varepsilon_0 = 8.85 \times 10^{-12}$ F/m and $\mu_0 = 4\pi \times 10^{-7}$ H/m. According to our notational conventions stated in the previous chapter, we shall omit the subscript r in the relative permittivity ε_r and permeability μ_r in our discussion. The study of the (linear) interactions between light and matter, essentially, involves determining the solutions to Maxwell's equations by using the constitutive relations along with appropriate boundary conditions.

At optical frequencies, the magnetic susceptibility χ_m in any conventional material diminishes for reasons to be elaborated in Chap. 5, and the relative permeability μ_r is taken normally to be unity. This condition substantially simplifies our description of optical materials – transparent ones in particular – by assigning a refractive index $n = \sqrt{\varepsilon}$ to each medium. Even though all media are dispersive and absorbent in a strict sense, the use of real numbers for refractive indices is extremely convenient, and therefore it has become standard practice in the design and analysis of optical components and devices. Particularly, the refraction and reflection behaviors of dielectric systems, including magnitude and phase information,

are well characterized by a set of Fresnel equations, which are simple algebraic formulas with refractive indices and incident angles as the only variables.

Although the refractive index of an isotropic, homogeneous and linear dielectric material can be viewed as a real number in many cases, we should note that for a rigorous treatment of light interacting with optical media, the frequency dependence of the material properties should be carefully considered. At optical frequencies, the oscillation of the electric field is so fast that the bound charges in atoms or molecules are unable to follow the electric field in time. Consequently, (2.2a) does not hold in the time domain for the high frequencies of the optical range. Instead, the electromagnetic response of the medium described by $D(t)$ at time t depends not only on the electric field E at that moment, but also on the value of E at all past times. Hence the constitutive relation has to involve time operators (convolution) as follows [3]:

$$D(t) = \varepsilon_0 E(t) + \varepsilon_0 \cdot \int_{-\infty}^t \chi_e(t - \tau) E(\tau) d\tau \quad (2.3)$$

Fortunately, the proportionality is still valid for the relationship between D and E in the frequency domain, as long as the material being considered is a linear medium (which means the susceptibility is independent of the strength of the electric field). We therefore write the frequency-domain constitutive relationship as:

$$D(\omega) = \varepsilon_0 \varepsilon(\omega) E(\omega) = \varepsilon_0 [1 + \chi_e(\omega)] E(\omega). \quad (2.4)$$

As mentioned in the introduction of the book, most metamaterials with metal-dielectric composite units are strongly dispersive. In the visible or near-infrared wavelength region, the origin of the dispersion in a metamaterial is mostly ascribed to the metallic part, because metals are much more dispersive than transparent dielectric media. Nevertheless, it is very helpful to study the frequency sensitivity of the dielectric function $\varepsilon(\omega)$ in dielectric media. In particular, when we extend our interest to the whole optical spectrum ranging from the near-UV (200–400 nm) to the mid-infrared (tens of microns), the dispersion of even the best transparent material is no longer a negligible feature. The transparency window for most dielectric materials is bounded at the long-wavelength side by the infrared absorption mode of phonons due to lattice vibrations, while at the high-frequency side the window is bounded by interband electron-hole transitions. The approximate spectral transparency ranges for a number of important dielectric materials are shown in Fig. 2.2 [1, 2, 4]. When designing an optical metamaterial, it is important to make sure that the selected dielectric constituent is transparent within the wavelength range of interest. Otherwise substantial loss may arise from electron or photon resonances in the dielectric, which are detrimental to the performance of the metamaterial in most cases.

The dielectric function $\varepsilon(\omega)$ can be expressed in a classical Helmholtz–Drude model:

$$\varepsilon(\omega) = 1 + \sum_j \frac{S_j \omega_j^2}{\omega_j^2 - \omega^2 - i\omega\gamma_j}, \quad (2.5)$$

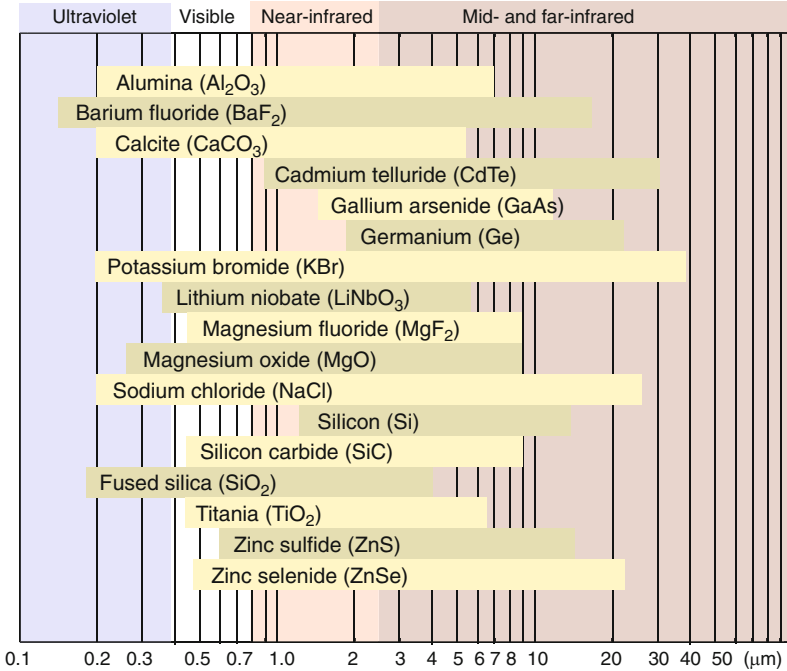


Fig. 2.2 The spectral range of transparency for several important dielectric materials

where ω_j is the resonance frequency of the j th mode, and S_j and γ_j represent the strength and the damping constant of the j th mode, respectively. A typical frequency-dependent permittivity of a usual, transparent dielectric is plotted in Fig. 2.3. In this example, two resonances are included in the oscillator formula, with ω_1 representing the phonon resonance in the mid-infrared, and ω_2 corresponding to the electron transition in the UV range due to the bandgap of the crystal. The dielectric function exhibits a Lorentz line shape at each resonance along with a distinct peak in the imaginary part of $\varepsilon(\omega)$, which indicates the loss feature associated with the resonance. We see from the example in Fig. 2.3 that, between the two resonance frequencies, the permittivity curve is rather flat with a negligible imaginary part. This explains why a common dielectric like quartz or alumina is transparent to the visible light.

The real part of $\varepsilon(\omega)$ exhibits a Lorentz line shape around each resonance. The real part ε' is large and positive at the low-frequency side of the resonance, and it has a negative value when the frequency is slightly higher than that of the resonance. A negative dielectric constant is somewhat counterintuitive, because transparent materials have positive dielectric functions in the visible range. A negative value of ε' implies that the response (in our case, the polarization density P or the electric displacement D) is directed opposite to the electric field E . The electromagnetic response of a material around a resonance is illustrated in Fig. 2.4, where a

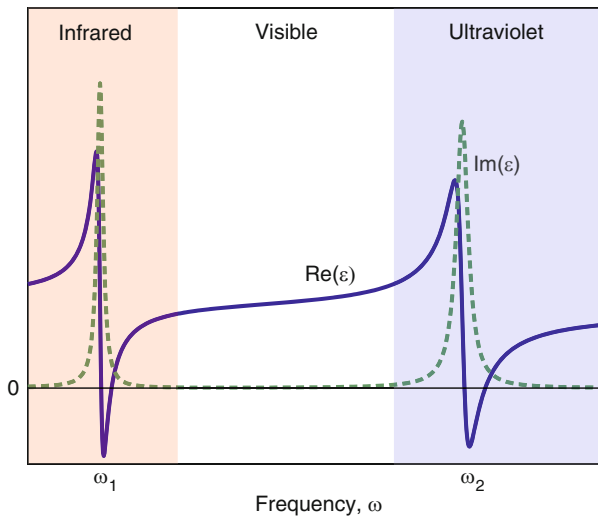


Fig. 2.3 The dielectric function $\varepsilon(\omega)$ for a typical dielectric material with the lattice resonance and electron transition resonance marked as ω_1 and ω_2 , respectively

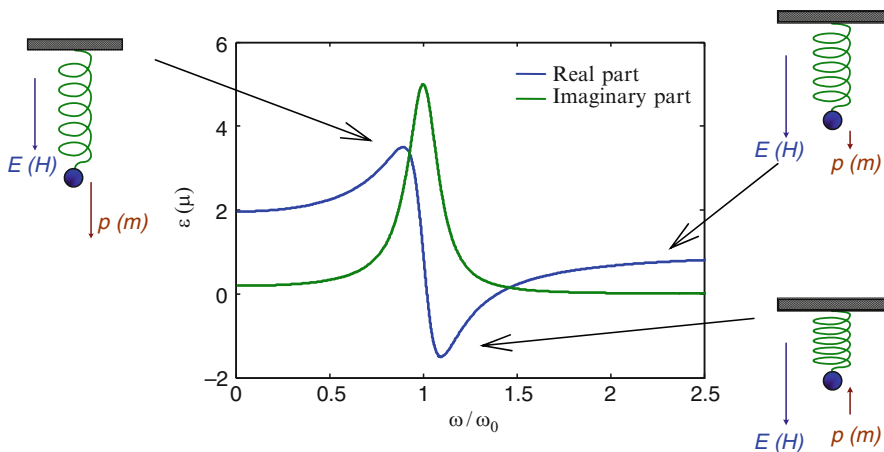


Fig. 2.4 The positive and negative electromagnetic responses around a resonance. The three spring-mass oscillators are used as a mechanic analogue of the scenario

spring-mass oscillator is used to facilitate understanding. Away from the resonance, the response is able to follow the driving force with no delay. When the frequency is slightly lower than the resonance frequency ω_0 , the function (ε or μ) is increasingly positive and the response (P for electric resonances and M for magnetic ones) is enhanced. On the other side of the resonance peak, the function can take a negative value, thus the response is opposite to the driving force.

The simple square-root relationship between the refractive index and the permittivity still holds in the frequency domain. Therefore the frequency-dependent refractive index $n(\omega)$, being a complex value in the general case, is related to the dielectric function $\varepsilon(\omega)$ by

$$n(\omega) = n'(\omega) + i n''(\omega) = \sqrt{\varepsilon(\omega)}. \quad (2.6)$$

In many optics textbooks and in most published literature, the real part of the complex number $n(\omega)$ is simply called the refractive index or the index of refraction, while the imaginary part $n''(\omega)$ is referred to as the absorption index. In addition, the notation k or κ is frequently used for the same quantity. Some basic algebra leads us to the useful relations between the real and imaginary parts of the refractive index and those of the dielectric function:

$$\varepsilon' = n'^2 - n''^2; \quad \varepsilon'' = 2n'n'' \quad (2.7a)$$

$$n'^2 = \left[\varepsilon' + \sqrt{\varepsilon'^2 + \varepsilon''^2} \right] / 2; \quad n''^2 = \left[-\varepsilon' + \sqrt{\varepsilon'^2 + \varepsilon''^2} \right] / 2 \quad (2.7b)$$

In (2.7) we omit the argument ω to make the equations concise. In standard material handbooks [2, 5, 6], either the complex refractive index or the complex dielectric function may be provided for a set of wavelength or frequency values.

The frequency dependence of $n(\omega)$ is very similar to the plot given in Fig. 2.3 for the permittivity $\varepsilon(\omega)$, except for the fact that the curve for the real part $n'(\omega)$ is raised (offset) along the vertical axis to avoid a negative value in the real part of the index. Since the imaginary part $n''(\omega)$ is negligibly small (usually less than 10^{-5}) for common transparent dielectrics in the visible range, the refractive index of such materials can be modeled in a form similar to (2.5) without involving the imaginary part or the damping constants. In this situation, (2.5) reduces to the widely used Sellmeier dispersion formula:

$$n(\lambda)^2 = 1 + \sum_j \frac{S_j \lambda^2}{\lambda^2 - \lambda_j^2} \quad (2.8)$$

Some modified forms of the Sellmeier formula also exist in the literature in which an empirical approximation for $n(\lambda)$ instead of $n(\lambda)^2$ is provided. Power series approximations to the Sellmeier formula are also used, where the index $n(\lambda)$ or $n(\lambda)^2$ is expressed as the sum of powers of wavelength as $\sum_j A_j \lambda^j$, where the index j can be both positive and negative.

For weakly absorptive media, the absorption coefficient α is routinely used to characterize the attenuation of light propagating in the material. The absorption coefficient is the exponential index appearing in Beer's law, which says that the intensity I_0 of light will decrease to $I_0 \exp(-\alpha z)$ as the light travels a distance z in a medium. Since the electric field E changes along the propagation direction following the function $\exp[i2\pi(n' + i n'')z/\lambda_0]$, and the intensity is proportional to E^2 , it

is easy to see that the absorption coefficient α is connected to the imaginary part the refractive index by

$$\alpha = 4\pi n''/\lambda_0. \quad (2.9)$$

The absorption coefficient α has dimensions of reciprocal length, and it is usually expressed in the units of cm^{-1} .

Up to this point, we have covered most of the necessary, fundamental information on the optical properties of dielectric materials that may be directly pertinent to metamaterial studies. The properties of bulk crystals that are not discussed here include, for example, optical anisotropy and nonlinear responses, which we touch on briefly now. Optical anisotropy and birefringence are intrinsic properties of crystalline dielectrics. In an anisotropic medium such as uniaxial or biaxial crystals, the optical response to the external field is directionally dependent. Moreover, the polarization field P is not necessarily aligned with the electric field, so tensors of rank 2 instead of scalar values must be used for the electric susceptibility χ and the permittivity ϵ . In optical metamaterials, however, the length scale of the continuous dielectric portion of the unit structure is so small – being much smaller than the light wavelength – that all dielectric components tend to have an “amorphous” state without a preferred direction. Therefore in the design and simulation of optical metamaterials, a scalar value is usually sufficient for the permittivity or the refractive index of the dielectric constituent. As for the nonlinear properties of dielectrics, they are normally neglected because most of today’s optical metamaterials are operated in the linear response region. Even when the nonlinearity of metamaterials are included (see Chap. 7), the nonlinear effects will typically result from the meta-molecules as a whole plus the surface states of the metallic part, while the nonlinearity of the dielectric itself plays a very minor role.

2.3 Optical Properties of Metals

Conventionally, the use of metals in optical systems is limited to only a few applications like mirrors and optical thin films. In optical metamaterials, however, most of the designs being studied incorporate metals in the unit structure of the metamaterial. The sharp contrast between the optical response of metals and that of dielectrics is essential to making meta-atoms functional elements. In this section we briefly review the physical processes involved in light-metal interactions and emphasize the modification of metal behaviors at the nanoscale.

Common impressions from everyday experience tell us two of the most pronounced features of metals at optical frequencies. First, metals are opaque – you cannot look through a piece of metal unless it’s thinner than the so-called skin depth, which is on the scale of few tens of nanometers. Secondly, metals are highly reflective. Most of light impinging on a smooth metal surface will be rebounded or reflected from the surface. Both of these properties originate from behavior of electrons in metals. Let us look again at the energy band diagram for metals, as

shown in the right panel of Fig. 2.1. The Fermi level in metals sits inside a continuous energy band, and there is no gap between the empty energy levels and the occupied ones. Consequently, the photon energy from any electromagnetic radiation is enough to excite an electron to a higher level. Since the empty electron states are continuously available, light of all frequencies that enters into a metal (which is not easy at all) can be absorbed within a tiny propagating length, usually less than 100 nanometers. Many metals, like silver and aluminum, have a bright silvery appearance when exposed to sunlight because they are highly reflective across the entire visible spectrum. Some metals, including gold and copper, are colored because the high-frequency components of light are not well reflected, and the light we perceive from them contains predominantly colors in the yellow to red wavelength range. All these phenomena can be explained using the dielectric functions of different metals, which will be covered in this section.

Similar to the study of dielectric materials in the previous section, most of the mechanisms behind light-metal interactions are ascribed to the frequency-dependent permittivity of metals. The starting points in the evaluation of metal permittivity are the constitutive relations in (2.2)–(2.4), in addition to the behavior of free electrons in a driving electric field, which are described in terms of an electron gas.

The electromagnetic response of a metal is largely dictated by the collective movement of free electrons within the metal crystalline structure. In the following treatment we will extend the Lorentz harmonic oscillator model to metals. In this case, the electrons are considered to be freely able to move about in the metal lattice, without any restoring force or spring constant. Therefore, the resonance frequency ω_0 from the standard Lorentz model is zero in this case, and it does not appear in the analysis below. This model for electron motion in a metal is known as the Drude free electron model. With a time harmonic incident electric field $E_0 e^{-i\omega t}$, the equation of motion for a free electron is

$$m \frac{\partial^2 \vec{r}(t)}{\partial t^2} + m\Gamma \frac{\partial \vec{r}(t)}{\partial t} = -e \vec{E}_0 e^{-i\omega t}, \quad (2.10)$$

where m and e represent the effective mass and the charge of the electron, respectively, and Γ is the damping constant. Solving this differential equation, we obtain the displacement r of the electron from its original position:

$$\vec{r}(t) = \frac{e}{m} \frac{\vec{E}_0 e^{-i\omega t}}{(\omega^2 + i\Gamma\omega)}. \quad (2.11)$$

The polarization density P , by definition, is the total dipole moment per unit volume. Therefore, the polarization can be expressed as $P = ner$, where n denotes the density of free electrons in the metal. From (2.11) and (2.2a), we obtain the frequency dependence of the dielectric function:

$$\varepsilon(\omega) = 1 - \frac{\omega_p^2}{\omega^2 + i\Gamma\omega} = 1 - \frac{\omega_p^2}{\omega^2 + \Gamma^2} + i \frac{\omega_p^2 \Gamma}{\omega(\omega^2 + \Gamma^2)}, \quad (2.12)$$

Table 2.2 Plasma frequency ω_p , damping constant Γ and Fermi velocity v_F of selected noble metals

<i>Metal</i>	ω_p (eV)	ω_p (10^{15} s^{-1})	Γ (eV)	Γ (10^{15} s^{-1})	v_F (10^6 ms^{-1})
Silver	9.2	14.0	0.021	0.032	1.4
Gold	9.1	13.8	0.072	0.11	1.4
Copper	8.8	13.4	0.092	0.14	1.6
Aluminum	15.1	22.9	0.605	0.92	2.0

where ω_p is the volume plasma frequency at which the density of the electron gas oscillates:

$$\omega_p = \sqrt{\frac{ne^2}{\epsilon_0 m}}. \quad (2.13)$$

Note that the damping constant Γ , which represents the electron collision rate, is absolutely necessary to provide an imaginary part in $\chi(\omega)$ or $\epsilon(\omega)$. Sometimes the inverse of Γ – the mean electron collision time $\tau = \Gamma^{-1}$ – is used in the Drude model. Hence the damping constant Γ is related to the electron mean free path l and the Fermi velocity v_F by

$$\Gamma = v_F/l. \quad (2.14)$$

The volume plasma frequency ω_p , the damping constant Γ and the Fermi velocity v_F for several noble metals (silver, gold, copper and aluminum) are shown in Table 2.2 [1, 7]. Although the Fermi velocity v_F does not explicitly enter into the Drude model in (2.12), it will be used when we evaluate the size-effect dependence on the dielectric function, so we choose to include the data of v_F in the table for reference.

The Drude model for the dielectric function in (2.12) is an elegant and concise treatment for the optical properties of noble metals. However, it has to be modified to adequately reflect reality. One common observation that is not predicted by the Drude model is that gold and silver, with almost identical plasma frequencies, appear so different when exposed to visible light. Since gold is “golden” in color, what happens to the green and blue portions of the white light spectrum when gold is viewed under white-light illumination?

It is clear that our model has to be improved. This is not unexpected, since we have only accounted for free electrons, but not all electrons in a metal are free. Although the behavior of noble metals is dominantly governed by the free electron response, the contribution from bound electrons should also be taken into account when working at high frequencies, including the visible range. Both the Drude model and the energy band diagram for metals in Fig. 2.1 describe only the electrons in the outer atomic orbitals, namely the 5s, 6s and 4s states for silver, gold and copper, respectively. However, interband transitions such as the transition from the 5d state to the 6sp state in gold, for example, do exist in metals when excited by light waves. Even in silvery-colored metals like silver or alkali metals where the interband transition occurs well beyond the visible spectrum, the influence of such transitions is still needed to supplement the Drude model. The contribution from the interband transitions of bound electrons to the dielectric function $\epsilon(\omega)$ is quite similar to the

corresponding resonance in dielectric materials (see, for example, the resonance at ω_2 in Fig. 2.3), and these transitions can be written in a standard Lorentz form as:

$$\varepsilon_{ib}(\omega) = 1 + \frac{\omega_1^2}{\omega_0^2 - \omega^2 - i\gamma\omega}, \quad (2.15)$$

where ω_0 denotes the oscillation frequency of a bound electron under an applied electric potential, and ω_1 and γ are related to the density and damping of bound electrons, respectively. The overall dielectric function of the metal therefore contains both the Drude term for free electrons and $\varepsilon_{ib}(\omega)$ for bound ones:

$$\varepsilon(\omega) = \varepsilon'(\omega) + i\varepsilon''(\omega) = \varepsilon_{ib}(\omega) + 1 - \frac{\omega_p^2}{\omega^2 + i\Gamma\omega}. \quad (2.16)$$

As an example of the interband contribution to the dielectric function of metals, in Fig. 2.5 we plot $\varepsilon_{ib}(\omega)$ for gold with an interband transition in the visible region based on function (2.15). The central frequency ω_0 of the resonance is 2.8 eV, which corresponds to a wavelength of 450 nm. In the calculation, the values $\omega_1 = 3.0$ eV and $\gamma = 0.6$ eV are used. From Fig. 2.5 we can see that the interband transition of bound electrons indeed exerts a huge influence on the properties of gold in the visible frequencies. The dielectric function of gold is distorted, moving towards the positive ε direction (more dielectric-like), associated with increased loss for blue and green light. This is the physical origin behind the bright yellow color of the metal – the blue and green light is more strongly absorbed by the gold, leaving predominantly yellow light reflected back to the observer.

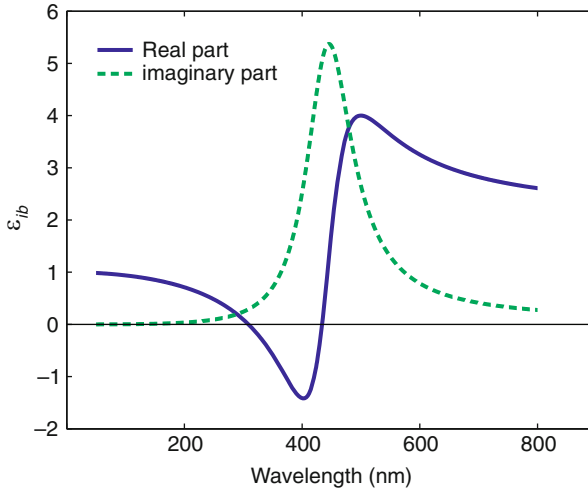


Fig. 2.5 Contribution of the interband transition to the permittivity of gold at visible frequencies calculated with (2.15)

Another noticeable feature of the interband transition is that it has a non-zero impact on the dielectric function of the metal even at wavelengths much longer than the resonance wavelength. This can be seen from the long-wavelength side of Fig. 2.5, or from 2.15 by setting $\omega \rightarrow 0$. Therefore, when working at longer wavelengths away from the interband resonance (infrared range for gold, and visible plus infrared for silver), we can replace the frequency-dependent $\varepsilon_{ib}(\omega)$ in (2.16) by a constant offset denoted ε_∞ . For example, the interband offset contribution for gold in Fig. 2.5 is about 1.2. It is important to note that, due to the complicated band structure of bound electrons in noble metals, there are usually multiple interband transitions in the UV or deep UV spectrum. Hence the offset ε_∞ is a sum or integral value after taking all pertinent transitions into account. Eventually, then, the modified Drude model taking into account the constant offset of interband transitions becomes:

$$\varepsilon(\omega) = \varepsilon'(\omega) + i\varepsilon''(\omega) = \varepsilon_\infty - \frac{\omega_p^2}{\omega^2 + i\Gamma\omega} = \varepsilon_\infty - \frac{\omega_p^2}{\omega^2 + \Gamma^2} + i \frac{\omega_p^2\Gamma}{\omega(\omega^2 + \Gamma^2)}. \quad (2.17)$$

The empirical values for ε_∞ for silver and gold are about 5 and 9, respectively. The terms containing Γ^2 in the denominators of the rightmost side can be neglected for quick calculations because Γ is much smaller than ω at optical frequencies.

In Fig. 2.6 we show the calculated dielectric function of silver compared to the widely accepted experimental data from [7]. Using the parameters given in Table 2.2, a reasonable agreement between the analytical model of (2.17) and the measured data across the visible and near-IR range is achieved for both the real and the imaginary parts of the permittivity. Tabulated data for other metals can be found in optics handbooks like [2, 5, 6].

As opposed to dielectric materials, which are characterized by a positive permittivity at optical frequencies, the real part of the dielectric function for noble metals is distinctively negative. A negative value for the permittivity implies that the free electrons in metals oscillate out of phase with respect to the driving electric field. Thus

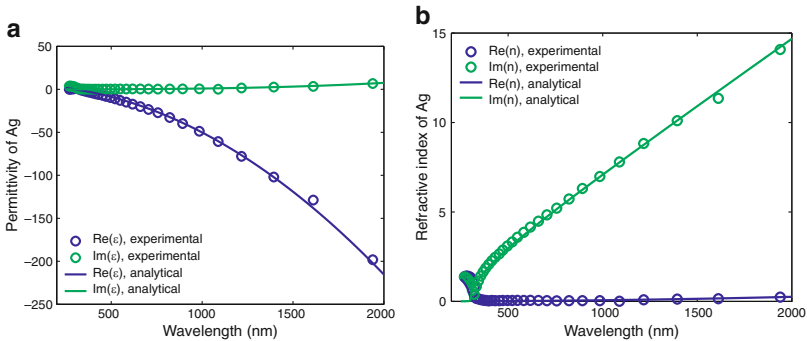


Fig. 2.6 Comparison between the experimental data from [7] and the modified Drude model for (a) the dielectric function and (b) the complex refractive index of silver

most of incident photons are reflected at the interface between a metal and a dielectric. A better way to illustrate this point is to use the refractive index of metal. From (2.7) along with (2.17), we can obtain the complex refractive index of metals, as plotted in Fig. 2.6b for silver. At optical frequencies, $\varepsilon'' \ll |\varepsilon'|$ holds for the permittivity function of metals, therefore the refractive index has a pronounced imaginary part while the real part of the index is only slightly larger than zero. From the Fresnel equations, we know that the reflection coefficient expressed by $(n_1 - n_2)/(n_1 + n_2)$ must have an absolute value of unity when n_1 is real and n_2 is purely imaginary. As a result, at the boundary between a dielectric and a noble metal, almost all light is reflected as long as the wavelength is substantially longer than that of the interband transitions. Another phenomenon resulting from the large value of n'' is that light can only penetrate through a very thin layer of the noble metal. This travelling distance, called the skin depth, is the inverse of the absorption coefficient α in (2.9). The skin depth of noble metals at optical frequencies is about 50 nm.

When studying the interaction of light with nanostructured metals or metal-dielectric composites, the properties of metals need to be further modified due to the size effect. In the Drude free electron model, the damping parameter Γ is usually considered to be a constant at a given temperature. The fixed value of Γ , however, is no longer valid when the geometrical size of the metal goes below tens of nanometers. (2.14) tells us that Γ is a collision rate related to an electron's mean free path l in the metal, which can be estimated using the data in Table 2.2. When the length scale of the continuous metal portion of the metamaterial unit structure is comparable to or smaller than l , the movement of free electrons is further limited by the physical boundary of the metal structure, and the effective mean free path is reduced according to [8]:

$$\frac{1}{l_1} = \frac{1}{l} + \frac{1}{R}, \quad (2.18)$$

where R represents the size of the metal particle and l_1 is the size-limited mean free path of electrons. Combining (2.14) and (2.18), we find that the new damping parameter Γ_1 with the size effect included is:

$$\Gamma_1 = \Gamma + a \frac{v_F}{R}, \quad (2.19)$$

where the prefactor a is on the order of one and depends on the geometry specifics and some other factors. When evaluating the permittivity of metal in nanoscale, therefore, Γ_1 should be used as the damping constant in the modified Drude model of (2.17). Since the real part of the dielectric function is only marginally related to the damping constant while the imaginary part is proportional to Γ , we should recalculate the imaginary part $\varepsilon''(\omega)$ for nanostructured metals. The imaginary part of silver's permittivity for different size limits is plotted in Fig. 2.7. When the dimension of the metal is tens of nanometers or smaller, the magnitude of ε'' is substantially larger than its bulk value. This feature should be taken into account in the design and simulation of most optical metamaterials with metal-dielectric meta-atoms. For example, the metal nanostrips in Chap. 5 and the nano fishnet in Chap. 6 clearly require size-effect adjustments to accurately describe the metal permittivity.

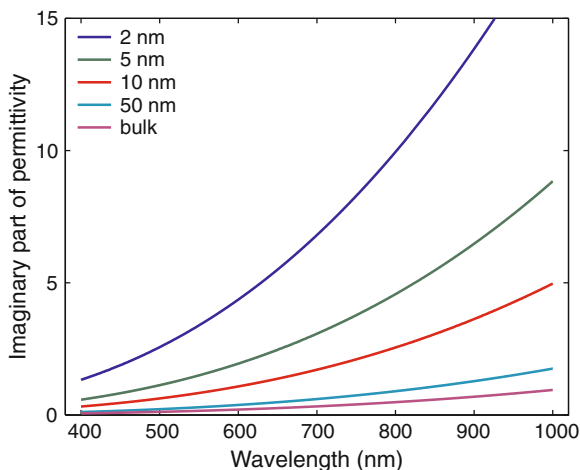


Fig. 2.7 The imaginary part of the dielectric constant of silver with the size effect taken into account

At the end of this section, we want to mention the rapidly growing research field of *plasmonics*, which is focused on the control and manipulation of light waves at the subwavelength scale using metallic structures. At optical frequencies, the free electrons in noble metals can sustain volume and surface charge density oscillations, called plasmons. Depending on the geometry of the metal structures and their surrounding environment, plasmons can take different forms, ranging from surface plasmon polaritons propagating along the metal-dielectric boundaries to localized plasmons with electrons oscillating inside metal nanoparticles. Plasmonics allows optical signals be squeezed into deep subwavelength scale, which helps to bridge length scale mismatch between typical optical systems and on-chip electronics. Many promising results in plasmonics research have revealed its tremendous potential for various applications, including subwavelength microscopy, light emission and detection, photovoltaic harvesting, biochemical sensing, optical signal processing, and many more.

2.4 Metal-Dielectric Composites and Mixing Rules

As has been stated earlier, most of the compositional units used in making the meta-atoms of photonic metamaterials are delicate, subwavelength structures containing both metal and dielectric components. The response of a metamaterial to an electromagnetic field is critically contingent on the specific architecture of the meta-atoms; therefore it is hard to develop a simple and unified method for analyzing the properties of an arbitrary structural unit of a metamaterial. However, for metamaterials without well-structured building blocks, there are generalized analytical approaches that allow us to estimate the average electromagnetic response of composite materials. In such randomly structured media, the metal and

dielectric components are arranged in a disordered fashion, and the overall optical properties of a metal-dielectric composite can be significantly different from those of its constituent materials. Random metal-dielectric metamaterials have found applications in diverse areas such as nonlinear optics and biochemical spectroscopy. Moreover, many metamaterial devices are designed and implemented based on random metal-dielectric composites. A few examples of such devices are discussed in Chaps. 8 and 9.

In a composite, where metal and dielectric components intersperse with each other in a disordered manner, the boundary conditions in the system are so complicated that the determination of its electromagnetic response by solving Maxwell's equations becomes practically impossible. Fortunately, under certain conditions the situation can be simplified significantly. For the study of the optical properties of a composite system with an inhomogeneity scale much smaller than the wavelength of interest, electrodynamic scattering by individual metal or dielectric particles is overshadowed by the average response of the whole system. Therefore, we can investigate the optical properties of a *microscopically heterogeneous* composite by evaluating the effective dielectric function of the *macroscopically uniform* medium. We obtain this effective dielectric function in terms of the permittivities of the individual components as well as their respective volume fractions. This method is known as the effective medium approach.

Two of the most widely used effective medium approaches are the Maxwell-Garnett theory (MGT) [9] and the Bruggeman effective medium theory (EMT) [10]. Each of these two methods is based upon slightly different assumptions regarding the composite topology and the material properties of each constituent in the mixture. Depending on the relative concentration of the inclusions and the process of fabrication, metal-dielectric composites may have different types of microscopic structures. To present this point more clearly, TEM images of two samples with typical topologies are shown in Fig. 2.8. In the first composite sample, the inclusions

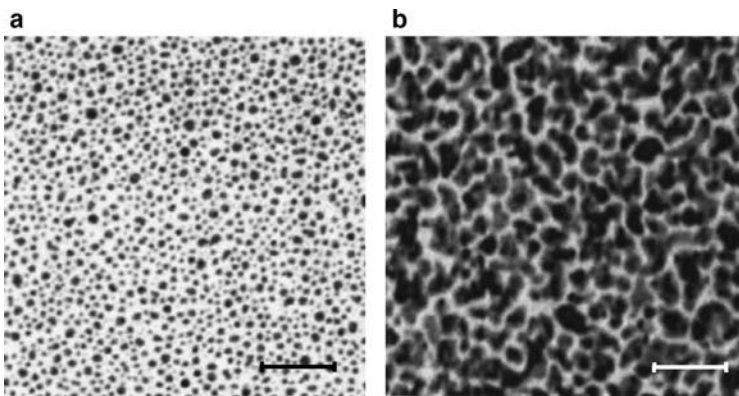


Fig. 2.8 TEM images of typical metal-dielectric composites in (a) the Maxwell-Garnett geometry and (b) the Bruggeman geometry. The dark and bright areas represent the metal and the dielectric components, respectively. Scale bar is 200 nm for both images

particles (the black areas of the image) embedded in the host material (the white areas of the image) are quite dilute and have well-defined, spherical shapes. This is usually called the Maxwell–Garnett geometry. When the two constituent materials intermingle with each other and the two materials play symmetric roles, as shown in Fig. 2.8b, it is difficult to say which is the host and which is the inclusion. This type of topology is commonly referred to as the Bruggeman geometry.

Besides MGT and Bruggeman’s EMT that we shall focus on in this section, the published literature on composites contains a range of other mixing rules including Polder and van Santen’s method [11], the Looyenga’s formula [12], the de Loor model [13], and many other approaches developed during the last three decades [14–17]. Most of these models can be derived from the Clausius–Mossotti formula (also known as the Lorentz–Lorenz equation), which was established by several pioneers of mean-field theory, namely O.-F. Mossotti, R. Clausius, L. Lorenz, and H. Lorentz. The early history of this field can be found in literature surveys conducted by Landauer [18], and a detailed treatment of the problem is available in textbooks on scattering of random media [19,20].

We shall start our analysis with the Lorentz local field expression. Without losing generality, let us consider the case of a dense optical medium with molecular dipoles arranged in a cubic lattice. Lorentz pointed out that the local field experienced by a molecule is not the macroscopically averaged field E but is instead E_L , where the subscript “ L ” represents “local.” This is not a surprising claim with today’s knowledge of the structure of solids – of course there are tremendous electric fields inside an atom or within the gaps between atoms, because all solids are shown to be non-uniform when examined at the atomic scale. However, all local fluctuation of the fields average out to zero if you look at the material at a scale much larger than the atomic features. Macroscopically, therefore, the magnitude of the field in a homogeneous medium is regarded as a constant if loss is not an issue. However, when we study the effects of an external field upon individual atoms, molecules or particles, the local features of electromagnetic field must be carefully analyzed.

To evaluate the local field E_L at the site of a molecule in a uniform solid, the molecule is imagined to be surrounded by a spherical cavity, which is appropriately called the Lorentz sphere. The radius R of the sphere is macroscopically small in order to accommodate the discrete nature of the medium very close to the molecule, but it is microscopically large enough so that the matrix lying outside may be treated as a continuous medium. The space inside the sphere is assumed to have a free space permittivity of ϵ_0 because the gaps between individual molecules contain nothing but vacuum. When an external electric field is applied, electric charges are distributed around the surface of the hypothetical sphere, which give rise to an additional field imposed upon the central molecule. A schematic for computing the local field using the Lorentz cavity concept is illustrated in Fig. 2.9.

In the Lorentz model, the local field acting on the central dipole can be decomposed into four components:

$$E_L = E_0 + E_d + E_s + E_{near}, \quad (2.20)$$

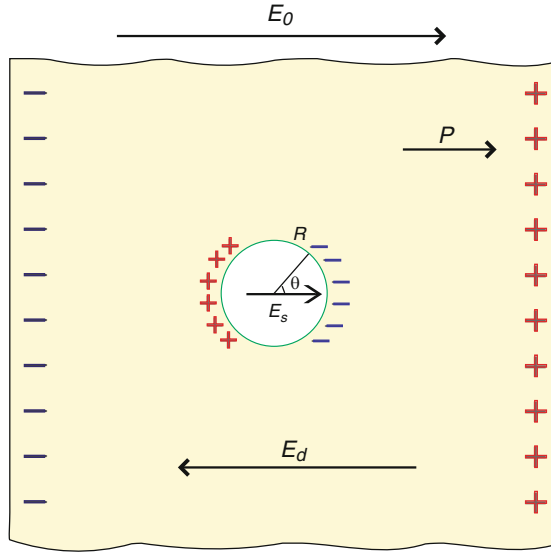


Fig. 2.9 The Lorentz sphere concept for calculating the local field E_L

where E_0 represents the external field. E_d is the depolarization field due to the polarization charges lying at the external surface of the medium. The relationship between E_d and the macroscopic polarization P is simply $E_d = -P/\epsilon_0$. E_s denotes the field due to the polarization charges lying on the surface of the Lorentz sphere, and E_{near} is the field induced by other dipoles lying within the sphere.

The sum of the first two terms on the right-hand side of (2.20), $E_0 + E_d$, is the homogeneous field averaged over the entire volume of the material. It is exactly the macroscopic field E that enters into the Maxwell equations. For a homogeneous medium, the field E has a constant magnitude throughout the medium. On the other hand, the local field E_L is a microscopic field that fluctuates rapidly within the medium. This field can be quite large at the molecular sites themselves.

Now it is the time to evaluate the third term, E_s , in the Lorentz local field expression. For this purpose, we relate the surface charge density on the surface of the Lorentz sphere to the polarization P in the medium. The total charge over a surface segment dS is $P \cos \theta dS$, where θ is the angle between P and the normal of the surface segment. This amount of surface charge produces, according to the Coulomb's law, an electric field dE_s along the radial direction given by:

$$dE_s = \frac{P \cos \theta dS}{4\pi \epsilon_0 R^2}. \quad (2.21)$$

Considering the symmetry of the system, the total field E_s resulting from all the surface charges on the Lorentz sphere is directed along the direction of the external field, with a magnitude of

$$E_s = \int_S \frac{P \cos^2 \theta dS}{4\pi \varepsilon_0 R^2} = \int_0^\pi \frac{P \cos^2 \theta}{4\pi \varepsilon_0 R^2} \cdot 2\pi R^2 \sin \theta d\theta = \frac{P}{3\varepsilon_0}. \quad (2.22)$$

As for the last unknown term in (2.20), the field E_{near} due to the dipoles within the spherical cavity is the only term that depends on the crystal structure. There are a few cases for which this term vanishes, for example in a liquid or a gas where the dipoles are randomly distributed in uncorrelated positions. In our example we assume a cubic crystal lattice, where the E_{near} term also vanishes owing to the lattice symmetry. We therefore obtain an expression of the total Lorentz local field in a surprisingly neat form:

$$E_L = E + \frac{P}{3\varepsilon_0}. \quad (2.23)$$

This is known as the Lorentz relation: the field acting at an atom site in a cubic lattice is the macroscopic field E plus $P/3\varepsilon_0$ from the polarization of other atoms in the system.

Similar to the treatment in the previous section where we derived the Drude model, we relate the polarization P to the electric dipole moment of each molecule. If we let α denote the polarizability of one molecule, the polarization P is expressed as

$$P = N\alpha E_L = N\alpha \left(E + \frac{P}{3\varepsilon_0} \right), \quad (2.24)$$

where N is the volume density of the dipoles

Combining (2.24) and the basic constitutive relation in (2.2a), we build the final connection between the polarizability α and the relative dielectric constant ε of the medium:

$$\frac{N\alpha}{3\varepsilon_0} = \frac{\varepsilon - 1}{\varepsilon + 2} \quad (2.25a)$$

and

$$\alpha = \frac{3\varepsilon_0}{N} \frac{\varepsilon - 1}{\varepsilon + 2}. \quad (2.25b)$$

This is the Clausius–Mossotti relation, which provides the essential link between the macroscopic observable ε and the microscopic parameter α . The significance of the formulation above should be viewed in a historical context. From this perspective, the dielectric function is nothing mysterious because there is a distinct connection between the electric response of individual molecules and the macroscopic behavior of bulk material as described by a dielectric constant or an electric susceptibility.

Now we will apply the Clausius–Mossotti relation to a metal-dielectric composite. We assume that spherical particles of one substance with a relative permittivity ε_1 are embedded in a host medium with relative permittivity ε_h . In this case, Clausius–Mossotti relation in (2.25a) should be rewritten as

$$\frac{N\alpha}{3\varepsilon_0\varepsilon_h} = \frac{\varepsilon - \varepsilon_h}{\varepsilon + 2\varepsilon_h}. \quad (2.26a)$$

The polarizability α in (2.25b) then becomes

$$\alpha = \frac{3\varepsilon_0\varepsilon_h f}{N} \frac{\varepsilon_1 - \varepsilon_h}{\varepsilon_1 + 2\varepsilon_h}, \quad (2.26b)$$

where f is the volume filling fraction of the ε_1 material in the composite. Note that the term $1/N$ in (2.25b) represents the volume occupied by each molecule, and is replaced by f/N in (2.26b) accordingly.

When dealing with a composite material, the parameter ε in (2.26a) should represent the effective permittivity of the composite. We substitute the polarizability α (2.26b) into (2.26a) and obtain

$$\frac{\varepsilon - \varepsilon_h}{\varepsilon + 2\varepsilon_h} = f \frac{\varepsilon_1 - \varepsilon_h}{\varepsilon_1 + 2\varepsilon_h}. \quad (2.27)$$

Alternatively, the effective permittivity ε can be expressed in an explicit way as:

$$\varepsilon = \varepsilon_h \frac{1 + 2f \frac{\varepsilon_1 - \varepsilon_h}{\varepsilon_1 + 2\varepsilon_h}}{1 - f \frac{\varepsilon_1 - \varepsilon_h}{\varepsilon_1 + 2\varepsilon_h}}. \quad (2.28)$$

The central formula in the Maxwell–Garnett theory (MGT), (2.28) is known as the Maxwell–Garnett formula, which describes the bulk effective permittivity of a composite in terms of the permittivity of the inclusion ε_1 and the host dielectric constant ε_h . For a metal–dielectric composite, we can view the metal as the inclusion while the dielectric component serves as the host. An equivalent form of (2.27), derived using the Rayleigh scattering theory, was first formulated by J. C. Maxwell Garnett when studying the color of glasses with embedded metal colloids [9].

Although the effective permittivity in MGT can reach the permittivities of the two constituents when the filling fraction approaches the two extreme values of $f = 0$ and $f = 1$, (2.27) clearly shows that MGT treats the matrix and the inclusion in an unsymmetrical manner. Therefore, before evaluating the effective parameters of a two-phase composite using MGT, one constituent has to be considered the “host” and the other the “inclusion.” This asymmetry is particularly strong when the difference in the permittivities of the two materials is large. In fact, MGT provides a reasonable estimation of the effective dielectric function only when the volume filling factor of the inclusion is substantially less than 1. In this case the MGT formula of (2.28) can be expanded using a Taylor series as:

$$\varepsilon = \varepsilon_h + 3f\varepsilon_h \frac{\varepsilon_1 - \varepsilon_h}{\varepsilon_1 + 2\varepsilon_h} + O(f^2) \quad (2.29)$$

Thus the Maxwell–Garnett formula, to the first order of approximation, is a linear function of the filling function f and does not yield a critical threshold f_c for the metal–insulator phase transition of a composite. The resonance in the MGT model occurring at $\varepsilon_1 = -2\varepsilon_h$ represents the surface plasmon resonance of an isolated spherical metal particle embedded in the host. The Drude model for noble metals in (2.12) indicates that this plasmon resonance occurs at

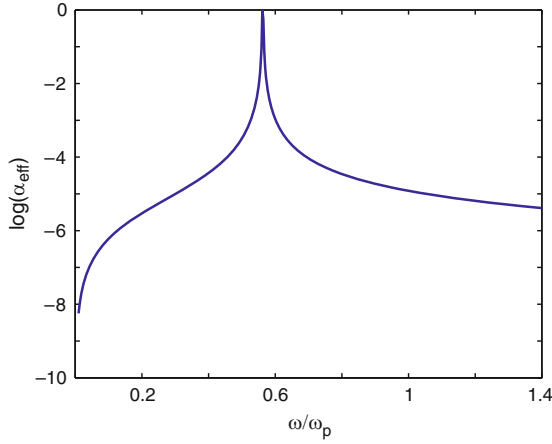


Fig. 2.10 The effective absorption coefficient of a dilute suspension of metal particles in a vacuum. A volume filling fraction $f = 0.05$ and a Drude damping constant of $0.002\omega_p$ are used in the calculation

$$\omega = \omega_p / \sqrt{1 + 2\varepsilon_h}. \quad (2.30)$$

In Fig. 2.10 the normalized absorption coefficient defined as $\alpha = (2\omega/c)\text{Im}\sqrt{\varepsilon_{\text{eff}}}$ for a dilute suspension of metal spheres in a vacuum is plotted as a function of the frequency normalized by ω_p [21]. A Drude metal with $\Gamma = 0.002\omega_p$ is assumed, and the metal filling fraction is taken as 5%. The spectral position of the prominent absorption peak in Fig. 2.10 approaches the surface plasmon frequency of a metal given by (2.30) in the limit of low filling fraction.

In order to evaluate the effective parameters of a composite medium without restricting the analysis only to the low- f cases, Bruggeman made a great improvement to the Maxwell–Garnett theory by finding a way to treat the two constituent materials in a symmetric fashion, thus overcoming many of the difficulties of MGT that we discussed above. Bruggeman’s EMT is, arguably, the most widely known version among a variety of mean-field theories.

Let us consider spherical particles of two different materials ($\varepsilon_1, \varepsilon_2$) that are dispersed in a host matrix with a dielectric constant of ε_h . The volume filling factors of the two inclusions are f_1 and f_2 , respectively. In this case (2.26a) should be modified to

$$\frac{\varepsilon - \varepsilon_h}{\varepsilon + 2\varepsilon_h} = \frac{N_1\alpha_1}{3\varepsilon_0\varepsilon_h} + \frac{N_2\alpha_2}{3\varepsilon_0\varepsilon_h}, \quad (2.31)$$

where polarizabilities α_1 and α_2 have forms as in (2.26b). After some algebra we obtain the counterpart of (2.27) for a two-inclusion composite:

$$\frac{\varepsilon - \varepsilon_h}{\varepsilon + 2\varepsilon_h} = f_1 \frac{\varepsilon_1 - \varepsilon_h}{\varepsilon_1 + 2\varepsilon_h} + f_2 \frac{\varepsilon_2 - \varepsilon_h}{\varepsilon_2 + 2\varepsilon_h}. \quad (2.32)$$

Clearly, the two inclusions are now induced in a symmetric manner. Note that in a two-phase composite where $f_1 + f_2 = 1$, each constituent should be regarded as

one inclusion, and the “host” medium is the composite material itself. Therefore in (2.32) we set $\varepsilon = \varepsilon_h$ and have:

$$f_1 \frac{\varepsilon_1 - \varepsilon}{\varepsilon_1 + 2\varepsilon} + f_2 \frac{\varepsilon_2 - \varepsilon}{\varepsilon_2 + 2\varepsilon} = 0. \quad (2.33)$$

This is the effective-medium expression first developed by D. A. G. Bruggeman in 1935 [10]. Because of its immense popularity in the research of composite media, in conventional terminology Bruggeman’s method and the result in (2.33) are simply referred to as the “effective medium theory.” A rigorous procedure for the derivation of Bruggeman’s expression can be obtained by requiring that the electric flux deviation spatially average to zero in the composite [22].

Unlike the Maxwell–Garnett theory, the two components here are symmetrical with respect to the exchange of roles of ε_1 and ε_2 . In other words, in EMT both phases are considered to be embedded in the effective medium, and there is no need to give preference to one phase over the other. Since each component is treated equally in the mixture, it is quite straightforward to generalize (2.33) to any number of components:

$$\sum_i f_i \frac{\varepsilon_i - \varepsilon}{\varepsilon_i + 2\varepsilon} = 0, \quad \sum_i f_i = 1. \quad (2.34)$$

Equation (2.33) is a quadratic equation with the solution

$$\varepsilon = \frac{1}{4} \left\{ (3f_1 - 1)\varepsilon_1 + (3f_2 - 1)\varepsilon_2 \pm \sqrt{[(3f_1 - 1)\varepsilon_1 + (3f_2 - 1)\varepsilon_2]^2 + 8\varepsilon_1\varepsilon_2} \right\}. \quad (2.35)$$

The sign in the formula above is chosen in such a way that the imaginary part of the effective permittivity is positive. This is required by causality in any passive media.

As an example, in Fig. 2.11 we show the effective permittivity of silver-silica composites for a series of metal filling factors. A typical silver–silica composite in

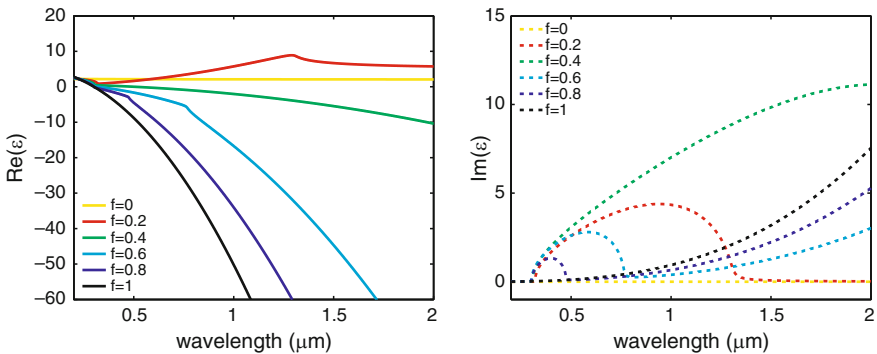


Fig. 2.11 The real and imaginary parts of the effective permittivity of silver-silica composites for a series of metal filling factors. The silver permittivity is from the modified Drude model in (2.17), and the dielectric function of silica is based on a Sellmeier formula

the Bruggeman geometry is illustrated in Fig. 2.8b. The real part of ε_{eff} approaches the silver permittivity with increasing metal filling fraction f , which is a rather intuitive result. Interestingly, the imaginary part of ε_{eff} shows a broadened resonance peak due to the electromagnetic interactions between the metal and dielectric grains.

In addition to the self-consistent symmetry feature, another important advantage of Bruggeman's EMT over MGT is that EMT predicts a critical filling fraction for metal, which is usually referred to as the percolation threshold. In Fig. 2.11 we see that the resonance band in ε_{eff}'' is very broad in the curve where $f = 0.4$. In fact, this peak can extend to an infinite bandwidth if the filling fraction approaches $1/3$, which is the percolation threshold for a three-dimensional metal-dielectric composite. Electronically, the percolation threshold represents the minimum volume fraction of conducting particles needed for the formation of a continuous conducting pathway. In a composite where the magnitude of the metal permittivity $|\varepsilon_1|$ is much larger than the permittivity of the dielectric component ε_2 , using (2.35) we can approximate the effective permittivity ε as:

$$\frac{\varepsilon}{\varepsilon_1} = \begin{cases} \frac{1}{2}(3f_1 - 1), & \text{if } \frac{1}{3} < f_1 \leq 1 \\ 0 & \text{if } 0 < f_1 \leq \frac{1}{3} \end{cases} \quad (2.36)$$

Equation (2.36) clearly indicates that the metal-dielectric composite acts as a dielectric medium for small metal concentrations of less than one third. Beyond the percolation threshold, the composite acts as a dilute metal with an effective permittivity proportional to $(f - 1/3)$.

The sudden change in the electronic conductivity at the percolation threshold can be proved by direct calculations using EMT because the conductivity is related to the imaginary part of permittivity by $\sigma(\omega) = \omega\varepsilon''(\omega)$. The effective conductivity of metal-dielectric composites for a series of metal filling factors is shown in Fig. 2.12. In this calculation, the same Drude metal as that from Fig. 2.10 is used as the metal component, and the dielectric part is assumed to be a vacuum. The broad resonance peaks in Fig. 2.12 are identical to the resonance bands shown in Fig. 2.11. The most interesting features in Fig. 2.12 are that spikes in the effective conductivity occur at $\omega \rightarrow 0$ when the metal filling fraction is larger than the percolation threshold of $1/3$. In other words, the composite electronically acts like an insulator with an extremely low DC conductivity when $f < 1/3$, and the composite becomes a conductor for $f > 1/3$ because a continuous metallic path is formed across the sample and the metal component forms an infinite cluster [20].

In all the foregoing analysis of this section, we assumed that the metal-dielectric composite is a three-dimensional medium, which seems to be a trivial assumption for any real samples. However, there is an important category of random media where the composite material is confined to a thin layer with a deeply subwavelength thickness. In this case, the composite should be considered to be a two-dimensional film. An easy way to generalize the MGT and EMT analyses for a d -dimensional medium is to replace the term $(\varepsilon_i + 2\varepsilon)$ in the denominators of the MGT and EMT

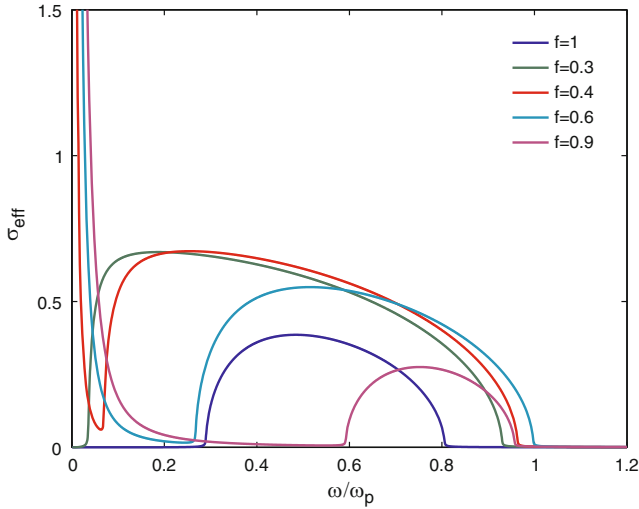


Fig. 2.12 The effective conductivity of metal-dielectric composites calculated by (2.35) for a series of metal filling factors

expressions in (2.27) and (2.33) by $[\varepsilon_i + (d - 1)\varepsilon]$. Specifically, the generalized MGT for a d -dimensional medium is:

$$\frac{\varepsilon - \varepsilon_h}{\varepsilon + (d - 1)\varepsilon_h} = f \frac{\varepsilon_1 - \varepsilon_h}{\varepsilon_1 + (d - 1)\varepsilon_h}, \quad (2.37)$$

and the EMT expression becomes

$$f_1 \frac{\varepsilon_1 - \varepsilon}{\varepsilon_1 + (d - 1)\varepsilon} + f_2 \frac{\varepsilon_2 - \varepsilon}{\varepsilon_2 + (d - 1)\varepsilon} = 0. \quad (2.38)$$

Accordingly, the resonance peak in MGT for a low- f metal-dielectric film will occur at $\omega_p/\sqrt{1 + (d - 1)\varepsilon_h}$, and the percolation threshold in EMT becomes $1/d$, which is 0.5 for a two-dimensional semicontinuous metal film.

Another important matter in all mean-field theories is the issue of particle shape in the composite material. The previous derivations of the Clausius–Mossotti relation, the Maxwell–Garnett Theory and the Effective Medium Theory are all based on the assumption that the inclusions are spherical particles. When the shape of the inclusion particles is notably non-spherical, modified forms of MGT or EMT must be used with an additional depolarization or screening factor that accounts for the effect of particle shape. To be more general, we consider an inclusion of ellipsoidal particles with semiaxes a_i , a_j and a_k . In this case, the polarizability is as follows [23]:

$$\alpha_{ii} = \frac{\varepsilon_0 \varepsilon_h (\varepsilon_1 - \varepsilon_h)}{(\varepsilon_1 - \varepsilon_h) L_i + \varepsilon_h} a_i a_j a_k, \quad (2.39)$$

where L_i is the depolarization factor given by:

$$L_i = \int_0^\infty \frac{a_i a_j a_k ds}{2(s + a_i^2)^{3/2} (s + a_j^2)^{1/2} (s + a_k^2)^{1/2}}, \quad (2.40)$$

The depolarization factor L_i depends on the shape of the particle and the direction of the incident light's electric field with respect to the particle axis a_i . The values of L_i lie between 0 and 1/3 when a particle is prolate along the a_i axis, while the L_i values are between 1/3 and 1 if the particle is disk-like along the a_i axis. The sum of all three depolarization factors $\sum L_i$ must equal unity for any particle shape. Numerical integrations and graphs for the depolarization factors of ellipsoids can be found in [24]. Simplified analytical formulas for special ellipsoids like prolate and oblate spheroids are also available [25]. However, we suggest that the interested reader calculate the integral in (2.40) directly, which can be easily handled with many computational software packages.

With the inclusion shape effect taken into consideration, the Maxwell–Garnett formula should be written as:

$$\frac{\varepsilon - \varepsilon_h}{\varepsilon + \kappa \varepsilon_h} = f \frac{\varepsilon_1 - \varepsilon_h}{\varepsilon_1 + \kappa \varepsilon_h}, \quad (2.41)$$

and the EMT formula becomes

$$f_1 \frac{\varepsilon_1 - \varepsilon}{\varepsilon_1 + \kappa \varepsilon} + f_2 \frac{\varepsilon_2 - \varepsilon}{\varepsilon_2 + \kappa \varepsilon} = 0, \quad (2.42)$$

where κ is the screening parameter determined by the shape and the orientation of the nanoparticles with respect to the external electric field. Factor κ is related to the Lorentz depolarization factor L by:

$$\kappa = (1 - L)/L. \quad (2.43)$$

Therefore, a long elliptical cylinder placed along the electrical field will have a depolarization factor close to zero and a screening factor κ approaching infinity. An extreme version of this scenario is a film of well-aligned, thin silver wires, which exerts full screening for light in one polarization but has no screening in the perpendicular direction. Such a film is routinely used as a linear polarizer in optical systems.

Notice that for spherical nanoparticles, $L = 1/3$ and $\kappa = 2$. Thus the formulas in (2.41) and (2.42) reduce to the commonly seen expressions for MGT and EMT, respectively. Just as MGT works well only when the filling factor is small, (2.41) is reliable only when the screening is not substantial. If the depolarization factor is close to zero, there is strong interaction between the nanoparticles and the external field, and the system will not behave in the way the shape-dependent MGT predicts. In this case, the modified EMT of (2.42) should be used even with a small metal filling fraction. Moreover, the shape-sensitive EMT also produces a modified percolation threshold, given as $f_c = L$. With even further statistical treatments,

the shape-dependent MGT or EMT formulas can be extended to randomly oriented ellipsoidal inclusions [26].

The effective medium approach can also be used “in reverse.” In nanocrystal research, it is a standard practice to calculate the permittivity of nanoparticles when the permittivity of the other component is known and that of the whole composite is measured [27]. In such applications, Bruggeman’s EMT is preferred over MGT because singularities may arise in reversed MGT calculations when the fraction of nanoparticles is large or when the contrast in the permittivities of the two phases is significant. Of course, when non-spherical nanoparticles are present in the system being considered, EMT with morphology information as in (2.42) should be used accordingly.

We note that the mean-field theories discussed above are just analytical approximations for the calculation of the effective permittivity of a composite. Although very simple and easy to implement, such theories fail to address the fine features of the composite down to the subwavelength scale. The most general effective medium approach is the spectral representation method (also known as the Bergman theory or the Bergman–Milton representation), in which a set of spectral density functions are used as fit functions and correlate with the geometrical information in the composite [28, 29]. In the spectral representation theorem, the micro- or nano-scale features are no longer simply neglected or described using numbers like the depolarization factor L , but are fully taken into account by defining geometrical functions whose analytical properties are quite general. The spectral representation method clearly distinguishes between the influence of the geometrical structure and that of the dielectric properties of the components on the effective behavior of the system. It generally holds without further restrictions, as long as the quasistatic approximation is valid. For spherical or well-aligned ellipsoidal inclusions, the solutions from the spectral representation method will simply reduce to the MGT or Bruggeman’s EMT expressions under certain assumptions. The mathematics of the spectra representation is quite involved, and a full discussion is out of the scope of this chapter. Readers that wish to explore this topic in detail can turn to the original papers [28–30] and specific books on the spectral representation method [21, 31].

References

1. Kittel C (2004) Introduction to solid state physics, 8th edn. Wiley, New York
2. Palik ED (ed) (1997) Handbook of optical constants of solids. Academic Press, New York
3. Jackson JD (1998) Classical electrodynamics. Wiley, New York
4. Trager F (ed) (2007) Springer handbook of lasers and optics. Springer
5. Bass M (ed) (1995) Handbook of optics, Vol.2. McGraw-Hill Professional, New York
6. Weber MJ (2002) Handbook of optical materials. CRC Press, Boca Raton, FL
7. Johnson PB, Christy RW (1972) Optical-constants of noble-metals. Phys Rev B 6:4370–4379
8. Karlsson AV, Beckman O (1967) Optical extinction in colloid system NaCl – Na. Solid State Commun 5:795–798
9. Maxwell Garnett JC (1904) Colours in metal glasses and in metallic films. Phil Trans R Soc Lond 203:385–420

10. Bruggeman DAG (1935) Calculation of various physics constants in heterogenous substances I. Dielectricity constants and conductivity of mixed bodies from isotropic substances. *Annalen Der Physik* 24:636–664
11. Polder D, Vansanten JH (1946) The effective permeability of mixtures of solids. *Physica* 12:257–271
12. Looyenga H (1965) Dielectric constants of heterogeneous mixtures. *Physica* 31:401–406
13. de Loor GP (1964) Dielectric properties of heterogeneous mixtures with a polar constituent. *Appl Sci Res B* 11:310–320
14. Bohren CF, Battan LJ (1982) Radar backscattering of microwaves by spongy ice spheres. *J Atmos Sci* 39:2623–2628
15. Sen PN, Scala C, Cohen MH (1981) A self-similar model for sedimentary-rocks with application to the dielectric-constant of fused glass-beads. *Geophysics* 46:781–795
16. Sihvola AH, Kong JA (1988) Effective permittivity of dielectric mixtures. *IEEE Trans Geosci Remote Sens* 26:420–429
17. Monecke J (1994) Bergman spectral representation of a simple expression for the dielectric response of a symmetrical 2-component composite. *J Phys Condens Matter* 6:907–912
18. Landauer R (1977) In: Garland JC and Tanner DB (eds) *Electrical conductivity in inhomogeneous media*. AIP conference proceedings, New York, pp. 2–45
19. Ishimaru A (1978) *Wave propagation and scattering in random media*. Academic, New York
20. Shalaev VM (2000) *Nonlinear optics of random media: fractal composites and metal-dielectric films*. Springer, Berlin
21. Bergman DJ, Stroud D (1992) *The physical properties of macroscopically inhomogeneous media*. Academic, New York
22. Choy TC (1999) *Effective medium theory*. Oxford University Press, New York
23. Stratton JA (1941) *Electromagnetic theory*. McGraw-Hill, New York
24. Osborn JA (1945) Demagnetizing factors of the general ellipsoid. *Phys Rev* 67:351
25. van de Hulst HC (1981) *Light scattering by small particles*. Dover, New York
26. Banhegyi G (1986) Comparison of electrical mixture rules for composites. *Colloid Polym Sci* 264:1030–1050
27. Black MR, Lin YM, Cronin SB, Rabin O, Dresselhaus MS (2002) Infrared absorption in bismuth nanowires resulting from quantum confinement. *Phys Rev B* 65:195417
28. Bergman DJ (1980) Exactly solvable microscopic geometries and rigorous bounds for the complex dielectric-constant of a 2-component composite-material. *Phys Rev Lett* 44:1285–1287
29. Milton GW (1980) Bounds on the complex dielectric-constant of a composite-material. *Appl Phys Lett* 37:300–302
30. Bergman DJ (1978) Dielectric-constant of a composite-material – problem in classical physics. *Phys Rep* 43:378–407
31. Milton GW (2002) *The theory of composites*. Cambridge University Press, Cambridge

Chapter 3

Experimental Techniques and Data Treatment

3.1 Fabrication of Two-Dimensional Optical Metamaterials

Like most branches of materials science, the central task of metamaterials research is not only design, testing or theoretical exploration, but also the fabrication of real structures. No matter how spectacular the predicted outcome seems to be, it is not much more than an illusion or a dream unless there is at least a remote hope of realization. In this sense, the recent boom in optical metamaterial research is only possible because of advances in nanofabrication technology developed during the last 20 years. Unlike metamaterials for microwave frequencies, whose unit structures can be handled even with bare hands, the fabrication of optical metamaterials is intrinsically challenging. The reason is simple: The definition of metamaterials requires that the size of the build blocks be substantially smaller than the wavelength under consideration, which is just a few hundred nanometers for visible light. Therefore, the creation of an optical metamaterial is bound to include the construction of meta-atoms at a deep subwavelength scale and the dense packing of the meta-atoms in an effective medium with prescribed properties. Undertaking such a task relies on quite complicated techniques such as electron-beam lithography, focused ion beam milling, nanoimprint lithography, interference optical lithography, direct laser writing, and more. In this section we will give a general overview of a range of fabrication techniques commonly used for two-dimensional (2D) and three-dimensional (3D) optical metamaterials. An extensive review of different fabrication processes has been presented in [1].

Although most optical materials in real-life devices have to be three-dimensional, the manufacturing of truly 3D plasmonic metamaterials creates daunting technological challenges. Moreover, many of the evolving techniques for 3D optical metamaterials are closely related to standard 2D fabrication methods. Therefore in the following discussion, we shall first focus our attention on the fabrication of 2D plasmonic nanostructures.

Despite the fact that photolithography is the dominant process used for microfabrication in the integrated circuit industry, the small periodicities and tiny feature sizes in most optical metamaterials still exceed the capability of the start-of-the-art, 193-nm photolithographic technology where deep ultraviolet light with $\lambda = 193$ nm

is used for exposure. As a result, the majority of the reported 2D layers of plasmonic metamaterials have been fabricated using electron-beam lithography, often abbreviated as e-beam lithography or EBL. Most of the milestone results in photonic metamaterials up to now have been achieved using the EBL technique. Examples include metamaterials with a negative index of refraction [2], prominent magnetic response [3], giant chiral effect [4], and so on.

In contrast to photolithography, EBL employs a focused beam of electrons instead of a light beam to form the desired patterns on a surface covered with an exposable film. The de Broglie wavelength of high-energy electrons is much smaller than that for light, and therefore EBL can significantly overcome the light-frequency diffraction limit that plagues all typical photolithography systems. The electron beam spot size can be as small as a few nanometers, which allows for extremely fine patterns down to the nanoscale regime. EBL is the most prevalent tool for the fabrication of planar nanostructures because it enjoys complete flexibility in patterning as far as 2D geometries are concerned. Moreover, EBL is a maskless process, unlike traditional photolithography, and so EBL does not require the fabrication of any mask plates before the fabrication can proceed. In addition, the patterns for EBL can be changed very easily through software control.

The main drawback of EBL is the relatively poor efficiency, both in terms of time and money. Compared to other common fabrication processes, EBL is very expensive and takes significantly longer to create the desired pattern. This is because the electron beam must be scanned across the pattern area serially, in a pixel-by-pixel fashion. Hence, within a reasonable time of a few hours, only a small area of sub-millimeter size can be patterned. The fabrication cost is also a major consideration, as EBL facilities are highly complex and require substantial maintenance. In addition to these issues, EBL patterns can also be very challenging when it comes to lifting off the pattern from the substrate if the size of the desired features is smaller than the thickness of e-beam resist. Therefore, EBL is not a suitable solution for patterning large areas or doing volume production of optical metamaterials. Despite these disadvantages, EBL still remains the tool of choice for fabricating quasi-2D optical metamaterials with metal-dielectric unit structures.

Another serial fabrication technique that can be used to make optical metamaterials is focused-ion beam (FIB) milling. Instead of an electron beam, a FIB system uses a focused beam of gallium ions to modify or pattern a design. While the electron beam in EBL only modifies the exposable resist, the accelerated ions in FIB have energies of tens of keV and are “strong” enough to sputter atoms – both metal and dielectric – from the surface of the specimen. FIB is primarily used as a micro-machining tool for purposes such as circuit modification and read-write head trimming. The focused spot size of the ion beam is around 10 nm, which make FIB an alternative technique for the fabrication of photonic metamaterials. Unlike EBL fabrication, where the e-beam writes a pattern on a resist layer and metal-dielectric layers are deposited afterwards, in FIB milling the ion beam directly carves pre-deposited layers into the desired nanostructures. With this technique, split-ring resonators (SRRs) operating at $\sim 1.5 \mu\text{m}$ were reported with a feature size of 100 nm across an area over $300 \mu\text{m}^2$ (see Fig. 3.1b) [5]. Although such a pattern is

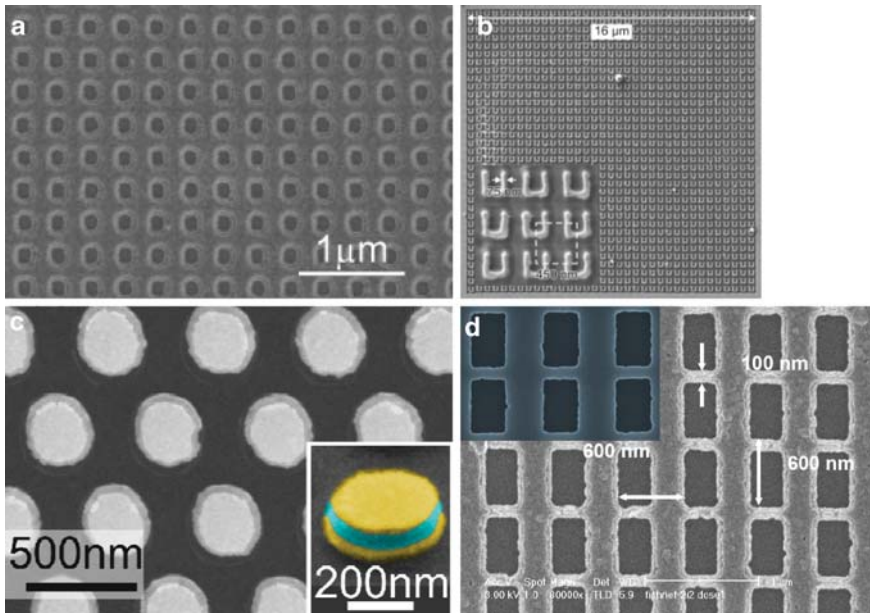


Fig. 3.1 Examples of 2D optical metamaterials using various fabrication techniques. (a) A negative-index material working at a red light frequency made by EBL. Reproduced from [13] by permission of the *MRS Bulletin*; (b) An array of planar SRRs from FIB milling. Reproduced with permission from [5]. Copyright Wiley-VCH Verlag GmbH & Co. KGaA; (c) A hexagonal array of “nano-burgers” made by IL. Reprinted with permission from [8]. Copyright (2007) OSA; (d) A fishnet structure generated by NIL, with inset showing the hard mold. Adapted from [10]

well within the capability of EBL, FIB milling does offer some advantages. Notably, EBL fabrication of such samples requires time-consuming dose tests and processing operations, leading to a relatively longer overall fabrication time. In contrast, FIB milling does not involve any post-processing steps, and the optimization procedure during the operation is less complicated than the EBL technique. It reportedly took as short as 20 min to create SRR patterns across a $16\ \mu\text{m} \times 16\ \mu\text{m}$ pattern area [5].

We note that although FIB milling is impressive in its time efficiency, it is not a good choice for making high-quality samples of optical metamaterials. The best attainable resolution for FIB milling is generally inferior to that from EBL systems. More importantly, FIB is inherently a destructive and contaminating process. When hitting the surface of the target, high-energy gallium ions can be implanted into the top surface of the sample. As a result, the dielectric component of the metamaterial may become porous, and the metal part may exhibit substantially altered properties. Such undesired modifications of the material properties can result in an unpleasant discrepancy between the predicted performance and the experimental observations of a metamaterial sample. Therefore, in some specific designs, FIB can serve as a good choice for rapid prototyping, but it is usually not considered as a general tool for the fabrication of arbitrary 2D optical metamaterials.

Both EBL and FIB milling techniques suffer from low throughput because they both perform a pixel-by-pixel scan throughout the desired pattern area. Consequently, neither EBL nor FIB is capable of large-scale or volume production. The largest possible size of the pattern area for these techniques is no more than the millimeter scale, and it takes an equally large amount of effort to simply reproduce the same structure. Fortunately, several techniques have been developed and adapted to manufacture 2D photonic metamaterials with much higher efficiency. Such novel techniques include interference lithography and nanoimprint lithography.

Interference lithography (IL), also known as holographic lithography, is a variation of photolithography that can pattern periodic features without the use of photomasks. In the IL process, two or more coherent light beams interfere to generate a standing wave, which can be recorded in a photoresist. For the fabrication of optical metamaterials, the most significant advantage of the IL technique is its capability of producing large-area patterns. Indeed, IL makes it possible to fabricate metamaterial films and coatings over a wide area, comparable to that of commercial optics (~ 1 inch. in size). Similar to standard optical lithography, IL uses a single-step exposure instead of a slow raster scan to modify the recording resist. Therefore, a pattern area similar to the coherent beam size is completed at once. This patterned area can be as large as the centimeter scale. Moreover, the periodic nature of interference patterns fits perfectly well with the arrangement of meta-atoms, which requires a certain ordering in most cases. Several metamaterials with artificial magnetism or a negative index of refractive in the near- or mid-infrared ranges have been reported based the IL process [6–8].

However, the IL technique has intrinsic constraints which prevent it from serving as a general tool for the fabrication of optical metamaterials. Interference lithography is within the category of photolithography in any case, so it suffers from the conventional diffraction limit. This is the major reason that most experimental demonstrations of IL-generated metamaterials work for the infrared range instead of the visible. Another serious concern is the pattern flexibility. Unlike EBL or standard photolithography that can produce almost any arbitrary shape in a pattern, in the IL process the geometry of unit cells and periodicities is rather limited. For example, the fringes from two-beam interference give rise exclusively to gratings or strips, and three-beam interference produces arrays with hexagonal symmetry and elliptic units. In order to create a rectangular lattice, either the delicate arrangement of four coherent beams or a double-step exposure of two-beam interference is required. Spatial coherence among the all the interfering beams is strictly required. Although recent advances in IL techniques such as immersion and multiple exposures have extended IL capabilities to some extent, this technique is not likely to become the candidate for the fabrication of arbitrarily designed optical metamaterials. The major merit of IL lies in its cost-efficiency in handling the mass production of some special metamaterial patterns.

For volume production of nanostructures with low processing cost, the recently developed process of nanoimprint lithography (NIL) offers a promising possibility. Unlike most lithographic approaches that achieve the desired pattern definition by modifying the chemical properties of a recording resist layer using exposure

with light or electrons, NIL accomplishes pattern transfer by direct mechanical deformation of the resist using a hard mold or stamp. The mold contains the nanoscale features to be produced and is pressed onto a soft resist under controlled environmental conditions. The resolution of NIL fabrication is not limited by any diffraction or scattering effects, and the smallest attainable features are solely defined by the mold fabrication, which can be on the order of 10 nm. The fabrication of the hard stamp is quite challenging, but once the appropriate hard mold is ready, the mass production of the same nanostructure can proceed with unparalleled efficiency. A review of the methods and material requirements of the NIL technique can be found in [9].

Several optical metamaterials created with NIL have been reported in literature. In [10], for example, large-area patterning of a fishnet structure with metal-dielectric-metal stacks was demonstrated. In that work, a negative refractive index at a near-infrared wavelength was observed. A mid-infrared magnetic metamaterial consisting of L-shaped resonators with fourfold dispersion symmetry was reported by the same group [11]. The NIL technique was also successfully applied to an infrared chiral metamaterial at room temperature [12]. Although NIL provides an attractive opportunity for high-throughput manufacturing, this technique is rarely used for testing novel designs of photonic metamaterials because the process of template or mold patterning is quite involved, and it must rely on other lithographic processing techniques like EBL, photolithography, or FIB as well as reactive ion etching methods.

To end this section, in Fig. 3.1 we provide SEM images for typical optical metamaterials from the four fabrication techniques discussed thus far. Figure 3.1a shows the SEM image of a negative-index metamaterial (NIM) that operates at a red light frequency and was made by EBL [13]. A FIB-generated array of planar SRRs exhibiting a magnetic resonance in the near-infrared is depicted in Fig. 3.1b [5]. As for large-scale 2D patterns, Fig. 3.1c shows a hexagonal array of “nano-burgers” fabricated with a three-beam IL technique, where a pyramid-shaped prism is used to generate three coherent waves from one largely expanded laser beam [8]. Finally, Fig. 3.1d illustrates the SEM image of a fishnet pattern made by the NIL technique that exhibits a negative index of refraction in the near-infrared range [10].

3.2 Approaching the Third Dimension

In the previous section we discussed the fabrication processes for 2D photonic metamaterials, where the produced structures typically have to lay on a flat substrate and have a thickness of much less than a wavelength. In order to make full use of the novel properties of optical metamaterials, a sufficient interaction length between the impinging light and the artificial medium is usually necessary in realizing functional devices. The importance of the effort in moving from planar patterns to truly 3D nanostructures cannot be overestimated. Unique fabrication techniques must be developed for the synthesis of 3D optical metamaterials with subwavelength, complicated meta-atoms.

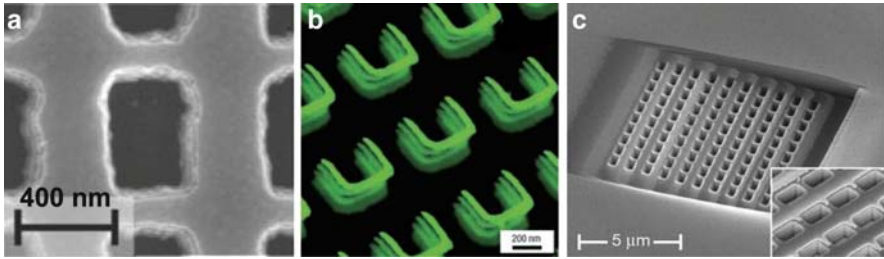


Fig. 3.2 Examples of 3D optical metamaterials fabricated in a layer-by-layer manner. (a) A near-infrared NIM with three functional layers made by EBL. Reprinted with permission from [15]. Copyright (2007) OSA; (b) Four layers of SRRs based on EBL with patterning-and-flattening approach. Reprinted from [16] by permission from Macmillan Publishers Ltd: Nat. Mater., copyright (2008); (c) A NIM wedge exhibiting negative refraction for visible light made by an advanced FIB technique. Reprinted from [17] by permission from Macmillan Publishers Ltd: Nature, copyright (2008). Courtesy of X. Zhang

Although still relatively rare in the literature, a number of approaches have been proposed and demonstrated for the creation of photonic metamaterials with sufficient thickness. One straightforward way of approaching the third dimension in metamaterials is to create more stacks in a standard EBL fabrication. For negative-index materials (NIMs) with the fishnet geometry, it has been shown in simulations that stacking multiple functional layers will not deteriorate the overall performance of the NIM [14]. This finding brings hope to the possibility of bulk optical metamaterials by stacking together planar layers of 2D structures. Based on this prediction, a NIM of three functional layers exhibiting a negative refractive-index in the near-infrared was demonstrated using a standard EBL process [15]. The produced sample is shown in Fig. 3.2a.

While the realization of a three-layered NIM can be viewed as an important step towards thicker metamaterial slabs, this method is not likely to be a viable candidate for making real 3D optical metamaterials. Anyway, the total thickness of the triple-layer NIM in [15] is less than 200 nm, much smaller than the wavelength of its negative-index band. It is not quite feasible to increase the number of layers much because there is a limit to the thickness of patterned structures that a standard EBL process can handle, for two reasons. First, for a given resolution of features, the thickness of the resist layer can not be arbitrary large due to constraints in the lift-off procedure. Secondly, the EBL procedure usually produces non-vertical side walls with a slanted angle of about 8° with respect to the substrate normal. Therefore, the cross-section of the resultant structure is trapezoidally shaped, with the opening at the bottom substantially smaller than that of the top layer. When the total thickness of the nanostructure is increased further, the openings of patterns close to the substrate can even diminish to zero.

In order to overcome the two constraints of the standard EBL process mentioned above, a patterning-and-flattening approach was presented for multiple-layered optical metamaterials [16]. When the first layer of metallic SRRs is completed using a conventional EBL process, a solidifiable polymer is spin-coated on the metallic

nanostructure to flatten the surface of the patterned sample. Afterwards, alignment, in-plane fabrication and planarization procedures are repeated to generate multiple layers. In a demonstration of this technique in [16], four layers of well-aligned SRRs were fabricated, as seen in Fig. 3.2b. A magnetic response in the SRRs at the near-to mid-infrared frequencies was observed in the produced sample. Although this layer-by-layer EBL technique using a planarization process is a promising method to create multi-layered samples of better quality compared to the standard, single-step EBL process, it might be too costly to create large-scale and thick 3D optical metamaterials in this way due to the tedious repetition of steps involved in the fabrication procedure.

The FIB milling technique discussed in the previous section can also be used to create optical metamaterials of multiple functional layers. For this purpose, alternating films of metal and dielectric materials with designed thickness are first evaporated on a substrate. After that, FIB milling is used to cut through the whole stack to form nano-sized patterns. Based on this FIB process, a fishnet NIM structure of ten functional layers was reported [17]. The aspect ratio in the milled nanostructure is rather high, with a side wall angle of only 4.3° . Moreover, in the work in [17] the fishnet stacks was milled into a wedge, and a reversed Snell's law was directly observed with the refracted beam bending in the "wrong" direction. The SEM image of the fishnet wedge is shown in Fig. 3.2c.

The fabrication of multilayered metal-dielectric metamaterials by FIB or EBL is a critical extension of the standard 2D nanopatterning techniques, but such a process can not be used to create truly 3D meta-atoms with an arbitrary design. From Fig. 3.2a–c we see that the geometry in each structure is basically invariant along the vertical direction, except for the slanted angles induced in the fabrication processes. All these structures, to some extent, can be viewed as the result of extruding 2D patterns, instead of genuine 3D architectures. Recently, a number of advanced techniques have been developed with the potential of 3D patterning of metallic structures. Below we outline some of these novel fabrication approaches.

One of these approaches is the technology of two-photon-photopolymerization (TPP), also referred to as direct laser writing (DLW), which makes use of polymerization via a nonlinear, multiphoton process that occurs at the focal point of a tightly focused laser beam [18]. By controlling the location of polymerization in a 3D matrix, TPP allows for the fabrication of 3D nanostructures at sub-diffraction-limit spatial resolutions. The 3D polymeric structure created with TPP serves as a skeleton that can be coated with metal to complete the plasmonic nanostructure, since such designs contain both metal and dielectric components. The metallization process is usually achieved through the deposition of metallic nanoparticles by means of electroless plating, which is a very flexible metallization approach and allows for site-selective metal coating [19, 20]. Figure 3.3a shows the SEM image of an array of silver-coated nano-springs fabricated by the TPP technique [21].

The DLW technique is capable of not only sculpting delicate 3D meta-atoms, but it also can create entire 3D arrays of bulk metamaterials. Many complicated photonic crystals with features of less than $1\ \mu\text{m}$ have been produced based on the DLW method. Compared to the application of TPP/DLW in 3D photonic crystals,

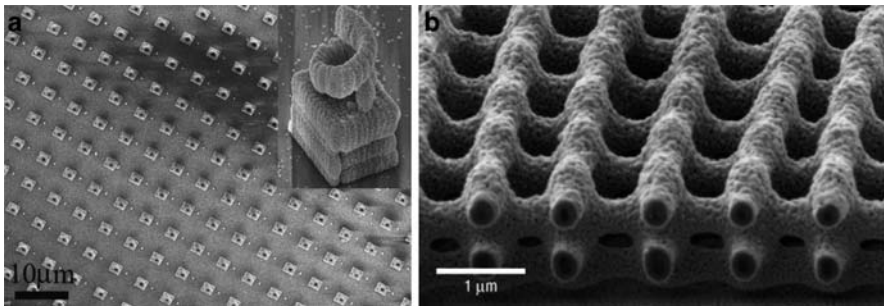


Fig. 3.3 Examples of 3D metal-dielectric nanostructures fabricated using a multiphoton polymerization technique. (a) Array of silver-coated nano-springs made by TPP and electroless plating, with inset showing in individual structure. Reprinted with permission from [21]. Copyright (2006) OSA. (b) 3D array of silver-coated nano-bars fabricated by direct laser writing and chemical vapor deposition. Reprinted from [23] by permission from Macmillan Publishers Ltd: Nat. Mater., copyright (2008)

however, the creation of bulk optical metamaterials is even more challenging in two regards. First, the features of metamaterials, by definition, should be smaller than those of photonic crystals for the same wavelength. Second, most metamaterials require metal components in their unit structures, which is not easily achievable with common metallization methods such as evaporation or sputtering. Fortunately, several approaches have been demonstrated for coating the polymer backbone with metals, sometimes within selectively preset areas [22]. The example of a 3D array of thin bars is shown in Fig. 3.3b, where a layer of silver is coated on the polymer backbone via chemical vapor deposition [23]. The silver on the sample in Fig. 3.3b appears to be somewhat granular, but it is connected nonetheless. An easy-to-understand review of the principles and applications of the multiphoton polymerization technique is presented in [24].

Other fabrication methods for 3D metal-dielectric nanostructures include direct electron-beam writing [25], focused-ion beam chemical vapor deposition [26], 3D holographic lithography [27], deep X-ray lithography [28], and multilayer nanoimprint lithography [29]. Some of these techniques may suffer from strict material and geometry limitations, but they have shown impressive capabilities in producing complicated 3D photonic crystals, and it will not be surprising to see delicate 3D metamaterials resulting from these techniques. A detailed discussion of all pertinent methods is beyond the scope of this section. Readers with a special interest may refer to comprehensive reviews on the fabrication of optical metamaterials or photonic crystals [1, 30].

Besides the top-down approaches discussed above, there are several bottom-up methods where 3D artificial media are created based on self-assembly or self-organization through controlled chemical processes. Such chemical synthesis approaches may be able to produce all the patterns in a bulk structure in parallel. Therefore, these methods would potentially cost much less than top-down methods that create a desired structure by carving the space point by point. However, we

should note that all self-assembly schemes are very specific, working only for some particular array patterns along with very strict material constraints. In most of cases, we cannot rely on self-assembly or self-organization in order to realize an arbitrarily designed metamaterial with prescribed properties. Nevertheless, there have been a number of experiments showing the potential of bottom-up fabrication methods for making some types of optical metamaterials. For example, self-assembly of opals was shown to serve as a versatile template, to which subsequent synthesis of guest materials including metals, semiconductors and insulators can be introduced [31]. Such opal templates have been successfully applied to silicon photonic crystals [32]. In another work, three-dimensional arrays of hollow silver spheres were created using polymer colloidal crystals as templates [33]. For large-scale metamaterials consisting of two-dimensional arrays of thin wires, the honeycomb structures of anodic alumina or silicon can work as amazing templates [34]. In another experiment, a bulk NIM was reported based on the self-organization of porous alumina and metal electroplating [35]. Under appropriate anodizing conditions, a self-ordered porous alumina structure with pores arranged in a hexagonal lattice can be produced. When the array of voids is fully formed, silver nanowires can be grown inside the nanopores of the template, and a uniform 2D array of silver wires in the alumina host is created. With the right geometrical parameters, such a bulk metamaterial can exhibit negative refraction in the red light wavelength range [35].

3.3 Characterization of Spectral Properties

When a photonic metamaterial is properly designed and successfully fabricated, the next step is to characterize the obtained nanostructure. In this section, we briefly discuss several common methods for determining the spectral properties of optical metamaterials. The characterization of optical nanostructures can be grouped into two categories: standard nano-characterization tools, and bench-top optical measurements. The former group includes instruments like scanning electron microscopes (SEM) and atomic force microscopes (AFM), as well as various near-field optical microscopes. Here we focus on the latter category, which usually consists of small-scale optical components and devices set up on optical tables and lab benches.

The testing approaches for metamaterials can be quite diverse. Depending on the specific objective of the study, there are a range of experimental observables routinely used for the analysis of the properties of structures at optical frequencies. When a probe light beam impinges upon a piece of a sample, the most prominent information from the specimen is contained in the reflected and transmitted light. As with all electromagnetic waves, the reflected and transmitted beams contain both magnitude and phase information, which are all important and whose values are deeply rooted in the properties of the sample. At optical frequencies, the magnitudes of reflectance R and transmittance T , which can be obtained via intensity measurements using various power detectors, are much more accessible than the phase information, which is attainable only with complicated interferometric

schemes. In the following discussion we consider several approaches suitable for the measurement of spectral magnitude information from photonic metamaterials. The possible methods to experimentally extract the phase information will be addressed at the end of this section.

The most commonly used characterization method for optical metamaterials is measurement of broadband transmission and reflection spectra. Although not a complete set of information due to the lack of phase properties, the spectrally dependent T and R curves help to locate the spectral positions and evaluate the relative strengths of resonances in a metamaterial. In fact, almost all experimental demonstrations of optical metamaterials present the T and R spectra as functions of the incident wavelength. Moreover, a reasonable agreement between the experimental spectra and data from simulations or calculations is usually considered to be convincing proof for the validity of the theoretical work and the success of fabrication procedures.

In most cases, we consider a layer of metamaterial to be a macroscopically planar and uniform slab. Consequently, when light is incident upon the sample, only regular transmission and specular reflection are considered, while all other scattering and diffusion processes are generally neglected. The principle behind the spectral measurement of T and R is quite simple. The probe light should come from a broadband or tunable light source, such as a tungsten-halogen lamp or a supercontinuum of light generated from nonlinear fibers. The probe light impinges upon the sample, and the transmitted or reflected beam is then introduced into a detection device, such as a photodiode, a charge-coupled device (CCD), or a photomultiplier. A monochromator is usually inserted in the optical path, either before or after the sample, in order to analyze the spectrum. The transmission and reflection spectra should be collected using appropriate references. In the transmission measurement, free space is a good reference for $T = 100\%$ if the whole specimen (including substrate) is considered to be the sample, or an empty substrate area without patterns can be used as the reference if only the nanostructured layer is to be evaluated. When measuring the reflectance, a good mirror or a special reflectance standard should be used to calibrate the $R = 100\%$ reference. Polarization control of the optical system is necessary, as most optical metamaterials are highly anisotropic.

Spectrophotometers are the standard commercial equipment for the collection of broadband T and R spectra. A spectrophotometer can be viewed as a combination of a spectrometer, which generates light of any selected wavelength, and a photometer that measures the radiant flux. Most spectrophotometers are configured in a dual-beam manner, where one beam is used to probe the sample and the other serves as a reference. In a typical spectrophotometer, the angle of incidence is easily adjustable in the transmission mode, while reflection at normal incidence is usually approximated using a small incidence angle in order to separate the incident and reflected beams. When the scattering and diffusion portions of the reflected and transmitted light are to be collected, an integration sphere can be used in the detection module.

In the characterization of optical metamaterials, however, the measurement of transmission and reflection usually cannot be carried out in a commercial spectrophotometer. Samples fabricated by EBL or FIB are usually very small, with a

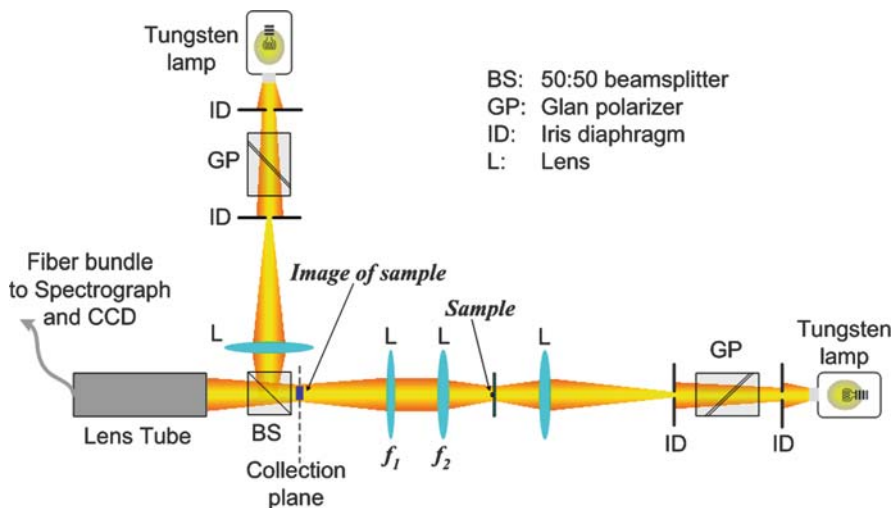


Fig. 3.4 A “home-made” setup for collecting broadband transmission and reflection spectra of small samples. Reprinted with permission from [3]. Copyright (2007) OSA

typical size on the order of a hundred micrometers. Such a sample area is not large enough for most spectrophotometers, and appropriate sample holders and accessories are not available for handling and locating the invisibly small pattern region. There are different ways to resolve this difficulty in optical experiments. Many advanced microscopes have detection modules and employ a highly focused light spot from objective lenses. Such a multifunctional piece of equipment allows for the observation and spectral measurement of a specimen simultaneously. The spectral measurement can also be carried out using a home-made setup with basic optical components. An example of such a setup is illustrated in Fig. 3.4, which utilizes an imaging approach. The small sample of size S is imaged onto the focal plane of the collection system, which may include a fiber bundle and a spectrograph. The magnified image size is $S \cdot (f_1/f_2)$, which is set to be significantly larger than the collecting area of the optical system to ensure reliable data collection. A high-quality polarizer like a Glan–Taylor prism is placed at the output of the broadband lamps to select light with the desired linear polarization. The transmission and reflection spectra can be normalized to a bare substrate and a calibrated silver mirror, respectively.

Since most metamaterials are absorptive, it is informative to present the absorption spectrum of the sample under investigation. More importantly, plasmonic resonances in optical metamaterials are always accompanied by distinct absorbance. Therefore, the peaks in the absorption curve are often used as fingerprints for identifying the resonance features. In most cases, the absorption (A) is not directly measurable, but is inferred from transmission and refraction data based on the simple relationship $A = 1 - T - R$.

In the infrared frequency range, there is another distinct approach for spectral characterization, namely the Fourier transform infrared spectroscopy (FTIR).

In contrast to spectral domain measurements that rely on dispersive elements to separate different wavelengths, FTIR is a time-domain measurement where spectra are indirectly determined based on the measurement of the temporal coherence of an infrared source. The FTIR method avoids using the usually slow scanning process in monochromator-based instruments. Instead, in a FTIR spectrometer, signals at all frequencies of a light source are measured simultaneously based on an interferometer, usually in a Michelson configuration. The mirror in one arm of the interferometer is stationary, while the other arm contains a moving mirror oscillating back and forth. The output of the interferometer is incident upon the sample and is then introduced into a detector. The resultant interferogram, which is an intensity pattern varying over time, can be viewed as an encoded signal containing information from all wavelengths of light coming from the infrared source. The detected interferogram signal is then decoded by Fourier transformation through computer software, and the frequency spectrum of the sample can be obtained. Once the FTIR is initiated and the sample is properly mounted, the whole data collection process is extremely fast – typically on the order of one second. A FTIR spectrum also enjoys a better signal-to-noise ratio compared to most dispersive spectrometers due to a greater optical throughput. In FTIR, all light from the source enters the detector simultaneously, while in conventional spectrometers, only light within a tiny portion of spectrum is collected at one time.

As mentioned above, the end of this section includes a brief discussion on the issue of phase measurement in optical metamaterials. In order to evaluate the phase shift of light when passing through a metamaterial layer, a combination of special interferometers and power measurement is usually necessary. When the metamaterial being studied is highly anisotropic, it is possible to estimate the phase shift property by measuring the phase difference between two orthogonally polarized light beams [2, 36]. An example of experimental setup for measuring the phase anisotropy of a thin metamaterial slab is shown in Fig. 3.5a. This setup employs the polarization interferometry to evaluate the difference in phase shifts between two orthogonally polarized waves, $\Delta\varphi = \varphi_{\parallel} - \varphi_{\perp}$. The spectra of $\Delta\varphi$ is capable of revealing the resonance property of the phase shift in the sample. A more informative approach for phase measurement is to directly detect the phase shift of a sample with respect to a well-defined reference. The walk-off interferometer shown in Fig. 3.5b provides such a capability. The walk-off configuration has two optical channels which differ in geometrical paths. It gives a phase shift φ_s introduced by a sample relative to that of a reference layer of air φ_r with the same thickness and the same boundary condition: $\delta\varphi = \varphi_s - \varphi_r$. The birefringence effect in uniaxial crystals like calcite is employed to separate the two beams with orthogonal polarizations and then bring them together to produce interference. Note that the difference between the obtained values of absolute phase shift for the two orthogonally polarized beams should be the same as the phase anisotropy measured by using the setup in Fig. 3.5a, as can be seen from the following relationship:

$$\Delta\varphi = \varphi_{\parallel} - \varphi_{\perp} = (\delta\varphi_{\parallel} + \varphi_r) - (\delta\varphi_{\perp} + \varphi_r) = \varphi_{s,\parallel} - \varphi_{s,\perp} \quad (3.1)$$

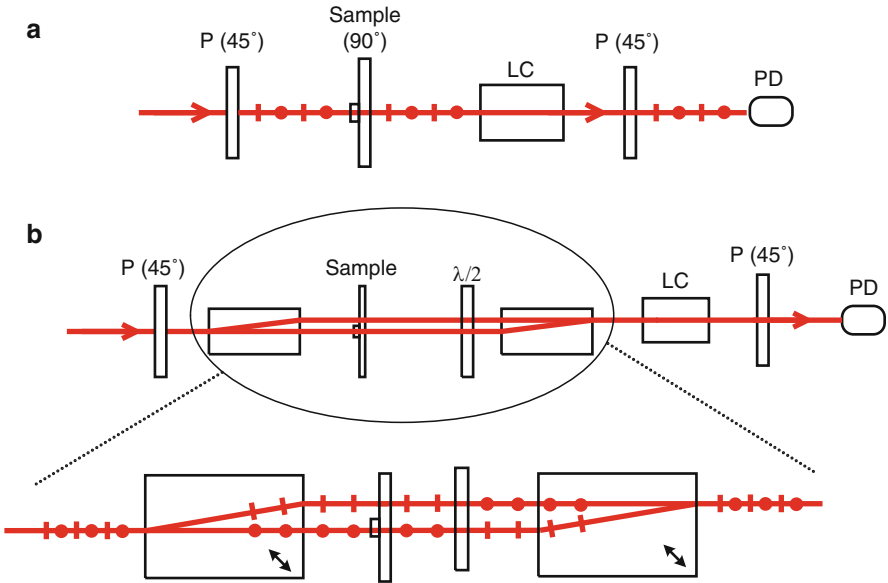


Fig. 3.5 The experimental setup for phase measurement. **(a)** The common-path polarization interferometer for phase anisotropy measurement. **(b)** The walk-off interferometer to detect the absolute phase shift of the sample. *P* polarizer; *LC* liquid crystal tunable waveplate; *PD* photodetector; $\lambda/2$ variable half waveplate. Orthogonal polarizations of light are shown by *dots* and *lines*

This provides an easy way to check the validation of the measured data. Detailed discussions of the two setups in Fig. 3.5 are available in [37, 38].

Another successful phase measurement of optical metamaterials with a different interferometric configuration has been conducted in [7]. The phase shift of light within a metamaterial layer can also be obtained using ultrashort pulses, as demonstrated in [39, 40]. It is also possible to extract phase information from metamaterials, to some extent, using ellipsometry techniques. In ellipsometry, the change in the polarization state of light reflected from the sample is measured. The ellipsometric coefficients Ψ and Δ provide as much information as a phase anisotropy measurement in the reflection mode at an inclined angle. In particular, spectroscopic ellipsometry employs a broadband spectrum of probe light, thus it is able to reveal some of the frequency-dependent phase information without using delicate home-made apparatus. Such measurements have been used in verifying a magnetic response from SRRs in the terahertz range [41].

3.4 Extraction of Homogenized Optical Parameters

For a given metamaterial with fine features much smaller than the wavelength of interest, one of the most critical tasks is to extract the effective parameters including the electric permittivity ϵ , magnetic permeability μ , refractive index n

and impedance Z from experimental observables. In the general case, all of these parameters are complex quantities with both real and imaginary parts. The four parameters are not independent, and they can be grouped into two sets. The first set, ε and μ , stems from the constitutive relations in (2.2), and directly enters Maxwell's equations. The other two quantities, n and Z , are more conveniently used in the description of wave phenomena at the boundary of different materials. The two sets are interrelated by $\varepsilon = n/Z$ and $\mu = nZ$. Strictly speaking, all these variables are frequency-dependent, as mentioned in Chap. 2.

For a uniform slab made of a metamaterial, an ideal retrieval process is expected to replace the microscopically inhomogeneous slab with a conceptually uniform medium with effective parameters (ε and μ , or n and Z) such that the far-field scattering patterns are faithfully reproduced. Even though the unit structures of a metamaterial can be very complicated, the local details of the electromagnetic responses are encapsulated by distilling the macroscopic parameters from the composite media. The philosophy involved here is not much different from the use of these quantities for conventional materials – the responses from a collection of scattering atoms or molecules are conveniently described in an averaged fashion, as we have detailed in the previous chapter. The most accessible experimental observables from which the homogeneous parameters are extracted include the complex transmission and reflection coefficients t and r . At microwave frequencies, equivalent quantities named the scattering parameters (S -parameters) are sometimes preferred among electrical engineers.

There are numerous methods to determine the complex refractive index $n = n' + in''$ of a conventional, non-magnetic ($\mu = 1$) medium. These methods, although usually not immediately applicable to obtaining the effective parameters of a metamaterial, are still of considerable interest among the researchers in this field. One of the most straightforward methods is the so-called (R, T) approach [42], where the only required observables are the magnitudes of reflection R and transmission T from the sample under test with a known thickness at normal incidence. The relations between (R, T) and n are described by the generalized Fresnel's law, including the coherence conditions between the different interfaces in the system [43]. Another approach is to measure only one of the magnitude spectra $R(\omega)$ or $T(\omega)$ at normal incidence over a broad spectral range, and then perform a Kramers-Kronig analysis. This method is more useful when the testing sample is opaque and thus only $R(\omega)$ is measurable [44]. However, if the reflection R at only some particular spectral lines is available, one has to gather both the magnitude and the phase information of the complex reflectivity r . This is the basic idea behind the ellipsometry technique.

We note, however, that all the schemes mentioned above cannot be directly applied to obtain the electromagnetic parameters in a metamaterial. For a general metamaterial, there are at least four variables to be determined, because both the effective permittivity ε and the permeability μ are complex quantities having unknown real and imaginary parts. Alternatively, one can use the other set of parameters $n = n' + in''$ and $Z = Z' + iZ''$ to characterize the sample, but again we face four unknowns. As a result, a measurement scheme based solely on the magnitudes of

R and T is not capable of retrieving all the necessary variables. Ellipsometry-type schemes suffer from the additional fact that almost all metamaterials are highly anisotropic with their properties being critically angular-dependent. Since all four unknowns enter into Fresnel's formulas, all the complex coefficients of both r and t are necessary to retrieve the effective parameters of a metamaterial.

Owing to the profound importance of the retrieval process in almost all metamaterial studies, the protocol to extract the effective parameters from experimental observables was investigated by Smith *et al.* soon after their first demonstration of a negative-index material [45]. Similar treatments were developed and reexamined by a number of other experts in metamaterial research [38, 46–49]. The basic physics underlying the retrieval process is rather straightforward. To start, let us consider a homogeneous slab of thickness d under normal incidence. Assuming that the slab is placed in a vacuum, the complex transmission coefficient t and reflection coefficient r are related to the impedance Z and the refractive index n by:

$$t = \left[\cos(nkd) - \frac{i}{2} \left(Z + \frac{1}{Z} \right) \sin(nkd) \right]^{-1} \quad (3.2)$$

and

$$r = -\frac{i}{2} \left(Z - \frac{1}{Z} \right) \sin(nkd) \cdot t, \quad (3.3)$$

where $k = 2\pi/\lambda_0$ is the free space wave vector. The above equations are available in many textbooks on thin film optics (for example, [43]), and can be obtained using a simple summation method based on Fresnel's formulas. Please note that for clarity in the subsequent derivations, the notation t here is a normalized value, which is equivalent to the conventional transmission coefficient times the factor e^{ikd} [45].

We invert the formulas in (3.2) and (3.3) and obtain the explicit expressions for Z and n [45]:

$$Z = \pm \left[\frac{(1+r)^2 - t^2}{(1-r)^2 - t^2} \right]^{1/2} \quad (3.4)$$

$$\cos(nkd) = \frac{1 - r^2 + t^2}{2t} \quad (3.5)$$

When n and Z are available, the other set of material parameters can be obtained immediately by the relationships $\varepsilon = n/Z$ and $\mu = nZ$.

Clearly, (3.4) and (3.5) lead to ambiguity in the retrieved parameters due to the multi-valued nature of trigonometric and square root functions. This problem can be resolved by the combination of several considerations. First of all, for any passive material, the imaginary parts of ε , μ , n and the real part of Z must be positive to obey the causality condition (with the complicated exception for ε'' and μ'' at anti-resonances, see [50] for a detailed explanation). With this constraint, the impedance

Z can be uniquely determined by (3.4). Similarly, the imaginary part of $n = n' + i n''$ is also immediately obtainable by solving (3.5):

$$n'' = \pm \frac{1}{kd} \operatorname{Im} \left[\cos^{-1} \left(\frac{1 - r^2 + t^2}{2t} \right) \right] \quad (3.6)$$

along with the additional requirement of $n'' > 0$. Note that the inverse cosine function $\cos^{-1}(x)$ allows arbitrary complex arguments, in which case the real part of $\cos^{-1}(x)$ is bound within $[0, \pi]$, but there is no such constraint for the range of its imaginary part.

Now it comes to the most nebulous part of the retrieval process, the real part of the refractive index. Equation (3.5) yields the following expression for n' [45]:

$$n' = \pm \frac{1}{kd} \operatorname{Re} \left[\cos^{-1} \left(\frac{1 - r^2 + t^2}{2t} \right) \right] + \frac{2\pi m}{kd}, \quad (3.7)$$

where m is an integer. So there are two ambiguities hidden within (3.7): the sign before the first term on the right-hand side, and the correct branch corresponding to a definite value of m . The first issue is relatively easy to resolve – the same sign as that of (3.6) should be taken since both equations stem from the same complex solution. As for the second ambiguity, for slabs with very small thickness $d \ll \lambda_0$, as in most 2D optical metamaterials, the branches with different values of m are well separated, and the correct branch can be identified by the fact that the frequency-dependent $n'(\omega)$ has to be continuous across a wide wavelength range. The retrieval process usually starts at a sufficiently large wavelength away from all pertinent resonances in the metamaterial. In this case $m = 0$ is taken for slabs of subwavelength thickness. The retrieval is then carried out towards shorter wavelengths, and the index m in (3.7) should be adjusted to counter any discontinuity in $n(\omega)$.

We note that when applying the retrieval process discussed above to metamaterial slabs, a couple of precautions should be taken into consideration. First, the thickness of the effective slab must be well-defined, because the slab thickness d is used as an input to the whole procedure of retrieving the effective parameters. This is not as trivial as it appears to be, because all metamaterials are inherently inhomogeneous when observed at a subwavelength scale. If the thickness of the metamaterial film is also deeply subwavelength, it is hard to identify the exact position of the two boundaries when we approximate the material as a slab with two parallel surfaces. Secondly, the magnitude of the two coefficients t and r should be sufficiently different from zero, otherwise substantial error and uncertainty may occur in the retrieval process. The extracted parameters would have little meaning if the retrieval procedure is highly sensitive to noise-level variations in the complex coefficients t and r . The issues of stability and accuracy of the retrieval algorithm were elaborated in [48,49]. As for the scale of inhomogeneities in the metamaterial, it is always desired to have the size of meta-atoms be much smaller than the illuminating wavelength so that the composite is safely within the metamaterial regime. However, it has been shown that the ε and μ values can be assigned to a metamaterial using the standard

retrieval procedure even when its unit cell has a size comparable to the wavelength of light [49, 51]. Finally, when dealing with metamaterials with apparent resonance behaviors, artifacts may appear in the retrieved effective parameters. Sometimes an anti-resonance accompanied by a nonphysical negative value in the imaginary part of ε (or μ) may occur around the magnetic (or electric) resonance in a metamaterial, owing to the periodic arrangement of the resonant unit cells. Such an anomaly has been observed in many reported results on plasmonic metamaterials.

To conclude this section, we briefly address the issue of uniqueness in the inverse scattering problem because it is a basic principle that makes the retrieval process possible. For a given piece of material under a known illumination, it is natural to accept the fact that a unique electromagnetic response would arise. The reverse statement – that a particular scattering property represented by a combination of t and r uniquely determines the constituent parameters ε and μ – is also true as long as only one component of each tensor (ε or μ) is involved in the light-matter interaction [52]. So the above retrieval procedure is valid when the metamaterial is characterized with normal incidence and a linear polarization is sustained during the light-matter interaction. More complicated protocols are necessary for metamaterials exhibiting chiral or bianisotropic behaviors [53, 54]. In these materials, different polarization states are coupled, and it is not sufficient to describe their electromagnetic responses using just the ε and μ tensors.

The retrieval protocol discussed thus far contains most of the essential physics for extracting effective parameters from the amplitudes and phases of the waves transmitted and reflected from a metamaterial slab. However, this technique is not immediately applicable to most optical metamaterials, because the procedure is based on the assumption that the metamaterial is in the form of a free-standing slab surrounded by a vacuum. In almost all reported metamaterials for the optical frequency, substrate layers are involved, and therefore the metamaterial slabs are embedded in an asymmetric environment. In the most usual case, where one side of the metamaterial slab is immediately attached to a microscopically thick substrate and the other side interfaces air or vacuum, the basic retrieval formulas in (3.4) and (3.5) should be modified to:

$$\cos(nkd) = \frac{1 - r^2 + n_s t^2}{[(n_s + 1) + r(n_s - 1)]t}, \quad (3.8)$$

and

$$Z = \frac{i[(r + 1) - t \cos(nkd)]}{n_s t \sin(nkd)}, \quad (3.9)$$

where n_s represents the index of refraction for the substrate. A general treatment of the retrieval procedure for multilayer systems is provided in [38].

At the end of this section, we want to emphasize that the retrieval of effective parameters from complex t and r coefficients is not only useful for the treatment of experimental data, but also an indispensable tool for the simulation and modeling of metamaterials. Most theoretical work on metamaterials relies on numerical

electromagnetic approaches such as finite-element methods (FEM), finite-difference time-domain (FDTD) methods, the finite integration technique (FIT), and the method of moments (MoM). A number of commercial packages are widely used by metamaterial researchers, including COMSOL Multiphysics[®], CST Microwave Studio[®], RSoft FullWAVE[®], and others. The output of such computational tools is usually the distribution of electromagnetic waves, which should be processed using the retrieval algorithm to extract the effective material parameters. Moreover, for those cases where a complete set of scattering parameters are not fully accessible in experiments, a good agreement between the measured T and R curves of the metamaterial and the simulated spectra is usually regarded as an essential prerequisite for validating the material parameters obtained from simulations, even though there is not sufficient data to extract these parameters purely from experiments.

References

1. Boltasseva A, Shalaev VM (2008) Fabrication of optical negative-index metamaterials: recent advances and outlook. *Metamaterials* 2:1–17
2. Shalaev VM, Cai WS, Chettiar UK, Yuan HK, Sarychev AK, Drachev VP, Kildishev AV (2005) Negative index of refraction in optical metamaterials. *Opt Lett* 30:3356–3358
3. Cai WS, Chettiar UK, Yuan HK, de Silva VC, Kildishev AV, Drachev VP, Shalaev VM (2007) Metamagnetics with rainbow colors. *Opt Express* 15:3333–3341
4. Plum E, Fedotov VA, Schwanecke AS, Zheludev NI, Chen Y (2007) Giant optical gyrotropy due to electromagnetic coupling. *Appl Phys Lett* 90:223113
5. Enkrich C, Perez-Willard R, Gerthsen D, Zhou JF, Koschny T, Soukoulis CM, Wegener M, Linden S (2005) Focused-ion-beam nanofabrication of near-infrared magnetic metamaterials. *Adv Mat* 17:2547–2549
6. Zhang S, Fan WJ, Minhas BK, Frauenglass A, Malloy KJ, Brueck SRJ (2005) Midinfrared resonant magnetic nanostructures exhibiting a negative permeability. *Phys Rev Lett* 94:037402
7. Zhang S, Fan WJ, Panoiu NC, Malloy KJ, Osgood RM, Brueck SRJ (2005) Experimental demonstration of near-infrared negative-index metamaterials. *Phys Rev Lett* 95:137404
8. Feth N, Enkrich C, Wegener M, Linden S (2007) Large-area magnetic metamaterials via compact interference lithography. *Opt Express* 15:501–507
9. Guo LJ (2007) Nanoimprint lithography: methods and material requirements. *Adv Mat* 19:495–513
10. Wu W, Kim E, Ponizovskaya E, Liu Y, Yu Z, Fang N, Shen YR, Bratkovsky AM, Tong W, Sun C, Zhang X, Wang SY, Williams RS (2007) Optical metamaterials at near and mid-IR range fabricated by nanoimprint lithography. *Appl Phys A* 87:143–150
11. Wu W, Yu ZN, Wang SY, Williams RS, Liu YM, Sun C, Zhang X, Kim E, Shen YR, Fang NX (2007) Midinfrared metamaterials fabricated by nanoimprint lithography. *Appl Phys Lett* 90:063107
12. Chen YF, Tao JR, Zhao XZ, Cui Z, Schwanecke AS, Zheludev NI (2005) Nanoimprint lithography for planar chiral photonic meta-materials. *Microelectron Eng* 78–79:612–617
13. Chettiar UK, Xiao S, Kildishev AV, Cai W, Yuan HK, Drachev VP, Shalaev VM (2008) Optical metamagnetism and negative-index metamaterials. *MRS Bull* 33:921–926
14. Zhang SA, Fan WJ, Panoiu NC, Malloy KJ, Osgood RM, Brueck SRJ (2006) Optical negative-index bulk metamaterials consisting of 2D perforated metal-dielectric stacks. *Opt Express* 14:6778–6787
15. Dolling G, Wegener M, Linden S (2007) Realization of a three-functional-layer negative-index photonic metamaterial. *Opt Lett* 32:551–553

16. Liu N, Guo HC, Fu LW, Kaiser S, Schweizer H, Giessen H (2008) Three-dimensional photonic metamaterials at optical frequencies. *Nat Mater* 7:31–37
17. Valentine J, Zhang S, Zentgraf T, Ulin-Avila E, Genov DA, Bartal G, Zhang X (2008) Three-dimensional optical metamaterial with a negative refractive index. *Nature* 455:376–379
18. Kawata S, Sun HB, Tanaka T, Takada K (2001) Finer features for functional microdevices – micromachines can be created with higher resolution using two-photon absorption. *Nature* 412:697–698
19. Formanek F, Takeyasu N, Tanaka T, Chiyoda K, Ishikawa A, Kawata S (2006) Selective electroless plating to fabricate complex three-dimensional metallic micro/nanostructures. *Appl Phys Lett* 88:083110
20. Takeyasu N, Tanaka T, Kawata S (2008) Fabrication of 3D metal/polymer microstructures by site-selective metal coating. *Appl Phys A* 90:205–209
21. Formanek F, Takeyasu N, Tanaka T, Chiyoda K, Ishikawa A, Kawata S (2006) Three-dimensional fabrication of metallic nanostructures over large areas by two-photon polymerization. *Opt Express* 14:800–809
22. Farrer RA, LaFratta CN, Li LJ, Praino J, Naughton MJ, Saleh BEA, Teich MC, Fourkas JT (2006) Selective functionalization of 3-D polymer microstructures. *J Am Chem Soc* 128:1796–1797
23. Rill MS, Plet C, Thiel M, Staude I, Von Freymann G, Linden S, Wegener M (2008) Photonic metamaterials by direct laser writing and silver chemical vapour deposition. *Nat Mater* 7:543–546
24. Li LJ, Fourkas JT (2007) Multiphoton polymerization. *Mater Today* 10:30–37
25. Griffith S, Mondol M, Kong DS, Jacobson JM (2002) Nanostructure fabrication by direct electron-beam writing of nanoparticles. *J Vac Sci Technol B* 20:2768–2772
26. Morita T, Kondo K, Hoshino T, Kaito T, Fujita J, Ichihashi T, Ishida M, Ochiai Y, Tajima T, Matsui S (2004) Nanomechanical switch fabrication by focused-ion-beam chemical vapor deposition. *J Vac Sci Technol B* 22:3137–3142
27. Campbell M, Sharp DN, Harrison MT, Denning RG, Turberfield AJ (2000) Fabrication of photonic crystals for the visible spectrum by holographic lithography. *Nature* 404:53–56
28. Ehrfeld W, Lehr H (1995) Deep X-ray-lithography for the production of 3-dimensional microstructures from metals, polymers and ceramics. *Radiat Phys Chem* 45:349–365
29. Kehagias N, Reboud V, Chansin G, Zelsmann M, Jeppesen C, Schuster C, Kubenz M, Reuther F, Gruetzner G, Torres CMS (2007) Reverse-contact UV nanoimprint lithography for multilayered structure fabrication. *Nanotechnology* 18:175303
30. Busch K, von Freymann G, Linden S, Mingaleev SF, Tkeshelashvili L, Wegener M (2007) Periodic nanostructures for photonics. *Phys Rep* 444:101–202
31. Galisteo JF, Garcia-Santamaria F, Golmayo D, Juarez BH, Lopez C, Palacios E (2005) Self-assembly approach to optical metamaterials. *J Opt A Pure Appl. Opt.* 7:S244–S254
32. Blanco A, Chomski E, Grabtchak S, Ibasate M, John S, Leonard SW, Lopez C, Meseguer F, Miguez H, Mondia JP, Ozin GA, Toader O, van Driel HM (2000) Large-scale synthesis of a silicon photonic crystal with a complete three-dimensional bandgap near 1.5 micrometres. *Nature* 405:437–440
33. Chen Z, Zhan P, Wang ZL, Zhang JH, Zhang WY, Ming NB, Chan CT, Sheng P (2004) Two- and three-dimensional ordered structures of hollow silver spheres prepared by colloidal crystal templating. *Adv Mat* 16:417–422
34. Masuda H, Fukuda K (1995) Ordered metal nanohole arrays made by a 2-step replication of honeycomb structures of anodic alumina. *Science* 268:1466–1468
35. Yao J, Liu ZW, Liu YM, Wang Y, Sun C, Bartal G, Stacy AM, Zhang X (2008) Optical negative refraction in bulk metamaterials of nanowires. *Science* 321:930
36. Kim E, Shen YR, Wu W, Ponziovskaya E, Yu Z, Bratkovsky AM, Wang SY, Williams RS (2007) Modulation of negative index metamaterials in the near-IR range. *Appl. Phys. Lett.* 91:173105
37. Drachev VP, Cai W, Chettiar U, Yuan HK, Sarychev AK, Kildishev AV, Klimeck G, Shalaev VM (2006) Experimental verification of an optical negative-index material. *Laser Phys Lett* 3:49–55

38. Kildishev AV, Cai WS, Chettiar UK, Yuan HK, Sarychev AK, Drachev VP, Shalaev VM (2006) Negative refractive index in optics of metal-dielectric composites. *J Opt Soc Am B* 23:423–433
39. Dolling G, Enkrich C, Wegener M, Soukoulis CM, Linden S (2006) Simultaneous negative phase and group velocity of light in a metamaterial. *Science* 312:892–894
40. Dolling G, Wegener M, Soukoulis CM, Linden S (2007) Negative-index metamaterial at 780 nm wavelength. *Opt Lett* 32:53–55
41. Yen TJ, Padilla WJ, Fang N, Vier DC, Smith DR, Pendry JB, Basov DN, Zhang X (2004) Terahertz magnetic response from artificial materials. *Science* 303:1494–1496
42. Nilsson PO (1968) Determination of optical constants from intensity measurements at normal incidence. *Appl Opt* 7:435–442
43. Heavens OS (1955) *Optical properties of thin solid films*. Butterworths, London
44. Roessler DM (1965) Kramers–Kronig analysis of reflection data. *Br J Appl Phys* 16: 1119–1123
45. Smith DR, Schultz S, Markos P, Soukoulis CM (2002) Determination of effective permittivity and permeability of metamaterials from reflection and transmission coefficients. *Phys Rev B* 65:195104
46. Markos P, Soukoulis CM (2003) Transmission properties and effective electromagnetic parameters of double negative metamaterials. *Opt Express* 11:649–661
47. Ziolkowski RW (2003) Design, fabrication, and testing of double negative metamaterials. *IEEE Trans Antennas Propag* 51:1516–1529
48. Chen XD, Grzegorzczak TM, Wu BI, Pacheco J, Kong JA (2004) Robust method to retrieve the constitutive effective parameters of metamaterials. *Phys Rev E* 70:016608
49. Smith DR, Vier DC, Koschny T, Soukoulis CM (2005) Electromagnetic parameter retrieval from inhomogeneous metamaterials. *Phys Rev E* 71:036617
50. Koschny T, Markos P, Smith DR, Soukoulis CM (2003) Resonant and antiresonant frequency dependence of the effective parameters of metamaterials. *Phys Rev E* 68:065602
51. Kyriazidou CA, Contopanagos HF, Merrill WM, Alexopoulos NG (2000) Artificial versus natural crystals: effective wave impedance of printed photonic bandgap materials. *IEEE Trans Antennas Propag* 48:95–106
52. Wolf E, Habashy T (1993) Invisible bodies and uniqueness of the inverse scattering problem. *J Mod Opt* 40:785–792
53. Chen X, Wu BI, Kong JA, Grzegorzczak TM (2005) Retrieval of the effective constitutive parameters of bianisotropic metamaterials. *Phys Rev E* 71:046610
54. Menzel C, Rockstuhl C, Paul T, Lederer F (2008) Retrieving effective parameters for quasiplanar chiral metamaterials. *Appl Phys Lett* 93:233106

Chapter 4

Electric Metamaterials

4.1 A Brief Overview of Artificial Dielectrics

The present chapter is focused on electric metamaterials, namely, metamaterials with prescribed electric properties. Most of the time the electric response of a medium is described using its electric permittivity ϵ , so the main purpose of studying electric metamaterials is to create artificial metal-dielectric structures that possess a permittivity of a desired value. Such a task, in fact, had been investigated long before the recent explosion of metamaterial research. For example, the beautiful Roman glass shown in Fig. 1.1 can be justly regarded as electric metamaterial consisting of gold nanoparticles embedded in a ruby host, and its color behavior is well-explained using the mixing rules for random metal-dielectric composites described in Chap. 2.

From the 1940s to the 1970s, electric metamaterials with periodic metal-dielectric compositional units were extensively studied under the aegis of radar development, although at that time such materials didn't bear the modern name of electric metamaterials. Instead, the term "artificial dielectrics" was widely used, especially in microwave technology, to describe the man-made materials with subwavelength metal particles periodically distributed in a uniform background host. These materials are called "artificial dielectrics" because they serve as the macroscopic analogue of natural dielectrics except that the atoms or molecules are artificially structured – exactly what we are doing in today's metamaterial research.

The first widely recognized pioneer of artificial dielectrics was probably Winston Kock, an engineer working at Bell Laboratories in the 1940s. In search for low loss, light weight and cost effective lenses for radio waves, Kock proposed several lens structures consisting of parallel metal plates or metallic sphere arrays embedded in a dielectric matrix [1, 2]. A few distinct features of Kock's work merit his recognition as a founding pioneer of the research field of metamaterials. First, he used equivalent material parameters to characterize the response of his artificial dielectrics to the impinging electromagnetic fields. Secondly, he investigated periodic metal-dielectric structures of different effective indices of refraction, both larger and smaller than unity, and he used the terms "phase delay" and "phase advance" to describe wave propagation properties [1, 2]. Moreover, Kock unambiguously pointed out the analogue between his artificial dielectrics and a natural crystalline dielectric material [2].

One of the most important artificial dielectric structures is the “rodded medium” where a periodically spaced lattice of metallic rods is embedded in vacuum or other dielectric material. Early researchers who contributed to the development of this topic include Brown [3], Golden [4], and Rotman [5]. The rodded medium, also known as the wire grid or wire mesh, offers the capability of mimicking a plasma similar to that of a Drude metal, and the plasma frequency of the composite material can be adjusted by varying the geometrical parameters of the wire array. A similar structure was reinvented by Sir John Pendry in the later years of the last century [6]. The application of Pendry’s result to a left-handed media in the year 2000 marked the birth of the metamaterial research field [7].

It is worth noting that although a periodically structured artificial dielectric working at optical frequencies was too difficult to make until the techniques of nanofabrication were developed, the language of optics was well-adopted in the early studies of artificial dielectrics. The index of refraction was quite routinely used when describing the wave behavior in such media at microwave frequencies, and the magnitude, value and dispersion in the effective refractive index of artificial dielectrics can be engineered in a controlled manner. Much literature on microwave artificial dielectrics include the term “optical properties” when the radio wave behavior is characterized using the refractive index, although no functionality at optical frequencies is discussed in these works. A nice review of the progress in the optical properties of artificial dielectrics before the early 1970s was conducted by Silin [8].

The reason why we devote this chapter to electric metamaterials is two-fold. First, optical artificial dielectrics are, incontrovertibly, within the category of photonic metamaterials, although they might not be so novel as to symbolize the metamaterial research field. More importantly, various artificial dielectrics, both periodic and disordered, serve as the bases for more complicated metamaterial structures and devices such as negative-index materials [9] and optical hyperlenses [10]. In fact, since any metamaterial must exhibit an electric response different from that of its constituent materials, it is not exaggerating to say that all metamaterials are at least electric metamaterials, no matter whether the resultant electric property is the primary output of the study or not. Artificial dielectrics are particularly necessary when the desired device requires a gradient in the material property. Examples of structures with a varying permittivity requirement include conventional devices like a Luneburg lens [11] and new inventions such as an optical cloak [12].

4.2 Optical Properties of Stratified Metal-Dielectric Composites

In this section we analyze a periodically layered composite with two isotropic constituent materials aligned in a parallel manner. The bulk permittivities of the two constituents are ϵ_1 and ϵ_2 , respectively. The volume filling fraction of material 1 is noted as f_1 , so the second constituent has a filling factor of $f_2 = 1 - f_1$. In such a system, there are two principal situations to be considered: when the external electric

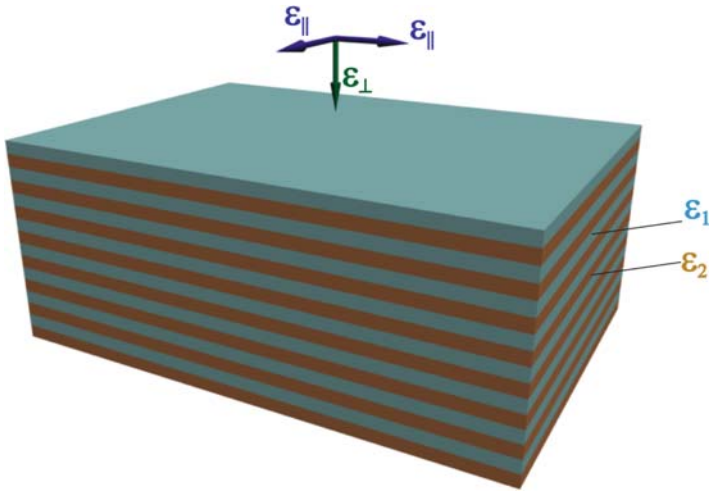


Fig. 4.1 Schematic of a layered metal-dielectric structure, with the permittivities of the two constituents given as ε_1 and ε_2 , respectively. Two principal effective permittivities are marked as ε_{\parallel} and ε_{\perp} .

field is directed either parallel or perpendicular to the planar interfaces. The scenario is depicted in Fig. 4.1. When the thickness of the layers is much smaller than the wavelength, the stratified system acts as a metamaterial and can be described using equivalent parameters. Our goal here is to evaluate the effective permittivity (ε_{\parallel} or ε_{\perp}) for the two principal polarizations.

Regardless of the incident wave electric field polarization, the basic constitutive relation holds for each constituent layer as well as for the whole composite:

$$D_i = \varepsilon_i E_i, \quad (4.1)$$

where the subscript i may be 1 or 2 for the two components or e for the overall effective medium. When the incident wave is polarized parallel to the interfaces of the layered system, the electric field E must be continuous across the boundary between the layers as dictated by Maxwell's equations:

$$E_1 = E_2 = E_e. \quad (4.2)$$

The effective electric flux density D_e is taken as the volume-averaged sum of the flux density in the two constituent layers:

$$D_e = f_1 D_1 + f_2 D_2. \quad (4.3)$$

Combining (4.1)–(4.3), we obtain the effective permittivity ε_{\parallel} of the composite material when the electric field is directed along the layers:

$$\varepsilon_{\parallel} = f_1 \varepsilon_1 + f_2 \varepsilon_2. \quad (4.4)$$

The situation is quite different when the stratified composite is subjected to an electric field polarized perpendicular to the interfaces. In this case the electric flux D_i must be continuous at the boundary between two adjacent layers due to the absence of a surface charge, while the effective electric field in the composite is evaluated in a weighted-average fashion:

$$D_1 = D_2 = D_e, \quad (4.5)$$

$$E_e = f_1 E_1 + f_2 E_2. \quad (4.6)$$

From (4.1), (4.5) and (4.6) we have:

$$\varepsilon_{\perp} = \frac{\varepsilon_1 \varepsilon_2}{f_2 \varepsilon_1 + f_1 \varepsilon_2}. \quad (4.7)$$

Alternatively, the two effective permittivities of a layered composite can be derived based on Bruggeman's effective medium theory with the modification from the shape effect, as given in (2.42):

$$f_1 \frac{\varepsilon_1 - \varepsilon}{\varepsilon_1 + \kappa \varepsilon} + f_2 \frac{\varepsilon_2 - \varepsilon}{\varepsilon_2 + \kappa \varepsilon} = 0. \quad (4.8)$$

The parameter κ in the above equation represents the screening of the external fields by a medium. The screening factor κ reaches its maximum value of infinity when all the boundaries of the composite are parallel to the electric field, and it reaches a value of zero if the field is normal to the boundaries. These two extreme cases correspond exactly to the two principal orientations of the layered system as shown in Fig. 4.1. By setting $\kappa \rightarrow \infty$ in (4.8), we reproduce the expression for ε_{\parallel} in (4.4). As for the perpendicular direction, (4.8) simply reduces to the value for ε_{\perp} in (4.7) when we set $\kappa = 0$.

The formulas of effective permittivity in (4.4) and (4.7) can be generalized for periodically layered systems consisting of more than two materials:

$$\varepsilon_{\parallel} = \sum_i f_i \varepsilon_i, \quad (4.9)$$

$$\varepsilon_{\perp}^{-1} = \sum_i f_i \varepsilon_i^{-1}. \quad (4.10)$$

In the equations above, $\sum f_i = 1$ should be fulfilled for the entire composite. Therefore, the permittivity of a layered composite is equal to the weighted arithmetic mean of the permittivities of all its constituents when the electric field is parallel to the interfaces, and the permittivity takes the value of the weighted harmonic mean of all the constituent permittivities when a perpendicular electric field is applied.

For an arbitrary two-phase composite, the permittivities in (4.4) and (4.7) provide the upper and lower bounds for the effective permittivity of the composite, because the electric field cannot be screened more than the full screening with $\kappa = 0$ or less than the zero screening of $\kappa \rightarrow \infty$. This fact was first revealed by Otto Wiener

in 1912 [13], therefore the expressions in (4.4) and (4.7) are sometimes referred to as the Wiener bounds. A nice way to visualize the Wiener bounds of a metal-dielectric composite is to use the complex permittivity plane, where the real and imaginary parts correspond to the horizontal and vertical axes, respectively [14]. The permittivity of each constituent ε_1 or ε_2 is represented by an isolated point on the complex plane. When varying the filling fractions f_1 and f_2 of the composite, the low-screening bound in (4.4) grows along a straight line connecting the two points given by $\varepsilon_1 = \varepsilon_1' + i\varepsilon_1''$ and $\varepsilon_2 = \varepsilon_2' + i\varepsilon_2''$, while the high-screening bound in (4.7) gives rise to an arc of a circle passing through ε_1 , ε_2 and the origin [15].

To illustrate this scenario, in Fig. 4.2 we plot the Wiener bounds for a titanium-silicon composite at a wavelength of 600 nm. The dielectric constants of the two constituents are $\varepsilon_1 = -4 + 12i$ for Ti and $\varepsilon_2 = 15 + 0.2i$ for Si [16]. When the metal filling fraction changes from $f = 0$ to $f = 1$, the effective permittivity ε_{\parallel} for the parallel polarization varies from ε_2 to ε_1 along the straight solid line, while the permittivity in the perpendicular direction ε_{\perp} grows according to the dashed circular arc. For a fixed metal filling factor, the shape-dependent EMT in (4.8) defines a thin curve in Fig. 4.2 indicating all the possible values for the effective permittivity of the composite, regardless of the microstructure the composite medium may exhibit.

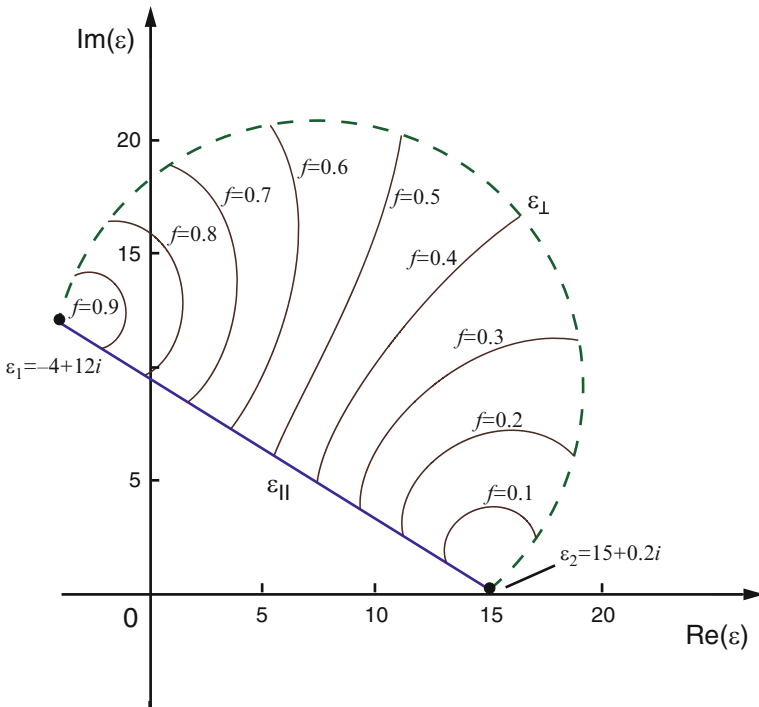


Fig. 4.2 The Wiener bounds for the permittivity of a titanium–silicon composite at $\lambda = 600$ nm. The thin solid lines represent the possible values for the effective permittivity of the composite with fixed metal filling fractions

Note that the thin curve for a given f lies between two points on the Wiener bounds for the same filling factor. This is exactly what Wiener's absolute bounds for the effective permittivity imply.

The Wiener bounds provide us with a convenient tool to estimate the accessible range of effective permittivities in a composite with given constituent materials. By using a layered metal-dielectric composite, the effective permittivity can reach very interesting values that are hard to access in conventional, bulk materials. For example, the dielectric constant of a composite with the electric field parallel to the interfaces can approach zero when the relationship $f_1/f_2 = -\varepsilon_2/\varepsilon_1$ is fulfilled in low-loss constituents. The expression for the perpendicular permittivity ε_{\perp} in (4.7) indicates that the effective permittivity can asymptotically approach infinity if $f_1/f_2 = -\varepsilon_1/\varepsilon_2$ is satisfied. This feature can also be observed using the complex permittivity plane of Fig. 4.2. When the imaginary parts of ε_1 and ε_2 are small, the two points corresponding to $f = 0$ and $f = 1$ both lie very close to the horizontal axis; therefore the circular arc for ε_{\perp} will extend to infinitely large values. Extreme values of permittivity such as $\varepsilon = 0$ and $\varepsilon = \infty$ have great potential in developing photonic nanocircuits, where subwavelength nanoparticles with appropriate dielectric constants are utilized as lumped elements working at optical frequencies [17]. In such nanocircuits, epsilon-infinity materials are needed as conducting wires for optical displacement currents, while the epsilon-near-zero media serve as insulators to isolate each functional element.

A number of metamaterial devices have been proposed and demonstrated based on layered metal-dielectric composites. With appropriate choices for the two constituent permittivities and filling fractions, it is possible to create a highly anisotropic material with ε_{\parallel} close to zero and ε_{\perp} approaching infinity simultaneously. Such layered media have found applications in several versions of superlenses and hyperlenses [10, 18–20]. With dedicated control of the spatially varying thickness combinations, the stratified metal-dielectric structure has also been used in the design of an optical cloaking device in a cylindrical geometry [21].

4.3 Periodic Array of Metallic Wires

In this section we will discuss the “rodded medium” where thin metallic wires are periodically arranged in vacuum or a dielectric matrix. Such wire mesh structures of 1D, 2D and 3D networks were systematically studied by Rotman about half a century ago [5]. Rotman investigated several arrangements of wire grids whose structures are illustrated in Fig. 4.3. The two-dimensional wire array in Fig. 4.3a is designed to produce a plasma resonance for a z -polarized electric field, and the layered grid structure in Fig. 4.3b works for any electromagnetic incidence whose wave vector is directed parallel to the normal of the grid plane. When the metallic wires form a three-dimensional mesh with a periodic cubic lattice, as depicted in Fig. 4.3c, the wire medium becomes quasi-isotropic and exhibits a plasma resonance for fields with arbitrary states of polarization. Such artificial wire composites have

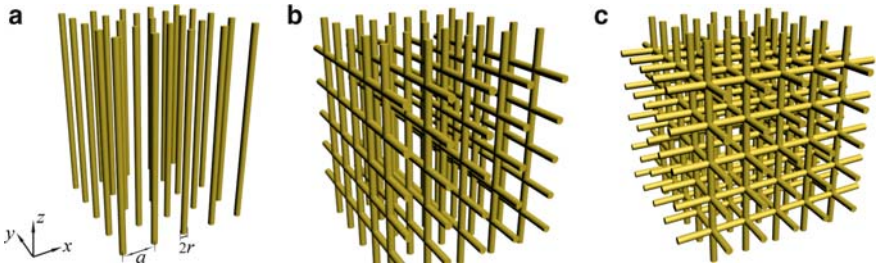


Fig. 4.3 The rodged media of different dimensions studied by W. Rotman. (a) A two-dimensional wire array for z -polarized electric field. (b) A three dimensional lattice for any electric field polarized within the $y - z$ plane. (c) A three-dimensional quasi-isotropic wire grid for arbitrary polarization

been shown to work as dilute plasmas that create a negative electric response with controllable strength. Although they were known for several decades among radio wave engineers as artificial dielectrics with configurable dielectric functions, the wire medium has gained immense prosperity in physics and material science during the last decade, thanks to its reintroduction by Sir John Pendry with a more physics-oriented flavor [6, 22].

The rodged medium can display a plasmonic response in a certain frequency band, depending mostly on the geometrical parameters, namely the wire diameter $2r$ and the length of the unit cell a . When the unit cell length (also known as the lattice constant) of the wire array is small in comparison with the wavelength of interest, the wire array system can be treated as an electric metamaterial because the electromagnetic radiation fails to resolve the wires, which are subwavelength in size for this scenario. In this regard, the primary goal of our study is to obtain the effective dielectric function $\varepsilon(\omega)$ of the wire grid. To simplify our task, we consider a two-dimensional wire array as shown in Fig. 4.3a. The composite medium is apparently anisotropic, and the polarization state we are interested in corresponds to a plane wave propagating in the xy plane with an electric field polarized along the thin wires. In the following analysis, therefore, we use $\varepsilon(\omega)$ to denote the element $\varepsilon_{zz}(\omega)$ in a general 3×3 permittivity tensor.

The effective permittivity $\varepsilon_{eff}(\omega)$ can be written in a Drude form as in (2.12) which includes an effective plasma frequency along with a damping constant representing the dissipation:

$$\varepsilon_{eff}(\omega) = 1 - \frac{\omega_p^2}{\omega(\omega + i\Gamma)}, \quad (4.11)$$

where ω_p and Γ represent the effective plasma frequency and the effective damping constant of the wire medium, respectively. As opposed to a real Drude metal whose plasma frequency and damping factor have definite physical meanings, the two parameters ω_p and Γ in the effective Drude model of (4.11) are closely tied to the geometry of the wire array as well as to the metal properties. Hence, in deriving the

effective dielectric function $\varepsilon_{eff}(\omega)$ for an electric metamaterial, one of the essential tasks is to approximate ω_p and Γ based on known quantities. There are different models for the expression of the effective plasma frequency in a rodged medium. In this section, we strictly follow the effective mass approach initiated by Pendry in his seminal paper [6].

As discussed in Sect. 2.3, the plasma frequency in a bulk metal depends on the density and mass of free electrons, and the plasma frequency is usually situated in the near-UV or visible spectrum for good conductors. In contrast, the plasma frequency of the wire medium is substantially reduced relative to that of the pure metal for two reasons. First, the effective electron density is diluted by a factor of $\pi r^2/a^2$ because the free electrons are restricted within the physical boundaries of the wires. The second reason was described by Pendry as an increase in the “effective electron mass” resulting from the induced current in the wire and the excited magnetic field. The self-inductance possessed in the metallic wires acts to oppose the rate of change in the current, which is a direct result of Lenz’s law. Consequently, the electrons in the wires act as if they have gained a prodigious amount of mass. This increased “effective electron mass” contributes to a reduced plasma frequency in the material. We note however that this notion of the “effective electron mass” should be understood here only in the context of the described self-inductance effect.

Modifying the equivalent plasma frequency expression to account for the reduced effective electron density is quite straightforward. The electron density in the wire array is taken in a volume-averaged manner:

$$N_{eff} = N \frac{\pi r^2}{a^2}, \quad (4.12)$$

where N refers to the actual electron density in the pure metal. Now we turn to the “effective mass” modifications in the plasma frequency expression. In order to evaluate the “effective mass” of electrons due to the self inductance, we apply the concept of generalized (canonical) momentum in quantum mechanics. In the Lagrangian formalism of a charged particle with a static mass m and charge q , the overall momentum has a form of $p = mv + qA$, where v is the charge velocity and A represents a vector potential. Therefore the “effective mass” from the self inductance is related to the magnetic vector potential by

$$m_{eff} = \frac{eA}{v}. \quad (4.13)$$

For a mean electron velocity v and a free electron density N in the metallic wires, the current flow in one wire is $\pi r^2 e N v$. According to Ampère’s law, this current flow gives rise to an azimuthal magnetic field around the wire:

$$H(R) = \frac{\pi r^2 e N v}{2\pi R}, \quad (4.14)$$

where R is the distance from the wire center. The magnetic field $H(R)$ can be written in terms of the curl of a vector potential which is directed along the z axis:

$$H(R) = \nabla \times A(R)/\mu_0. \quad (4.15)$$

Although generally speaking the vector potential $A(R)$ is not uniquely defined because of the issue of gauge choices, our assumption of $r \ll a$ as well as the lattice symmetry allows us to choose the vector potential in the following form:

$$A(R) = \frac{\mu_0 r^2 e N v}{2} \ln(a/R). \quad (4.16)$$

Since we have assumed that the wires are made from good conductors, the flow of free electrons is bound to the surface of the wires. Therefore, it is a fair estimate that all electrons feel a magnetic vector potential of $A(r)$. Combining (4.13) and (4.16), we obtain the ‘‘effective mass’’ of the electrons in the wire medium:

$$m_{eff} = \frac{\mu_0 r^2 e^2 N}{2} \ln(a/r). \quad (4.17)$$

With both N_{eff} and m_{eff} readily available, we obtain the plasma frequency of the wire medium:

$$\omega_p^2 = \frac{N_{eff} e^2}{\epsilon_0 m_{eff}} = \frac{2\pi c_0^2}{a^2 \ln(a/r)}, \quad (4.18)$$

where $c_0 = 1/\sqrt{\mu_0 \epsilon_0}$ is the vacuum light speed.

Several more complicated but precise derivations for the effective plasma frequency of the wire medium have been developed. Shalaev and Sarychev provide the following expression [23, 24]:

$$\omega_p^2 = \frac{2\pi c_0^2}{a^2 \left[\ln\left(\frac{a}{\sqrt{2}r}\right) + \pi/4 - 3/2 \right]}, \quad (4.19)$$

and Maslovski et al. show that the plasma frequency can be expressed as [25]:

$$\omega_p^2 = \frac{2\pi c_0^2}{a^2 \left[\ln(a^2/4r(a-r)) \right]}. \quad (4.20)$$

A comparison between these three models has been conducted in [26]. All three approaches in (4.18–4.20) agree reasonably well with transfer matrix simulations, and the improved expressions for ω_p in (4.19) and (4.20) indeed offer a better prediction of the plasma behavior. Another quite involved analytical formula for ω_p is available in [27].

To complete the Drude approximation for the effective permittivity of the wire array in (4.11), we need to evaluate the effective damping constant Γ , which describes the medium’s loss factor. The damping constant Γ vanishes if the wires are made

of a perfect conductor, and the permittivity of the wire medium is then simply $\varepsilon_{\text{eff}}(\omega) = 1 - \omega_p^2/\omega^2$. However, the finite conductivity of real metals results in ohmic loss in the thin wires, which can be introduced by modifying the inductance of the wire with an imaginary part. From the magnetic field $H(R)$ in (4.14) we can estimate the unit inductance of a wire:

$$L = \frac{\mu_0 \int_r^{\frac{a}{\sqrt{\pi}}} H(R) dR}{\pi r^2 e N v} \approx \frac{\mu_0}{2\pi} \ln\left(\frac{a}{r}\right). \quad (4.21)$$

The denominator in the equation above is equal to the current flow in the wire, and the upper limit $a/\sqrt{\pi}$ of the integration represents the equivalent radius of a unit cell in the wire array. The approximation in (4.21) holds for thin wires with $r \ll a$.

Comparing (4.18) and (4.21), we find that the plasma frequency ω_p of the wire medium is related to the inductance of a wire by:

$$\omega_p^2 = \frac{1}{\varepsilon_0 a^2 L}. \quad (4.22)$$

A detailed derivation of effective plasma frequency from the self-inductance perspective is presented in [25].

When the metal has a finite conductivity σ , the inductance of the wire is taken as a complex value with the following modification:

$$L \rightarrow L + \frac{\sigma \pi r^2}{i \omega}. \quad (4.23)$$

Combining (4.11), (4.21), (4.22) and (4.23), we finally obtain the expression for the effective permittivity of the wire medium in a Drude form [6]:

$$\varepsilon_{\text{eff}}(\omega) = 1 - \frac{\omega_p^2}{\omega(\omega + i \varepsilon_0 a^2 \omega_p^2 / \pi r^2 \sigma)}. \quad (4.24)$$

If the wire array is embedded in a host medium with a permittivity ε_h instead of a vacuum, the first term in the right-hand side of (4.24) should be replaced by ε_h .

Since the effective plasma frequency in a wire medium can be tuned by adjusting the medium's geometrical parameters, the spectral region of desired permittivity values can be engineered to occur practically at any frequency range from the microwave region to the optical range. Using metals made into an array of thin wires, the plasma frequency ω_p of a medium can be reduced by several orders of magnitude.

In the next part of this section, we provide an example of a wire medium with an effective plasma frequency in the gigahertz regime. We take a two-dimensional wire array with a wire radius of $r = 5 \mu\text{m}$ and a lattice constant of $a = 40 \text{ mm}$. The wires consist of silver, which has a free electron density of $N = 5.8 \times 10^{28} \text{ m}^{-3}$ and a conductivity of $6.3 \times 10^7 \text{ S m}^{-1}$ at room temperature. In the wire medium, the

electron concentration is diluted by eight orders of magnitude according to (4.12). As for the “effective electron mass,” (4.17) predicts that m_{eff} is 2.1×10^{25} kg, which is “heavier” than a silver atom. The substantially reduced electron density and increased “effective electron mass” together give rise to a reduction in the effective plasma frequency by six orders of magnitude. The expression by Pendry in (4.18) gives a plasma frequency of $\omega_p = 2\pi \times 1.0$ GHz, while (4.19) and (4.20) both indicate a slightly different value of $\omega_p = 2\pi \times 1.1$ GHz.

As for the dissipation in the wire medium, from (4.24) we obtain a damping constant of $\Gamma = 0.018\omega_p$. Therefore, the loss factor in our artificial dielectric is on the same order of that of usual conductors, considering that the ratio Γ/ω_p is 0.011 for copper. The effective permittivity of the wire medium in our example is plotted in Fig. 4.4.

Similar to a Drude metal, the wire array metamaterial has a negative permittivity for electromagnetic waves with frequencies lower than the effective plasma frequency. Above the plasma frequency, the effective permittivity is positive and the medium acts as a transparent dielectric. This feature shows the potential of using the wire array for filters and polarizers. Indeed, a plasmonic, high-pass filter based on a two-dimensional cubic lattice of gold wires has been reported for terahertz electromagnetic radiation [28]. It is worth noting that in practical applications, the wires do not necessarily consist of pure metals. Instead, a dielectric skeleton forming the lattice and coated with a desired metal works equally well as the pure metal case, as long as the metal coating is thicker than the metal’s skin depth at the operational frequency. This technique is especially useful when precious and therefore expensive metals like silver or gold are involved in design.

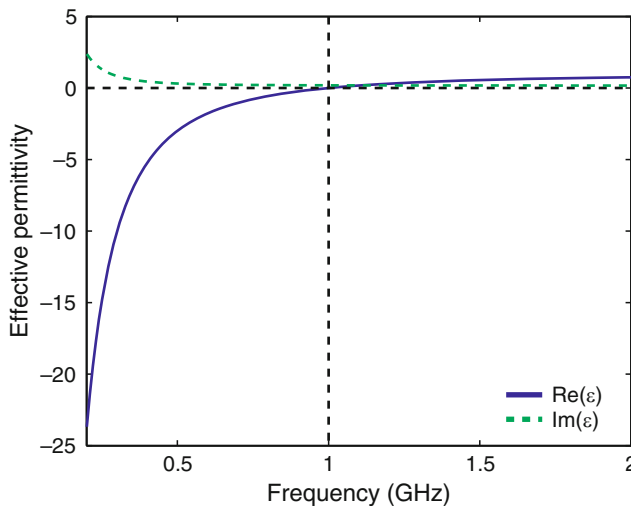


Fig. 4.4 The dielectric function of a silver wire array with $r = 5 \mu\text{m}$ and $a = 40$ mm. The horizontal axis represents the wave frequency $f = \omega/2\pi$. The effective plasma frequency is $\omega_p = 2\pi \times 1$ GHz, and the damping constant is $\Gamma = 0.018\omega_p$

The wire array in our example is comfortably within the applicability regime of the effective-medium limit and can be safely viewed as a metamaterial because the lattice constant a is only about one-tenth of the free space wavelength at 1 GHz ($\lambda = 0.3$ m). The metal filling fraction in the wire-array metamaterial is only a few parts per million. It is possibly surprising that such a low concentration of metal is enough to induce such a dramatic change in the effective dielectric function $\varepsilon(\omega)$. This feature, in fact, is not unexpected if we think of the rodged medium using the language described in Sect. 2.4. When the incident electric field is polarized along the wires, the field experiences a minimum of screening as indicated by a near-zero depolarization factor. Therefore, a small concentration of metal is sufficient to produce a substantial contribution to the overall dielectric function of the effective medium. In addition, the permittivity component normal to the wire direction should have a value identical to the dielectric constant of the host, because the wires and the external electric field experience a negligible interaction when they are perpendicular to each other.

The expression for the effective permittivity of the wire array in (4.24) is based on the assumption that the wires are made from a quasi-perfect conductor with a bulk permittivity approaching infinity. The finite conductivity in metal gives rise to the damping constant Γ of the effective medium, while the effective plasma frequency in (4.18–4.20) at first appears to be independent of the metal properties. This assumption, however, is only justified for electromagnetic wavelengths longer than the infrared range, where the magnitude of the negative permittivity in noble metals is sufficiently large. In the visible frequencies, the metal permittivity following a Drude model of $\varepsilon_m = 1 - \omega_{p,m}^2/\omega^2$ has a limited magnitude, and the effective plasma frequency ω_p of the wire medium is necessarily dependent on the plasma frequency of the bulk metal $\omega_{p,m}$ [29]:

$$\omega_p^2 = \frac{\pi r^2 \omega_{p,m}^2}{a^2}. \quad (4.25)$$

The result in (4.25) shows that the effective plasma frequency is proportional to the volume fraction of wires, which is quite intuitive as ω_p of the wire medium should move toward the bulk value of $\omega_{p,m}$ when the metal filling factor approaches unity.

At optical frequencies, wire arrays have been used in a wide variety of structures and devices. In optical negative-index metamaterials, arrays of metal wires and their analogues are the mainstream choice for creating a controllable negative- ε background, which is necessary in most designs for negative index media [9]. The wire medium is also used to construct metamaterials with ultralow refractive indices of less than unity. Such an ultralow index band corresponds to frequencies slightly higher than the effective plasma frequency, as can be observed in Fig. 4.4. Several intriguing phenomena with low-index wire media have been experimentally demonstrated, including total external reflection [30], air-core planar dielectric waveguides [31] and power splitters for air-core waveguides [32].

We note that, strictly speaking, the analysis for wire media in this section only applies to the “ideal” polarization where the electric field is parallel to the wires. If the

external field is directed along an arbitrary orientation, the wire mesh may support additional modes that cannot be adequately characterized by a local permittivity. In such situations, the electric response of the medium becomes non-local with spatial dispersion, which means that the induced polarization is dependent upon not only the point-wise field values, but also on the field variations at other points in space. A detailed discussion on this issue and possible ways to tame the spatial dispersion of wire grid metamaterials can be found in [33–35].

4.4 Semicontinuous Metal Films

In all the foregoing parts of this chapter, we focused on electric metamaterials with metal and dielectric components arranged in an ordered fashion. Although most of the metamaterial designs reported in the literature indeed exhibit a certain periodicity, there is yet another type of electric metamaterial without well-defined meta-atoms. Random metal-dielectric composites can be regarded as disordered metamaterials with very interesting optical properties that differ markedly from those of ordinary bulk materials. This type of nanostructured material has attracted enormous interest during the past few decades because of the rich physics and unique properties in disordered metal-dielectric systems. Such systems are also likely to become even more important with the miniaturization of electronic and optoelectronic components. In Chap. 2, we used the effective medium approach to characterize the macroscopic, average electromagnetic response of random metal-dielectric composites. In this section we will look at them more closely and study their local optical properties down to the nanometer scale.

Random metal-dielectric composites can be fabricated by a range of deposition techniques, including thermal evaporation, electron-beam evaporation, and sputtering as well as electroplating. Due to the nature of these deposition methods, the majority of random metal-dielectric composites are confined to a thin film or coating on a two- or three-dimensional substrate. Therefore, in most of cases, such random composites are treated as a two-dimensional system. Most metal-dielectric composites are formed by depositing metal onto a dielectric substrate, a process that can be described qualitatively as follows. During the deposition process, small and isolated metal islands nucleate first on the substrate, and a composite with a low metal filling fraction similar to the sample in Fig. 2.8a begins to develop. With additional deposition and the subsequent increase in metal concentration, the metal islands grow in size and begin to coalesce, forming irregularly shaped clusters of fractal geometry on the substrate. Figure 2.8b shows the appearance of a typical sample at this step. As the film grows and the cluster size increases, at a certain point the metal concentration f exceeds a critical value f_c , referred to as the percolation threshold. The physical essence and significance of the percolation threshold have been briefly addressed in Sect. 2.4. When the metal filling fraction reaches the value f_c , an infinite “backbone cluster” spanning the entire substrate is formed.

Before this critical point, the composite behaves as a dielectric, while for $f > f_c$ a conductor-like behavior is established.

The percolation threshold implies more than merely an insulator-to-metal transition. When the filling fraction of the metal component approaches the percolation threshold, a modest alteration of the film morphology will induce a drastic change in the optical response. Percolation films are characterized by a fractal geometry that will appear similar at different length scales. The self-similarity in fractals implies that a fractal system exhibits the same overall shape as one of its parts; therefore the fractal shows the same statistical properties at many scales. Interesting examples of fractals in nature include coastlines, snow flakes, lightning, fern leaves, cauliflowers and blood vessel systems. A percolation metal-dielectric composite is formed by clusters of all sizes, from the size of individual particles to the “infinite” fractal cluster that spans the whole film. Such a morphological feature results in the creation of localized plasmonic resonances, sometimes called “hot spots,” across a broad electromagnetic spectrum. This can be understood qualitatively based on very simple arguments described below. In the vicinity of the percolation threshold, the system is a scale-invariant fractal set as illustrated in the inset of Fig. 4.5. At optical frequencies, noble metals exhibit a high conductivity with a small loss factor as determined by the imaginary part of the metal’s permittivity. We can describe each metal grain or cluster as an inductance L connected in series to a resistance R . The dielectric gaps, in turn, act as capacitive elements and are represented by a capacitance C . By virtue of this description, composite films can be viewed as a network of RLC circuits [36]. If we use l to represent the size of the metal and dielectric grains, both the inductance L and the capacitance C should scale proportionally to l . The frequency at which such effective RLC circuits resonate is given by $\omega_r = 1/\sqrt{LC} \propto l^{-1}$. Consequently smaller clusters resonate at higher frequencies while larger clusters resonate at lower frequencies [36, 37]. Thus, metal-dielectric films can be thought of as a collection of resonating optical RLC circuits where R , L and C assume random values. The geometrical disorder in the composite determines these random values and gives rise to resonance frequencies covering a very wide spectral range from the UV to the mid-IR.

The light-induced plasmon modes in percolation metal-dielectric films can lead to dramatic enhancement of optical responses in a broad spectral range. The creation of electromagnetic “hot spots” in semicontinuous metal films is a phenomenon within the broad category of Anderson localization, a process named after P. W. Anderson who first predicted the localization of electron wave functions without diffusion in semiconductors with a certain degree of randomness [38]. There are a number of numerical models for the field fluctuations and higher-order field moments in semicontinuous films, which predict reasonably well the localization of the surface plasmons and the strong local field enhancement in percolation composites [36, 37, 39]. Experimental observations in accordance with the theoretical predictions have confirmed the existence of giant local fields, which can be enhanced by a factor of 10^5 for linear responses and over 10^{20} for nonlinear efficiencies [36, 40]. In Fig. 4.5 we show the local field enhancement in a percolating metal-dielectric

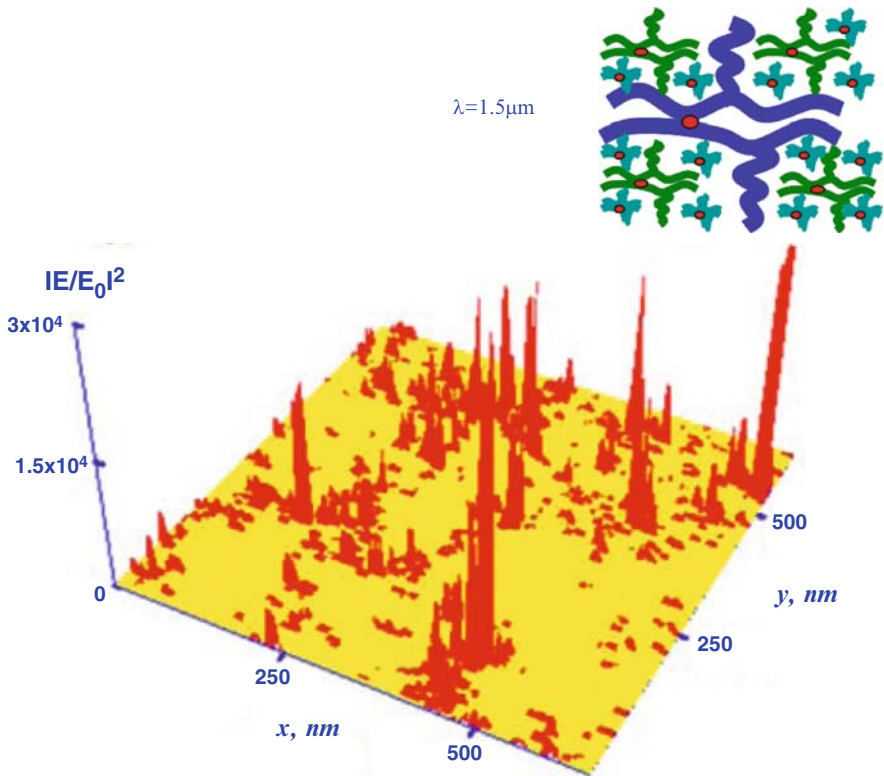


Fig. 4.5 The spatial distributions of the normalized local intensity in a typical silver-silica percolating film at an arbitrary wavelength of $1.5 \mu\text{m}$. The cartoon inset shows the self-similar features in the local film morphology

film at an arbitrary wavelength of $1.5 \mu\text{m}$. The local electric field is concentrated in nanometer-sized areas and is characterized by sharp peaks that exceed the applied field by several orders of magnitude.

Random metal-dielectric composites have had a growing impact in various topics in optics. The giant electric field fluctuations near the percolation threshold lead to huge enhancements of various nonlinear optical effects. Percolation metal-dielectric films make possible surface-enhanced Raman spectroscopy with unsurpassed detection sensitivity, because Raman scattering is proportional to the fourth moment of the electric field [41]. A similar enhancement is available for the optical Kerr effect and four-wave mixing [42]. Random metal-dielectric films are also widely used in applications like surface-enhanced infrared absorption [43], harmonic generation [44], and photovoltaics [45]. Semicontinuous metal films also find roles in optical data recording and mid-infrared filters, thanks to a recently developed frequency-selective photomodification technique [46,47].

References

1. Kock WE (1946) Metal-lens antennas. *Proc IRE* 34:828–836
2. Kock WE (1948) Metallic delay lenses. *Bell Syst Tech J* 27:58–82
3. Brown J (1953) Artificial dielectrics having refractive indices less than unity. *Proc IEE* 100:51–62
4. Golden KE (1965) Plasma simulation with an artificial dielectric in a horn geometry. *IEEE Trans Antennas Propag* 13:587–594
5. Rotman W (1962) Plasma simulation by artificial dielectrics and parallel-plate media. *IRE Trans Antennas Propag* 10:82–95
6. Pendry JB, Holden AJ, Stewart WJ, Youngs I (1996) Extremely low frequency plasmons in metallic mesostructures. *Phys Rev Lett* 76:4773–4776
7. Smith DR, Kroll N (2000) Negative refractive index in left-handed materials. *Phys Rev Lett* 85:2933–2936
8. Silin RA (1972) Optical properties of artificial dielectrics. *Radiophys Quantum Electron* 15:809–820
9. Shalaev VM (2007) Optical negative-index metamaterials. *Nat Photonics* 1:41–48
10. Liu ZW, Lee H, Xiong Y, Sun C, Zhang X (2007) Far-field optical hyperlens magnifying sub-diffraction-limited objects. *Science* 315:1686–1686
11. Luneburg RK (1944) *Mathematical theory of optics*. Brown University, Providence
12. Cai WS, Chettiar UK, Kildishev AV, Shalaev VM (2007) Optical cloaking with metamaterials. *Nat Photonics* 1:224–227
13. Wiener O (1912) *Die Theorie des Mischkorpers für das Feld der stationären Stromung*. *Abh Math-Phys Klasse Königlich Sachsischen Des Wiss* 32:509–604
14. Aspnes DE (1982) Local-field effects and effective-medium theory – a microscopic perspective. *Am J Phys* 50:704–709
15. Aspnes DE (1982) Optical-properties of thin-films. *Thin Solid Films* 89:249–262
16. Palik ED (ed) (1997) *Handbook of optical constants of solids*. Academic, New York
17. Engheta N (2007) Circuits with light at nanoscales: optical nanocircuits inspired by metamaterials. *Science* 317:1698–1702
18. Ramakrishna SA, Pendry JB, Wiltshire MCK, Stewart WJ (2003) Imaging the near field. *J Mod Opt* 50:1419–1430
19. Belov PA, Hao Y (2006) Subwavelength imaging at optical frequencies using a transmission device formed by a periodic layered metal-dielectric structure operating in the canalization regime. *Phys Rev B* 73:113110
20. Jacob Z, Alekseyev LV, Narimanov E (2006) Optical hyperlens: far-field imaging beyond the diffraction limit. *Opt Express* 14:8247–8256
21. Cai WS, Chettiar UK, Kildishev AV, Shalaev VM (2008) Designs for optical cloaking with high-order transformations. *Opt Express* 16:5444–5452
22. Pendry JB, Holden AJ, Robbins DJ, Stewart WJ (1998) Low frequency plasmons in thin-wire structures. *J Phys Condens Matter* 10:4785–4809
23. Sarychev AK, Shalaev VM (2001) Comment on paper “Extremely low frequency plasmons in metallic mesostructures”. [JB Pendry et al (1996) *Phys Rev Lett* 76:4773]. arXiv:cond-mat/0103145
24. Sarychev AK, Shalaev VM (2007) *Electrodynamics of metamaterials*. World Scientific, Singapore
25. Maslovski SI, Tretyakov SA, Belov PA (2002) Wire media with negative effective permittivity: a quasi-static model. *Microw Opt Tech Lett* 35:47–51
26. Markos P, Soukoulis CM (2003) Absorption losses in periodic arrays of thin metallic wires. *Opt Lett* 28:846–848
27. Belov PA, Tretyakov SA, Viitanen AJ (2002) Dispersion and reflection properties of artificial media formed by regular lattices of ideally conducting wires. *J Electromagnet Wave Appl* 16:1153–1170

28. Wu DM, Fang N, Sun C, Zhang X, Padilla WJ, Basov DN, Smith DR, Schultz S (2003) Terahertz plasmonic high pass filter. *Appl Phys Lett* 83:201–203
29. Silveirinha MG (2006) Nonlocal homogenization model for a periodic array of epsilon-negative rods. *Phys Rev E* 73:046612
30. Schwartz BT, Piestun R (2003) Total external reflection from metamaterials with ultralow refractive index. *J Opt Soc Am B* 20:2448–2453
31. Schwartz BT, Piestun R (2004) Waveguiding in air by total external reflection from ultralow index metamaterials. *Appl Phys Lett* 85:1–3
32. Rodriguez-Esquerre VF, Koshiba M, Hernandez-Figueroa HE, Rubio-Mercedes CE (2005) Power splitters for waveguides composed by ultralow refractive index metallic nanostructures. *Appl Phys Lett* 87:091101
33. Belov PA, Marques R, Maslovski SI, Nefedov IS, Silveirinha M, Simovski CR, Tretyakov SA (2003) Strong spatial dispersion in wire media in the very large wavelength limit. *Phys Rev B* 67:113103
34. Shapiro MA, Shvets G, Sirigiri JR, Temkin RJ (2006) Spatial dispersion in metamaterials with negative dielectric permittivity and its effect on surface waves. *Opt Lett* 31:2051–2053
35. Demetriadou A, Pendry JB (2008) Taming spatial dispersion in wire metamaterial. *J Phys Condens Matter* 20:295222
36. Sarychev AK, Shalaev VM (2000) Electromagnetic field fluctuations and optical nonlinearities in metal-dielectric composites. *Phys Rep* 335:276–371
37. Genov DA, Sarychev AK, Shalaev VM (2003) Plasmon localization and local field distribution in metal-dielectric films. *Phys Rev E* 67:056611
38. Anderson PW (1958) Absence of diffusion in certain random lattices. *Phys Rev* 109:1492–1505
39. Shalaev VM (2000) *Nonlinear optics of random media: Fractal composites and metal-dielectric films*. Springer, Berlin
40. Gresillon S, Aigouy L, Boccard AC, Rivoal JC, Quelin X, Desmarest C, Gadenne P, Shubin VA, Sarychev AK, Shalaev VM (1999) Experimental observation of localized optical excitations in random metal-dielectric films. *Phys Rev Lett* 82:4520–4523
41. Brouers F, Blacher S, Lagarkov AN, Sarychev AK, Gadenne P, Shalaev VM (1997) Theory of giant Raman scattering from semicontinuous metal films. *Phys Rev B* 55:13234–13245
42. Shalaev VM, Sarychev AK (1998) Nonlinear optics of random metal-dielectric films. *Phys Rev B* 57:13265–13288
43. Osawa M, Ikeda M (1991) Surface-enhanced infrared-absorption of para-nitrobenzoic acid deposited on silver island films – contributions of electromagnetic and chemical mechanisms. *J Phys Chem* 95:9914–9919
44. Yagil Y, Deutscher G (1992) Third-Harmonic generation in semicontinuous metal-films. *Phys Rev B* 46:16115–16121
45. Rand BP, Peumans P, Forrest SR (2004) Long-range absorption enhancement in organic tandem thin-film solar cells containing silver nanoclusters. *J Appl Phys* 96:7519–7526
46. Safonov VP, Shalaev VM, Markel VA, Danilova YE, Lepeshkin NN, Kim W, Rautian SG, Armstrong RL (1998) Spectral dependence of selective photomodification in fractal aggregates of colloidal particles. *Phys Rev Lett* 80:1102–1105
47. Nyga P, Drachev VP, Thoreson MD, Shalaev VM (2008) Mid-IR plasmonics and photomodification with Ag films. *Appl Phys B* 93:59–68

Chapter 5

Magnetic Metamaterials

5.1 Negligible Optical Magnetism in Nature

For materials at optical frequencies, the dielectric permittivity ε is generally different from that in vacuum. For example, negative permittivity values are routinely observed in noble metals at frequencies less than their plasma frequency. In contrast, the magnetic permeability μ for naturally occurring materials is always close to its free space value in the optical range. The nearly absence of a magnetic response seems like a general rule in the field of optics. Indeed, in the famous textbook by Landau and Lifshitz [1], there is a quite general statement on the reason why a magnetic response resulting from orbital currents in atoms should be negligible at optical frequencies, and consequently, “the magnetic permeability $\mu(\omega)$ ceases to have any physical meaning at relatively low frequencies. . . There is certainly no meaning in using the magnetic susceptibility from optical frequencies onwards, and in discussion of such phenomena we must put $\mu = 1$ ” [1].

The major reason behind the absence of optical magnetism in nature is that the magnetic field component of light couples to atoms much more weakly than the electric component, making light interacting with matter a “one-handed” situation. The magnetic coupling to an atom is proportional to the Bohr magneton $\mu_B = e\hbar/2m_e c = \alpha e a_0/2$, while the electric coupling is $e a_0$. The induced magnetic dipole also contains the fine structure constant $\alpha \approx 1/137$, so the effect of light on the magnetic permeability is α^2 times weaker than light’s effect on the electric permittivity. This means that of the two field components of light – electric and magnetic – only the electric “hand” efficiently probes the atoms of a material, while the magnetic component remains relatively unused. Consequently, in all conventional optical materials and devices, only the electric component of light is directly controlled. The magnetic field component of light plays merely an auxiliary role through its relation with the electric field governed by Maxwell’s equations. The magnetic response (which is due to electronic spin states) in naturally-occurring materials diminishes at frequencies higher than a few gigahertz. Moreover, there are no free magnetic monopoles, and thus it is not feasible to obtain a magnetic plasma as we can accomplish with electrons. Therefore, it is indeed a challenging issue to achieve any magnetic response in the microwave frequencies and higher, let alone more extreme values like negative permeability.

Recently, however, the emergence of metamaterial research has fundamentally altered the situation. In metamaterials that consist of artificial subwavelength structures with tailored properties, the magnetic response is not limited anymore to the electronic spin states of individual atoms. Instead, magnetism can be achieved even in optical frequencies by specially designed “meta-atoms” – functional units of the metamaterial that are smaller than the wavelength. Therefore, artificial magnetism is possible in metamaterials as long as the magnetic field component of the incident light can interact effectively with the “meta-atoms.” In this chapter we discuss a series of magnetic elements developed during the last few years in metamaterial research, including split-ring resonators (SRRs), metallic staple arrays, coupled nanorods, nanoplates and nanostrips. The magnetic response in these structures has spanned several decades of the electromagnetic spectrum, from microwave frequencies up to the blue portion of visible light.

5.2 Split-Ring Resonators

The pursuit of magnetically active structures at high frequency is one of the core tasks in metamaterial research. The problem of low coupling to the magnetic field of light can be overcome by using metamaterials that mimic magnetism at high frequencies. For the microwave range, a recipe was suggested by Pendry in which he predicted that a pair of concentric split-ring resonators (SRRs) with subwavelength dimensions and facing in opposite directions would give rise to an effective permeability different than unity [2]. Actually, the term “split-ring resonator” was coined long before Pendry’s work. In the early 1980s, Hardy used a similar structure and this exact term to describe a hollow metallic cylinder with a linear cut that exhibited a magnetic resonance at about 1 GHz [3]. Pendry and coworkers reinvented the structure in its modern form, a design that has become a prototype for many metamagnetic elements in today’s metamaterial research. A schematic of the Pendry’s SRR structure is illustrated in Fig. 5.1a [2].

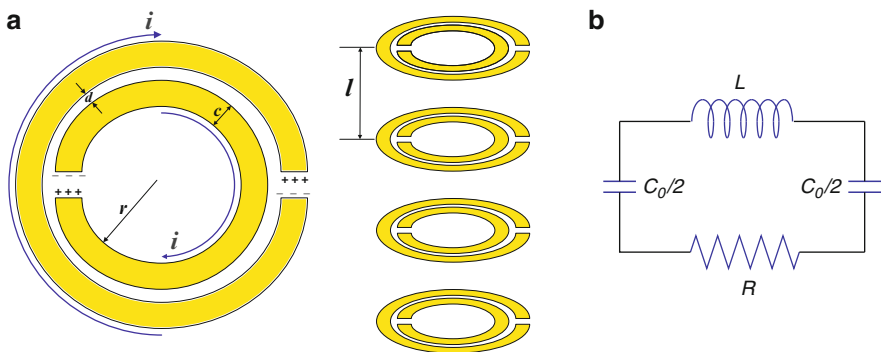


Fig. 5.1 (a) The double split-ring resonator as the building block of a metamaterial with magnetic response at microwave frequencies. (b) The equivalent circuit of a double SRR

Because the SRR structure is the first magnetic meta-atom and is still playing a dominating role in artificial magnetism at microwave frequencies, it is helpful to have an intuitive tour about how such an elegant but complicated unit evolves from a bulk piece of metal. First let us consider a circular metal plate placed in an oscillating electromagnetic wave with the magnetic field polarized normal to the flat surface. Is the metal plate magnetically active in this case? The answer is yes, but very weakly so. The oscillating magnetic field induces a circular current in the round plate, which produces a magnetic flux opposing the external magnetic field. In fact this can be viewed as a simple result of Lenz's law: any induced electromotive force will be in the direction such that the flux it creates will oppose the change in the flux that produces it. Consequently, a metal plate is weakly diamagnetic, and an array of such plates would exhibit an effective permeability slightly less than unity.

Because the circular current is mostly confined to the outer perimeter, we can remove the inner part of the plate, and the plate evolves into a ring. The response of a metallic ring to the external magnetic field is purely inductive and non-resonant. To introduce a resonance behavior and enhance the magnetic response, capacitance can be purposely introduced. As seen in Fig. 5.1a, a gap in each metallic ring prevents the formation of a complete circular current, and charges accumulate across the gaps. With both capacitance and inductance, the SRR is a resonant element. Capacitance is more effectively introduced when two rings are placed concentrically with their gaps opposite of each other (see Fig. 5.1a), which is one reason why double SRRs are preferable to single SRRs in metamaterial designs. Note that the pair of rings in a double SRR acts as one meta-atom. Another reason why double SRRs are preferred over single SRRs is the consideration of minimizing the electric polarizability in the system. In a single SRR, the accumulated charges around the gap induce a pronounced electric dipole moment, which may overshadow the desired magnetic dipole moment. With two SRRs placed in the manner shown in Fig. 5.1a, the fundamental electric dipole moments of the two rings tend to cancel each other, and the magnetic dipole moment dominates. Therefore, a standard double SRR structure is most often used in SRR-based metamaterial designs.

It is important to remember that the goal of the design is to create artificial magnetic "atoms" for a metamaterial. Therefore the size of each SRR should be much smaller than the free space wavelength at the frequency range of interest. From the equivalent circuit point of view, each SRR essentially behaves as a quasistatic LC circuit in response to the external field, as shown in Fig. 5.1b. A careful estimation of the equivalent inductance L and capacitance C can give us an estimate of the resonance frequency in an SRR acting as a magnetic meta-atom. The ring forms the inductive portion, which in total give rise to an inductance of $L \approx 2\mu_0 r$. The estimation of the capacitance C is more involved because capacitance can arise from the slot between the two rings as well as the two cuts of each individual ring. An analysis of the current flow and charge distribution show that the current lines (conductive current plus displacement current) excited by the external magnetic field follow a complicated path with the pair of the rings, extending from one ring to the other across the slot in between [4]. Therefore, the capacitance between the two rings is the dominating source of the total capacitance, and the gap capacitance in each

ring is comparably small. Note that the total capacitance between two ring-shaped electrodes, $C_0 \approx 2\pi r \epsilon_0 (c + t)/d$, is not a good evaluation for the equivalent capacitance because the total capacitance of a double SRR should be regarded as the series connection of two separated capacitors, each representing one half of the double SRR with a value of $C_0/2$ [4]. Hence, the equivalent capacitance for calculating the resonance frequency is $C \approx C_0/4$. If we take into account the ohmic loss in the structure, a resistance element $R \approx \pi r/c\delta\sigma$ should be added to form a RLC circuit, with δ and σ being the skin depth and the conductivity of the metal, respectively [5]. With all this preparation, the magnetic resonance frequency of the double SRRs can be estimated as $\omega_0 = \sqrt{1/(L + R/j\omega_0)C}$. Note that such an analysis based on an equivalent circuit model is very coarse. Nevertheless, a lumped-element model provides us a straightforward perception of the physics behind standard double SRRs and offers a quick tool for roughly estimating the resonance frequency range. Moreover, such a model helps us to visualize how the resonance frequency varies with respect to the geometrical parameters.

The strength of the magnetic response and the effective permeability of an array of SRR elements can be estimated from the magnetic moment $m_H = \pi r^2 I$ of each SRR unit. A first-order estimation gives the following expression [6]:

$$m_H = \pi^2 r^4 \mu_0 H / (\omega_0^2 / \omega^2 - 1) L \quad (5.1)$$

where H is the external magnetic field. Therefore, the effective permeability of the overall system is $\mu_{eff} = 1 + m_H/VH$, with V being the volume of each unit cell of the SRR array. Such an expression leads to a dia- or paramagnetic SRR array response to the external magnetic field, depending on whether the wavelength of the incoming magnetic field is shorter or longer than the resonance wavelength. The effective permeability is therefore different from unity, even though the natural materials comprising the SRR array have unity permeability at frequencies at about a gigahertz or higher. Again, we note that this is a very rough analysis, and specifically it does not take into account important SRR phenomena like electric coupling and bianisotropic behavior. More thorough and detailed analyses of double SRRs using analytical models and numerical simulations have been studied extensively in Refs. [4–6].

SRRs operating in the GHz regime were first demonstrated by Smith et al., in which the rings had a diameter of several millimeters [7]. The fabrication of double SRRs for use at microwave frequencies is now a routine practice using printed circuit board (PCB) technology. Such structures have been used as magnetic building blocks for various applications at microwave frequencies, most notably in the experimental demonstration of the first negative-index materials as detailed in the next chapter. The symbolic importance of SRRs in metamaterial researches is hard to overestimate. In fact, the publication of the double SRR design shown in Fig. 5.1a was the first time in the literature where the term “metamaterial” is explicitly used.

Since the successful demonstration of artificial magnetism in the microwave range, significant effort has been devoted to designing and demonstrating magnetic metamaterials at infrared and optical frequencies. Intuitively, the concept of

SRRs can be moved towards higher frequencies by simple scaling (shrinking). Since Maxwell's equations are scalable, shrinking this design in size could lead to a similar response at higher frequencies. However, we note that the materials properties of metals do not actually scale; metals, which are important components of metamaterials, have very different properties in the optical range, where the plasmon resonance is of critical importance, as opposed to the microwave case. Also, it is not feasible to simply scale down the double SRRs of Fig. 5.1 due to the fabrication difficulties involved in such an undertaking. As the required dimensions of the SRR elements decrease, fabrication moves past the capabilities of standard PCB technology and into the optical lithography or electron-beam lithography regimes. These lithography techniques have been used to make structures with smaller characteristic sizes, but they also have limitations for SRR fabrication. Lithographic techniques used for the fabrication of submicron metal structures are usually performed in a layer-by-layer fashion. However, the standard SRR-based magnetic response requires the plane of the SRR to be parallel to the incident wave-vector to guarantee magnetic field penetration through the SRR plane. This is hard to accomplish when the SRRs are lying flat on a substrate. One easy method to partially alleviate this issue is to use oblique incidence for the external electromagnetic wave. This provides a magnetic field that obliquely penetrates the SRR planes.

Using scaling techniques along with inclined incidence, the resonance frequency of double SRRs has been pushed up to 1 THz [8]. A sample with terahertz SRRs and the associated polarization condition is illustrated in Fig. 5.2. The size of each SRR in this case is about $40\ \mu\text{m}$. Near the resonance frequency, the effective permeability exhibits a Lorentzian spectral dependence with minimum and maximum values of -1 and 4 , respectively.

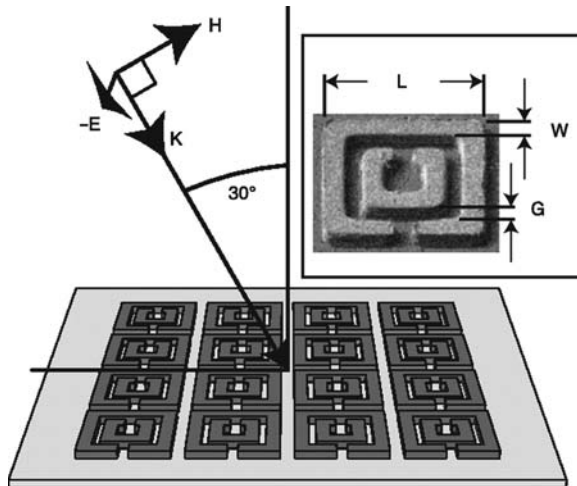


Fig. 5.2 Double SRR structure with terahertz magnetic response using oblique incidence. Adapted from [8]. Reprinted with permission from AAAS. Courtesy of X. Zhang

5.3 Optical Magnetic Elements

In this section, we discuss different routes for pushing the operational frequency of magnetic metamaterials into the optical regime. As of early 2009, various structures have been proposed to achieve magnetic responses at higher and higher frequencies. The basic principle behind these designs is that the unit structures can support a principal eigenmode with a circular current distribution that gives rise to a magnetic moment. Such a magnetic moment introduces resonance behavior for the structure. The magnetic moment is parallel to the incident magnetic field and gives rise to $\mu > 1$ below the resonance frequency. Above the resonance frequency, the magnetic moment is anti-parallel to the incident magnetic field and produces $\mu < 1$ for the structure.

In order to obtain a metamagnetic response at higher frequencies without playing the trick of inclined incidence, different variations of SRRs have been explored. One of the most important designs for achieving a magnetic resonance toward the optical regime is based on arrays of single SRRs lying in a plane perpendicular to the direction of wave propagation. In contrast to the standard SRR operation, where a magnetic field normal to the SRR plane is required to excite the magnetic response, the single in-plane SRRs may act as magnetic dipoles without the involvement of the incident magnetic field at all [9]. The different orientations of SRRs with respect to the external field are illustrated in Fig. 5.3. The standard application of SRRs with an H field component penetrating the SRR plane is shown in Fig. 5.3a. The fabrication difficulties in making such a structure based on micro- or nano-fabrication techniques are obvious. In Fig. 5.3b, c, the SRR arrays lie on a substrate, a design that is certainly compatible with standard lithography and deposition techniques. In the latter two situations, the applied magnetic field is parallel to the SRR plane, but it cannot play a role in creating magnetic dipoles in the structure. However, there is an amazing property in the configuration in Fig. 5.3b. When the electric field is parallel to the gap-bearing side of the SRR, there is an asymmetric current mode in the two arms of the ring, and a magnetic dipole can be obtained. If the electric

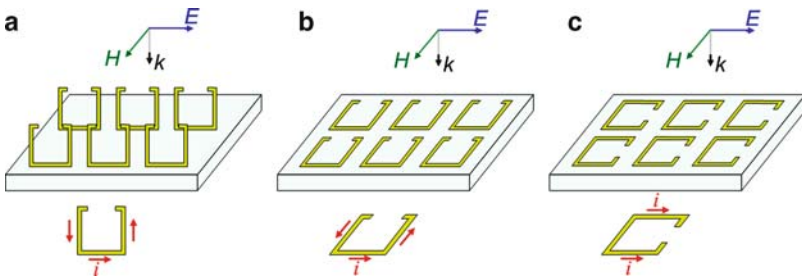


Fig. 5.3 Different orientations of single SRR arrays. (a) The standard SRR operation where the magnetic dipole can be excited by the external H field. (b) The magnetic dipole is possible due to the asymmetric mode of excited current. (c) No magnetic response is obtained when the E field is parallel to the arms of SRR

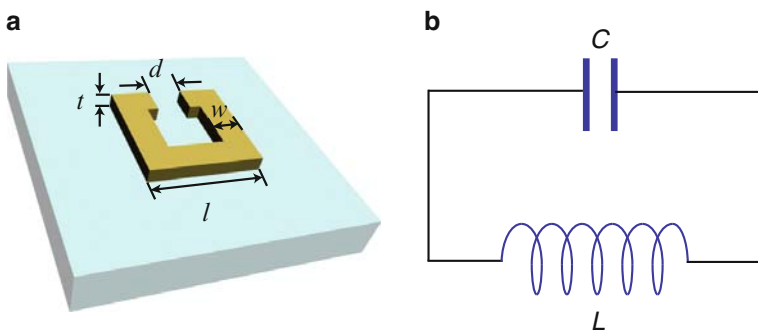


Fig. 5.4 (a) A single-SRR as a magnetic element and (b) its equivalent LC circuit

field is polarized along the two arms (Fig. 5.3c), however, identical currents will be excited in the two arms of SRR, and no loop-like current flow can be obtained to produce a magnetic dipole.

Besides the current symmetry considerations, the underlying physics in planar single SRRs can also be interpreted from an equivalent circuit point of view. The discussion below closely follows the work on metamagnetics at 100 THz in Ref. [10]. As discussed in the previous section, an SRR such as that shown in Fig. 5.4 can be viewed as an LC oscillator, with the inductance corresponding to the ring and the gap serving as the capacitance. For such an oscillator, there are two means to excite resonance: either the magnetic field vector must penetrate the inductor “coil” (the ring), or the electric field vector must be aligned normal to the capacitor “plate” (the surfaces of the cut). The standard operational mode of SRRs shown in Fig. 5.3a corresponds to the first excitation method, while the capacitance excitation method with the electric field polarized along the gap-bearing side is represented in Fig. 5.3b. In the third case of Fig. 5.3c, both the inductance and the capacitance do not interact with the external field; therefore no resonance behavior is expected for the case shown in the last panel.

Magnetic resonance with electric field excitation has been achieved in the mid-infrared wavelength of $3\ \mu\text{m}$ [10]. The experimental spectra are shown in Fig. 5.5 using single SRRs with sizes of about $320\ \text{nm}$ (from [10]). When the electric field polarization is rotated by 90° , the magnetic resonance disappears completely in good agreement with the reasoning above. By further reducing the size of SRRs, magnetic responses based on this principle have been achieved from the far-infrared to the long wavelength end of the visible spectrum [11].

It is important to note that the electrically coupled magnetic resonance is an indirect one, and it is inevitably weak compared to the magnetic resonance excited by the magnetic field directly. The retrieved effective parameters in the work discussed above [10] show that the minimum value of the effective permeability around the $3\ \mu\text{m}$ magnetic resonance is as large as 0.8, only marginally smaller than that of a magnetically inactive medium. This is the major reason why metamagnetics in planar single-SRRs cannot be used in many interesting applications of artificial magnetism, including negative-index materials and electromagnetic cloaking devices.

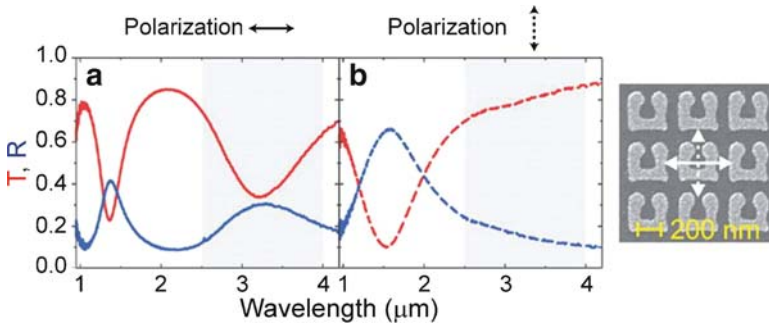


Fig. 5.5 The transmission and reflection spectra of planar single-SRRs under two polarization configurations for magnetic resonance at $3 \mu\text{m}$. An electron micrograph of the sample is shown on the *right-hand side*. Adapted from [10]. Reprinted with permission from AAAS

Another serious drawback of planar SRRs is the breakdown of geometrical scaling and subsequent saturation of the resonance frequency. This saturation effect fundamentally prevents SRRs from providing magnetic resonance at the “true” optical frequencies – the visible range. The scaling breakdown of single SRRs is described below and was first explained in Ref. [12] in terms of the kinetic energy of electrons and electron self-inductance, which results from the plasmonic behavior of noble metals in the optical regime. Similar conclusions have been drawn using an equivalent circuit model as detailed in Ref. [13]. Note that this saturation effect is an intrinsic property of an SRR as a resonator, and is independent of how the SRR is excited. In other words, the analysis below applies to both the planar SRRs with an electrically coupled magnetic response as well as the standard SRRs whose response is driven by the external magnetic field directly.

Consider the single SRR in Fig. 5.4a, which is essentially an LC resonator with a magnetic resonance occurring at the eigenfrequency $\omega_m = 1/\sqrt{LC}$. To the first order of approximation, the equivalent lumped elements of the LC circuit are $L = \mu_0 l^2/t$ and $C = \varepsilon_0 wt/d$. We use a to denote the unit cell size of the single SRR. That is, a serves as a scaling factor, and all the geometrical parameters (l, d, t, w) vary in proportion to a . The simple expressions of L and C show that both scale with a . This gives rise to an important relation between the resonance frequency and the scaling factor of the SRRs: $\omega_m = c_0 \sqrt{d/wl^2} \propto 1/a$ [14]. Within this simple expression lies the basic scaling capability of SRRs: the resonance frequency is inversely proportional to the size of the SRR.

This simple but crude reasoning, however, is based on the assumption of perfect metal with infinite carrier density. In this case, the current excited by the external field is carried by electrons with zero velocity. In reality, since a metal has a finite electron density and hence a finite plasma frequency, there must be finite electron velocity proportional to the current I in the loop. Hence, there is additional kinetic inductance L_{kin} that accounts for the total kinetic energy of the moving electrons [12]. Derivations show that the additional inductance L_{kin} is inversely proportional to the scaling factor a . As a result, the magnetic resonance frequency

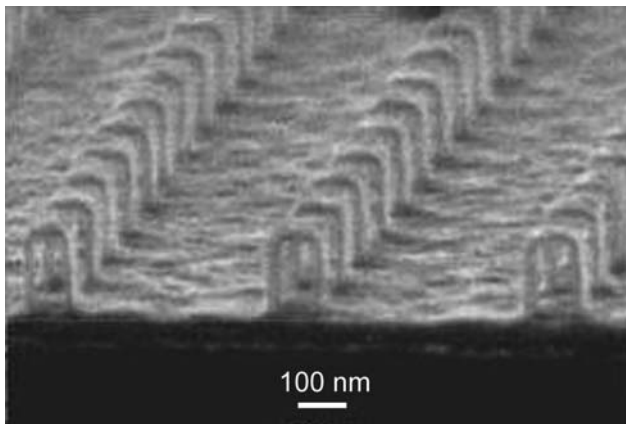


Fig. 5.6 Array of nano-staples with a mid-infrared magnetic resonance. Reprinted with permission from [15]. Copyright (2005) by the American Physical Society

$\omega_m = 1/\sqrt{(L + L_{kin})C} = 1/\sqrt{a^2 + const.}$, where the constant comes from the product of C and L_{kin} and is origin of the scaling saturation effect in SRRs. Simulations show that the saturation effect determines a maximum resonance of $2\pi \times 373 THz$, which corresponds to a wavelength of about 800 nm [14].

The intrinsic limit to scaling SRR size for obtaining a magnetic response in the optical range has pushed researchers to seek alternative designs for magnetic meta-atoms. The objective is to find a structure that fulfills the following requirements: (1) compatibility with available nanofabrication techniques, (2) magnetic resonance excited by external magnetic field directly, and (3) negligible saturation effects for high-frequency operation. One alternative to double SRRs is to fabricate a staple-like structure facing a metallic mirror as shown in Fig. 5.6 [15]. The structure consists of an array of gold “staples” separated from a continuous gold film by a ZnS spacing layer. From an equivalent circuit point of view, the upper loop of the staple works as an inductance while the staples footings serve as capacitors. Each staple can be viewed as a pair of staples facing each other, because the uniform gold film works as an imaging mirror. The experimental demonstration in Ref. [15] used an array periodicity of 600 nm, and a Lorentz resonance in the effective permeability was observed with a minimum value of about -0.5 at the frequency of $\sim 65 THz$. Understandably, the magnetic activity in this nano-staple structure is much stronger than that of the planar SRRs in the previous section because the staples are effectively “standing-up” SRRs that allow direct coupling to the external magnetic field. Simulations also showed that it is possible to extend the negative permeability to higher frequencies of near-IR (near $1.3 \mu m$) by reducing the pitch size and dimensions of the arrays [15].

More advanced artificial elements for magnetic metamaterials include arrays of pairs of metallic rods, plates or strips. Each of these structures is capable of supporting a principal eigenmode with an anti-symmetric current distribution in the coupled system. The optical diamagnetic response in pairs of metallic rods was

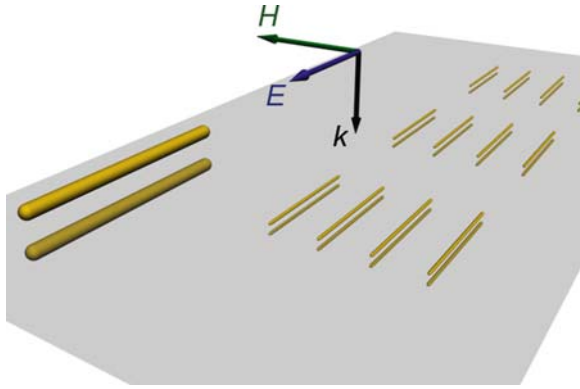


Fig. 5.7 A composite consists of pairs of metallic nanorods can support magnetic resonance at optical frequencies

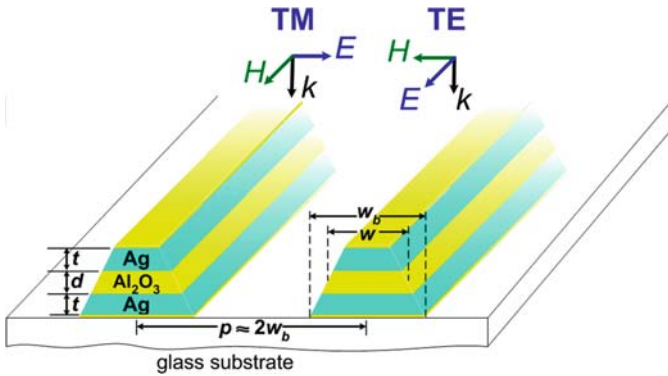


Fig. 5.8 Schematic of the structure consisting of coupled nanostrips

first predicted in 2002 [16]. A composite comprising pairs of parallel nanorods along with the required incident field polarization is illustrated in Fig. 5.7. The magnetic field oscillates through the gap between the rods and excites a current loop in each pair of nanorods. Such a nanorod system may also exhibit a negative index of refraction, as detailed in the next chapter. In the actual fabrication of paired nanorod arrays using electron-beam lithography and direct deposition, the cross-section of each rod would become a thin rectangle or trapezoid whose thickness is much smaller than its length and width. Therefore in the literature, nanorod pairs are sometimes called by other names like cut-wire pairs or plate pairs [17]. Sometimes square-shaped plate pairs are favored because the geometry eliminates undesirable polarization anisotropy in the metamaterial. Negative effective permeabilities from square nano-plate pair arrays has been observed at near-IR wavelengths between 1.0 and 1.5 μm [17].

One of the most successful magnetic metamaterials proposed thus far is the pair of metal strips shown schematically in Fig. 5.8. These strips support asymmetric

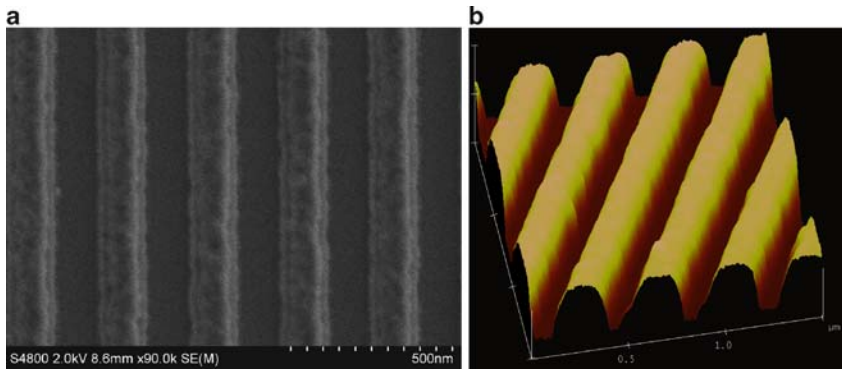


Fig. 5.9 The FE-SEM image (a) and the AFM image (b) of a typical nanostrip sample

currents in the metal structures induced by the perpendicular magnetic field component of light. The paired metal strip design is closely related to the system of pairs of rods. By simply extending the pairs of rods in Fig. 5.7 along the direction of the external magnetic field H , pairs of strips are obtained. The magnetic resonance in such a structure was first predicted in Ref. [18], and, simultaneously and independently, in Ref. [19].

The basic structure of the nanostrip magnetic metamaterial consists of a pair of metallic nanostrips spaced by a dielectric layer, as illustrated in Fig. 5.8 [20]. Reflecting the realities of fabrication, the upper and lower strips are purposely depicted to be non-identical, and therefore the overall cross-section of the strip pair is trapezoidal in shape. Figure 5.9a, b show the field-emission scanning electron microscope (FE-SEM) and atomic force microscope (AFM) images of a representative paired nanostrip structure fabricated by electron-beam lithography and vacuum deposition techniques. The nanostrip structures exhibit both magnetic and electric resonances under TM illumination with the magnetic field polarized along the strips (see Fig. 5.8 for polarization definition). For TE polarization with the electric field aligned with the strips, the structure has no resonant effects. In Fig. 5.10 we plot the experimentally collected transmission, reflection and absorption spectra of a typical paired-nanostrip sample under the TM polarization with the magnetic and electric resonance wavelengths marked as λ_m and λ_e , respectively.

To illustrate the nature of the magnetic and electric resonances, consider the simulation for the field distribution at the two resonance wavelengths λ_m and λ_e of a representative coupled nanostrip sample obtained from a commercial finite element software (COMSOL Multiphysics®), as shown in Fig. 5.11. The figure depicts a cross-sectional view of the paired nanostrips with the three thick layers representing the Ag–Al₂O₃–Ag sandwich structure. The arrows show the electric displacement while the color map represents the magnetic field. At the magnetic resonance (Fig. 5.11b), the electric displacement forms a loop resulting in an artificial magnetic moment. Also, note the strong magnetic field inside the loop between the two metal strips. At the electric resonance (Fig. 5.11a), the electric displacement

Fig. 5.10 The transmission (T), reflection (R) and absorption (A) spectra of a representative paired-nanostrip sample under TM polarization

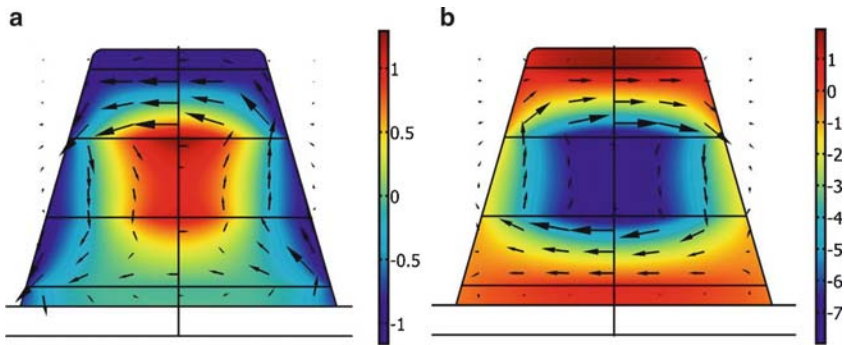
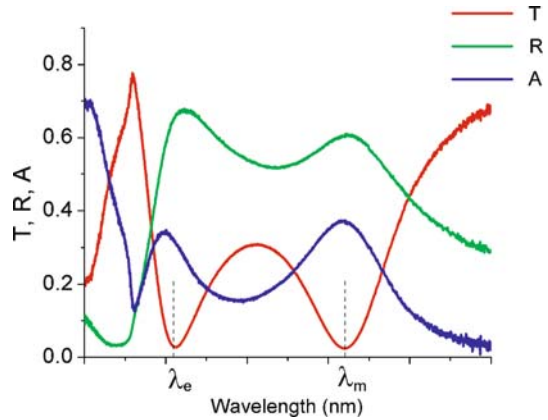


Fig. 5.11 Simulated electric displacement and magnetic field distributions at (a) the electric resonance λ_e and (b) the magnetic resonance λ_m . Electric displacement is shown by *arrows*, while magnetic field strength is indicated by *color*. Reprinted with permission from [20]. Copyright (2007) OSA

is predominantly aligned along one direction with a small circulating component. The magnetic field is also lower compared to the magnetic resonance. The small circulating component of the electric displacement results in a small magnetic moment, which manifests itself as a magnetic anti-resonance. The physics of anti-resonances has been discussed extensively in Refs. [21–23].

5.4 Magnetism in the Visible Spectrum

Let us briefly review the major facts of magnetic metamaterials that we have discussed thus far. During the first few years of the intense study of metamaterials, SRRs and their analogues have been the magnetic “meta-atoms” of choice, and their magnetic response has spanned several decades of the electromagnetic spectrum from C-band microwave frequencies up to the optical wavelength of 800 nm.

At visible wavelengths, however, other structures like coupled nanorods or nanostrips are preferred. This is because of the intrinsic limits to scaling the sizes of SRRs for obtaining a magnetic response in the optical range. In this section, we present a route to strong and controllable magnetic responses in the visible wavelength range based on a structure consisting of arrays of paired, thin silver strips.

The magnetism in coupled nanostrips has been discussed theoretically and was first demonstrated experimentally at the very red end of the visible range [22]. By spatially tuning the dimensions and creating a family of paired-strip samples with varying geometries, magnetic responses can be achieved across the entire visible spectrum [20]. The dependence of the magnetic resonance wavelength on the geometric parameters, which was both experimentally observed and analytically studied, provides a general recipe for producing optical magnetism with controllable strength for any visible frequency. We note that any optical magnetic responses, whether they have a positive or negative permeability, are important for various applications such as negative refraction, subwavelength waveguides and antennas, spectrally selective filters, and total external reflection. Most importantly, devices based on transformation optics including an electromagnetic cloak, which may be the most exciting potential applications of metamaterials, are based on the delicately designed distribution of both the permittivity and permeability, and these values can be either positive or negative depending on the specific design requirements.

Before we proceed with discussing experimental demonstrations of magnetism in the visible range, it is important to address one issue regarding the constituent materials used in metal-dielectric metamaterials for visible light frequencies. For metamaterials that are operational from microwave frequencies to the near infrared, different metals have been used to create functional units. Copper is commonly used in microwave metamaterials, partially because it is the standard material in PCB fabrications. For the infrared band of the optical frequencies, both gold and silver structures are routinely used; gold is usually preferred owing to its better performance in various nano-fabrication techniques and its stability against environmental degradation such as oxidation. For metamaterials at visible frequencies, however, silver is the metal of choice mainly because of its superior (smaller) loss factor compared to any other metal. Gold has roughly three times more loss than silver, which makes it less favored in high-frequency metamaterials. Moreover, the absorption edge of gold due to interband transitions ($5d \rightarrow 6sp$) falls within the visible range, which essentially rules it out as a metal for metamaterials at visible frequencies. Therefore in magnetic nanostrips operating in the visible range, silver is chosen to form the pairs of metal strips. As for the dielectric spacer between the silver nanostrips, a material with a relatively large dielectric constant is favored to obtain better field confinement. Therefore in the present structure, alumina ($n > 1.6$) is used instead of silica ($n < 1.5$) as the spacer dielectric. Note that semiconductors with very high dielectric constants like silicon or germanium should not be used for visible-light metamaterials because of the substantial loss caused by electron transitions across the bandgap.

We now move into the discussion of experimental demonstrations of magnetism in the visible range using nanostrip pair samples [20]. As illustrated in Fig. 5.8, the

Table 5.1 Geometric parameters of magnetic nanostrip samples

Sample #	Bottom width	Average width	Periodicity	Coverage % ^a
	w_b	w	p	
A	95	50	191	0.50
B	118	69	218	0.54
C	127	83	245	0.52
D	143	98	273	0.52
E	164	118	300	0.55
F	173	127	300	0.58

^aCover ratio is calculated by the ratio of bottom width w_b to the periodicity p

whole nanostrip pair stack is trapezoidally shaped with an average width of w and a bottom width of w_b due to fabrication limitations. The thickness of each silver layer and the alumina spacer are $t = 35$ nm and $d = 40$ nm, respectively. These parameters are optimized values based on a spatial harmonic analysis [24]. For different samples, the width w of the strips was varied to obtain optical magnetic resonances at a set of wavelengths. Six different structures with varying widths were prepared, as shown in Table 5.1. The periodicity p in different samples was changed in correspondence to the width, such that the overall coverage ratio of each sample is roughly 50%. This ensures that the strengths of the magnetic resonances in different samples are comparable. The samples were fabricated by electron beam lithography techniques. The geometries of the samples were first defined on a glass substrate with a thin (15 nm) layer indium-tin-oxide via an electron beam writer. Then, standard vacuum electron beam deposition methods were used to produce a stack of silver and alumina layers corresponding to Fig. 5.8. Note that two thin alumina layers of 10 nm were added to the top and bottom of the Ag–Al₂O₃–Ag sandwich stacks for fabrication stability. The desired paired nanostrip structures were obtained after a lift-off process. All six samples are on the same substrate and were fabricated simultaneously for a fair comparison. Each sample is $160\ \mu\text{m} \times 160\ \mu\text{m}$ in size.

To qualitatively illustrate the resonance properties of the magnetic samples with different strip widths, optical microscopy images of the samples were collected for two orthogonal polarizations, as shown in Fig. 5.12. For the resonant TM polarization case (Fig. 5.12a, c), there are distinct colors in the different samples in both the transmission and reflection modes, indicating the various resonant frequencies in different samples. For the non-resonant TE polarization, however, the colors are the same for all samples. In this case the samples act as diluted metals with a behavior similar to perfect metals: more reflection and less transmission at longer wavelengths. This is why the non-resonant images all appear blue in transmission mode (Fig. 5.12b) and red in reflection mode (Fig. 5.12d).

The transmission and reflection spectra (Fig. 5.13) of the samples have been collected to reveal the nature of the resonances quantitatively. As expected, there are strong resonances in both the transmission and reflection spectra for TM polarization (Fig. 5.13a, c). For TE polarization, the spectra display a non-resonant wavelength dependence over a broad wavelength range (Fig. 5.13b, d). The slopes of the spectra in the TE mode confirm that the samples act as diluted metal in this

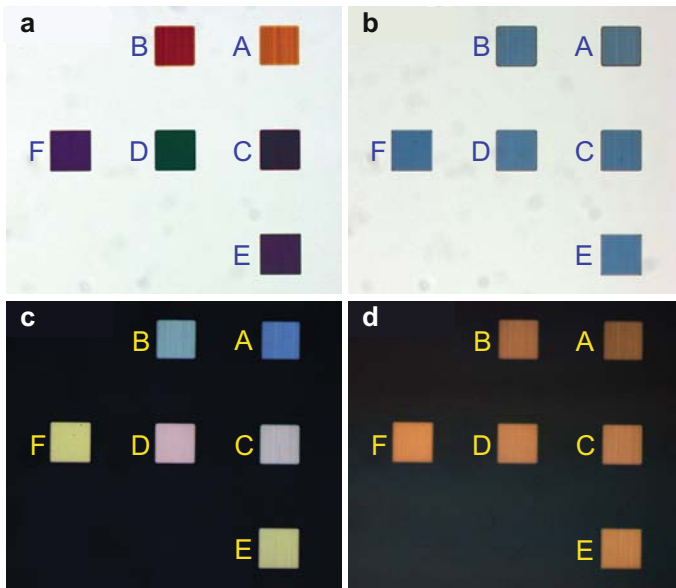


Fig. 5.12 Optical microscopy images of the magnetic samples for two orthogonal polarizations. (a) Transmission mode with TM polarization; (b) transmission mode with TE polarization; (c) reflection mode with TM polarization; (d) reflection mode with TE polarization. Letters A–F correspond to the sample naming in Table 5.1. Reprinted with permission from [20]. Copyright (2007) OSA

case and explain again why samples look blue in transmission mode (Fig. 5.12b) and red in reflection mode (Fig. 5.12d). The six samples were fabricated with a range of strip widths from 50 nm (Sample A) to 127 nm (Sample F), and magnetic resonances occurring from 491 to 754 nm were obtained. This functional frequency range covers most of the visible spectrum. It is important to note that the positions of the resonant wavelengths in the TM mode move towards the blue when decreasing the width of the strips from Sample F to Sample A, which verifies that these coupled nanostructure exhibit a well-behaved magnetic resonance scaling property.

The spectra for TM polarization exhibit important features at three distinct characteristic wavelengths. Figure 5.14 shows the transmission, reflection and absorption (including diffractive scattering) spectra of a typical paired-strip sample (Sample E) under TM polarization with three characteristic wavelengths marked on the curves. The magnetic resonance around λ_m results from an anti-symmetric current flow in the upper and lower strips, which forms a circular current and gives rise to a magnetic dipole response. This magnetic resonance is the major feature that we are pursuing in the coupled nanostructure. In addition to the anti-symmetric current mode, the strip pair also supports a symmetric current mode near λ_e , which results in an electric resonance. These two resonances induce the two local minima in the transmission spectra and local maxima in reflection, as illustrated in Fig. 5.14. The absorption spectrum in Fig. 5.14 shows enhanced absorption

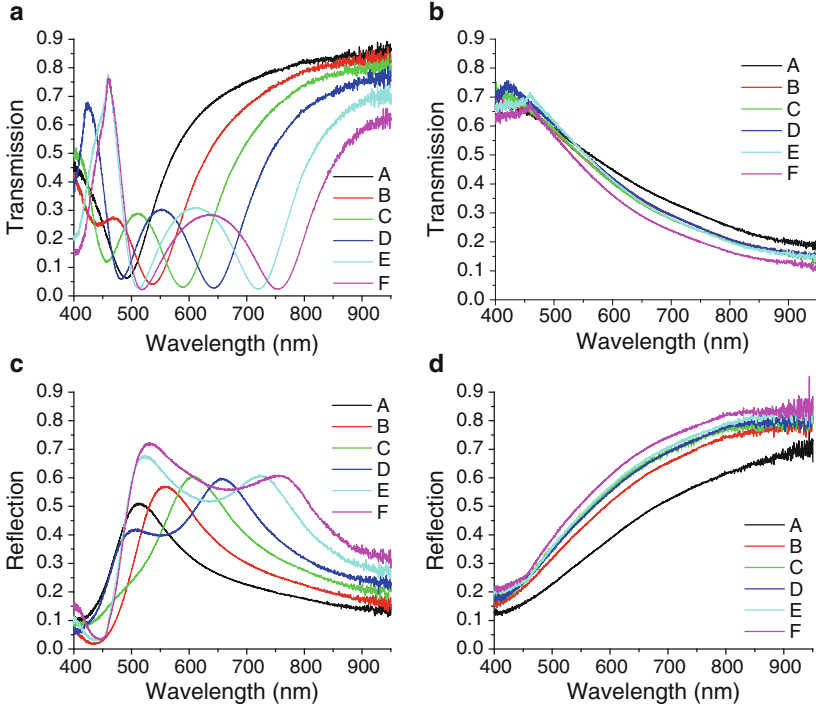


Fig. 5.13 Transmission (T) and reflection (R) spectra of the coupled nanostrip samples for two orthogonal polarizations. (a) T with TM polarization; (b) T with TE polarization; (c) R with TM polarization; (d) R with TE polarization. Letters A–F correspond to the sample naming in Table 5.1. Reprinted with permission from [20]. Copyright (2007) OSA

near the two resonance wavelengths λ_m and λ_e , which is natural for plasmonic resonances in metal-dielectric structures. The transmission spectrum also displays a sharp turn-back at a relatively short wavelength λ_d . This characteristic wavelength indicates the diffraction threshold and serves as a fingerprint for such grating-like structures. For a one dimensional grating with a periodicity p , a diffraction channel is created whenever the wavelength λ reaches below a diffraction threshold given by $\lambda_{d,j} = n_s p / j$, where j is an integer and n_s is the refractive index of the grating substrate (in our case, $n_s = 1.52$ for the glass substrate) [25]. When the wavelength λ falls below $\lambda_{d,j}$, strong distortion in the transmission spectrum is present and substantial optical power transfers to diffractive scattering, which is usually attributed to Wood's anomaly [26]. In the experimental results discussed here, this threshold is observed for Samples D, E and F, whose first-order thresholds $\lambda_{d,1}$ are within the detection range of $\lambda > 400$ nm. The positions of $\lambda_{d,1}$ obtained from Fig. 5.13a for the three samples agree extremely well with calculated values, exhibiting deviations of less than 1%.

In addition to experimental characterizations, the properties of the coupled nanostrip samples were investigated by numerical simulation with a commercial

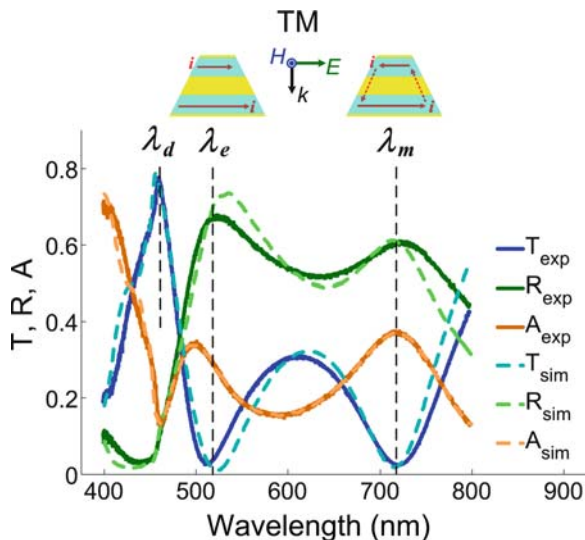


Fig. 5.14 Transmission (T) and reflection (R) and absorption (A, including diffractive scattering) spectra under TM polarization for a typical coupled nanostrip sample (Sample E) with three characteristic wavelengths indicated. *Solid lines* show the experimental data, and *dashed lines* represent simulated results. The two cross-sectional schematics of the strip pair illustrate the current modes at electric and magnetic resonances, respectively. Reprinted with permission from [20]. Copyright (2007) OSA

finite element package (COMSOL Multiphysics[®]). The material properties of silver were taken from well-accepted experimental data [27], with the imaginary part of the permittivity serving as an adjustable parameter to reflect the actual imperfections of the nanostrip pair fabrication quality. A detailed description of the techniques used in simulating such structures is discussed in Ref. [22]. The transmission, reflection and absorption spectra for a representative sample (Sample E) are plotted in Fig. 5.14 along with the experimental data. All of the features observed in the experimental spectra are reproduced remarkably well in the numerical simulations.

5.5 Analytical Model of Magnetic Nanostrips

For practical designs and applications, it is desirable to have an analytical expression for the relation between the magnetic resonance wavelength λ_m and the geometric parameters (w , d , t) of paired-strip structures [20]. Following the cavity model approach discussed in Ref. [28], we can see that for the range of parameters used in the experiments shown above where $\lambda_m > 2n_d w$, the cavity resonant wavelengths λ_m are well described by

$$\varepsilon'_m(\lambda_m) = 1 - \frac{n_d^2}{t\kappa} \left[1 + \coth\left(\frac{d\kappa}{2}\right) \right], \quad \kappa = \sqrt{(\pi/w)^2 - (2\pi n_d/\lambda_m)^2}, \quad (5.2)$$

where ε'_m is the real part of the metal permittivity and n_d is the refractive index of the spacer. Because the fabricated structures are indeed more complicated than the ideal case described by the cavity model, there are small deviations between λ_m calculated with (5.2) and the experimentally observed values. Such deviations can be fully accounted for by introducing in (5.2) the effective strip width w_{eff} . For the range of the parameters used in the experiments, calculations show that w_{eff} is only slightly smaller than the bottom width w_b of the coupled strips, namely $w_{eff} = 0.96w_b$.

Equation (5.2) has no analytical solution, although it allows useful approximations in some cases. First-order approximations for the hyperbolic cotangent function in (5.2) with $d\kappa/2 \ll 1$ can be incorporated to simplify the expression. In addition, the second term in the square root can be neglected assuming $2n_d w \ll \lambda_m$. The permittivity ε'_m of silver is approximated by the Drude model with $\varepsilon'_m(\lambda) = 5 - \lambda^2/\lambda_p^2$, where $\lambda_p = 134.6$ nm is the plasma wavelength of silver [27]. Using these simplifications, the approximate solution to (5.2) can be written as:

$$\lambda_m = \sqrt{4 + \frac{n_d^2 w}{\pi t} + \frac{2n_d^2 w^2}{\pi^2 t d}} \lambda_p. \quad (5.3)$$

This approximation provides physical insight and confirms the intuitive conclusion that scaling down the width w of the strips results in a shorter resonant wavelength λ_m . Moreover, there is a less intuitive conclusion that reducing the thickness t of the metal strips tends to give λ_m a red-shift, which has been observed in both simulations and experiments [22]. Another interesting approximation for (5.2) can be obtained if the dimensions of coupled strips are relatively large ($w^2 \gg \lambda_p^2$ and $td \gg \lambda_p^2$) while $d\kappa/2 \ll 1$. In this case, the resonant wavelength λ_m is independent of the thickness t and separation d , and it depends only on the geometric parameter w : $\lambda_m \approx 2n_d w(1 + \lambda_p^2/4\pi^2 td) \approx 2n_d w$. This limiting case accurately describes, for example, microwave magnetic media using paired metal wires [29], where the resonant wavelength is solely dependent on the length of the wires. Not surprisingly, the second approximation leads to a natural solution for the basic mode of an electromagnetic cavity with a characteristic size of w .

In Fig. 5.15 we plot the dependence of the magnetic resonance wavelength λ_m with respect to the average width w of the trapezoidal-shaped paired-strip samples from both experiments and analytical approaches. The experimental data for the relationship between λ_m and w is taken from Fig. 5.13a, c. In plotting the results of (5.2), $w_{eff} = 0.96w_b$ is used for calculations. From Fig. 5.15 we can see that the results obtained from the analytical method of (5.2) match the experimental data remarkably well. Therefore, the equations can be used as a general recipe for producing paired-strip magnetic metamaterials at any desired optical wavelength. Figure 5.13 also exhibits negligible saturation due to size scaling, which indicates

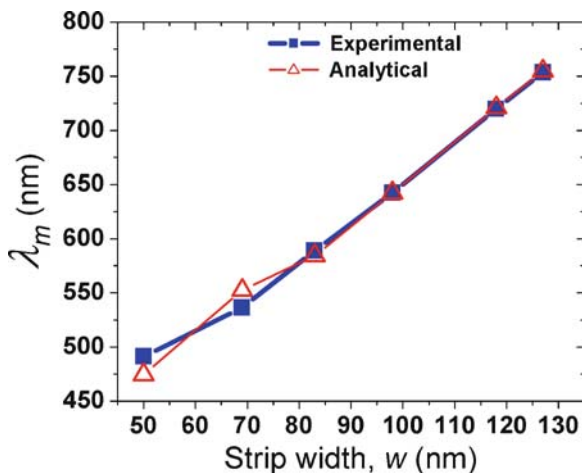


Fig. 5.15 The dependence of the magnetic resonance wavelength λ_m on the average width w of the trapezoidal-shaped paired-strip samples. *Square*: experimental data for λ_m as a function of w taken from Fig. 5.13 (a, c); *triangles*: analytical $\lambda_m(w)$ relationship determined by (5.2)

that such a structure is capable of producing optical magnetism at even shorter wavelengths.

As for the strength of the magnetic responses in the experimentally studied paired-strip samples, the effective permeability μ' of each sample around the magnetic resonance wavelength λ_m was retrieved using numerical simulations with the homogenization technique of [30]. For each sample, the material properties and geometrical parameters used in the retrieval procedure guarantee good agreement between the simulated and experimental broadband spectra. The minimum values of permeability for the six coupled-strip samples are shown in Fig. 5.16. The permeability obtained in each sample is distinct from unity, as opposed to conventional optical materials, and is found to be -1.6 in Sample F for dark-red light of 750 nm and 0.5 in Sample A at the blue wavelength of less than 500 nm. We note that for all the samples, the magnetic resonance wavelength λ_m is at least five times larger than the strip width w , and therefore the coupled-strip samples can be regarded as two-dimensional metamaterials at the wavelengths of interest.

The experimental and numerical studies of a family of coupled nanostrips with varying dimensions have offered a universal structure to create optical magnetic responses across the whole visible spectrum. The obtained dependence of the magnetic resonance wavelength on the geometric parameters provides us with a general recipe for designing such magnetic metamaterials at any desired optical frequency. Additionally, it is possible to tune the magnitude of the effective permeability μ' by changing the coverage percentage of the strips. Therefore, the coupled nanostrip structure can serve as a general building block for producing controllable optical magnetism for various practical implementations.

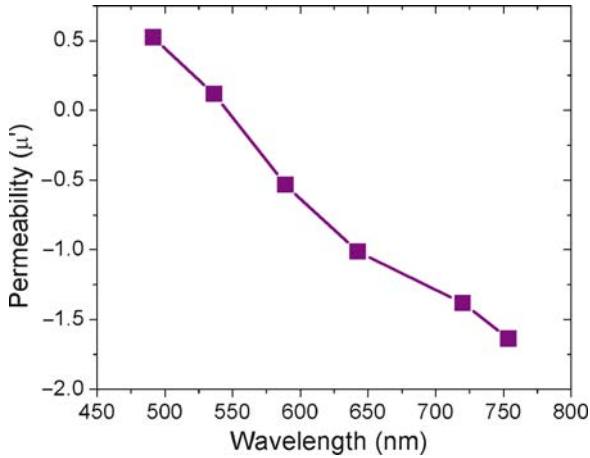


Fig. 5.16 The minimum values of the retrieved permeability μ' at various the magnetic resonance wavelengths λ_m for the six samples experimentally studied

5.6 High-Permittivity Route to Artificial Magnetism

In the previous sections we achieve metamagnetic responses by using plasmonic resonances to introduce asymmetric current modes in subwavelength metal structures. There is an alternative approach to obtain artificial magnetism that relies instead on the Mie resonances in subwavelength dielectric resonators. Subwavelength particles with very high positive dielectric permittivity support strong resonances with a large displacement current, which may give rise to strong magnetic field induced by contra-directional displacement currents. Moreover, the large dielectric constant implies a small wavelength inside the high-permittivity region; therefore the physical size of the resonator can be many times smaller than the free-space wavelength. This situation justifies the treatment of the system as a macroscopically homogenous medium, and the use of effective constitutive parameters to describe its interaction with external waves is applicable.

Although the choices are relatively limited, a number of materials do exist with very high permittivity for both microwave frequencies and the mid- to far-infrared. At microwave frequencies, ferroelectric ceramics like $\text{Ba}_x\text{Sr}_{1-x}\text{TiO}_3$ (BST) are attractive candidates for this purpose [31]. Such materials can exhibit a relative dielectric constant of several hundred at gigahertz frequencies and at room temperature without an external driving dc voltage. For the far- or mid-infrared, polaritonic materials like LiTaO_3 , TlBr , TlCl or SiC have been used in this scheme [32]. When placing the subwavelength resonators together to form a metamaterial, it is not essential to follow any particular lattice symmetry because the Mie resonance is localized. The critical quantities are the geometry (size and shape) of individual rods or spheres, which determine the spectral position and the properties of the Mie resonances. Intuitively, the packing density of the resonators does have an impact on the

effective parameters of the metamaterial because the macroscopic electromagnetic parameters describe the volume-averaged response of the material.

Following the discussion in Ref. [31], we use a square lattice of high-permittivity cylinders as an example to show the strong magnetic resonances in such structures. A schematic is depicted in Fig. 5.17a, where dielectric cylinders with diameter of $2a$ are placed in a two-dimensional periodic matter with a lattice constant of d . The incident magnetic field is polarized along the axes of the cylinders. The scattering property of a cylindrical particle can be solved analytically using Mie scattering theory. With the calculated field distribution, the effective permeability of the system along the direction of the cylindrical axis can be evaluated using $\mu_{\text{eff}} = \langle B \rangle / \mu_0 \langle H \rangle$, where the average value of B is taken over a unit-cell area of $d \times d$, and the average magnetic field H is taken along a line at the unit-cell boundary parallel to the cylinders [31]. Assuming the permittivity of cylinders is $200 + 5i$, the effective permeability for a system with a lattice constant of 5 mm and cylinder diameter 2 mm is plotted in Fig. 5.17b. A strong Lorentz-shaped resonance in the effective permeability near the microwave frequency of 4 GHz is observed.

Among all the ferroelectric and phonon-polaritonic materials for the high-permittivity scheme, SiC is by far the most attractive one in optical metamaterial research because its phonon resonance band falls into the mid-infrared range of the optical spectrum. SiC is a polaritonic material with its phonon resonance band centered at $12.5 \mu\text{m}$ (800 cm^{-1}), which introduces a sharp Lorentzian behavior in its electric permittivity. The dielectric function of SiC in the mid-infrared is well described with the following model [33, 34]:

$$\varepsilon_{\text{SiC}} = \varepsilon_{\infty} [\omega^2 - \omega_L^2 + i\gamma\omega] / [\omega^2 - \omega_T^2 + i\gamma\omega] \quad (5.4)$$

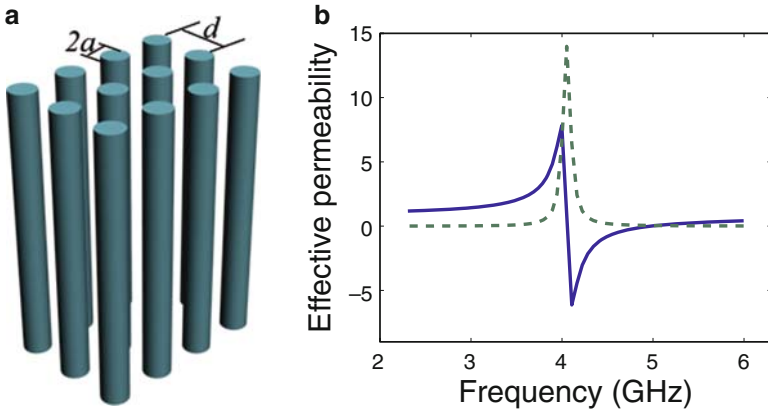
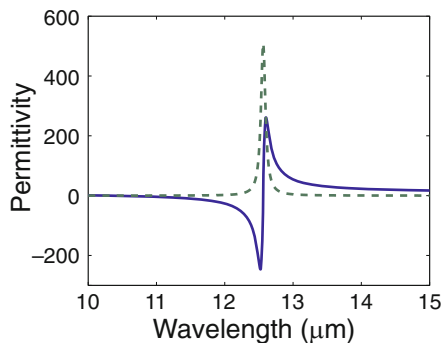


Fig. 5.17 (a) A square lattice of high-permittivity cylinders with a lattice constant of d and cylinder diameter of $2a$. (b) The resonance behavior in the effective permeability of the system. The solid and dashed lines represent the real part and imaginary parts of the permeability, respectively

Fig. 5.18 The dielectric function of silicon carbide (SiC) around its polaritonic resonance in the mid-infrared calculated with the analytical model of (5.4)



where $\varepsilon_\infty = 6.5$, $\omega_L = 972 \text{ cm}^{-1}$, $\omega_T = 796 \text{ cm}^{-1}$ and $\gamma = 5 \text{ cm}^{-1}$. The dielectric function of SiC around its polaritonic resonance frequency is plotted in Fig. 5.18. On the high-frequency side, the dielectric function is strongly negative, which makes its optical response similar to that of metals and has been utilized in applications like a mid-infrared superlens [35]. At frequencies lower than the resonance frequency, the permittivity can be strongly positive, which makes SiC an attractive candidate for producing dielectric-based magnetic metamaterials using high-permittivity Mie resonators in the mid-infrared wavelength range [36].

We note, however, that this technology cannot be extended into the visible or near-infrared optical regime because the permittivity of such ferroelectric or polaritonic materials becomes relatively small for frequencies above the dielectric relaxation frequency. Nevertheless, artificial magnetism with dielectric materials like SiC is of great interest for various applications. In Chap. 9 we will present a design of an invisibility cloaking device operating at the mid-infrared where the desired distribution of the magnetic permeability is accomplished by specially arranged SiC nanowires.

References

1. Landau LD, Lifshitz EM, Pitaevskii LP (1984) *Electrodynamics of continuous media*, Chapter 79. Pergamon, New York
2. Pendry JB, Holden AJ, Robbins DJ, Stewart WJ (1999) Magnetism from conductors and enhanced nonlinear phenomena. *IEEE Trans Microw Theory Tech* 47:2075–2084
3. Hardy WN, Whitehead LA (1981) Split-ring resonator for use in magnetic-resonance from 200–2000 MHz. *Rev Sci Instrum* 52:213–216
4. Baena JD, Marques R, Medina F, Martel J (2004) Artificial magnetic metamaterial design by using spiral resonators. *Phys Rev B* 69:014402
5. Marques R, Mesa F, Martel J, Medina F (2003) Comparative analysis of edge- and broadside-coupled split ring resonators for metamaterial design – theory and experiments. *IEEE Trans Antennas Propag* 51:2572–2581
6. Marques R, Medina F, Rafii-El-Idrissi R (2002) Role of bianisotropy in negative permeability and left-handed metamaterials. *Phys Rev B* 65:144440

7. Smith DR, Padilla WJ, Vier DC, Nemat-Nasser SC, Schultz S (2000) Composite medium with simultaneously negative permeability and permittivity. *Phys Rev Lett* 84:4184–4187
8. Yen TJ, Padilla WJ, Fang N, Vier DC, Smith DR, Pendry JB, Basov DN, Zhang X (2004) Terahertz magnetic response from artificial materials. *Science* 303:1494–1496
9. Katsarakis N, Koschny T, Kafesaki M, Economou EN, Soukoulis CM (2004) Electric coupling to the magnetic resonance of split ring resonators. *Appl Phys Lett* 84:2943–2945
10. Linden S, Enkrich C, Wegener M, Zhou JF, Koschny T, Soukoulis CM (2004) Magnetic response of metamaterials at 100 terahertz. *Science* 306:1351–1353
11. Enkrich C, Wegener M, Linden S, Burger S, Zschiedrich L, Schmidt F, Zhou JF, Koschny T, Soukoulis CM (2005) Magnetic metamaterials at telecommunication and visible frequencies. *Phys Rev Lett* 95:203901
12. Zhou J, Koschny T, Kafesaki M, Economou EN, Pendry JB, Soukoulis CM (2005) Saturation of the magnetic response of split-ring resonators at optical frequencies. *Phys Rev Lett* 95:223902
13. Tretyakov S (2007) On geometrical scaling of split-ring and double-bar resonators at optical frequencies. *Metamaterials* 1:40–43
14. Klein MW, Enkrich C, Wegener M, Soukoulis CM, Linden S (2006) Single-slit split-ring resonators at optical frequencies: limits of size scaling. *Opt Lett* 31:1259–1261
15. Zhang S, Fan WJ, Minhas BK, Frauenglass A, Malloy KJ, Brueck SRJ (2005) Midinfrared resonant magnetic nanostructures exhibiting a negative permeability. *Phys Rev Lett* 94:037402
16. Podolskiy VA, Sarychev AK, Shalaev VM (2002) Plasmon modes in metal nanowires and left-handed materials. *J Nonlinear Opt Phys Mater* 11:65–74
17. Dolling G, Enkrich C, Wegener M, Zhou JF, Soukoulis CM (2005) Cut-wire pairs and plate pairs as magnetic atoms for optical metamaterials. *Opt Lett* 30:3198–3200
18. Kildishev AV, Cai WS, Chettiar UK, Yuan HK, Sarychev AK, Drachev VP, Shalaev VM (2006) Negative refractive index in optics of metal-dielectric composites. *J Opt Soc Am B* 23:423–433
19. Shvets G, Urzhumov YA (2006) Negative index meta-materials based on two-dimensional metallic structures. *J Opt A Pure Appl Opt* 8:S122–S130
20. Cai WS, Chettiar UK, Yuan HK, de Silva VC, Kildishev AV, Drachev VP, Shalaev VM (2007) Metamagnetics with rainbow colors. *Opt Express* 15:3333–3341
21. Chettiar UK, Kildishev AV, Klar TA, Shalaev VM (2006) Negative index metamaterial combining magnetic resonators with metal films. *Opt Express* 14:7872–7877
22. Yuan HK, Chettiar UK, Cai WS, Kildishev AV, Boltasseva A, Drachev VP, Shalaev VM (2007) A negative permeability material at red light. *Opt Express* 15:1076–1083
23. Koschny T, Markos P, Smith DR, Soukoulis CM (2003) Resonant and antiresonant frequency dependence of the effective parameters of metamaterials. *Phys Rev E* 68:065602
24. Kildishev AV, Chettiar UK (2007) Cascading optical negative index metamaterials. *Appl Comput Electromagn Soc J* 22:172–183
25. Puscasu I, Schaich WL, Boreman GD (2001) Modeling parameters for the spectral behavior of infrared frequency-selective surfaces. *Appl Opt* 40:118–124
26. Wood RW (1935) Anomalous diffractive gratings. *Phys Rev* 48:928
27. Johnson PB, Christy RW (1972) Optical-constants of noble-metals. *Phys Rev B* 6:4370–4379
28. Lomakin V, Fainman Y, Urzhumov Y, Shvets G (2006) Doubly negative metamaterials in the near infrared and visible regimes based on thin film nanocomposites. *Opt Express* 14:11164–11177
29. Zhou JF, Zhang L, Tuttle G, Koschny T, Soukoulis CM (2006) Negative index materials using simple short wire pairs. *Phys Rev B* 73:041101
30. Smith DR, Schultz S, Markos P, Soukoulis CM (2002) Determination of effective permittivity and permeability of metamaterials from reflection and transmission coefficients. *Phys Rev B* 65:195104
31. O'Brien S, Pendry JB (2002) Photonic band-gap effects and magnetic activity in dielectric composites. *J Phys Condens Matter* 14:4035–4044
32. Huang KC, Povinelli ML, Joannopoulos JD (2004) Negative effective permeability in polaritonic photonic crystals. *Appl Phys Lett* 85:543–545
33. Spitzer WG, Kleinman D, Walsh D (1959) Infrared properties of hexagonal silicon carbide. *Phys Rev* 113:127–132

34. Korobkin D, Urzhumov Y, Shvets G (2006) Enhanced near-field resolution in midinfrared using metamaterials. *J Opt Soc Am B* 23:468–478
35. Taubner T, Korobkin D, Urzhumov Y, Shvets G, Hillenbrand R (2006) Near-field microscopy through a SiC superlens. *Science* 313:1595
36. Schuller JA, Zia R, Taubner T, Brongersma ML (2007) Dielectric metamaterials based on electric and magnetic resonances of silicon carbide particles. *Phys Rev Lett* 99:107401

Chapter 6

Negative-Index Metamaterials

6.1 A Brief Historical Review

The refractive index is one of the most important parameters for an optical medium. Defined as $n = c/v$, it measures the comparative velocity of light in different media. When a light beam travels across the boundary between two different materials, it bends owing to the change in refractive index at the interface. This phenomenon, refraction, gives the reason why a water pool appears shallower than it actually is, why a straw placed partially in water at a slant seems to bend towards the surface, and why people can use eyeglasses to adjust the path of light in front of their eyes and alleviate the effects of conditions such as myopia.

The refractive index is a complex number $n = n' + in''$, where the imaginary part n'' characterizes the losses in the material. Using the electromagnetic description of light given by Maxwell's equations, the refractive index n is related to basic material parameters, namely the permittivity ϵ and the permeability μ , via $n^2 = \epsilon\mu$. Therefore there is ambiguity in choosing the sign of n because mathematically there are two solutions for the refractive index: $n = \pm\sqrt{\epsilon\mu}$. For all known naturally occurring transparent materials like water or glass, both ϵ and μ are positive and thus the refractive index can be written as $n = \sqrt{\epsilon\mu}$. For anisotropic media like crystals or absorbing materials such as metals, the situation is more complicated and a tensor or complex value of the refractive index is required for describing the optical behavior of such materials. However, for any naturally existing material it is always true that the positive square root should be chosen.

But what about a negative sign in front of the square root? Is there any fundamental law of physics that prevents such a thing from happening? If not, what would happen to electromagnetic fields in a medium with a negative index of refraction? And finally, how could we create such a material in reality? All these questions are to be addressed in this chapter.

Although the research field of negative-index materials (NIMs) is a fairly new topic that has blossomed in the literature for fewer than 10 years, it is probably not that surprising to learn that a few scientific giants actually considered phenomena related to NIMs quite some time ago. These studies were perhaps so early that they could not be fully appreciated by contemporaries. Negative phase velocity and its

consequences were discussed in works by Sir Arthur Schuster and Lamb as early as 1904 [1, 2]; later the optical properties of NIMs were studied by Russian physicists Mandel'stam [3] and Sivukhin [4]. The first systematic study of the general properties of a hypothetical medium with a negative refractive index is attributed to Veselago, then with the Lebedev Physical Institute in Moscow, who analyzed the consequences for electromagnetic waves interacting with such a medium and reported on his initial effort in searching for such materials [5]. He pointed out that when both ε and μ are simultaneously negative, the negative square root must be chosen in the refractive index equation. Veselago coined the term “left-handed materials (LHMs)” for such media, because the field vectors E , H and the wave vector k form a left-handed system. He also noted that many remarkable properties would be associated with a negative index medium. The recent boom in NIMs was indeed inspired by Sir John Pendry, who not only provided a practical recipe on the building blocks for NIMs [6, 7], but also made critical predictions on the possible applications of metamaterials including perfect lenses and superlenses with subwavelength resolution [8], and an electromagnetic cloak of invisibility [9].

Left-handed materials are probably the most prominent class of metamaterials among all branches in the present metamaterial research. In fact, during the first few years of the metamaterial boom, the idea of a negative index of refraction was emphasized so much that the term metamaterial was often taken to be synonymous with negative index materials or left-handed materials.

Although the term “left-handed materials” introduced by Veselago was initially assumed to be applicable for materials with ε , μ and n being simultaneously negative (and real), this term now has been used in a much broader context and includes other optical systems that possess antiparallel phase velocity and Poynting vector. Such a “left-handedness” property can occur in a variety of systems, including photonic crystals, highly-anisotropic materials, metal-insulator-metal waveguides, and more. Some of these systems will be discussed in the last section of this chapter. Also it is worth noting that the term “left-handed materials” may introduce unnecessary confusion because this term also arises in the study of chiral materials. Therefore nowadays the term “negative-index (meta)materials” prevails among researchers in related fields. Another term used by metamaterial researchers for the same substance is “double-negative materials,” which emphasizes the fact that both ε and μ have negative values in such a material. There are also other terms for NIMs, such as “backward wave media,” “negative phase-velocity media,” etc. These names, however, appear relatively sparsely in the literature.

Because the index of refraction is a fundamental material parameter that enters into almost all basic formulae for optics, bringing the refractive index into a new domain of negative values has truly excited the imagination of researchers worldwide. These NIMs bring the concept of refractive index into a new domain of exploration and thus promise to create entirely new prospects for manipulating light, with revolutionary impacts on present-day optical technologies.

6.2 Reversed Phenomena in Negative-Index Media

Due to the ambiguity in determining the sign of $n = \pm\sqrt{\varepsilon\mu}$, the question arises even for the simplest case of “negative” materials: which sign for n is to be chosen when both ε and μ are equal to -1 ?

The right sign needs to be assigned in order to satisfy the causality condition. For any realistic passive medium, there is a positive imaginary part for both ε and μ , even though they may be quite small. With $\varepsilon = -1 + i\delta_1$ and $\mu = -1 + i\delta_2$ and taking the case when $0 < \delta_1 \ll 1$ and $0 < \delta_2 \ll 1$, we have

$$\begin{aligned} n &= \pm\sqrt{(-1 + i\delta_1)(-1 + i\delta_2)} = \pm\sqrt{(1 - \delta_1\delta_2) - i(\delta_1 + \delta_2)} \\ &\approx \pm\left[1 - \frac{i(\delta_1 + \delta_2)}{2}\right]. \end{aligned} \quad (6.1)$$

Causality requires that the imaginary part of n has to be positive for any passive material. Therefore in the equation above, the minus sign must be chosen when the real parts of both ε and μ are negative.

Negative refractive is of course more than a mathematical trick. The arrival of NIMs provides a rather unique opportunity for researchers to reconsider and possibly even revise the interpretation of very basic laws. Because the real part of the refractive index n' denotes the relative decrease in phase velocity of light when compared with vacuum, the negative refractive index in NIMs implies that the phase velocity is directed against the flow of energy. Considering a plane wave propagating in the z direction with free-space wave-vector k and angular frequency ω , a direct conclusion from the wave form of $e^{i(nkz - \omega t)}$ is that the phase of the electromagnetic wave traveling in a NIM becomes advanced instead of retarded as in common materials. A discussion of the relations among the vectors \vec{E} , \vec{H} , and \vec{k} can make this point more clear. For a plane wave, Maxwell's equations give the following relations for the three vectors:

$$\begin{cases} \vec{k} \times \vec{H} = -\omega\varepsilon_0\varepsilon\vec{E} \\ \vec{k} \times \vec{E} = \omega\mu_0\mu\vec{H} \end{cases} \quad (6.2)$$

Thus for a common material with positive ε and μ , the vectors \vec{E} , \vec{H} , and \vec{k} form a right-handed coordinate system and \vec{k} is parallel to the Poynting vector $\vec{E} \times \vec{H}$, which indicates the direction of energy propagation. However, in a NIM where both ε and μ have negative values, from the two equations above it is clear that the vectors \vec{E} , \vec{H} , and \vec{k} form a left-handed system. This is the reason why NIMs are sometimes called left-handed materials, as noted in the seminal paper by Veselago. Note that in such a system the wave-vector \vec{k} is anti-parallel to the Poynting vector. Again we reach the apparently astonishing results that in a NIM the energy propagates against the wave-vector and the phase is advanced in the propagation direction. Many exotic phenomena result from this unique phase reversal effect in NIMs.

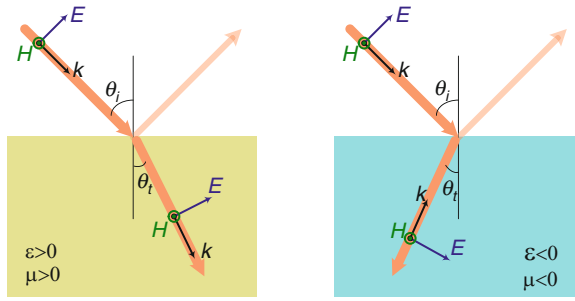


Fig. 6.1 The refraction of a light beam when passed through the boundary of air and a PIM (*left*) or a NIM (*right*)

The most intuitive result of a negative refractive index is the modified Snell's law. Snell's law is the simple formula used to calculate the refraction angle of light traveling across the interface between two media of differing refractive indices, $n_1 \sin \theta_i = n_2 \sin \theta_t$. If we extend this law to account for negative refraction, when a light beam passes through the boundary between a positive index material (PIM) and a NIM, the angle of refraction θ_t has to be a negative value. This indicates that the refracted beam is bent at the same side of the normal to the interface. A schematic of this scenario with negative refraction is depicted in Fig. 6.1.

The bending of light at the PIM/MIM interface can be determined in another way with richer physics. As discussed previously, in a NIM the wave-vector \vec{k} is oriented opposite to the light ray represented by the Poynting vector. At the interface of any two media the tangential component of the wave-vector must be continuous, which is inferred by one of the most fundamental laws in physics – momentum conservation. Hence the only possible way to implement the refracted ray is as shown in Fig. 6.1.

Many interesting phenomena result from the negative index and phase reversal exhibited in NIMs, including a reversed Doppler effect, reversed Cerenkov radiation and a reversed Goos–Hänchen shift [5].

The Doppler effect is the apparent change in frequency of a wave that is perceived by a detector moving relative to the source of the wave. During the relative motion, the detector is always pursuing points of the wave that correspond to some definite phase. The frequency “felt” by the detector is $\omega = \omega_0 + \vec{k} \cdot \vec{v}$, where ω_0 is the actual frequency, \vec{k} is the wave-vector of the wave detected by the observer, and \vec{v} is the velocity of the source with respect to the detector. The velocity is positive when the source is approaching the detector. A well-known example of this effect is the perceived frequency of the sound wave emanating from an ambulance siren as it rushes past a stationary observer. The perceived frequency is higher when the vehicle is moving towards the observer because \vec{k} and \vec{v} are in the same direction, while the frequency is perceived to be lower when the siren is moving away due to the negative value of the dot product $\vec{k} \cdot \vec{v}$. A similar phenomenon happens in optical

waves except that there is a prefactor of $\gamma = 1/\sqrt{(1 - v^2/c^2)}$, which takes into account the effect of the special theory of relativity. However, in a NIM the light wave perceived by the detector has the wave-vector \vec{k} pointing from the detector to the source instead of the opposite as in any common material. Consequently, the frequency measured by the detector would be lower when the light source is approaching it because \vec{k} and \vec{v} are anti-parallel in this case.

Cerenkov radiation is the electromagnetic radiation in a cone of angles emitted by a charged particle passing through an insulator at a speed greater than that of light in the medium. The angle of the cone corresponds to the condition when the emitted photons interfere constructively. The angle of the Cerenkov cone with respect to the particle motion direction is determined by $\cos \varphi = 1/n\beta$, where β is the speed of the particle normalized by the vacuum light speed. Hence the Cerenkov radiation will go backward in a NIM because an obtuse angle for the cone must be chosen when n is negative.

There are other basic laws in optics that need to be modified to account for negative refraction, such as the Goos-Hänchen shift occurring at total reflection [10] and the Brewster's angle in polarizing optics [11]. Generally speaking, in the field of NIMs we need to carefully reconsider nearly all optical phenomena that are related to the phase information of light.

6.3 Negative Refraction in Microwave Frequencies

One of the main objectives at the very beginning of metamaterial research was to construct and verify a negative-index material. Before we proceed with discussing possible strategies for this goal, it is useful to clarify the reason why there is no naturally occurring material with a negative index of refraction readily observed, even though there is no theoretical obstacle which would hamper the existence of such a material. As we have discussed in Chap. 1, for any naturally occurring material such as crystals or man-made materials whose scale of inhomogeneities is much smaller than the incident wavelength, the electromagnetic response of the material is well-characterized by using the macroscopic parameters ε and μ . Negative values of the two parameters do exist in nature. For example, noble metals at optical frequencies are good examples of materials with negative ε . As for the negative value of μ , some antiferromagnets and insulating ferromagnets have been shown to provide negative effective magnetic permeability [12, 13]. A material would have a negative refractive index if both ε and μ are simultaneously negative at the same frequency (this is a sufficient but not necessary condition [14]), which is represented by the third quadrant in Fig. 1.2. Furthermore, the possibility of realizing simultaneously negative effective values of ε and μ in uniaxial antiferromagnets was briefly discussed several decades ago [15]. Unfortunately, in natural materials the negative electrical resonance mostly occurs for frequencies of at least a few terahertz, while any natural magnetic resonance dies off for such a high frequency.

Since magnetic coupling to electromagnetic fields is a precursor for negative refraction, one of the most critical steps for achieving a NIM is to overcome the low-frequency barrier of magnetic response in conventional materials. Thanks to the advances in metamaterial research, it is now possible to make electromagnetic waves “two-handed” at high frequencies by using artificially engineered metal-atoms with a strong magnetic coupling. During the last few years, NIMs have been demonstrated across several decades of the electromagnetic spectrum, from the X-band microwave frequencies up to the red end of the visible light.

Although the term “refractive index” is more commonly used in optics, earlier experimental demonstrations (before 2005) of negative indices of refraction were focused on microwave frequencies. Prepared with the knowledge of controllable electric responses from Chap. 4 and artificial magnetism from Chap. 5, the construction of NIMs no longer seems to be such a mysterious and challenging task. Negative index materials were first realized in a very rudimentary form in which the negative index was presented along only one principal direction [16]. Later on, two-dimensional [17] and three-dimensional NIMs [18] were demonstrated using similar techniques. The famous two-dimensional NIM made by a group at the University of California – San Diego is shown in Fig. 6.2a, where a periodic array of SRRs was fabricated with wires placed uniformly between the split rings. This metamaterial consists of two building blocks – the wires with negative effective permittivity $\epsilon_{eff}(\omega)$ giving rise to an electric response, and the SRRs with negative effective permeability $\mu_{eff}(\omega)$ resulting from the response to an applied magnetic field. Combining the use of SRRs and metal wires, the UCSD group built a two-dimensional periodic array, and a negative index of refraction in the microwave frequency range was verified that was appropriate to a modified Snell’s law [17]. Two years later, Parazzoli et al. used a similar structure to create a three-dimensional cube operating in free space, and measurements confirming the negative index of refraction of the structure were performed at a distance much larger than the wavelength [18]. This experiment removed any doubts regarding the possibility of fabricating NIMs. The structures used in these first demonstrations is the prototype utilized in most of the early NIMs reported in the literature. Only recently have researchers developed new geometries to obtain a magnetic response at optical frequencies.

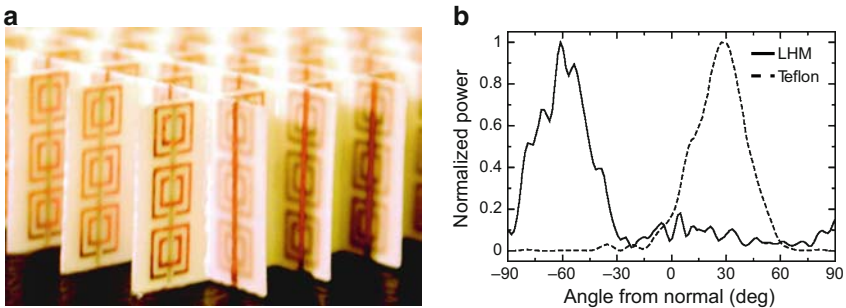


Fig. 6.2 (a) The NIM at microwave frequency built by the UCSD group. (b) The experimental result verified the modified Snell’s law. Adapted from [17]. Reprinted with permission from AAAS

6.4 The Debut of Optical Negative-Index Materials

Although first obtained in the microwave range, scaling negative refraction up to the optical range is very important for both the theoretical significance and for the application value that such materials could provide. Indeed, the refractive index is a concept conventionally used at optical frequencies rather than microwave frequencies. Similar to the considerations shown in Chap. 5 for optical magnetism, direct downward scaling of microwave NIM structures is not a realistic method to produce optical NIMs due to both fabrication challenges and, more importantly, material limitations. The electromagnetic response of metals in the optical range is vastly different than at lower frequencies, where ϵ is extremely large and metals behave as nearly perfect conductors. This distinction prohibits the design of optical NIMs using the same structures as their microwave counterparts. On the other hand, at optical frequencies, ϵ in metals can be comparable to the dielectric permittivity of a host material, enabling the excitation of a surface plasmon resonance. This opens up a new method of achieving negative permittivity and permeability.

The challenges in optical NIM research lay not only in design and fabrication, but also in experimental characterization. The experimental verification of optical negative-index metamaterials is far more complicated than that of their microwave counterparts. Refractive index, by definition, implies the bending of the direction of the Poynting vector of light at an interface. Unfortunately, to date most of the reported optical NIMs were in the form of planar layers of subwavelength thicknesses fabricated by optical or electron-beam lithography [19–25]. This limitation in fabricated NIMs has prohibited experimentalists from directly observing the negative bending of a beam of light from a wedge-like structure, as was done in microwave NIM experiments. Another approach for directly observing a negative refractive index is based on geometrical optics, where one could detect the lateral displacement at the output interface of a homogeneous NIM slab for obliquely incident light beams. This method is limited in a similar way as the wedge approach, however, because the subwavelength thickness of available optical NIM samples precludes the experimental observation of any lateral shift of light beams. More critically, methods relying on the direction of the Poynting vector with inclined incidence at interfaces are, in principle, not capable of unambiguously identifying the sign of the effective index of refraction in an anisotropic material. Actually, a negative angle of refraction is an intrinsic property of uniaxial media and has been observed in natural crystals like calcite and yttrium orthovanadate (YVO₄) [26].

Now let us come back to the material properties required of a negative-index material. To make a NIM, it is essential to tune the resonance property of the (artificial) material in such a way that the frequencies for the negative electric response and those for the negative magnetic response occur in an overlapping spectral range. A negative effective permittivity at controlled frequencies can be obtained using artificial materials consisting of periodic metallic structures. The electric response of such a material can be designed to mimic the Lorentz model, and the characteristic frequency parameters ω_0 and ω_p are largely dependent on the geometry of the lattice and the metallic element [6]. A controllable magnetic response at

gigahertz frequencies and above has been studied extensively, as detailed in the previous chapter. Therefore the key in NIM demonstrations is to combine the electric response and magnetic response in an appropriate manner. We should again note that the condition of simultaneously negative ε and μ given in Veselago's seminal paper is a sufficient but not necessary condition for constructing NIMs. A possible approach to achieve a negative refractive index in a passive medium is to design a material where the (isotropic) permittivity $\varepsilon = \varepsilon' + i\varepsilon''$ and the (isotropic) permeability $\mu = \mu' + i\mu''$ obey the equation:

$$\varepsilon'\mu'' + \mu'\varepsilon'' < 0 \quad (6.3)$$

This leads to a negative real part of the refractive index $n = n' + in'' = \sqrt{\varepsilon\mu}$ [14, 27]. The inequality above is always satisfied if both $\varepsilon' < 0$ and $\mu' < 0$. However, due to the natural inertness of magnetic permeability at optical frequencies, it is a practical challenge to obtain an effective permeability very different from 1, especially at very high frequencies such as the frequency of visible light. Equation (6.3) strictly implies that $n' < 0$ cannot occur in a magnetically inactive medium with $\mu = 1 + 0i$. Consequently, a magnetic response is essential in a NIM. The good news implied in (6.3) is that, instead of relying on a negative μ' , a negative index of refraction can be achieved in a magnetically lossy medium with a negative ε' along with $\mu'' > 0$. In this case the inequality in (6.3) may still be fulfilled, and therefore a negative real part of the refractive index n' can be obtained. Actually both of the earliest reported optical NIMs (in 2005) belong to this category. However, the figure of merit $F = |n'|/n''$ in these cases is typically small.

The necessary condition for an NIM in (6.3) can be achieved in an array of coupled nanorods. It was shown in an early paper by Lagarkov and Sarychev that a pair of metal nanorods can have a large paramagnetic response [28]. Then, Podolskiy et al. showed that such a pair of metal nanorods is also capable of a diamagnetic response and, most importantly, negative n' in the optical range [29]. Following these theoretical predictions, the first optical metamaterial with a negative index of refraction was experimentally demonstrated by a research group at Purdue University using a layer of paired metal nanorods [19].

The building block of the metamaterial is a pair of nanorods, as illustrated in Fig. 6.3. An AC electric field parallel to both rods induces parallel currents in both rods. The magnetic field, which is oriented perpendicular to the plane of the rods, causes anti-parallel currents in the two rods as shown in Fig. 6.3. These anti-parallel currents cause the magnetic response of the system. The magnetic response will be dia- or paramagnetic depending on whether the wavelength of the incoming magnetic field is shorter or longer than the magnetic resonance of the coupled rods. The two parallel rods form an open current loop, which acts as a transmission line with a current resonance. Such a current loop is closed at the ends of the rod-pair through the displacement current. For normally-incident light with the electric field polarized along the rods and the magnetic field perpendicular to the pair, both the electric and the magnetic responses can experience resonant behavior at certain frequencies. Above the resonance frequency, the circular current in the pair of rods

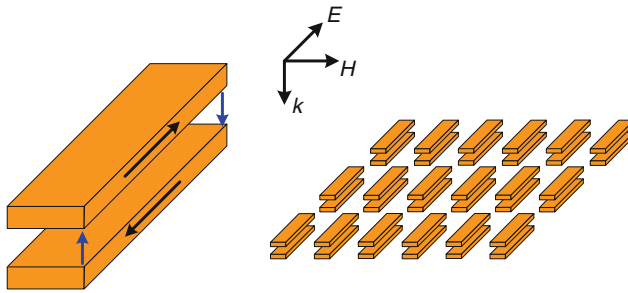


Fig. 6.3 Schematic of the array of paired nanorods

and the displacement current at the ends of the rods can lead to a magnetic field opposing the external magnetic field of the incident light. In this design the electrical component of the incident wave excites a symmetric current mode in each rod pair, whereas the magnetic component excites an anti-symmetric mode. The excitation of plasmon resonances for both the electric and the magnetic light components in an overlapping frequency range results in resonant behavior for the refractive index, which can become negative above the resonance as previously predicted. This can be thought of as a resonance in an optical LC circuit, with the metal rods providing the inductance L and the dielectric gaps between the rods acting as capacitive elements C .

The sample was fabricated using electron-beam lithography. The designed unit cell of the paired nanorods array is shown in Fig. 6.4a. Figure 6.5 shows field-emission scanning electron microscope (FE-SEM) images of a portion of the sample and a closer view of a single pair of nanorods.

We emphasize that a full characterization of the complex transmission and reflection coefficients, including the magnitude and phase information, is critical in experimental work on negative refractive index materials. The spectra of the magnitudes of the transmission and reflection are important to identify the positions, spectral widths and relative strength of the electromagnetic resonances in a nanofabricated material. However, these values are not sufficient to verify and characterize the negative index in the structure, and to retrieve the important parameters like the effective permittivity (ϵ), permeability (μ), impedance (Z) and refraction index (n) ambiguously. The measurement of the phase shift in the metamaterial layer is also of critical importance, because it is closely related to the definition of the refractive index – the phase of wave is retarded in normal PIMs and is advanced in NIMs.

The complex coefficients for transmittance and reflectance needed for the retrieval of the refractive index were measured directly in the paired nanorod experiments. The transmission ($T = |t|^2$) and reflection ($R = |r|^2$) spectra were collected with a spectrophotometer using linearly polarized light. The phase measurements were performed using polarization and walk-off interferometry techniques, as we discussed in Chap. 3. Along with the experimental investigation, the optical properties of the paired nanorod structure were also simulated based on a

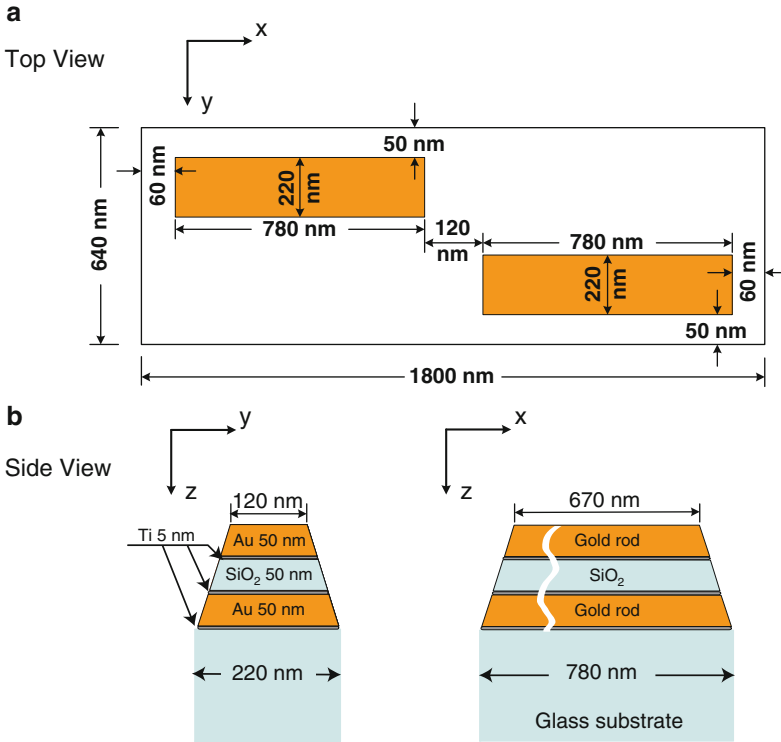


Fig. 6.4 (a) The designed elementary cell of the paired nanorod structure. (b) Dimensions of a pair of trapezoidal-shaped nanorods on a glass substrate

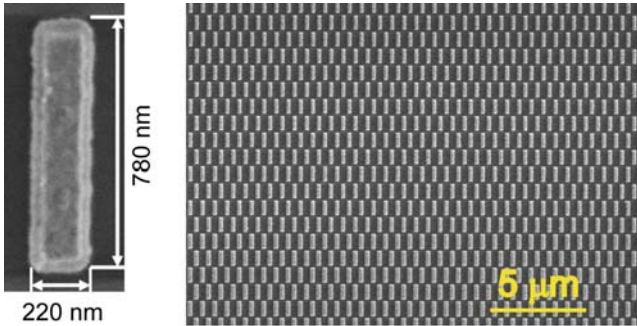


Fig. 6.5 Field-emission scanning electron microscope images of the fabricated array (*top view*). *Left*: a single pair of nanorods. *Right*: a fragment of the pattern

3D finite-difference time domain (FDTD) method. Figure 6.6 illustrates the results for the phase measurements, including the phase anisotropy and the absolute phase shift, both of which are compared with 3D FDTD simulations. The phase anisotropy curve $\Delta\varphi$ for transmitted light shows a strong resonant dependence with a negative

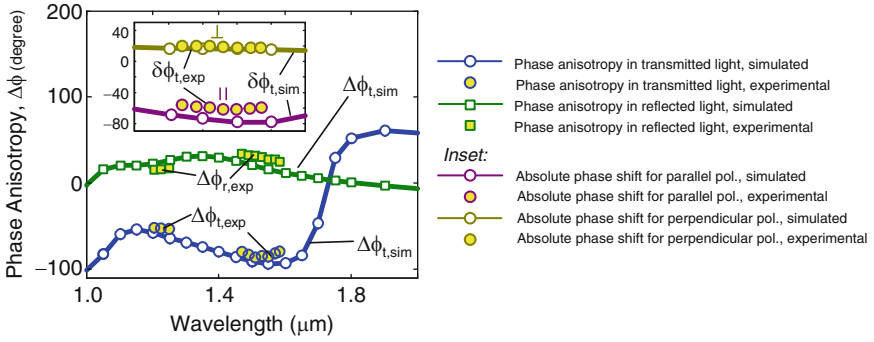


Fig. 6.6 Experimental data for phase measurement along with simulations. *Inset*: absolute phase shift for transmitted light

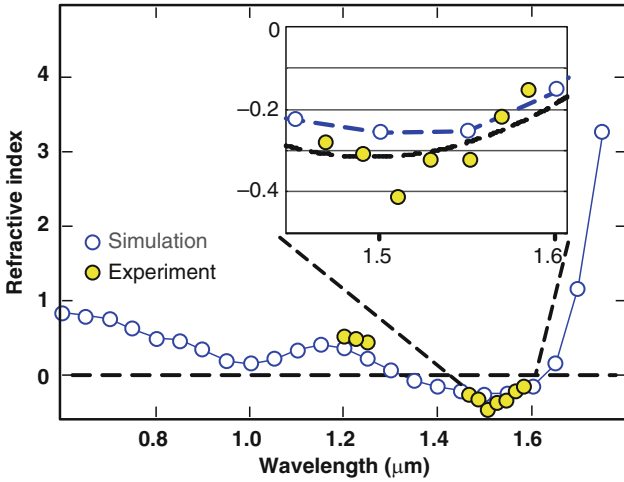


Fig. 6.7 Real part of the refractive index retrieved from experiments (*blue*) and simulations (*black*). The *inset* is a zoomed view of the region around $1.5 \mu\text{m}$ where the index of refraction is negative

value as much as $\sim -100^\circ$ around the communication wavelengths of $\sim 1.5 \mu\text{m}$. From the inset of Fig. 6.6 we can see that the phase shift of the sample with respect to an air slab of the same thickness is $\varphi_{s,\parallel} = -61^\circ$ for light transmittance at $\lambda = 1.5 \mu\text{m}$. The magnitude of this value is well below the phase shift in an air slab of 165 nm $\varphi_r = 40^\circ$ at $1.5 \mu\text{m}$, so the negative phase acquired in the sample is $\varphi_s \approx -21^\circ$. This negative value indicates that the effective index of refraction is negative for the wavelengths discussed above. Note that a rather high transmittance of about 25% is obtained at $\lambda \approx 1.5 \mu\text{m}$.

Based on the effective parameter retrieval technique discussed in Chap. 3, we can obtain the effective index of refraction for two different polarizations using r and t coefficients. Figure 6.7 is a zoomed view of the real part of the retrieved index of

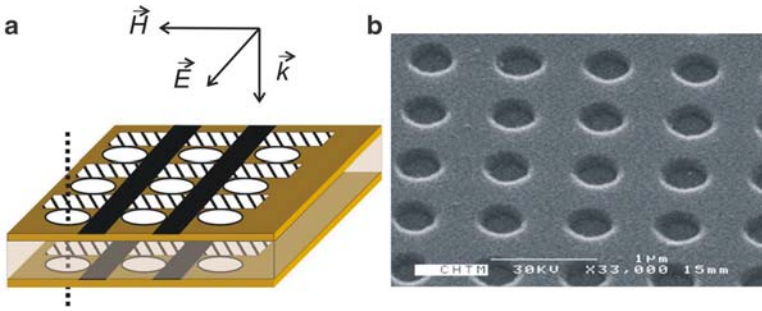


Fig. 6.8 (a) Schematic of the paired gold films with dielectric voids. (b) SEM picture of the structure. Reprinted with permission from [20]. Copyright (2005) by the American Physical Society

refraction using experimental data and the simulated results. Experimental studies of the nanorod sample provide a value of $n = -0.3 \pm 0.1$ at $1.5 \mu\text{m}$. The results in Fig. 6.7 indicate good agreement between measurements and simulations.

An optical negative index is also possible in the inverse of the coupled-nanorod structure, that is, pairs of elliptically shaped voids in metal films [20]. A negative refractive index at about $2 \mu\text{m}$ was reported using such an inverse, resonant structure (note that this observation was obtained at about the same time as [19]). A schematic and a representative SEM image of such a geometry are illustrated in Fig. 6.8. In order to construct the coupled-void structure, we begin with two thin films of metal separated by a dielectric spacer layer. Then, elliptically shaped voids are etched in the two metal films to form the paired elliptical voids. This creates the inverse of the original structure of paired metal ellipses. However, both types of samples should exhibit similar resonance behaviors if the orientation of the electric and magnetic fields are also interchanged. This is a result of the Babinet principle. It is useful to note then that, due to the Babinet principle, inverted NIMs such as elliptical or rectangular dielectric voids in metal films are physically equivalent to paired metal rods embedded in a dielectric host. This gives us increased flexibility in designing NIM structures that are actually realizable with current fabrication methods.

We should also note that the first optical NIMs in Refs. [19, 20] were only rudimentary demonstrations. This is the case because the negative indices in those demonstrations were accomplished in part because of the significant contribution from the imaginary part of the magnetic permeability μ'' , which typically does not allow for a sufficiently low loss factor.

6.5 General Recipe for Construction

While the two earliest optical NIMs discussed in the preceding section have proven that NIMs are possible at optical frequencies, they both possessed significant losses as indicated by a very large imaginary part n'' in the effective refractive index. Based on our discussion about the sufficient and necessary conditions for the negative

index of refraction, we can categorize NIMs into two types: double-negative NIMs (DN-NIMs) in which Veselago's requirement of both $\varepsilon' < 0$ and $\mu' < 0$ is satisfied, or single-negative NIMs (SN-NIMs) where only the necessary condition in (6.3) is fulfilled with $\varepsilon' < 0$ and $\mu' > 0$. The NIMs with pairs of nanorods in Fig. 6.5 and nano-voids in Fig. 6.8 both belong to the SN-NIM class, which inevitably exhibit a low figure of merit (FOM).

As we have briefly discussed in Sect. 6.4, for NIMs the ratio $-n'/n''$ is often taken as a FOM because low-loss NIMs are desired in most applications. The FOM of NIMs can be expressed in terms of the effective permittivity and permeability:

$$\text{FOM} = -\frac{|\mu| \varepsilon' + |\varepsilon| \mu'}{|\mu| \varepsilon'' + |\varepsilon| \mu''} \quad (6.4)$$

Equation (6.4) indicates that a DN-NIM with $\varepsilon' < 0$ and $\mu' < 0$ will have a lower n'' value than an SN-NIM with the same $n' < 0$ and $\mu' > 0$. In addition, DN-NIMs can provide better impedance matching to common positive-index materials than SN-NIMs.

Although both negative ε' and negative μ' can be realized based on electric and magnetic resonances, respectively, it is not a good practice to combine the two types of plasmonic resonances at an overlapping frequency range. First, it is typically very difficult to obtain a system where both resonances occur at the same frequency. Second, any plasmonic resonance always brings loss to the system. Since an electric resonance is not really necessary in order to obtain a negative ε' , we should try to avoid using an electric resonance in our design. A possible solution to this generic problem is to use a resonant magnetic structure along with a non-resonant metallic structure that provides "background" negative permittivity in a broad spectral range, including the wavelength band where the magnetic resonance occurs. This is not hard to achieve since noble metals like gold and silver have negative permittivities at optical frequencies below their plasma frequencies. Hence, merely adding a metal film above and below the magnetic resonator, for example, should provide the necessary negative permittivity for a NIM [30]. An alternative method proposed to achieve the background negative permittivity is to use pairs of continuous metal wires that do not have an electrical resonance at the wavelength of interest [31]. Then a magnetic resonance with a negative permeability is obtained by including appropriately designed pairs of metallic wires or plates.

The general guidelines above result in the "fishnet" structure, also known as the double-grating structure, which is today's prevailing structure for negative-index metamaterials at optical frequencies [21]. In the fishnet structure, the pairs of broader metal strips provide negative permeability via asymmetric currents (as described in Chap. 5), whereas the pairs of narrower metal strips (wires) act as a diluted metal. This situation is more clearly illustrated in Fig. 6.9. The fishnet can be viewed as a resonant magnetic structure combined with a non-resonant electric structure. It is important to note that in the fishnet structure of Fig. 6.9, the pairs of narrower strips act as such off-resonant wires and, at the wavelength where the magnetic resonance occurs in the broader strips, they simply provide a background negative permittivity.

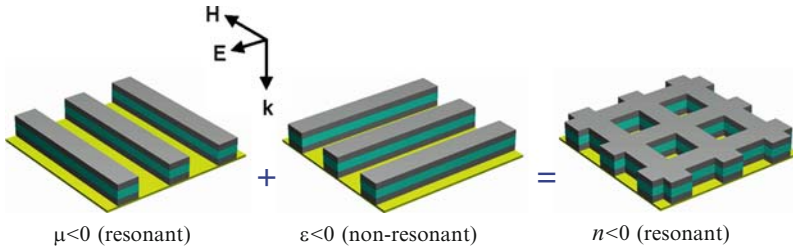


Fig. 6.9 The fishnet structure: resonant magnetic strips combined with a non-resonant electric grating

Based on the fishnet structure, several groups around the world have demonstrated a negative index of refraction in the near-infrared and the visible ranges. A double-negative fishnet was first reported at a wavelength of $1.8 \mu\text{m}$ with an FOM above 1 [21], and then at $1.4 \mu\text{m}$ with an FOM of about 3 [22]. A three-layer, double-negative fishnet was also demonstrated at $1.4 \mu\text{m}$, which shows that stacking multiple layers of the fishnet structure will not deteriorate the NIM performance in terms of optical loss [32]. The Purdue group successfully pushed the double-negative band of fishnet NIMs into the visible light spectrum. In an early report, the Purdue team showed a dual-band fishnet NIM exhibiting a double-negative behavior at 813 nm with an effective refraction index of $n' \approx -1$ and an FOM of 1.3 [25]. For a different polarization, the same sample also processes a single-negative band around 770 nm , which sits at the very red end of the visible spectrum. Later, the same group reported a DN-NIM at 725 nm with a similar geometry, where an FOM of ~ 1.1 was observed [33]. For the orthogonal polarization, the sample displays SN-NIM behavior with an FOM of 0.5 at $\sim 710 \text{ nm}$, also an improvement in comparison with the earlier work [25].

The SEM image of the fishnet structure discussed in Ref. [33] is shown in Fig. 6.10a. The sample is fabricated using standard e-beam lithography, e-beam evaporation and lift-off processes. A schematic figure of a unit cell of the fishnet structure along with the incident polarization is illustrated in Fig. 6.10b. The properties of the plasmonic resonances in the structure can be visualized by simulating the field distribution in the sample at a few interesting wavelengths, as depicted in Fig. 6.10c, d. In the field maps, the color depicts the magnetic field, while the arrows show the electric displacement. Figure 6.10c shows an electric resonance at a wavelength of 540 nm , where the electric displacements in both the top and bottom strips are aligned together. We emphasize that this electric resonance is not related to the negative-index behavior we are pursuing. The important electric behavior of the sample is that at the longer wavelength side of the electric resonance, the effective dielectric function exhibits a non-resonant Drude behavior, which serves perfectly as a broadband, background negative ϵ . Figure 6.10d shows the field distribution of the magnetic resonance at 720 nm , which is essentially identical to the magnetic response of paired nanostrips that were discussed in Chap. 5.

The retrieved effective parameters for the fishnet sample are plotted in Fig. 6.11 [33]. Figure 6.11a clearly indicates that the electric behavior beyond the electric

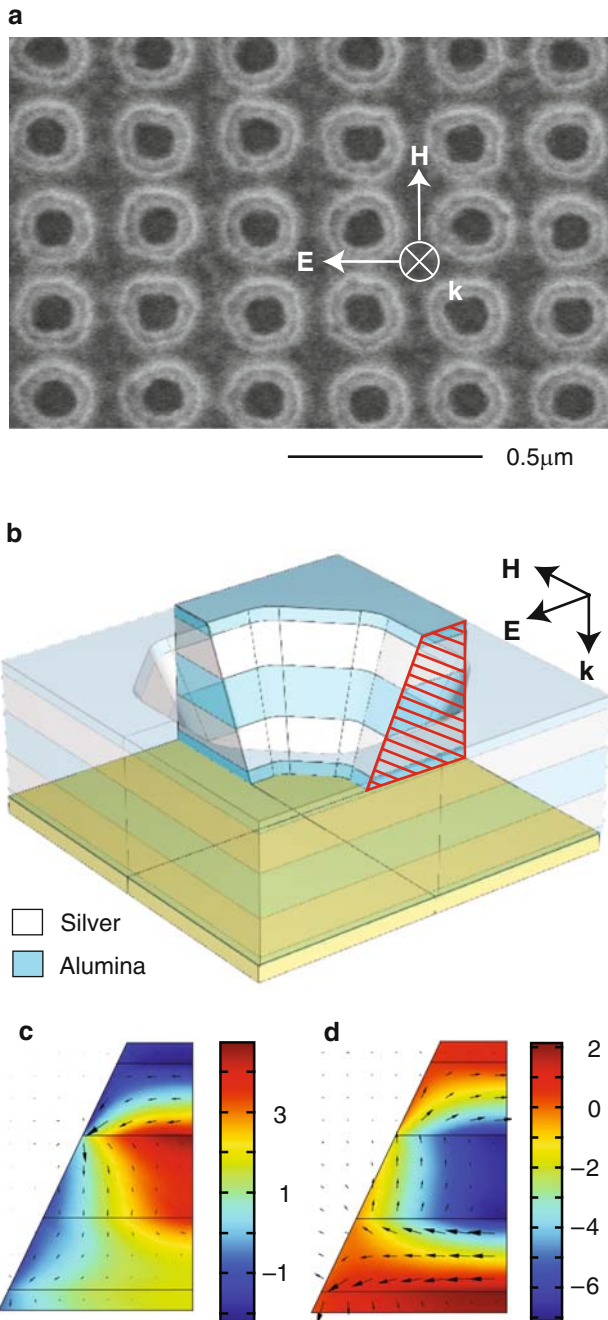


Fig. 6.10 (a) SEM image of the fishnet structure. (b) Schematic of a unit cell of the fishnet structure. (c) and (d) show the field maps of the region marked with red lines in (a) at wavelengths of 540 and 720 nm, respectively. Reproduced from [33] by permission of the *MRS Bulletin*

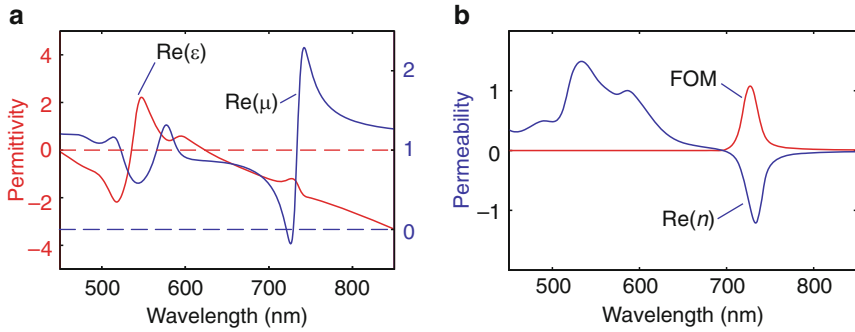


Fig. 6.11 (a) Real parts of the permittivity (ϵ) and permeability (μ) for the DN-NIM sample; (b) Real part of refractive index (n) and figure of merit (FOM) for the DN-NIM sample. Reproduced from [33] by permission of the *MRS Bulletin*

resonance of ~ 540 nm is similar to that of a dilute metal. This is the desired response and is in agreement with our discussion of the general recipe for broadband, background negative ϵ from the beginning of this section. The magnetic resonance at ~ 720 nm gives rise to a negative effective permeability, which is necessary for a DN-NIM. Figure 6.11b reveals a negative index of about -1 along with an FOM of above 1 at a wavelength of 725 nm, corresponding to red light. As a “by-product,” at the other polarization the same sample also displays a single-negative response at the slightly shorter wavelength of ~ 710 nm. Not surprisingly, the FOM of the single-negative band is 0.5, much lower than that of the double-negative band.

A number of interesting NIM phenomena have been observed in fishnet structures. In an experiment with a fishnet NIM irradiated at a wavelength near $1.5 \mu\text{m}$ and probed by a chain of femtosecond pulses, simultaneously negative phase and group velocities were observed, which means both the carrier wave oscillation and the pulse envelope moved against the direction of energy propagation [23]. Another experiment with a fishnet structure at the near-infrared wavelength of $\sim 1.7 \mu\text{m}$ realized optical modulation of the effective refractive index, where the photoexcitation of an amorphous silicon spacer resulted in the dynamic tuning of the metamaterial properties [34]. The fishnet geometry also allows for truly three-dimensional optical NIMs. In Ref. [35] a stack of fishnets designed to show NIM behavior for visible light was milled into a wedge, and a reversed Snell’s law at the PIM/NIM interface was directly verified by observing that the refracted beam bent in the “wrong” direction. An SEM image of this fishnet wedge was shown in Fig. 3.2c in Chap. 3.

6.6 Alternative Approaches

The techniques discussed in the preceding two sections represent the standard approach for realizing NIMs at optical frequencies. In this standard method, delicate meta-atoms are carefully designed and arranged into a metamaterial whose

macroscopic electromagnetic responses are characterized by a negative effective permittivity ϵ and a negative (or positive but lossy) effective permeability μ . In this section we consider several other schemes to achieve a negative effective refractive index or a negative angle for a refracted light beam at optical frequencies. Alternative approaches include photonic crystals, anisotropic materials, chirality methods, plasmonic waveguides, nano-transmission lines, and more.

Negative refraction of light can be realized due to band-folding effects in specially-designed photonic crystals. Photonic crystals are usually periodic dielectric structures that are designed to affect the behavior of photons in a method similar to the way a semiconductor's periodic potential affects the behavior of electrons. Strictly speaking, photonic crystals cannot be considered as metamaterials, and the behavior of light waves inside them typically cannot be characterized by an effective refractive index. This is because the periodicity in photonic crystals is comparable to the operational wavelength. Therefore, it is hard to distinguish between the effects of refraction and diffraction in photonic crystals. Nevertheless, by designing appropriate dispersion relations in photonic crystals, a negative angle of refraction and an anti-parallel relationship between the wave-vector and the energy propagation are indeed possible.

In fact, the phenomenon of negative refraction in photonic crystals was suggested long before the first demonstration of an optical NIM [36]. In 2000, Notomi pointed out that in a strongly-modulated photonic crystal, light propagation properties are not very sensitive to the angle of incidence, and therefore the propagation becomes refraction-like in the vicinity of the photonic band gap. In such a situation, the effective refractive index can be defined, and its sign and absolute value can be varied by changing the crystal structure, the refractive indices of constitutive materials, and the incident wavelength. The effective index of refraction can be negative or less than unity for this scenario. A good analogy of the effective refractive index in photonic crystals is the effective mass in semiconductors. The effective mass is a measure of the band curvature near the bandgap in semiconductors, and the effective index plays a very similar role in photonic crystals. More advanced theoretical work on negative refraction in photonic crystals was carried out in Refs. [37, 38]. Negative refraction of light at near-infrared wavelengths has been experimentally observed in a two-dimensional, group III–V photonic crystal [39] and in a silicon-polymer photonic-crystal membrane [40].

We note that although negative light refraction can be realized in photonic crystals, not all the exotic properties predicted in homogeneous NIMs can be expected in photonic crystals. For instance, the amplification of evanescent waves contributing to the super-resolution predicted by Pendry can only be partially realized in photonic-crystal NIMs. This is due to the fact that, for the very large k -vector components carrying information about the smallest features of an object, the structural periodicity is too large, and the photonic crystal cannot be considered to be an effective medium supporting all values of the transverse wavevector for evanescent waves [37]. On the other hand, NIMs based on photonic crystals may hold certain advantages over plasmonic NIMs. Most prominently, photonic-crystal NIMs are entirely dielectric media with little loss, while in metal-dielectric metamaterials

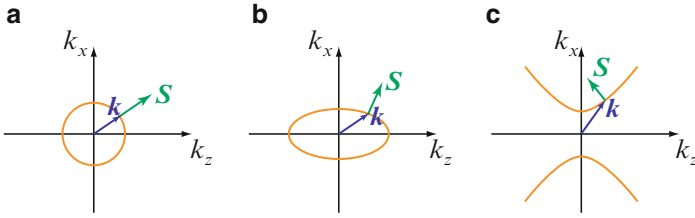


Fig. 6.12 Wave vector surfaces and isofrequency curves for (a) an isotropic medium with $\varepsilon_x = \varepsilon_z > 0$; (b) an anisotropic crystal with $\varepsilon_x > 0$ and $\varepsilon_z > 0$; (c) a highly anisotropic material with $\varepsilon_x < 0$ and $\varepsilon_z > 0$. Reprinted with permission from [43]. Copyright (2006) OSA

the loss is the most painful obstacle for many practical applications. NIMs based on photonic crystals also avoid the requirement of a magnetic response, which is always a daunting task at optical frequencies.

Another nonmagnetic route to low-loss negative refraction is based on strongly anisotropic materials [41–43]. Instead of engineering subwavelength units with desired ε and μ values, the starting point for anisotropy-based negative refraction is the exploration of the possible relationships between the wavevector k and the Poynting vector S in nonmagnetic, homogenous media. In an ideal NIM, the two vectors k and S are antiparallel to each other, which implies an angle of 180° between them. In a common uniaxial crystal, generally there is a non-zero angle between k and S , determined by the birefringence of the crystal as well as the incidence direction. If we can substantially increase this angle, the projections of k and S along certain orientations will be directed opposite to each other, and a NIM-like behavior is expected.

This scenario can be better explained with the help of the isofrequency curves, as shown in Fig. 6.12. Assuming that the light propagates within the x – z plane, the isofrequency curve shows the dispersion relation, given as [43]:

$$\frac{k_x^2}{\varepsilon_z} + \frac{k_z^2}{\varepsilon_x} = \frac{\omega^2}{c^2}. \quad (6.5)$$

For a given point on the isofrequency curve, the wavevector k is represented by a vector from the origin to that point, and the angle of the Poynting vector S is normal to the tangent of the curve at the point. In the isotropic case with $\varepsilon_x = \varepsilon_z$, the wave vector surface is circular and the vectors k and S are collinear, as shown in Fig. 6.12a. An anisotropic crystal corresponds to the case in Fig. 6.12b, where the wave vector surface becomes ellipsoidal and, as a result, the angle between k and S is non-zero. Finally, for a material with negative transverse dielectric permittivity $\varepsilon_x < 0$ and positive in-plane permittivity $\varepsilon_z > 0$, the dispersion relation becomes hyperbolic. The curvature of the hyperbola is such that the signs of k_z and S_z are opposite, as shown in Fig. 6.12c. This opposite directionality between k_z and S_z leads to a negative effective index of refraction. In particular, an effective negative refractive index has been predicted in a waveguiding system when an anisotropic

material with $\varepsilon_x < 0$ and $\varepsilon_z > 0$ is used as a core of a planar (in the y - z plane) waveguide with metallic walls [42]. For the propagating modes in such a waveguide, the wave vector and the energy flux are antiparallel.

The strong anisotropy required in these scenarios can be achieved via different schemes. For example, as we discussed in Chap. 4, stratified metal-dielectric composites may exhibit highly anisotropic optical properties, with the two principal effective permittivities given by (4.4) and (4.7). Strong anisotropy is also possible in a two-dimensional rod system as depicted in Fig. 4.3a, where the effective permittivity is negative for light polarized along the metallic wires, and it is positive for the perpendicular polarization. An experimental demonstration of negative refraction based on strong anisotropy was shown at the mid-infrared wavelength of $\sim 10 \mu\text{m}$ [44]. In this experiment, alternating layers of highly doped InGaAs and intrinsic AlInAs were used to form the low-loss, three-dimensional, all-semiconductor metamaterial, and negative refraction for all angles of incidence has been observed [44]. A two-dimensional wire system has also been used to demonstrate anisotropy-based negative refraction. In Ref. [45] a Berkeley group created an alumina/silver system where silver wires are electrochemically deposited in a porous alumina template prepared by electrochemical anodization. In this wire system, a reversed Snell's law was observed at a red light wavelength of $\sim 700 \text{ nm}$.

Negative refraction in waveguides is possible not only for photons, but also for plasmon polaritons. It has been shown that metal-insulator-metal (MIM) waveguides can function as all-angle negative index media for surface plasmon modes in such structures [46, 47]. Many intriguing phenomena associated with NIMs, including a negative angle of refraction and subwavelength imaging, have been predicted in MIM systems. In experiments, MIM waveguides with negative-index behavior for plasmon polariton modes have been verified [48]. In that demonstration, a bimetal Au-Si₃N₄-Ag waveguide was used to support a dispersion curve with a negative slope at green light frequencies. Such abnormal dispersion implies antiparallel group and phase velocities for plasmons in the MIM waveguide. When connecting this bimetal waveguide to a conventional Ag-Si₃N₄-Ag slot waveguide, all-angle negative refraction at the interface between the two waveguides is observed within the visible spectrum of light. We note that although MIM structures may display negative-refraction properties, they should not be viewed as negative-index media for light waves, but instead as negative-index media only for surface plasmon polaritons. In addition, although such special waveguides are interesting structures, they are not considered to be metamaterials. A negative slope in the dispersion curve for plasmon polaritons or exciton-polaritons can also be realized in other systems, including organic crystals, gyrotropic materials, and metallic thin films [49].

A few other approaches for optical NIMs have been proposed, but as of yet they have not been confirmed through experiments. For example, nanoscale metallic and dielectric particles can serve as optical lumped elements such as nanoresistors, nanoinductors and nanocapacitors, analogous to circuit elements in electronics [50, 51]. When fused together, nanoparticles with different permittivities can form parallel and serial nanoelements that can be arranged into optical nanotransmission lines. Such nanotransmission lines at optical frequencies may exhibit negative-index

behavior, similar to the reported transmission-line NIMs at microwave frequencies [52, 53]. A negative index of refraction has also been proposed in frequency-selective surfaces [54] and three- or four-level atomic systems [55, 56].

Finally, there is a chiral route to negative refraction. As independently suggested by Pendry and Tretyakov [57, 58], the effective refractive index in chiral materials can be expressed as:

$$n_{L,R} = \sqrt{\varepsilon\mu} \pm \xi, \quad (6.6)$$

where ξ is a parameter characterizing the strength of the chirality, and the subscripts L and R denote the two circularly polarized eigenstates. Therefore, one of the two circularly polarized beams in a strongly chiral medium may exhibit a negative index of refraction, as long as the product $\varepsilon\mu$ is small enough so that the chirality parameter ξ dominates in the right-hand side of (6.6). Chirality-based NIMs have been experimentally demonstrated in both the microwave frequency range and the terahertz range [59, 60]. Given the fact that giant chiral responses in optical metamaterials have been reported by at least two groups [61, 62], it would not be surprising to see an optical NIM based on chiral responses in the near future.

References

1. Schuster A (1904) An introduction to the theory of optics. Arnold, London
2. Lamb H (1904) On group-velocity. Proc Lond Math Soc 1:473–479
3. Mandel'shtam LI (1945) Group velocity in a crystal lattice. Zh Eksp Teor Fiz 15:475–478
4. Sivukhin DV (1957) The energy of electromagnetic waves in dispersive media. Opt Spektrosk 3:308–312
5. Veselago VG (1968) Electrodynamics of substances with simultaneously negative values of sigma and mu. Sov Phys Usp 10:509–514
6. Pendry JB, Holden AJ, Stewart WJ, Youngs I (1996) Extremely low frequency plasmons in metallic mesostructures. Phys Rev Lett 76:4773–4776
7. Pendry JB, Holden AJ, Robbins DJ, Stewart WJ (1999) Magnetism from conductors and enhanced nonlinear phenomena. IEEE Trans Microw Theory Tech 47:2075–2084
8. Pendry JB (2000) Negative refraction makes a perfect lens. Phys Rev Lett 85:3966–3969
9. Pendry JB, Schurig D, Smith DR (2006) Controlling electromagnetic fields. Science 312:1780–1782
10. Berman PR (2002) Goos–Hanchen shift in negatively refractive media. Phys Rev E 66:067603
11. Fu CJ, Zhang ZMM, First PN (2005) Brewster angle with a negative-index material. Appl Opt 44:3716–3724
12. Thompson GHB (1955) Unusual waveguide characteristics associated with the apparent negative permeability obtainable in ferrites. Nature 175:1135–1136
13. Hartstei A, Burstein E, Maradudi AA, Brewer R, Wallis RF (1973) Surface polaritons on semi-infinite gyromagnetic media. J Phys C Solid State Phys 6:1266–1276
14. Depine RA, Lakhtakia A (2004) A new condition to identify isotropic dielectric-magnetic materials displaying negative phase velocity. Microw Opt Technol Lett 41:315–316
15. Camley RE, Mills DL (1982) Surface-polaritons on uniaxial antiferromagnets. Phys Rev B 26:1280–1287
16. Smith DR, Padilla WJ, Vier DC, Nemat-Nasser SC, Schultz S (2000) Composite medium with simultaneously negative permeability and permittivity. Phys Rev Lett 84:4184–4187
17. Shelby RA, Smith DR, Schultz S (2001) Experimental verification of a negative index of refraction. Science 292:77–79

18. Parazzoli CG, Greigor RB, Li K, Koltjenbah BEC, Tanielian M (2003) Experimental verification and simulation of negative index of refraction using Snell's law. *Phys Rev Lett* 90:107401
19. Shalaev VM, Cai WS, Chettiar UK, Yuan HK, Sarychev AK, Drachev VP, Kildishev AV (2005) Negative index of refraction in optical metamaterials. *Opt Lett* 30:3356–3358
20. Zhang S, Fan WJ, Panoiu NC, Malloy KJ, Osgood RM, Brueck SRJ (2005) Experimental demonstration of near-infrared negative-index metamaterials. *Phys Rev Lett* 95:137404
21. Zhang S, Fan WJ, Malloy KJ, Brueck SRJ, Panoiu NC, Osgood RO (2006) Demonstration of metal-dielectric negative-index metamaterials with improved performance at optical frequencies. *J Opt Soc Am B* 23:434–438
22. Dolling G, Enkrich C, Wegener M, Soukoulis CM, Linden S (2006) Low-loss negative-index metamaterial at telecommunication wavelengths. *Opt Lett* 31:1800–1802
23. Dolling G, Enkrich C, Wegener M, Soukoulis CM, Linden S (2006) Simultaneous negative phase and group velocity of light in a metamaterial. *Science* 312:892–894
24. Dolling G, Wegener M, Soukoulis CM, Linden S (2007) Negative-index metamaterial at 780 nm wavelength. *Opt Lett* 32:53–55
25. Chettiar UK, Kildishev AV, Yuan HK, Cai WS, Xiao SM, Drachev VP, Shalaev VM (2007) Dual-band negative index metamaterial: double negative at 813 nm and single negative at 772 nm. *Opt Lett* 32:1671–1673
26. Chen XL, He M, Du YX, Wang WY, Zhang DF (2005) Negative refraction: an intrinsic property of uniaxial crystals. *Phys Rev B* 72:113111
27. McCall MW, Lakhtakia A, Weiglhofer WS (2002) The negative index of refraction demystified. *Eur J Phys* 23:353–359
28. Lagarkov AN, Sarychev AK (1996) Electromagnetic properties of composites containing elongated conducting inclusions. *Phys Rev B* 53:6318–6336
29. Podolskiy VA, Sarychev AK, Shalaev VM (2002) Plasmon modes in metal nanowires and left-handed materials. *J Nonlinear Opt Phys Mater* 11:65–74
30. Chettiar UK, Kildishev AV, Klar TA, Shalaev VM (2006) Negative index metamaterial combining magnetic resonators with metal films. *Opt Express* 14:7872–7877
31. Zhou JF, Zhang L, Tuttle G, Koschny T, Soukoulis CM (2006) Negative index materials using simple short wire pairs. *Phys Rev B* 73:041101
32. Dolling G, Wegener M, Linden S (2007) Realization of a three-functional-layer negative-index photonic metamaterial. *Opt Lett* 32:551–553
33. Chettiar UK, Xiao S, Kildishev AV, Cai W, Yuan HK, Drachev VP, Shalaev VM (2008) Optical metamagnetism and negative-index metamaterials. *MRS Bull* 33:921–926
34. Kim E, Shen YR, Wu W, Ponziovskaya E, Yu Z, Bratkovsky AM, Wang SY, Williams RS (2007) Modulation of negative index metamaterials in the near-IR range. *Appl Phys Lett* 91:173105
35. Valentine J, Zhang S, Zentgraf T, Ulin-Avila E, Genov DA, Bartal G, Zhang X (2008) Three-dimensional optical metamaterial with a negative refractive index. *Nature* 455:376–379
36. Notomi M (2000) Theory of light propagation in strongly modulated photonic crystals: refractionlike behavior in the vicinity of the photonic band gap. *Phys Rev B* 62:10696–10705
37. Luo C, Johnson SG, Joannopoulos JD, Pendry JB (2002) All-angle negative refraction without negative effective index. *Phys Rev B* 65:201104
38. Foteinopoulou S, Soukoulis CM (2003) Negative refraction and left-handed behavior in two-dimensional photonic crystals. *Phys Rev B* 67:235107
39. Berrier A, Mulot M, Swillo M, Qiu M, Thylen L, Talneau A, Anand S (2004) Negative refraction at infrared wavelengths in a two-dimensional photonic crystal. *Phys Rev Lett* 93:073902
40. Schonbrun E, Tinker M, Park W, Lee JB (2005) Negative refraction in a Si-polymer photonic crystal membrane. *IEEE Photonics Technol Lett* 17:1196–1198
41. Belov PA (2003) Backward waves and negative refraction in uniaxial dielectrics with negative dielectric permittivity along the anisotropy axis. *Microw Opt Technol Lett* 37:259–263
42. Podolskiy VA, Narimanov EE (2005) Strongly anisotropic waveguide as a nonmagnetic left-handed system. *Phys Rev B* 71:201101

43. Alekseyev LV, Narimanov E (2006) Slow light and 3D imaging with non-magnetic negative index systems. *Opt Express* 14:11184–11193
44. Hoffman AJ, Alekseyev L, Howard SS, Franz KJ, Wasserman D, Podolskiy VA, Narimanov EE, Sivo DL, Gmachl C (2007) Negative refraction in semiconductor metamaterials. *Nat Mater* 6:946–950
45. Yao J, Liu ZW, Liu YM, Wang Y, Sun C, Bartal G, Stacy AM, Zhang X (2008) Optical negative refraction in bulk metamaterials of nanowires. *Science* 321:930
46. Alu A, Engheta N (2006) Optical nanotransmission lines: synthesis of planar left-handed metamaterials in the infrared and visible regimes. *J Opt Soc Am B* 23:571–583
47. Shin H, Fan SH (2006) All-angle negative refraction for surface plasmon waves using a metal-dielectric-metal structure. *Phys Rev Lett* 96:073907
48. Lezec HJ, Dionne JA, Atwater HA (2007) Negative refraction at visible frequencies. *Science* 316:430–432
49. Agranovich VM, Shen YR, Baughman RH, Zakhidov AA (2004) Optical bulk and surface waves with negative refraction. *J Lumin* 110:167–173
50. Engheta N, Salandrino A, Alu A (2005) Circuit elements at optical frequencies: nanoinductors, nanocapacitors, and nanoresistors. *Phys Rev Lett* 95:095504
51. Engheta N (2007) Circuits with light at nanoscales: optical nanocircuits inspired by metamaterials. *Science* 317:1698–1702
52. Grbic A, Eleftheriades GV (2003) Periodic analysis of a 2-D negative refractive index transmission line structure. *IEEE Trans Antennas Propag* 51:2604–2611
53. Grbic A, Eleftheriades GV (2004) Overcoming the diffraction limit with a planar left-handed transmission-line lens. *Phys Rev Lett* 92:117403
54. Khoo IC, Williams Y, Diaz A, Chen K, Bossard JA, Li L, Werner DH, Graugnard E, King JS, Jain S, Summers CJ (2006) Liquid-crystals for tunable photonic crystals, frequency selective surfaces and negative index material development. *Mol Cryst Liq Cryst* 453:309–319
55. Oktel MO, Mustecaplioglu OE (2004) Electromagnetically induced left-handedness in a dense gas of three-level atoms. *Phys Rev A* 70:053806
56. Thommen Q, Mandel P (2006) Electromagnetically induced left handedness in optically excited four-level atomic media. *Phys Rev Lett* 96:053601
57. Tretyakov S, Nefedov I, Sihvola A, Maslovski S, Simovski C (2003) Waves and energy in chiral nihility. *J Electromagn Waves Appl* 17:695–706
58. Pendry JB (2004) A chiral route to negative refraction. *Science* 306:1353–1355
59. Plum E, Zhou J, Dong J, Fedotov VA, Koschny T, Soukoulis CM, Zheludev NI (2009) Metamaterial with negative index due to chirality. *Phys Rev B* 79:035407
60. Zhang S, Park YS, Li JS, Lu XC, Zhang WL, Zhang X (2009) Negative refractive index in chiral metamaterials. *Phys Rev Lett* 102:023901
61. Plum E, Fedotov VA, Schwanecke AS, Zheludev NI, Chen Y (2007) Giant optical gyrotropy due to electromagnetic coupling. *Appl Phys Lett* 90:223113
62. Decker M, Klein MW, Wegener M, Linden S (2007) Circular dichroism of planar chiral magnetic metamaterials. *Opt Lett* 32:856–858

Chapter 7

Nonlinear Optics with Metamaterials

7.1 Recent Advances of Nonlinear Effects in Metamaterials

In all the preceding chapters, we studied the linear properties of optical metamaterials, assuming that the effective electric permittivity ε and magnetic permeability μ are independent of the incident light intensity. Indeed, an overwhelming portion of the experimental results on metamaterials reported thus far are exclusively focused on the linear response of metamaterials to external electromagnetic radiation. However, nonlinear effects in metamaterials have become an emerging field of study, particularly among theoretical physicists. A range of nonlinear phenomena in a variety of metamaterials, especially negative-index materials (NIMs), have been theoretically investigated to a considerable extent. The studied topics include general treatments for nonlinear wave propagation and nonlinear Schrödinger equations in NIMs [1, 2], as well as specific nonlinear processes such as second-harmonic generation (SHG) and parametric amplification [3–6].

The linear responses of metamaterials have substantially augmented the linear properties available from naturally-occurring materials. In the same way, the studies of nonlinear metamaterials may have a revolutionary impact on the entire field of nonlinear optics. Conventional studies of nonlinear optics are mainly focused on the exploration of various high-order processes in different crystals. The capability to design custom nonlinear materials, which is possible in metamaterials, is bound to open entirely new outlooks for nonlinear light-matter interactions. A good example of nonlinear phenomena in artificial media is the case of supercontinuum generation in photonic crystal fibers [7]. Although supercontinuum generation in glass and liquids has been known for several decades, the technique of using artificially structured holey fibers immediately became the standard method for supercontinuum generation soon after its invention at the beginning of this century, while supercontinuum generation from conventional materials has become sparsely mentioned since then.

The theoretical exploration of nonlinear processes in metamaterials began shortly after the very first demonstration of a NIM, which consisted of arrays of metallic wires and split-ring resonators (SRRs). The initial idea of the investigation is quite straightforward: If the metallic building-blocks of the NIM are embedded in a

nonlinear dielectric, an intensity-dependent response from the whole metamaterial should be reasonably expected [8]. As discussed in Sect. 4.3, the expression for the effective permittivity ϵ_{eff} for wire arrays given in 4.24 contains the dielectric constant of the surrounding medium. Therefore, a nonlinear electric response is produced in the metamaterial when, for example, an optical Kerr medium is used as the host matrix. More interestingly, the effective permeability μ_{eff} of this NIM would also exhibit a nonlinear response owing to a rather complicated chain of relationships. In Chap. 5 we have shown that the SRR structure can be viewed as a *LC* resonator, where the capacitance element in a single SRR primarily results from the gap. In the present case, that gap is filled with a nonlinear material, and the resonance behavior μ_{eff} will be sensitive to the magnitude of the electric field localized within the gap. This magnitude is in turn related to the current flow inside the ring generated by the external magnetic field [8].

Here we see one of the striking features of metamaterials used as nonlinear media. The nonlinear effects in all conventional crystals depend on a specific power of the electric field, while the magnitude of the magnetic field seems to play no role in the nonlinear processes. This claim is a natural extension of our discussion in Sect. 5.1 on the natural “inertness” of magnetic responses in the optical frequency range. In sharp contrast to this, however, the giant magnetic response in magnetic and negative-index metamaterials allows for the dependence of both ϵ and μ on the intensity of the electromagnetic field.

The optical properties of nonlinear metamaterials are sensitive to the strength of external fields. Such a feature has made it possible to design active metamaterial devices with various tunable functionalities such as switching and filtering. At microwave frequencies, such reconfigurable metamaterials can be achieved by introducing power-dependent lumped elements such as varactor diodes [9]. Several microwave metamaterials based on varactor devices have been experimentally reported, ranging from tunable SRRs as notch filters [10] to second-harmonic generation in transmission-line NIMs [11].

As for the optical frequencies, although novel nonlinear properties in optical metamaterials have been extensively studied, up to now the experimental demonstration of nonlinearity within the optical range is an extremely rare event. In addition, regrettably, most of the exotic nonlinear effects in photonic metamaterials predicted by theorists largely remain unverified in reality. Among the very few notable exceptions is harmonic generation from planar arrays of gold SRRs reported by a group at Karlsruhe University, Germany [12, 13]. In their experiment, the SHG efficiency from the magnetic dipole resonance in SRRs was shown to surpass that from the electric resonance by several orders. Such remarkable SHG and third-harmonic generation (THG) efficiencies are claimed to be attributed to the magnetic component of the Lorentz force acting upon the metal electrons [12]. Although the experimental data for harmonic generation in SRRs is undoubted, it remains open to debate whether the metamagnetic response explains the mechanism behind the observed phenomena. Indeed, enhanced frequency conversion efficiency is known to occur in plasmonic nanostructures without the involvement of any magnetic resonance [14–16]. Later studies by the same group have shown that similar SHG signals

can be produced in an array of complementary SRRs, which has an electric-dipole resonance instead of a magnetic one, according to Babinet's principle [17]. Further theoretical studies have shown that the dominant reason for the strong SHG in SRRs stems from the convective derivative of the continuous electron current, which can be fully analyzed using the tools of cold plasma electrodynamics theory [17, 18].

Another important experiment on the nonlinear response of optical metamaterials was carried out by a Berkeley group using a fishnet NIM [19]. In this work, a spectroscopic study covering several nonlinear processes including SHG, THG and four-wave mixing from a sandwich fishnet structure was conducted with varying wavelengths for the fundamental signal. In the spectral domain, the observed nonlinear resonances are much narrower than the linear absorption, and the spectral widths are further reduced for processes of higher orders. This investigation indicates that the major reason for the enhanced nonlinearity in fishnet NIMs is the plasmonic nature of the light-NIM interaction and the associated local field enhancement from the plasmon resonances.

Interesting nonlinear phenomena occur not only within metamaterials, but also at the interfaces between metamaterials and conventional media. It has been pointed out that stable nonlinear surface waves can be supported at the boundary between a NIM and a conventional, positive-index material (PIM) [20]. Under certain conditions, such surface waves possess the property of bulk NIM waves, where the energy flow is directed opposite to that of the phase propagation [21]. Things get even more intriguing when we stack nonlinear interfaces together. In the linear region, it has been known for some time that a photonic band gap corresponding to a zero averaged index of refraction can be created in a layered heterostructure consisting of interlaced ordinary PIMs and NIMs [22]. When the positive-index layers exhibit a Kerr nonlinearity, a hysteresis behavior occurs in the transmittance of the stratified system as a function of the incident intensity, which may lead to bistability and the creation of zero-index gap solitons [23]. Later it was revealed that such bistability behavior is possible in a bilayer with just one NIM layer and one Kerr optical slab [24]. The bistability and gap solitons can also be formed in other NIM-PIM structures, such as a nonlinear coupler where one channel is filled with a NIM and the other channel has a positive index of refraction [25, 26]. The hysteresis and solitons in the nonlinear coupler result from an effective feedback mechanism due to the opposite directionality of the phase velocity and the Poynting vector in the NIM arm. Similar solitons can be generated even without using NIMs. For example, it has been suggested that subwavelength discrete solitons can be supported in layered electric metamaterials consisting of metallic and nonlinear dielectric slabs [27]. The formation of such discrete solitons arises from the threefold interplay between diffraction, nonlinear focusing and surface plasmon tunneling.

In Ref. [28], a family of solitary wave solutions is found, which is similar to pulses associated with self-induced transparency in the framework of the Maxwell-Bloch model. The evolution of incident optical pulses is studied, as are the collision dynamics of the solitary waves. These simulations reveal that the collision dynamics vary from near perfectly elastic to highly radiative, depending on the relative phase of the initial pulses [28].

Nonlinear phenomena in metamaterials also offer promise in various real-world applications. For example, the bistability mentioned above and discussed in Refs. [23, 24] can easily switch from low transmission to a perfectly transmitting state, which may be used for optical switching, optical limiting and memory devices. Nonlinear effects also provide hope for better, low-loss optical metamaterials. It has been suggested that the power absorption in NIMs can be efficiently compensated via different schemes, including optical parametric amplification [6] and resonant four-wave mixing [29]. In addition, nonlinear metamaterials may help in the development of a superlens that is more robust against material imperfections such as chromatic dispersion and power dissipation. With an appropriate quadratic nonlinear response, an image of the second-harmonic field with subwavelength resolution can be achieved even for a slab lens that is opaque at the fundamental frequency [30]. The wave-mixing in second-order nonlinear NIMs can also be used for terahertz wave generation from optical signals [31].

The efficiency of most nonlinear wave-mixing processes critically depends on the phase-matching of the participating waves. In NIMs, the anti-parallel relationship between the phase velocity and energy velocity in combination with the strong frequency dispersion of the material parameters play a pivotal role in most nonlinear optical phenomena. In particular, they facilitate a fundamentally new regime of phase matching – backward phase matching. In the following sections, we analyze in detail a number of second-order nonlinear processes in NIMs, with emphasis given to the salient features of these phenomena in NIMs as compared to their counterparts in conventional PIMs. Specially, in Sect. 7.2 we analyze the general wave equations for second-order nonlinear optics and apply them to the SHG process. The modified Manley–Rowe relations in NIMs are also presented. In Sect. 7.3 we discuss optical parametric amplification in NIMs and its application to loss compensation in metamaterials. Unlike all of the other parts of this book, where SI units are assumed, in this chapter we use the Gaussian system of units because it is a convention in most of the literature on nonlinear optics.

7.2 Second-Harmonic Generation and the Manley–Rowe Relations in Negative-Index Materials

Since its discovery in the early 1960s, second harmonic generation, also referred to as frequency doubling, is by far the most fundamental and best understood optical nonlinear interaction. Naturally, then, SHG was one of the first nonlinear processes examined in the context of NIMs. In this section we focus on the unique properties of the SHG process occurring in a dispersive negative-index material. First we begin with a general treatment of second-order nonlinear optics using a set of wave equations. When two electromagnetic waves with frequencies ω_1 and ω_2 propagate in a quadratic nonlinear medium characterized by a nonlinear electric susceptibility $\chi_P^{(2)}$, a number of new frequencies can be generated including $\omega_1 \pm \omega_2$ (sum- and difference-frequency generation), $2\omega_1$ and $2\omega_2$ (SHG of each fundamental

frequency). Strictly speaking, all nonlinear media are dispersive and the conversion efficiency of these nonlinear processes is critically dependent on the relationship among the wave vectors involved. Such a relationship, usually called the phase-matching condition, results from the photon momentum conservation and it is a matter of foremost consideration for frequency mixing in bulk nonlinear media.

The general equations describing three-wave interactions in a $\chi^{(2)}$ medium, using the slowly varying envelope and phase approximations, can be written in the following form [32, 33]:

$$\left(\hat{k}_1 \frac{\partial}{\partial z} + \frac{1}{v_1} \frac{\partial}{\partial t} \right) A_1 = i \frac{2\pi\omega_1^2 \mu(\omega_1)}{c^2 k_1} P^{NL}(\omega_1) \exp(-ik_1 z), \quad (7.1a)$$

$$\left(\hat{k}_2 \frac{\partial}{\partial z} + \frac{1}{v_2} \frac{\partial}{\partial t} \right) A_2 = i \frac{2\pi\omega_2^2 \mu(\omega_2)}{c^2 k_2} P^{NL}(\omega_2) \exp(-ik_2 z), \quad (7.1b)$$

$$\left(\hat{k}_3 \frac{\partial}{\partial z} + \frac{1}{v_3} \frac{\partial}{\partial t} \right) A_3 = i \frac{2\pi\omega_3^2 \mu(\omega_3)}{c^2 k_3} P^{NL}(\omega_3) \exp(-ik_3 z), \quad (7.1c)$$

where $k_j^2 = (\omega_j/c)^2 \varepsilon(\omega_j) \mu(\omega_j)$, c represents the vacuum light speed, and \hat{k}_j is the sign of the refractive index n_j . Note that (7.1) is quite general, with all possible combinations of ε_j and μ_j considered. The nonlinear polarization terms are:

$$P^{NL}(\omega_1) = \chi^{(2)}(\omega_1; \omega_3, -\omega_2) A_3 A_2^* \exp[iz(k_3 - k_2)], \quad (7.2a)$$

$$P^{NL}(\omega_2) = \chi^{(2)}(\omega_2; \omega_3, -\omega_1) A_3 A_1^* \exp[iz(k_3 - k_1)], \quad (7.2b)$$

$$P^{NL}(\omega_3) = \chi^{(2)}(\omega_3; \omega_1, \omega_2) A_1 A_2 \exp[iz(k_1 + k_2)], \quad (7.2c)$$

where A_j denotes the amplitude of wave ω_j .

The above equations describe the process of the SHG if $\omega_1 = \omega_2 \equiv \omega$ and $A_1 = A_2 \equiv A_\omega$ are the frequency and the complex amplitude of the fundamental wave, and $\omega_3 = 2\omega_1 \equiv 2\omega$ and $A_3 = A_{2\omega}$ are those of the second-harmonic signal. Another important second-order nonlinear phenomenon is the optical parametric amplification, where a signal beam at ω_s passes through a nonlinear medium together with a pump beam of a higher frequency ω_p , and photons of the pump light are converted into signal photons as well as idler photons at the frequency of $\omega_i = \omega_p - \omega_s$. This process can also be described by (7.2). If $\omega_1 = \omega_s$ and $A_1 \equiv A_s$ correspond to the frequency and the complex amplitude of the signal wave, $\omega_2 = \omega_i$ and $A_2 \equiv A_i$ are those of the idler wave, and $\omega_3 = \omega_p$ and $A_3 \equiv A_p$ correspond to the pump wave. Also, it is convenient to simplify the notations as $\varepsilon(\omega_j) \equiv \varepsilon_j$ and $\mu(\omega_j) \equiv \mu_j$.

Second-harmonic generation behavior in NIMs is drastically different from that in usual, positive-index nonlinear media, mostly owing to the inherent dispersion and the antiparallel phase and energy velocity directions in NIMs. Since in NIMs a negative index can occur only within a rather limited frequency range, the fundamental wave at ω and the frequency-doubled wave at 2ω cannot simultaneously fall within the negative-index band of a nonlinear metamaterial. Consequently, most of

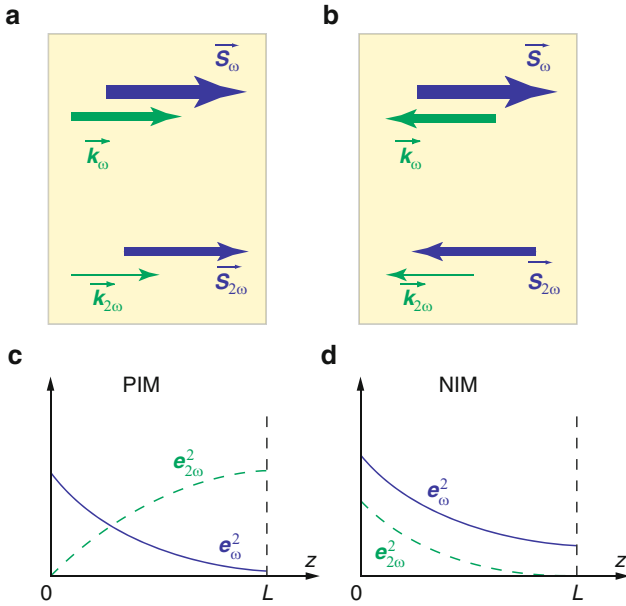


Fig. 7.1 The schematics of the SHG processes in (a) a PIM and (b) a NIM, and the distribution of fundamental and frequency-doubled waves across the slab in (c) a PIM and (d) a NIM

the characteristic relationships in SHG, including the phase-matching condition, the dependence of conversion efficiency on interaction length, and the Manley–Rowe relation have to be fundamentally modified for nonlinear metamaterials [3, 4, 34].

Here we consider the SHG process arising from the nonlinear electric polarization instead of the nonlinear magnetization. This assumption allows us to conveniently compare the SHG process in NIMs to the conventional SHG process in PIMs, where only the electric response is actively involved in the nonlinear phenomenon. Schematics of the SHG processes in PIM and NIM slabs are shown in Fig. 7.1. It is assumed that the nonlinear material is a NIM at the fundamental frequency ω and has a positive refractive index at the second-harmonic frequency 2ω . The fundamental wave is incident upon both nonlinear slabs from the left interface; therefore, the energy flow of the fundamental frequency always travels from left to right, regardless the type of the nonlinear material. The scenario of SHG process in a conventional PIM is shown in Fig. 7.1a, where the energy and phase of both the fundamental wave and the frequency-doubled beam flow to the right, in good agreement with our intuition for nonlinear phenomena. In sharp contrast, the directions of the Poynting vector and the phase velocity are opposite in NIMs, so in that material slab the phase of the wave at the fundamental frequency ω propagates from right to left while the energy flows from left to right. In order to satisfy the phase-matching requirement of $k_{2\omega} = 2k_\omega$, the k -vector of the generated second-harmonic wave has to be directed to the left, as illustrated in Fig. 7.1b. Finally, since the second harmonic experiences a positive index at the frequency 2ω , its energy flow is

co-directed with the phase velocity and, therefore, the energy propagates from right to left as well. This new type of phase-matching condition, known as “backward phase-matching,” provides a fundamentally new regime for the SHG process [3, 4, 34].

With the above picture of the novel SHG interaction in mind, we shall go through the wave equations from (7.1) and (7.2) to treat the SHG process in NIMs analytically. Equation (7.1) is immediately adaptable to the SHG in NIMs, with \hat{k}_1 in (7.1a) taking a negative sign. Assuming the continuous wave case and using the symmetry properties of the tensor $\chi^{(2)}$ [32, 33] (7.1) can be written in the form:

$$\frac{\partial A_\omega}{\partial z} = -i \frac{2K\omega^2 \mu_\omega}{c^2 k_\omega} A_{2\omega} A_\omega^* \exp[-i \Delta k z], \quad (7.3a)$$

$$\frac{\partial A_{2\omega}}{\partial z} = i \frac{4K\omega^2 \mu_{2\omega}}{c^2 k_{2\omega}} A_\omega^2 \exp[i \Delta k z], \quad (7.3b)$$

where $\Delta k = 2k_\omega - k_{2\omega}$ represents the phase mismatch, and $K = \frac{\pi}{c^2} \chi^{(2)}(\omega)$ is a constant for the specific SHG process.

From the wave equations in (7.3), we can derive the Manley–Rowe relation, which describes the balance in the photon fluxes of waves participating in a nonlinear optical process. Combining the two equations above, we have:

$$\frac{k_\omega}{\mu_\omega} \frac{d|A_\omega|^2}{dz} - \frac{k_{2\omega}}{2\mu_{2\omega}} \frac{d|A_{2\omega}|^2}{dz} = 0, \quad (7.4)$$

or, for the energy flow:

$$\frac{d|S_\omega|}{dz} - \frac{d|S_{2\omega}|}{dz} = 0. \quad (7.5)$$

If we assume that the nonlinear slab is lossless and that the phase-matching condition $k_{2\omega} = 2k_\omega$ is satisfied (implying that $\varepsilon_{2\omega} = -\varepsilon_\omega$ and $\mu_{2\omega} = -\mu_\omega$), the spatially invariant Manley–Rowe relation takes the form:

$$|A_\omega|^2 - |A_{2\omega}|^2 = C^2 = \text{const}. \quad (7.6)$$

In a conventional SHG process in PIMs, the Manley–Rowe relation requires that the sum of the squared amplitudes is constant. This is fairly intuitive – since both the fundamental wave and the harmonic wave propagate along the same direction, it is reasonably expected that the generated wave at 2ω grows as the fundamental photons are annihilated. However, when the nonlinear medium behaves as a NIM for the fundamental wave, the input interface of the fundamental beam becomes the output interface for the generated SHG beam, as shown in Fig. 7.1b. Consequently, it is the difference instead of the sum of the squared amplitudes that remains invariant along the propagation direction. The unusual form of Manley–Rowe relation in NIMs stems from the fact that the Poynting vectors for the fundamental and the second harmonic beams are antiparallel, while their wave vectors are parallel to each other.

If we decompose the complex amplitudes into real amplitudes and phases as $A_{\omega,2\omega} = e_{\omega,2\omega} \exp(i\varphi_{\omega,2\omega})$, the wave equations in (7.3) can be rewritten as:

$$\frac{de_{\omega}}{dz} = \kappa e_{\omega} e_{2\omega} \sin(\varphi_{2\omega} - 2\varphi_{\omega}), \quad \frac{de_{2\omega}}{dz} = \kappa e_{\omega}^2 \sin(\varphi_{2\omega} - 2\varphi_{\omega}), \quad (7.7a)$$

$$\frac{d\varphi_{\omega}}{dz} = -\kappa e_{2\omega} \cos(\varphi_{2\omega} - 2\varphi_{\omega}), \quad \frac{d\varphi_{2\omega}}{dz} = \kappa \frac{e_{\omega}^2}{e_{2\omega}} \cos(\varphi_{2\omega} - 2\varphi_{\omega}), \quad (7.7b)$$

where $\kappa = \frac{4K\omega^2\mu_{2\omega}}{c^2k_{2\omega}}$. Taking into account the equations for φ_{ω} and $\varphi_{2\omega}$, it is found that $\varphi_{2\omega} - 2\varphi_{\omega} = 3\pi/2$. Then we obtain:

$$\frac{de_{2\omega}}{dz} = -\kappa e_{\omega}^2 = -\kappa [C^2 + e_{2\omega}(z)^2]. \quad (7.8)$$

For the SHG process in a NIM slab with a finite length L , the boundary conditions are given by $e_{\omega}(0) = e_{10}$ and $e_{2\omega}(L) = 0$. Therefore, we obtain the solutions for the wave magnitudes e_{ω} and $e_{2\omega}$ as functions of the propagating length z :

$$e_{\omega}(z) = \frac{C}{\cos[C\kappa(L-z)]}, \quad (7.9a)$$

$$e_{2\omega}(z) = C \tan[C\kappa(L-z)], \quad (7.9b)$$

where $C\kappa L = \cos^{-1}(C/e_{10})$.

We see that the spatially invariant intensity difference in the modified Manley–Rowe relation given by (7.6) depends on the slab thickness. Owing to the boundary conditions for the second harmonic wave at the rear interface of the slab, the conversion at any point within the NIM slab depends on the total thickness of the slab. The development of the fundamental and SHG wave amplitudes along the propagation direction in a nonlinear NIM is shown in Fig. 7.1d. This behavior is radically different from the PIM case, where the right-hand side of (7.7a) would have opposite signs, and the boundary conditions are simply $e_{\omega}(0) = e_{10}$ and $e_{2\omega}(0) = 0$. As a result, the wave solutions for SHG in PIMs are:

$$e_{\omega}(z) = \frac{C}{\cosh(\kappa Cz)}, \quad (7.10a)$$

$$e_{2\omega}(z) = C \tanh(\kappa Cz), \quad (7.10b)$$

where the constant C is the same as e_{10} . Therefore, under the conditions of phase-matching, the fundamental wave decays as it goes through the nonlinear medium, while the SHG wave accumulates an increasing magnitude, as shown in Fig. 7.1c.

The above analysis for SHG in a NIM slab with thickness L can be easily extended to the case of a semi-infinite lossless NIM at $z > 0$. Since both waves should disappear as $z \rightarrow \infty$, the constant C is equal to zero. Consequently, $e_{\omega}(z) = e_{2\omega}(z)$ throughout the semi-infinite NIM, as implied by the Manley–Rowe relation in (7.6).

So the incoming radiation at the fundamental frequency can be converted to the second-harmonic signal in the opposite direction with an efficiency approaching 100% in a semi-infinite, lossless NIM slab, provided that the phase matching condition $\Delta k = 0$ is satisfied. In this sense, the NIM acts as a nonlinear perfect mirror. By applying the boundary condition $e_\omega(0) = e_{10}$, we obtain the expression for the wave amplitudes:

$$e_\omega(z) = e_{2\omega}(z) = \frac{e_{10}}{\kappa e_{10}z + 1}, \quad (7.11)$$

which implies a concurrent decrease of both waves of equal amplitudes along the z -axis.

7.3 Optical Parametric Amplifications in Negative-index Materials

The significance of the backward phase-matching condition in nonlinear NIMs is not limited only to the SHG process. Instead, it has a profound effect on all kinds of wave mixing phenomena. In this section, we discuss the unique properties of second-order optical parametric amplification (OPAs) in NIMs. Similar to the assumption we used in the previous section, we take the left-handed behavior to be present only within a certain frequency range, and hence we assume that the signal wave at frequency ω_1 experiences a negative index of refraction while both the idler wave at ω_2 and the pump at ω_3 fall into the positive-index range. The schematics of OPA processes in PIMs and NIMs are shown in Fig. 7.2a and b, respectively. In the NIM case, all wave vectors are directed from left to right, while the energy of the signal wave flows against the traffic due to the nature of the nonlinear medium as a NIM at frequency ω_1 .

In the parametric amplification process, high-energy photons at the pump frequency ω_3 are down-converted into signal (ω_1) and idler (ω_2) photons with the frequency relationship $\omega_3 = \omega_1 + \omega_2$. With the undepleted pump approximation given as $A_3 = A_p = \text{constant}$, the wave equations in (7.1) can be applied to the OPA process in a NIM in the following form:

$$\frac{dA_1}{dz} = -i \frac{4\pi\omega_1^2 \chi^{(2)} \mu_1}{c^2 k_1} A_3 A_2^* \exp(i \Delta k z), \quad (7.12a)$$

$$\frac{dA_2}{dz} = i \frac{4\pi\omega_2^2 \chi^{(2)} \mu_2}{c^2 k_2} A_3 A_1^* \exp(i \Delta k z), \quad (7.12b)$$

where $\Delta k = k_3 - k_1 - k_2$ represents the phase mismatch in the nonlinear interaction. In contrast to the previous section on SHG, where a lossless nonlinear material is assumed, in the following treatment of OPA we include the loss factors α_1 and α_2 for the signal and idler waves, respectively. Since loss is one of the major problems in existing NIMs and especially in those operating at optical frequencies, the OPA

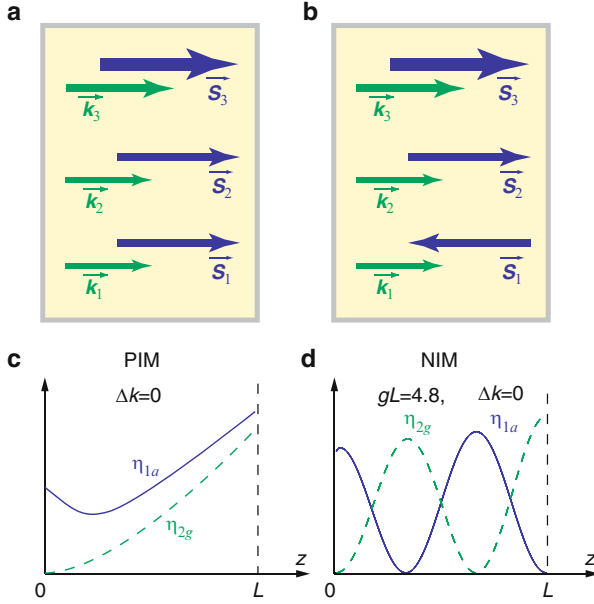


Fig. 7.2 The schematics of OPA processes in (a) a PIM and (b) a NIM, and the phase-matched amplification factor η_{1a} for the signal wave and the conversion factor η_{2g} for the idler wave in (c) a PIM and (d) a NIM. The absorption is set at $\alpha_1 L = 1$ and $\alpha_2 L = 1/2$

process may serve as a gain source that can help to compensate the dissipative loss in NIMs [6]. To incorporate the loss effect into the wave equations, we rewrite (7.12) as:

$$\frac{da_1}{dz} = -iga_2^* \exp(i \Delta kz) + \frac{\alpha_1}{2} a_1, \quad (7.13a)$$

$$\frac{da_2}{dz} = iga_1^* \exp(i \Delta kz) - \frac{\alpha_2}{2} a_2, \quad (7.13b)$$

where $a_j^2 = \sqrt{\frac{\epsilon_j}{\mu_j}} \frac{A_j^2}{\omega_j}$ and $g = \frac{4\pi}{c} \chi^{(2)} A_3 \frac{\sqrt{\omega_1 \omega_2}}{\sqrt{\epsilon_1 \epsilon_2 / \mu_1 \mu_2}}$.

To solve the differential equations in (7.13), a set of boundary conditions should be appropriately imposed. Due to the negative index experienced by the signal wave at ω_1 , the boundary conditions for a_1 are defined at the opposite side of the slab ($z = L$), as opposed to the boundary conditions for the idler a_2 (with a positive index), which are defined at the front slab interface. With the boundary conditions $a_1(L) = a_{1L}$ and $a_2(0) = a_{20}$, the solutions to (7.13) are [3, 6]:

$$a_1(z) = C_1 \exp\left[\left(\beta_1 + i \frac{\Delta k}{2}\right) z\right] + C_2 \exp\left[\left(\beta_2 + i \frac{\Delta k}{2}\right) z\right], \quad (7.14a)$$

$$a_2^*(z) = \kappa_1 C_1 \exp\left[\left(\beta_1 - i \frac{\Delta k}{2}\right) z\right] + \kappa_2 C_2 \exp\left[\left(\beta_2 - i \frac{\Delta k}{2}\right) z\right], \quad (7.14b)$$

where

$$\beta_{1,2} = \frac{\alpha_1 - \alpha_2}{4} \pm iR, \quad \kappa_{1,2} = \frac{\pm R + is}{g}, \quad R = \sqrt{g^2 - s^2}, \quad s = \frac{\alpha_1 + \alpha_2}{4} - \frac{i\Delta k}{2},$$

$$C_{1,2} = \pm \frac{a_{1L}\kappa_{2,1} - a_{20}^* \exp\left[\left(\beta_{2,1} + i\frac{\Delta k}{2}\right)L\right]}{D},$$

$$D = \kappa_2 \exp\left[\left(\beta_1 + i\frac{\Delta k}{2}\right)L\right] - \kappa_1 \exp\left[\left(\beta_2 + i\frac{\Delta k}{2}\right)L\right].$$

When the input interface has a zero idler magnitude $a_2(0) = a_{20} = 0$, the amplification factor for the left-handed signal wave at ω_1 is given by $\eta_{1a} = |a_{10}/a_{1L}|^2$, where:

$$\frac{a_{10}}{a_{1L}} = \frac{\exp\left[-\left(\frac{\alpha_1 - \alpha_2}{4} + i\frac{\Delta k}{2}\right)L\right]}{\cos RL + \left[\frac{\alpha_1 + \alpha_2}{4R} - i\frac{\Delta k}{2R}\right] \sin RL}. \quad (7.15)$$

The solutions in (7.14) and (7.15) reveal several unusual properties of parametric amplification in NIMs. In particular, the amplification factor for the signal wave and the conversion efficiency for the idler wave exhibit oscillating behavior even with perfect phase matching $\Delta k = 0$, which is in sharp contrast to the case in PIMs. This difference is illustrated in Fig. 7.2c, d. Importantly, the amplification in NIMs depends on the product gL rather than simply on g as in PIMs, where g is the factor proportional to the product of the quadratic nonlinear susceptibility and the intensity of the pump field. The reason for this behavior is that the signal and the idler are determined by the boundary conditions on the opposite sides of the slab, and they increase in opposite directions. The important advantage of backward OPA in NIMs is the effective distributed feedback, which enables oscillations without a cavity. In the NIM case, each spatial point serves as a source for the generated wave in the reflected direction, whereas the phase velocities of all interacting waves are co-directed. We also note that the OPA process in NIMs enables the generation of entangled, counter-propagating photons in the signal and idler beams. Photons from these two beams also have different handedness: vectors \mathbf{E} , \mathbf{H} , and \mathbf{k} form a left-handed system in the signal and a right-handed triad in the idler [6].

The OPA process described above can serve as an efficient loss-compensation mechanism in NIMs. Losses are known to be the major obstacle that may prohibit many practical applications of optical NIMs. As we have discussed in Chap. 6, due to causality requirements, lossless resonant NIMs cannot be realized without the incorporation of some active components. It has also been argued that the Kramers–Kronig relation imposes certain limitations on achieving negative refraction without losses [35] (which is still possible, at least for a narrow spectral range [36]). However, the latter statement relies on a linear Kramers–Kronig relation in a purely linear system, while in the general nonlinear case such a relation is either not applicable

or should be modified [33]. Therefore, nonlinear optical effects such as the OPA process have a strong potential for loss compensation in NIMs. The OPA system we have shown in this section indicates the possibility of using electromagnetic waves with frequencies outside the negative index range to provide loss-balancing signal amplification at a frequency within the negative-index band. Indeed, parametric amplification has been demonstrated experimentally, although it was in a negative-index nonlinear transmission line medium rather than in an optical system [37]. A detailed analysis of the feasibility of compensating losses in NIMs by OPA is presented in Ref. [6].

In addition to second-order nonlinear interactions, the cubic OPA process has also been theoretically investigated [38, 39]. The third-order OPA system may employ embedded four-level centers that can be tuned, resulting in the possible realization of tunable transparency windows in NIMs. This technique relies on a four-wave interaction process in a medium with a cubic nonlinearity. In this case, two control (pump) fields at frequencies ω_1 and ω_2 combine to create two fields – the signal and the idler fields – at frequencies ω_3 and ω_4 . Similar to the quadratic OPA case, the cubic parametric amplification process also strongly relies on backward phase-matching between the interacting waves. Laser-induced transparency, quantum switching, frequency tunable, narrow-band filtering, amplification, and a miniature mirrorless optical parametric generator of the entangled backward and ordinary waves are among the possible applications of the OPA process in NIMs [39, 40].

References

1. Agranovich VM, Shen YR, Baughman RH, Zakhidov AA (2004) Linear and nonlinear wave propagation in negative refraction metamaterials. *Phys Rev B* 69:165112
2. Scalora M, Syrchin MS, Akozbek N, Poliakov EY, D'Aguanno G, Mattiucci N, Bloemer MJ, Zheltikov AM (2005) Generalized nonlinear Schrödinger equation for dispersive susceptibility and permeability: application to negative index materials. *Phys Rev Lett* 95:013902
3. Popov AK, Shalaev VM (2006) Negative-index metamaterials: second-harmonic generation, Manley–Rowe relations and parametric amplification. *Appl Phys B* 84:131–137
4. Shadrivov IV, Zharov AA, Kivshar YS (2006) Second-harmonic generation in nonlinear left-handed metamaterials. *J Opt Soc Am B* 23:529–534
5. Scalora M, D'Aguanno G, Bloemer M, Centini M, de Ceglia D, Mattiucci N, Kivshar YS (2006) Dynamics of short pulses and phase matched second harmonic generation in negative index materials. *Opt Express* 14:4746–4756
6. Popov AK, Shalaev VM (2006) Compensating losses in negative-index metamaterials by optical parametric amplification. *Opt Lett* 31:2169–2171
7. Ranka JK, Windeler RS, Stentz AJ (2000) Visible continuum generation in air-silica microstructure optical fibers with anomalous dispersion at 800 nm. *Opt Lett* 25:25–27
8. Zharov AA, Shadrivov IV, Kivshar YS (2003) Nonlinear properties of left-handed metamaterials. *Phys Rev Lett* 91:037401
9. Lapine M, Gorkunov M, Ringhofer KH (2003) Nonlinearity of a metamaterial arising from diode insertions into resonant conductive elements. *Phys Rev E* 67:065601
10. Gil I, Garcia-Garcia J, Bonache J, Martin F, Sorolla M, Marques R (2004) Varactor-loaded split ring resonators for tunable notch filters at microwave frequencies. *Electron Lett* 40:1347–1348

11. Kozyrev AB, Kim H, Karbassi A, van der Weide DW (2005) Wave propagation in nonlinear left-handed transmission line media. *Appl Phys Lett* 87:121109
12. Klein MW, Enkrich C, Wegener M, Linden S (2006) Second-harmonic generation from magnetic metamaterials. *Science* 313:502–504
13. Klein MW, Wegener M, Feth N, Linden S (2007) Experiments on second- and third-harmonic generation from magnetic metamaterials. *Opt Express* 15:5238–5247
14. Simon HJ, Mitchell DE, Watson JG (1974) Optical second-harmonic generation with surface plasmons in silver films. *Phys Rev Lett* 33:1531–1534
15. Lesuffleur A, Kumar L, Gordon R (2006) Enhanced second harmonic generation from nanoscale double-hole arrays in a gold film. *Appl Phys Lett* 88:261104
16. van Nieuwstadt JAH, Sandtke M, Harmsen RH, Segerink FB, Prangsma JC, Enoch S, Kuipers L (2006) Strong modification of the nonlinear optical response of metallic subwavelength hole arrays. *Phys Rev Lett* 97:146102
17. Feth N, Linden S, Klein MW, Decker M, Niesler FBP, Zeng Y, Hoyer W, Liu J, Koch SW, Moloney JV, Wegener M (2008) Second-harmonic generation from complementary split-ring resonators. *Opt Lett* 33:1975–1977
18. Zeng Y, Hoyer W, Liu J, Koch SW, Moloney JV (2009) Classical theory for second-harmonic generation from metallic nanoparticles. *Phys Rev B* 79:235109
19. Kim E, Wang F, Wu W, Yu ZN, Shen YR (2008) Nonlinear optical spectroscopy of photonic metamaterials. *Phys Rev B* 78:113102
20. Shadrivov IV, Sukhorukov AA, Kivshar YS, Zharov AA, Boardman AD, Egan P (2004) Nonlinear surface waves in left-handed materials. *Phys Rev E* 69:016617
21. Darmanyan SA, Neviere M, Zakhidov AA (2005) Nonlinear surface waves at the interfaces of left-handed electromagnetic media. *Phys Rev E* 72:036612
22. Li J, Zhou L, Chan CT, Sheng P (2003) Photonic band gap from a stack of positive and negative index materials. *Phys Rev Lett* 90:083901
23. Hegde RS, Winful HG (2005) Zero-n gap soliton. *Opt Lett* 30:1852–1854
24. Litchinitser NM, Gabitov IR, Maimistov AI, Shalaev VM (2007) Effect of an optical negative index thin film on optical bistability. *Opt Lett* 32:151–153
25. Litchinitser NM, Gabitov IR, Maimistov AI (2007) Optical bistability in a nonlinear optical coupler with a negative index channel. *Phys Rev Lett* 99:113902
26. Maimistov AI, Gabitov IR, Litchinitser NM (2008) Solitary waves in a nonlinear oppositely directed coupler. *Opt Spectrosc* 104:253–257
27. Liu YM, Bartal G, Genov DA, Zhang X (2007) Subwavelength discrete solitons in nonlinear metamaterials. *Phys Rev Lett* 99:153901
28. Gabitov IR, Indik RA, Litchinitser NM, Maimistov AI, Shalaev VM, Soneson JE (2006) Double-resonant optical materials with embedded metal nanostructures. *J Opt Soc Am B* 23:535–542
29. Popov AK, Myslivets SA, George TF, Shalaev VM (2007) Four-wave mixing, quantum control, and compensating losses in doped negative-index photonic metamaterials. *Opt Lett* 32:3044–3046
30. Zharov AA, Zharova NA, Shadrivov IV, Kivshar YS (2005) Subwavelength imaging with opaque nonlinear left-handed lenses. *Appl Phys Lett* 87:091104
31. Chowdhury A, Tataronis JA (2008) Long wave-short wave resonance in nonlinear negative refractive index media. *Phys Rev Lett* 100:153905
32. Shen YR (1984) *The principles of non-linear optics*. Wiley, New York
33. Boyd RW (2002) *Nonlinear optics*, 2nd ed. Academic, San Diego
34. Popov AK, Slabko VV, Shalaev VM (2006) Second harmonic generation in left-handed metamaterials. *Laser Phys Lett* 3:293–297
35. Stockman MI (2007) Criterion for negative refraction with low optical losses from a fundamental principle of causality. *Phys Rev Lett* 98:177404
36. Kinsler P, McCall MW (2008) Causality-based criteria for a negative refractive index must be used with care. *Phys Rev Lett* 101:167401
37. Kozyrev AB, Kim H, van der Weide DW (2006) Parametric amplification in left-handed transmission line media. *Appl Phys Lett* 88:264101

38. Popov AK, Shalaev VM (2007) Nonlinear optical switching from lossy to amplifying negative-index metamaterials. Proceedings of OSA topical meeting “Photonic metamaterials: from random to periodic”, Jackson Hole, WY
39. Popov AK, Myslivets SA, Shalaev VM (2009) Resonant nonlinear optics of backward waves in negative-index metamaterials. *Appl Phys B* 96:315–323
40. Popov AK, Myslivets SA, Shalaev VM (2009) Microscopic mirrorless negative-index optical parametric oscillator. *Opt Lett* 34:1165–1167

Chapter 8

Super Resolution with Meta-Lenses

8.1 Perfect Lens with Subwavelength Resolution

In the previous two chapters, we described many intriguing properties in negative index materials (NIMs). One of the most striking predictions regarding NIMs as well as an exciting potential application is the “perfect lens.” Since light entering a NIM from free space will take a sharp turn at the interface, it is straightforward to see that a planar slab of NIM with sufficient thickness can act as a lens, sometimes dubbed as the Veselago lens. As depicted in Fig. 8.1c, diverging light rays from an object are negatively refracted at the first surface of the NIM slab, and the negative refraction of rays is repeated again at the second boundary. Consequently, the NIM slab creates an image within the slab and a second non-inverted image in the free space after the output interface. Compared to a conventional convex lens, the NIM lens looks quite exotic in that it does not have any axis or curvature, nor does it focus parallel rays or magnify small objects. All of these features were recognized in the seminal paper by Veselago [1]. The amazing properties of such a slab lens were first analyzed by J. B. Pendry, who pointed out that a slab with refractive index $n = -1$ placed in vacuum allows the imaging of objects with sub-wavelength precision [2].

Due to the Abbe diffraction limit, conventional lenses based on positive-index materials with curved surfaces (Fig. 8.1a) are not able to resolve objects smaller than approximately half of the illuminating wavelength λ_0 . The waves scattered by an object have all of the Fourier components with the wavevector in the propagating direction $k_z = \sqrt{k_0^2 - k_x^2 - k_y^2}$, where k_0 is the free-space wavevector, and each pair of (k_x, k_y) corresponds to a Fourier component of the waves from the object. The total transverse wavevector is $k_t = \sqrt{k_x^2 + k_y^2}$. When k_t is smaller than k_0 , k_z is a real number and the wave can propagate in any common material without significant power loss. However, when the value of k_t exceeds k_0 , k_z becomes an imaginary value and the wave decays exponentially in the propagation direction. Such waves, usually called “evanescent waves,” are confined to the vicinity of the object and do not have any contribution to the image obtained by standard lenses. However, these evanescent waves carry the sub-wavelength features of an object, because to probe the fine details it is required that the transverse

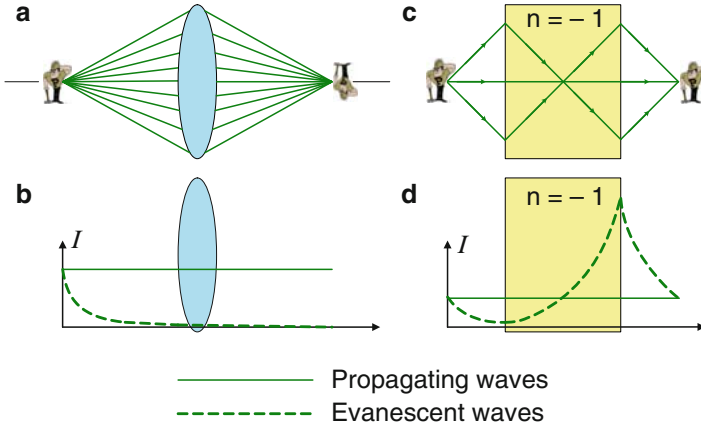


Fig. 8.1 The limitation of conventional lens and the idea of the NIM slab lens. (a) A conventional lens only collects the propagating waves. (b) The loss of the evanescent waves in conventional imaging system. (c) The focusing ability of a NIM slab. (d) The growth of evanescent waves in the NIM slab and the restoration of both the propagating and evanescent waves

wavelength $\lambda_t = 2\pi/k_t$ be smaller than the scale of the features, otherwise the wave will overlook the fine details of the object. Since the maximum possible value of k_t for propagating waves is identical to the free-space wavevector k_0 , the highest resolution can be estimated as $2\pi/k_{t,\max} = \lambda_0$. Therefore, conventional imaging systems cannot provide sub-wavelength resolution since they are unable to restore the evanescent waves (Fig. 8.1b) [3]. More precise analysis shows that the diffraction limit or Abbe's limit for a conventional lens is $\lambda_0/(2n \sin \alpha)$, where n is the refractive index of the medium in which the imaging system is immersed, and α represents the semi-aperture angle of the lens.

In order to beat the diffraction limit and obtain images with subwavelength features, researchers have managed to probe and collect the evanescent waves before they fade away. This is exactly the mechanism behind near-field scanning optical microscopy, where a probe is placed in the near field to collect evanescent waves. For many years, there seemed to be no alternative to explore evanescent modes, except for using a tip or probe in extremely close proximity to the surface of a specimen. In 2000, however, Pendry made a groundbreaking prediction, saying that a NIM slab is capable of producing flawless images because of its unique property of amplifying evanescent waves. Along the propagating direction, the field component of each Fourier mode from the object can be expressed as $\exp(-i\omega t + ik_z z)$. In free space, $k_z = \sqrt{k_0^2 - k_x^2 - k_y^2}$ is a positive quantity for propagating waves, and $k_z = i\kappa_z = i\sqrt{k_x^2 + k_y^2 - k_0^2}$ for the decaying near fields. In a NIM the value of the wavevector k_z is

$$k_z = -\sqrt{\frac{\epsilon\mu\omega^2}{c^2} - k_x^2 - k_y^2} \quad (8.1)$$

for propagating waves. The material parameters ε and μ possess negative values, and their product remains positive. The negative value of k_z in (8.1) describes the phase reversal effect in NIMs, as we have discussed in Chap. 6. More interestingly, k_z for evanescent waves in NIMs exhibits a negative imaginary value:

$$k_z = -i\kappa_z = -i\sqrt{k_x^2 + k_y^2 - \frac{\varepsilon\mu\omega^2}{c^2}}. \quad (8.2)$$

Consequently, the evanescent Fourier components inside a planar NIM slab grow exponentially along the z direction, following the function $\exp(\kappa_z z)$, where κ_z is a positive real number. When a NIM slab is used as a Veselago lens, the growth of evanescent waves inside the NIM fully compensates for the decay in the rest of the optical path, therefore evanescent waves revert to their original level at the imaging plane. This scenario is illustrated in Fig. 8.1d. As for the propagating components in a NIM lens, their amplitudes remain constant throughout the system, while their phase values accumulate to zero from the object plane to the image plane, owing to the reversed phase propagation in the NIM slab. Therefore, ideally all Fourier modes from the object, including both propagating waves and evanescent components, are fully recovered at the image plane, and a resolution far below the diffraction limit can be obtained.

It is important to note that the amplification of evanescent waves in NIMs does not violate energy conservation, because evanescent waves carry no energy. In an ideal, lossless NIM slab, the Poynting vector of evanescent waves is zero, so no energy transport is involved during the growth of evanescent modes in NIM slabs. The critical mechanism of NIM lenses is related to the resonant surface waves excited by the evanescent components of light at the NIM surface. The large energy density associated with these surface waves is built up over time. The energy source of the surface waves is light scattered from the object, and the evanescent waves serve as a coupling medium between the source and the surface modes.

It is also worth noting that the conditions for the “perfect lens” are rather severe, and the far-field “perfect lens” may only have theoretical significance. Rigorous analysis shows that any realistic losses, anisotropy or impedance mismatch that are inevitable in today’s resonance-based designs of NIMs can eliminate the desired effect of flawless imaging [4–6]. Moreover, the image of a “perfect lens” is intrinsically unstable [7]. To date, all the NIMs based on resonance properties of plasmonic metamaterials are highly dissipative, anisotropic, and lossy. That is the major reason why so far there has been no far-field demonstration of super-resolution using a planar NIM slab, except for a few rudimentary results at microwave frequencies using NIM slabs with thicknesses close to or even smaller than the operating wavelength [8–10].

8.2 Near-Field Superlens

Fortunately, there is another version of the slab lens that is relatively easier to achieve. Although not perfect, it is still capable of imaging with sub-wavelength resolution. This design could be called a “poor man’s superlens,” as suggested by Pendry. Provided that all of the dimensions of a system are much smaller than the wavelength, the electric and magnetic fields can be regarded as quasi-static and independent, and the requirement for superlensing of p -polarized waves (TM mode) is reduced to only $\varepsilon = -\varepsilon_h$, where ε_h is the permittivity of the host medium interfacing the lens [2]. The near-field version of the perfect lens, usually referred to as “near-field superlens (NFSL),” does not require optical magnetism and therefore is relatively easier to achieve. Although limited to the near-field zone only, this kind of near-field super-lens (NFSL) still allows many interesting applications including biomedical imaging and sub-wavelength lithography. Since a NFSL relies on a negative- ε material, noble metals are an attractive option due to their negative dielectric responses at optical frequencies, as we discussed in Chap. 2. In particular, silver is usually regarded as the metal of choice, because in the optical range silver has a much lower loss factor (described by the imaginary part of permittivity) as compared to all other metals. Similar to the case of a “perfect lens,” where surface modes at the NIM interface are critical for the amplification of evanescent waves, the interface between silver and air is capable of supporting surface-plasmon polaritons when the NFSL condition $\varepsilon = -1$ is satisfied. This is the reason that the frequency at which the metal permittivity is equal to -1 is commonly referred to as the metal’s surface plasmon frequency. For silver, the wavelength corresponding to its surface plasmon frequency is about 340 nm, a value in the near-ultraviolet regime.

The growth of evanescent waves in silver slabs, which is a prerequisite for the superlensing effect with silver, has been experimentally verified [11]. The experiment proved that the magnitude of evanescent waves can indeed be enhanced along the propagation distance in a silver slab until particular distance is reached where the material loss dominates over the amplification of the evanescent waves. The results in Ref. [11] show that enhancement in the evanescent wave magnitude can reach a factor of over 30 when an optimized film thickness of 50 nm is used. Soon after these results were published, experimental evidence of the superlensing effect with silver slabs was observed by two research groups [12, 13]. A schematic of the experimental configuration of the Berkeley experiment is illustrated in Fig. 8.2, where near-field optical lithography was used to examine the imaging capability of a silver slab sandwiched between photoresist layers. Using a 35-nm ultra-flat film of silver as the lens at an ultraviolet wavelength of 365 nm, the researchers successfully recorded the images of a grating with a 60-nm ($\sim\lambda_0/6$) half pitch as well as an arbitrary object with a 40-nm line width. Further details of the Berkeley NFSL experiment were presented in Ref. [14].

Analogous to the surface plasmon polaritons supported by metals, surface phonon polariton modes in SiC have enabled near-field superlensing in the mid-infrared at a frequency around 10 μm [15]. As we described previously in Chap. 5, the phonon-resonance property of SiC gives rise to negative permittivity on the

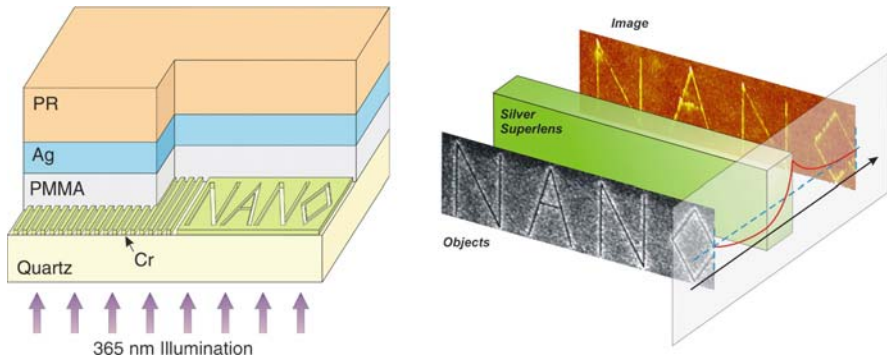


Fig. 8.2 Optical superlensing with a silver slab operating at a near-ultraviolet wavelength. An image with a resolution of ~ 40 nm is recorded by the photoresist layer next to the silver superlens. Reprinted from [12] with permission from AAAS. Courtesy of X. Zhang

high-frequency side of the resonance. In an experimental demonstration of this in Ref. [15], a planar SiC slab of 440 nm thickness was sandwiched between two SiO₂ thin films of 220 nm each. The best superlensing performance occurred at a wavelength of 10.8 μm where the NFSL operational condition $\text{Re}(\epsilon_{\text{SiC}}) = -\text{Re}(\epsilon_{\text{SiO}_2})$ is fulfilled. The image transferred through the SiC slab was collected by near-field scanning microscopy, and a resolution of $\sim \lambda_0/20$ was confirmed in the experiment.

There have been several variations of superlens designs based on a single silver slab. For example, several groups proposed the use of layered metal-dielectric composite as the superlens material [16–19]. Numerical studies indicate that a superlens based on metal-dielectric multilayers may have certain advantages over a pure silver superlens, especially when the issue of robustness against loss is concerned. Under a certain circumstance, layered metal-dielectric structures can support subwavelength resolution even without the involvement of evanescent wave amplification. This operational regime is referred to as canalization, where the layered system works as a transmission device which delivers images with subwavelength features from one interface of system to the other [20].

The capability of super-resolution in NFSL designs is limited by a number of factors. First and foremost, the distance between the object and image planes must be subwavelength, as implied by the definition of “near-field.” Otherwise, the retardation effect resulting from the traveling-wave nature through the lensing system will invalidate the assumption of static fields and the uncoupling of the electric and magnetic field components, which is a requirement for near-field superlensing. Second, any loss in the NFSL material will substantially deteriorate the desired super-resolution. Although silver is usually considered to be a low-loss metal in the near-ultraviolet and visible spectral range, the imaginary part of its permittivity is still comparable to unity, which is significant enough to be a primary limiting factor. The surface roughness and imperfections in any actually fabricated negative- ϵ slab will further limit the experimentally achievable super-resolution in a NFSL. The overall performance of a NFSL imaging system is determined by the number of evanescent waves with different $k_t > k_0$ that can be restored in the image plane.

8.3 “Tunable” Superlens Using Random Composites

We note, however, that the silver NFSL can operate only at a single frequency ω satisfying the lens condition $\varepsilon(\omega) = -\varepsilon_h$, which is indeed a significant drawback of a lens based on bulk metals. As we discussed in Chap. 2, the permittivity of a noble metal can be well approximated by the Drude model in the form of (2.17). Thus for any given host material with dielectric constant ε_h , the condition $\varepsilon_m' = -\varepsilon_h$ is satisfied only at one particular wavelength; for a silver slab in air, for example, this occurs at $\lambda \approx 340$ nm. The operational wavelength λ_{op} can be shifted if a host material other than air is used. However, in practice for a particular desired λ_{op} it remains a problem to find a host material such that the operating condition $\varepsilon_m'(\lambda_{op}) = -\varepsilon_h(\lambda_{op})$ is exactly fulfilled. In addition, it is difficult to obtain λ_{op} beyond the visible range since the value $-\varepsilon_m'(\lambda_{op})$ is too large to match any realistic host medium.

The situation can be changed dramatically when we consider using metal-dielectric composite as the lens material. As we showed in Sect. 2.4, in sharp contrast to pure metal slabs, metal-dielectric composite films are characterized by an effective permittivity ε_e that depends critically on the permittivities and the filling factors of both the metal and dielectric components. As a result, for a given host medium, $\varepsilon_e = \varepsilon_e(\omega, p)$ may have the value of $-\varepsilon_h$ at practically *any* wavelength in the visible and NIR region. The wavelength corresponding to $Re(\varepsilon_e) = -\varepsilon_h$ depends on the structure of the composite and the material constants of the metal and dielectric components in the composite. A schematic for such a “tunable” NFSL is shown in Fig. 8.3.

The optical properties of metal-dielectric composites are well described by the effective medium theory (EMT) [21]. According to the EMT, the effective permittivity ε_e for a d -dimensional composite material comprising metal particles with permittivity ε_m and a volume filling factor p , along with a dielectric component with permittivity ε_d and a filling factor $1 - p$:

$$\varepsilon_e = \varepsilon_e' + i\varepsilon_e'' = \frac{1}{2(d-1)} \left\{ (dp-1)\varepsilon_m + (d-1-dp)\varepsilon_d \pm \sqrt{[(dp-1)\varepsilon_m + (d-1-dp)\varepsilon_d]^2 + 4(d-1)\varepsilon_m\varepsilon_d} \right\} \quad (8.3)$$

where the sign should be chosen such that $\varepsilon_e'' > 0$.

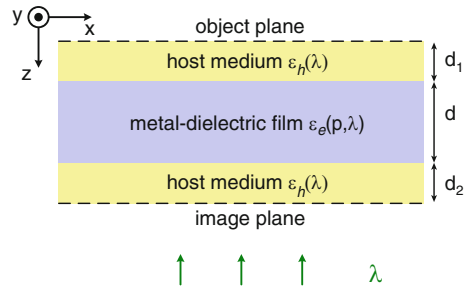


Fig. 8.3 Schematic of the tunable NFSL based on a metal-dielectric composite

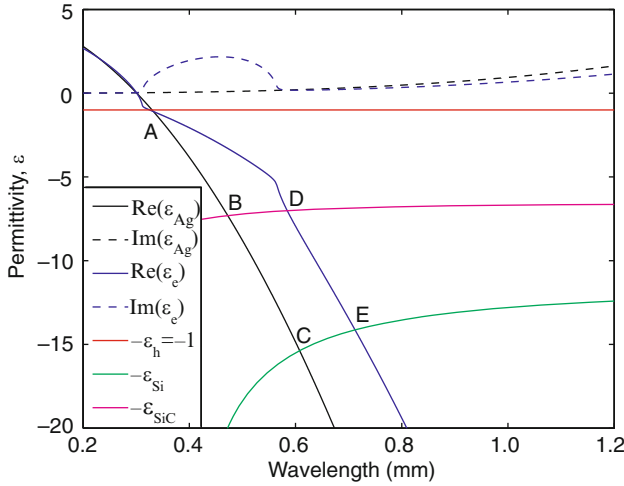


Fig. 8.4 Principle of NFSL operation. The composite used is an Ag–SiO₂ film with metal filling factor $p = 0.85$. The operational points are: (a) silver lens with air host ($\lambda_{op} = 340$ nm); (b) silver lens with SiC host; (c) silver lens with Si host; (d) composite lens with SiC host; (e) composite lens with Si host

The dependence of the effective dielectric permittivity ϵ_e on the light wavelength λ and on the metal filling factor p is the key to realizing the tunable NFSL [22]. The operational wavelength defined by the condition $Re[\epsilon_e(p, \lambda_{op})] = -\epsilon_h(\lambda_{op})$ depends on p and thus can be controlled by varying the metal filling factor. This makes it possible to tune the operating point over a wide wavelength range of interest.

The principle of the tunable NFSL operation is illustrated in Fig. 8.4. The permittivity of silver is given by the Drude model. The effective permittivity of a composite Ag – SiO₂ film with a metal filling factor $p = 0.85$ is calculated by the two-dimensional EMT model. The real part of the effective permittivity ϵ_e is smaller than that of pure metal in magnitude; the imaginary part describes a broad surface-plasmon absorption band resulting from the electromagnetic interactions between individual grains in the composite. The permittivities of air, silicon (Si) and silicon carbide (SiC) are also shown in the figure (we used the tabulated data of [23] and fitted it with functions providing excellent agreement within the visible and NIR range).

For a pure silver slab, the operation wavelengths determined by the condition $Re[\epsilon_e(p, \lambda_{op})] = -\epsilon_h(\lambda_{op})$ are indicated in Fig. 8.4 by points A, B, and C for host media of air, SiC and Si, respectively. For the composite NFSL, semiconductor materials like Si and SiC with large ϵ_h are beneficial to use as the host materials because they can move λ_{op} outside the plasmon absorption band and thus avoid significant losses that are associated with large values of ϵ_e'' and hence detrimental to the achievable resolution. The imaginary parts of the permittivities of Si and SiC within the wavelength range of interest are negligible and thus do not contribute to

losses. As seen in Fig. 8.4, using SiC or Si as the host material, a NFSL with a composite Ag – SiO₂ film at $p = 0.85$ operates at points D and E, respectively, which are both outside the absorption band of the composite.

Thus, for a given host material, one can fabricate a metal-dielectric film with an appropriate filling factor to work at any desired wavelength within a wide wavelength range. For example, with a composite Ag – SiO₂ film as the lens and SiC as the surrounding medium, the operational wavelength can be any value to the right of point B (B corresponds to the pure metal with $p = 1.0$) in Fig. 8.4 until a pre-defined cutoff condition (discussed later) is reached, which determines the long-wavelength and low- p limits for the NFSL operation. Moreover, at the operational point the loss of the lens material can be less than that of pure metal if the resonance peak is avoided. As shown in Fig. 8.4, the curve representing ϵ_e'' is lower than that of pure metal at the wavelengths corresponding to points D and E. The adverse effect of absorption is less of an issue when semiconductors with high permittivities are used as the host material. This is because such materials provide a better spatial resolution, which is approximately proportional to $1/\ln(|\epsilon'/\epsilon''|)$ for a lens material with permittivity $\epsilon = \epsilon' + i\epsilon''$ [24].

Figure 8.5a shows the required metal filling factor p for superlens operation using an Ag – SiO₂ composite lens. The filling factors were found from the superlens equation $Re[\epsilon_e(p, \lambda_{op})] = -\epsilon_h(\lambda_{op})$ for different wavelengths with Si or SiC as the host medium. For each kind of host material, the lower limit of the operational wavelength range corresponds to the pure metal ($p = 1$) case. A lower metal filling factor is required for a longer operational wavelength. For very long wavelengths, the required filling factor for the composite approaches the percolation threshold where the broad resonance peak in $\epsilon_e''(\lambda)$ reduces the super resolution effect. In Fig. 8.5a the upper limit of the possible wavelength range is determined such that $Im(\epsilon_e)/Re(\epsilon_h) = 0.1$ at the longer wavelength end of the operational range. Note that the criterion we use here is a very conservative one. For a silver lens working in air as first proposed in Ref. [2] or polymethyl methacrylate

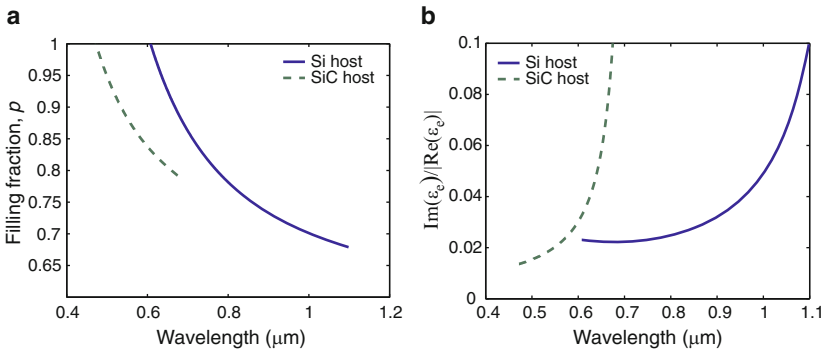


Fig. 8.5 Performance of an Ag–SiO₂ composite lens with Si or SiC as the host medium. (a) The required metal filling factor p for different wavelengths. (b) The value of $Im(\epsilon_e)/Re(\epsilon_h)$ for different wavelengths

(PMMA) as studied in Refs. [12, 25], the value of $Im(\varepsilon_e)/Re(\varepsilon_h)$ was as large as 0.4 while sub-wavelength resolution was still achievable. As seen in Fig. 8.5a, with an Ag – SiO₂ composite as the lens material the operation ranges are 0.47–0.67 μm for SiC host material and 0.61–1.10 μm for Si host material. Therefore, combining the results of the two host media we can achieve a possible operational wavelength range of 0.47–1.10 μm , which covers nearly the whole visible spectrum and the shorter part of NIR band. The operational range can be expanded even further by using other host media or other constituent materials for the metal-dielectric composite. The value of $Im(\varepsilon_e)/Re(\varepsilon_h)$ as a function of the operational wavelength is plotted in Fig. 8.5b.

To illustrate the imaging ability of the proposed tunable NFSL based on metal-dielectric films, we calculate the optical transfer function (OTF) of the system and the image obtained at the imaging plane for a given object. For simplicity we assume invariance along the y direction for the whole system (coordinates are shown in Fig. 8.3). The OTF from the object plane to the image plane is written as

$$OTF(k_x) = T_p(k_x) \exp(ik_z^{(1)}d_1) \exp(ik_z^{(2)}d_2) \quad (8.4)$$

where $T_p(k_x)$ is the transmission coefficient of the slab for the p -wave (TM mode). The index “1” represents the material between the object plane and the lens and the index “2” represents the material between the lens and the image plane. The transmission coefficient is given as [26]:

$$T_p(k_x) = \frac{4(k_z^{(1)}/\varepsilon_1)(k_z^{(e)}/\varepsilon_e) \exp(ik_z^{(e)}d)}{(k_z^{(1)}/\varepsilon_1 + k_z^{(e)}/\varepsilon_e)(k_z^{(2)}/\varepsilon_2 + k_z^{(e)}/\varepsilon_e) - (k_z^{(1)}/\varepsilon_1 - k_z^{(e)}/\varepsilon_e)(k_z^{(2)}/\varepsilon_2 - k_z^{(e)}/\varepsilon_e) \exp(2ik_z^{(e)}d)} \quad (8.5)$$

where $k_z^{(i)} = \sqrt{\varepsilon_i k_0^2 - k_x^2 - k_y^2}$.

As an example, the performance of the Ag – SiO₂ NFSL with SiC as the host and operating at 632.8 nm is illustrated in Fig. 8.6. At this wavelength the host permittivity $\varepsilon_h = 6.94$, the effective permittivity of the lens $\varepsilon_e = -6.94 + i0.31$, and the required metal filling factor given by the relation $Re[\varepsilon_e(p, \lambda_{op})] = -\varepsilon_h(\lambda_{op})$ is $p = 0.82$. The thickness of the lens is chosen to be $d = 20$ nm. The modulation transfer function (MTF), which is defined as $MTF(k_x) = |OTF(k_x)|^2$, represents a useful way to evaluate the imaging ability of a NFSL [27]. In Fig. 8.6a the MTF of the imaging system (solid line) together with the MTF from the object plane to the image plane without the lens are plotted as functions of the transverse wavevector k_x . For the perfect lens $MTF(k_x) = 1$ for all k_x and thus a perfect image can be produced. For free space, as shown by the dashed line in Fig. 8.6a, $MTF(k_x) = 1$ for propagating waves (when $k_x/k_0 < 1$) and it decays exponentially for evanescent waves (when $k_x/k_0 > 1$). For the composite NFSL with the parameters given above, the MTF can maintain a value comparable to unity for a range of k_x up to $15k_0$, which indicates a resolution of about $\pi/15k_0 = \lambda/30$ can be obtained. Figure 8.6b illustrates the simulated result of the image of a pair of slits of width d and center-to-center separation $2d$. The result shows that the composite lens is capable of reconstructing the object at the image plane. Without the lens, the pair

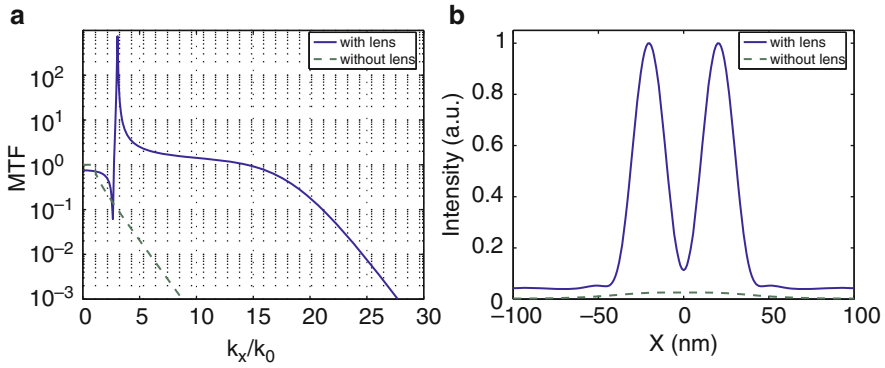


Fig. 8.6 The imaging ability of a 20 nm Ag–SiO₂ composite lens with SiC as the host medium working at 632.8 nm. (a) The MTF of the imaging system as a function of the transverse wavevector k_x . (b) The simulated result of the image of a pair of slits of width d and center-to-center separation $2d$

of slits cannot be resolved, as shown by the dashed curve in Fig. 8.6b. Note that the procedure to calculate the MTF and the image as described above is exact (no quasi-static or other approximations were used). The only assumption is y -invariance and p -wave illumination.

It is worth noting that the effective permittivity of the metal-dielectric composite calculated using the two-dimensional EMT is a method of approximation, which provides a simple analytical way to evaluate the effective properties of the composite film. To assure that the composite NFSL does give acceptable resolution, we re-visit the properties of the composite film using the block-elimination (BE) method. The BE method is an exact numerical approach to calculate the effective parameters and local-field distribution of a metal-dielectric film. The detailed procedure is demonstrated in Ref. [28]. Compared to the results by EMT, the resonance range of the effective permittivity calculated by the BE method has a longer tail. Therefore, the value of ϵ_e'' at the operational wavelength of the NFSL obtained by the BE method is somewhat larger compared to the EMT results. The imaginary part of permittivity of an Ag–SiO₂ composite with different metal filling factors calculated by the EMT and the BE method are illustrated in Fig. 8.7a and b, respectively; the two calculations are in reasonable agreement. Because the BE algorithm is time-consuming, it is not feasible to calculate the exact $p = p(\lambda)$ relationship of the composite NFSL using this method. However, using the $p = p(\lambda)$ relation given in Fig. 8.5a as a starting point, one can verify that the ϵ_e'' obtained by the exact BE method is indeed acceptable for the composite NFSL to provide the superlensing effect.

There is no unambiguous way to define the resolution of an imaging system. Here we use a modified version of Rayleigh's criterion to evaluate the limit of resolution for the proposed composite NFSL system. Similar to the example in Fig. 8.6b, we consider a NFSL system where the lens thickness is d and the object is a pair of slits of width d and center-to-center separation $2d$. At the image plane, the two slits are regarded as barely resolvable if the intensity at the midpoint of the slit

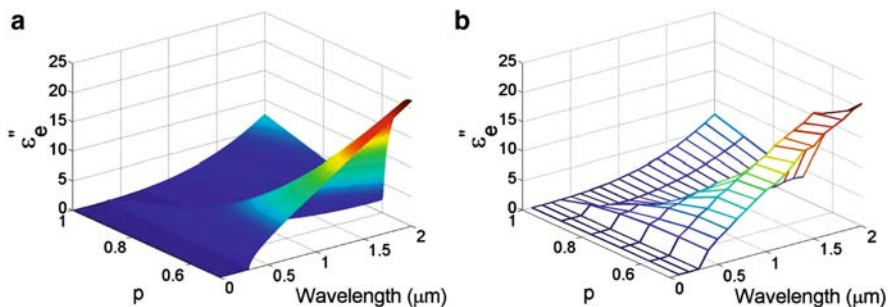


Fig. 8.7 (a) The imaginary parts of the effective permittivity ϵ_e'' of an Ag–SiO₂ composite calculated by the EMT. (b) ϵ_e'' calculated by the BE method

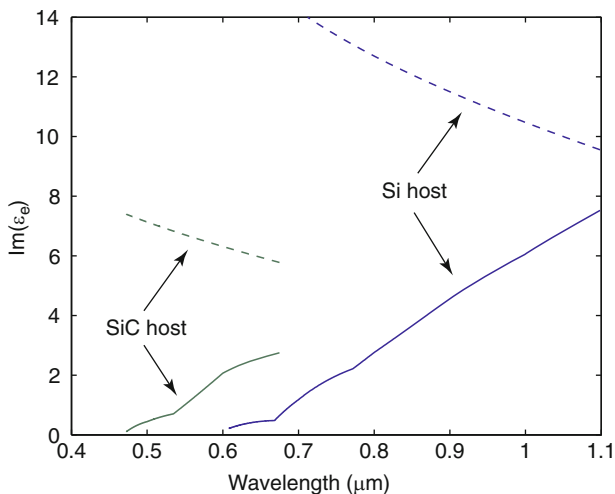


Fig. 8.8 The upper bound of ϵ_e'' determined by the Rayleigh criterion (*dashed*) and the ϵ_e'' at the operational wavelength calculated by the BE method (*solid*). The NFSL system is a 20-nm Ag–SiO₂ composite with Si or SiC as the host medium. The object is the same as that in Fig. 8.6b

pair is $8I_0/\pi^2 = 0.811I_0$, where I_0 is the maximum intensity [29]. This criterion provides an upper bound for the detrimental effects on NFSL performance such as loss, impedance mismatch, retardance, and others.

Considering an Ag – SiO₂ composite NFSL of $d = 20$ nm with Si or SiC as the surrounding medium, the upper bound of ϵ_e'' determined by the Rayleigh criterion is shown in Fig. 8.8, together with the values of ϵ_e'' within the operational wavelength range obtained by the BE method using linear interpolation. We see that the ϵ_e'' calculated by the exact two-dimensional BE method is still far below the upper bound of ϵ_e'' defined by the Rayleigh criterion, which verifies that the composite NFSL can give near-field super-resolution.

8.4 Potential Applications of the Composite Lens

As seen from the considerations above, random metal-dielectric composite films have potential for use in the development of versatile and wavelength-controllable NFSL designs. Such versatility and wavelength selectivity can make the difference in a wide range of applications including bio-sensing, spectroscopy, sub-wavelength imaging, and nanolithography. A few examples of these applications are briefly discussed in this section.

The first application of the proposed composite lens is surface-enhanced, remote sensing of bio-molecules such as proteins, using, for example, the phenomenon of surface-enhanced Raman scattering (SERS). In SERS, a metal surface with nanoscale roughness provides field enhancement to the Raman scattering process, greatly enhancing the scattered signal intensity. In this approach, however, a composite superlens is used to image a SERS-active substrate to a different place in space where analyte bio-molecules are located. In this way, the bio-molecules are physically separated from the SERS-active substrate. This method has advantages over typical SERS schemes because it is known that in SERS the molecules directly in contact with the metal surface typically experience undesired modifications and denaturing due to at least the charge transfer effect [30], causing significant changes in their optical spectra and biological activity. As a result, SERS spectra often represent signatures of metal-molecule complexes rather than the molecules themselves. A metal-dielectric composite lens offers a solution to the problem by “imaging” the high local fields of the SERS substrate to the other side of the composite lens, where bio-molecules are placed, as illustrated in Fig. 8.9a. Using this technique, the molecules are removed from the metal and thus do not undergo any modification caused by the metal, but they still experience the dramatic enhancement provided by the metal surface. In addition, the use of a tunable NFSL based on a composite film is certainly more convenient here compared to a pure silver lens, which would only work at a single wavelength in UV range. Moreover, it is known that a semi-continuous film used as a SERS substrate is more effective for longer wavelengths [21], which would not be possible at all for a pure silver lens.

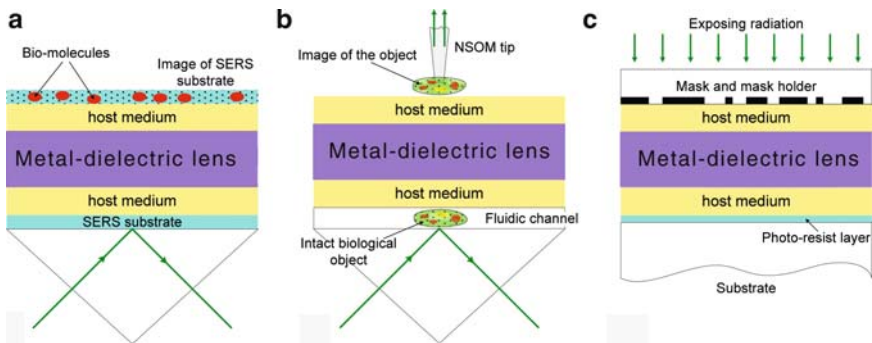


Fig. 8.9 Examples of applications for composite NFSL designs. (a) Remote SERS sensing; (b) non-contact bio-molecule probing; (c) nanoscale lithography

For various biomedical and detection applications it is of critical importance to be able to optically probe the internal structure of intact cells, spores, and other biological objects with sub-wavelength resolution. Near-field scanning optical microscopy (NSOM) is a method that can accomplish sub-wavelength resolution imaging by employing a tiny optical fiber tip and bringing the tip to within a few nanometers of an object. However, NSOM imaging cannot probe inside a cell or object directly, since the technique requires that the fiber tip be within a few nanometers of the area of interest. Thus the tip would need to penetrate inside the object, which can often modify or even destroy the object. However, we can avoid this fate by using a metal-dielectric superlens, allowing us to observe the various internal structures in intact cells and other objects. The metal-dielectric lens would allow us to place the image of a bio-object on the other side of the lens. We can then scan the object's image with an NSOM tip without touching the object itself. The schematic for the proposed technique is depicted in Fig. 8.9b. Such remote, non-invasive, intra-object imaging is of particular interest for biomedical analysis and sensing of biological agents.

The proposed tunable NFSL may also find applications in nanoscale optical manufacturing. There are already promising results in this area obtained using a silver slab lens [13]. Using an appropriately designed composite NFSL rather than a silver slab, we could use any of a number of available laser sources that can make the proposed nano-fabrication more versatile and less expensive. A schematic illustrating this scheme is shown in Fig. 8.9c. The tunable NFSL produces an image of the mask in the image plane, where photo-resist has been placed. The spatial resolution in this case can be well below the diffraction limit, which makes laser nano-manufacturing possible.

8.5 Far-Field Imaging with Super-Resolution

In the foregoing sections, we have described in detail the mechanism of operation and the realization of NFSLs that allow for sub-diffraction-limited resolution. Although these are very intriguing and fundamentally important issues, the superlensing effect in such systems is limited to the near field. This fact greatly restricts the possible use of superlenses in many applications such as the direct observation of the subwavelength features of objects using common cameras or even the human eye. According to Pendry's initial perfect-lens proposal, a thick slab of a negative-index medium is theoretically capable of providing far-field super-resolution. However, losses inherent in today's plasmonic negative-index metamaterials eliminate any chance of far-field superlensing. Therefore, the goal of this section is to explore the possibility of subwavelength resolution in the far-field without the use of NIMs. Most experimental breakthroughs on this topic were achieved by a Berkeley group led by Xiang Zhang.

One way to break the diffraction limit in the far-field is to convert the enhanced evanescent waves in a NFSL into propagating waves by a coupling element. This coupling mechanism can be achieved by adding a periodic grating on the outer

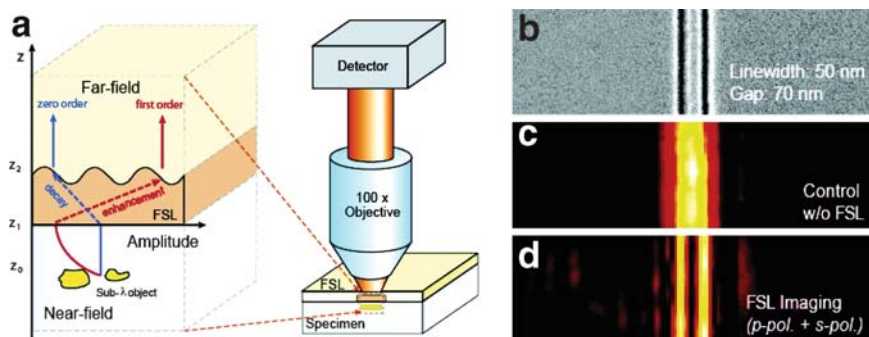


Fig. 8.10 The far-field superlens with a silver slab plus periodic corrugations. (a) Schematic of the far-field superlens and its adaptation in a conventional microscope; (b) SEM image of a nanoslit-pair object; (c) diffraction-limited image of the object from a regular optical microscope; (d) the far-field superlens resolves the subwavelength details of the object. Adapted with permission from [32]. Copyright (2007) American Chemical Society. Courtesy of X. Zhang

surface of the silver superlens [31, 32]. The role of such periodic corrugations in the coupling between light waves and surface plasmons has been known for a long time [33] and is widely used for applications such as extraordinary optical transmittance and subwavelength light concentration [34, 35]. Figure 8.10a depicts a schematic of the far-field optical superlens reported in Ref. [32]. A properly designed, subwavelength grating is added onto a 35-nm-thick silver superlens in order to convert some evanescent modes into propagating waves. When inserting the specimen as well as the corrugated silver slab into a conventional optical microscope, a far-field imaging system with subwavelength resolution can be achieved. Similar to the silver superlens, the far-field lens works at the surface plasmon frequency of the silver-polymer interface, which occurs at 377 nm in this demonstration. The experiment shows that the far-field superlens is capable of imaging a pair of 50-nm-wide nanoslits separated by a gap of 70 nm, as shown in Fig. 8.10d. Without the far-field superlens, a conventional optical microscope fails to resolve such small features, as seen in Fig. 8.10c.

Compared with near-field scanning optical microscopes, the far-field superlens provides a relatively efficient method for image collection. This new invention projects the subwavelength details of an object into the far field, thus avoiding the point-by-point scanning commonly seen in most near-field techniques. However, there are a number of limitations regarding the imaging capability of a far-field superlens. First, although the image can be transported to the far zone, the specimen has to be placed very close to the silver superlens surface. Otherwise, the evanescent waves will diminish to a negligible magnitude before they interact with the metal. Second, the one-dimensional grating only allows for the scattering of evanescent modes to propagating waves along a single direction. As a result, the system in Fig. 8.10 can only resolve the subwavelength features of a one-dimensional object, such as the thin slit pair used in the demonstration. This limitation may be partially circumvented by introducing more sophisticated corrugations and advanced image reconstruction techniques [36]. More fundamentally, there is an intrinsic limitation

to the wavevector band within which the evanescent modes can be manipulated [32]. For the far-field superlens shown in Fig. 8.10, only the evanescent waves with transverse vector between nk_0 and $nk_0 + k_\Lambda$ can be reliably retrieved, where n is the refractive index of the surrounding material and k_Λ represents the grating wavevector. This limitation to the maximum allowed wavevector of evanescent waves, in turn, sets the bound for the best achievable resolution in a far-field superlens. More complicated, multiple measurements with high-order coupling elements must be used if a wider bandwidth in the Fourier space is to be probed.

An optical “hyperlens” consisting of alternating metal and dielectric layers in a cylindrical geometry offers an alternative method to convert evanescent waves into propagating waves that can be collected in the far zone. Instead of completing the wave conversion with specific corrugations on the superlens surface, in a hyperlens the transverse wavevectors of an object’s evanescent waves are gradually suppressed as the waves travel outward from inside the cylinder. Eventually the transverse wavevectors are reduced to such an extent that they become smaller than the light wavevector, and therefore the evanescent waves evolve into propagating waves in free space or in the surrounding dielectric medium. This mechanism was proposed by two teams independently [37,38], and was later confirmed experimentally by the Zhang group at Berkeley [39].

As we showed in Chap. 3, a stratified metal-dielectric composite can work as a metamaterial with very anisotropic optical properties along its two principal directions. For the construction of a hyperlens, the metallic and dielectric layers are arranged concentrically in a cylindrical system in such a manner that the two effective permittivities have opposite signs: $\varepsilon_r < 0$ and $\varepsilon_\theta > 0$. If this condition is satisfied, the isofrequency curve of the composite medium is hyperbolic. The reader may better visualize the scenario by referring to Fig. 6.14c and replacing the k_x and k_z there by k_r and k_θ , respectively. The hyperbolic wavevector surface gives rise to two essential features necessary for a hyperlens. First, the wavevector for a fixed frequency can take on arbitrarily large values [37]. More importantly, since the Poynting vector is indicated by the normal to the isofrequency curve, the Poynting vectors for most Fourier components are directed largely parallel to each other, being perpendicular to the asymptote of the hyperbolic curve [40]. This effect is particularly evident when the hyperbolic dispersion curve is nearly flat, a feature adopted in the hyperlens design. Consequently, a point source placed inside a hyperlens generates a beamlike radiation along the radial direction, as illustrated in Fig. 8.11a. Furthermore, the directional nature of radiation and the cylindrical symmetry together give rise to a magnification of the object, with the magnification equal to the ratio between the outer and inner radii of the hyperlens. The magnification causes the image of the subwavelength features of the object to be enlarged and observable using conventional optical devices.

In the experimental demonstration of a hyperlens working at an ultraviolet wavelength of 365 nm [39], a curved periodic stack of silver and alumina layers were deposited on a half-cylinder cavity etched on a quartz substrate, as shown in the schematic of Fig. 8.11b. The entire hyperlens consisted of 16 alternating layers of Ag/Al₂O₃, with the thickness of each layer held constant at 35 nm. The

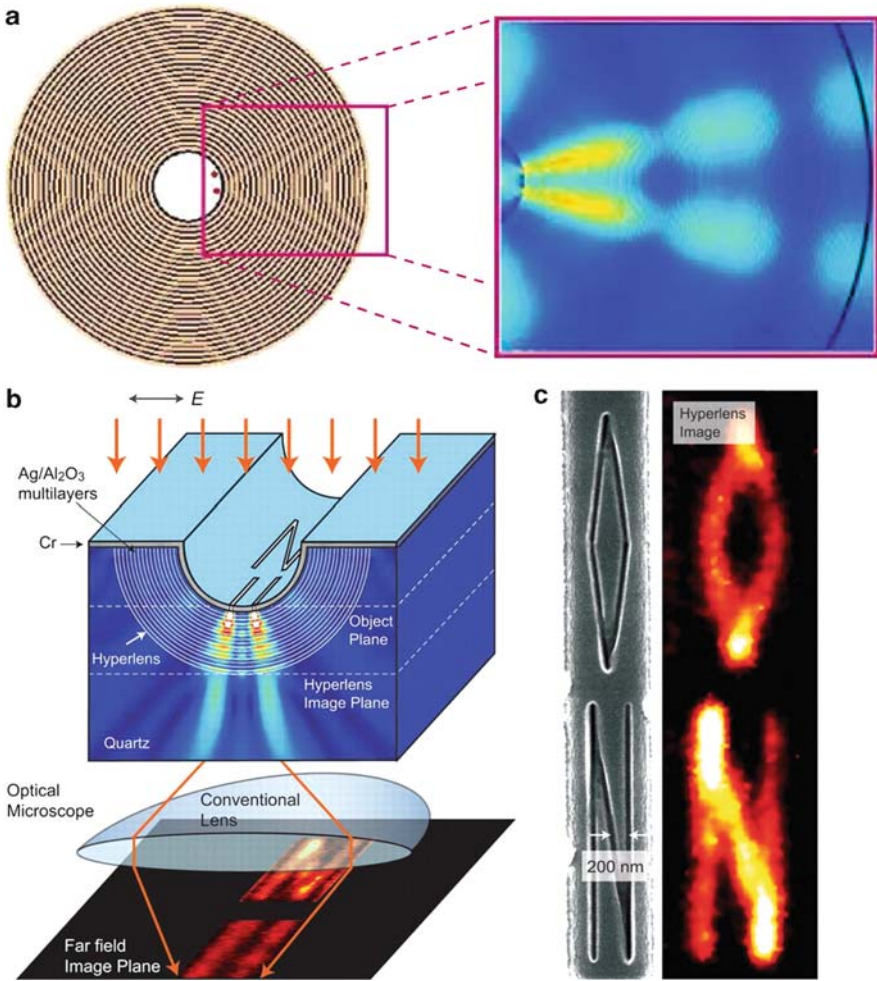


Fig. 8.11 (a) Magnification and beaming effects in a hyperlens consisting of alternating metal and dielectric layers. Reprinted with permission from [37]. Copyright (2006) OSA. (b) Schematic of the hyperlens demonstrated by the Berkeley group; (c) an arbitrary object (the text “ON”) and its hyperlens image with sub-diffraction resolution. Reprinted from [39] with permission from AAAS. Courtesy of X. Zhang

magnification of this hyperlens was about 2.3. The object was formed by inscribing nanoscale patterns into a chrome layer located on the inner surface of the half-cylindrical hyperlens. By incorporating the hyperlens with a regular optical microscope, a sub-diffraction-limited resolution of 130 nm was achieved. One example of the imaged object is the arbitrary pattern consisting of the text “ON” with a line width of ~ 40 nm, as shown in Fig. 8.11c. The performance of the hyperlens can be improved if a spherical geometry instead of the cylindrical shape is used. In this

case, the object is uniformly magnified and faithfully restored at the outer surface of the spherical hyperlens.

Another demonstration of a magnifying, cylindrical lens was realized for surface plasmons confined in a two-dimensional surface [41]. The reported device was formed of concentric polymer rings on a gold surface. At the designed operational wavelength of ~ 500 nm, the dispersion curves for surface plasmon waves at gold-polymer and gold-air interfaces exhibit opposite slopes. As a result, the effective refractive indices as perceived by the surface plasmons are alternately positive and negative for the concentric layers, fulfilling the hyperlens requirement [37, 38]. The magnifying action of the plasmonic hyperlens was demonstrated by imaging rows of polymer dots placed inside the inner ring, and the magnified images were captured by collecting the scattered radiation using a conventional microscope. A deeply subwavelength resolution on the order of 70 nm was obtained in the plasmonic imaging system.

In Ref. [42], it was shown that the use of nonperiodically distributed thicknesses of the hyperlens layers may result in better performance. We also note that the originally proposed hyperlens suffers from strong reflections at its inner and outer cylindrical surfaces, causing reduced light throughput. With local control of the electromagnetic response of metamaterials, the impedance matching at these boundaries can be improved [43]. Moreover, the actual fabrication and use of the hyperlens is extremely challenging, as in its original concept it requires cylindrical symmetry. Such symmetry is needed to slowly increase the electromagnetic mode wavelength as the wave spreads away from the center of the device to the point where propagation in air becomes possible [44]. In addition, its cylindrical symmetry limits applications, because placing an object of interest in the hyperlens' inner cylindrical cavity is often impossible. One would be better served by a planar hyperlens – if it were possible. The approach of “engineering optical space” based on the transformation optics with local control of a metamaterial's response offers a direct solution to this problem [45]. The process of “slowing down” the evanescent waves required for converting them into propagating waves in air can be achieved by properly varying the dielectric tensor within the hyperlens. Simulations for the proposed flat hyperlens show that it can produce magnified far-field images of sub- λ structures [46]. Such a planar, magnifying hyperlens could eventually become a standard add-on to conventional microscopes. By enabling nanoscale resolution in optical microscopy, metamaterial-based transformation optics could allow one to literally see extremely small objects with the eye, including biological cells, viruses and, possibly, even DNA molecules.

A number of other schemes have been proposed for far-field sub-diffraction-limited resolution based on optical metamaterials. Numerical studies from the Kawata group in Osaka, Japan, showed that subwavelength images can be transferred over distances of at least many wavelengths using a lens made of stacked silver nanorods [47]. The chains of nanorods with weakly damped plasmon resonances project images from one end of the system to the other end in a pixel-to-pixel fashion, as illustrated in Fig. 8.12a. The situation very much resembles that of a conventional fiber image waveguide consisting of thousands of optical fibers,

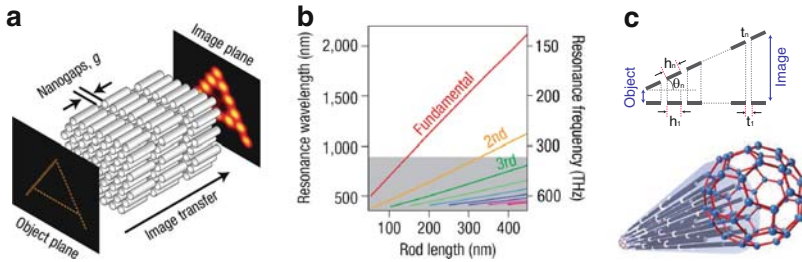


Fig. 8.12 Metallic nanolens with chains of silver nanorods. (a) Schematic of far-field imaging with stacked arrangement of silver nanorod arrays; (b) spectral dependence of plasmon resonance modes as a function of rod length; (c) magnification of images based on tapered arrangement of nanorod arrays. Reprinted from [47] by permission from Macmillan Publishers Ltd: Nat Photonics, copyright (2008)

which transmit images to a remote end. However, there is one fundamental difference between the common fiber bundle system and this new invention. In a fiber-bundle imaging guide, each fiber transmits a pixel with a size subject to the diffraction limit. In the proposed nanorod arrays, however, each chain of nanorods is capable of capturing the local features of an object with a typical size of no more than tens of nanometers. Thus the resolution of the nanorod-bundle system is not limited by diffraction.

The most fascinating feature of the proposed silver-wire lens scheme lies in its potential for color imaging. The nanorod chain can be designed such that different orders of plasmons at several wavelengths within the visible spectrum can be supported simultaneously. This effect can be visualized by the frequency dependence of plasmon modes as a function of the rod length, as shown in Fig. 8.12b. From the color theory in visual arts we know that a set of three colors is usually enough to mix and produce all other perceivable colors (for example, the RGB color model). Therefore, real-time color imaging is in principle possible in the silver-wire lens system. Magnification in this lens is also not a problem, since the stacked layers of metallic nanorods can follow a tapered arrangement to provide magnification. In addition, the separation between adjacent pixels at the exit end can be large enough to allow for observation with conventional optics. A schematic for the magnification effect is shown in Fig. 8.12c. A similar mechanism for a magnifying lens using tapered arrays of continuous metallic wires was proposed earlier in Ref. [48].

There is yet another way proposed to achieve subwavelength imaging even without the recovery of evanescent waves. This scheme makes use of the “super-oscillation” effect, which relies on the fact that band-limited functions can oscillate arbitrarily faster than the highest Fourier components they contain [49]. Such super-oscillating fields can be generated by some patterned metal surfaces. Using this effect, subwavelength focusing of light and one-to-one imaging of point sources to the far-field were experimentally verified [50, 51]. In these experiments, a quasi-periodic array of nanoholes in a thin metal screen was utilized to achieve the transition between super-oscillation and super-resolution.

At the end of this section, we want to note that none of the schemes discussed above can be regarded as being close to an ideal far-field imaging system with super-resolution. They are usually highly sensitive to material losses and imperfections, and they are mostly subject to operational limitations such as subwavelength working distances and narrow working bandwidths. They are, nonetheless, very real in today's science. With continuing efforts to optimize the designs, explore new physical phenomena and postulate new structures, metamaterial researchers may create a robust and versatile far-field lens with sub-diffraction resolution in the distant but foreseeable future.

References

1. Veselago VG (1968) Electrodynamics of substances with simultaneously negative values of σ and μ . *Sov Phys Usp* 10:509–514
2. Pendry JB (2000) Negative refraction makes a perfect lens. *Phys Rev Lett* 85:3966–3969
3. Pendry JB, Smith DR (2004) Reversing light with negative refraction. *Phys Today* 57:37–43
4. Smith DR, Schurig D, Rosenbluth M, Schultz S, Ramakrishna SA, Pendry JB (2003) Limitations on subdiffraction imaging with a negative refractive index slab. *Appl Phys Lett* 82:1506–1508
5. Podolskiy VA, Narimanov EE (2005) Near-sighted superlens. *Opt Lett* 30:75–77
6. Webb KJ, Yang M, Ward DW, Nelson KA (2004) Metrics for negative-refractive-index materials. *Phys Rev E* 70:035602
7. Rao XS, Ong CK (2003) Subwavelength imaging by a left-handed material superlens. *Phys Rev E* 68:067601
8. Grbic A, Eleftheriades GV (2004) Overcoming the diffraction limit with a planar left-handed transmission-line lens. *Phys Rev Lett* 92:117403
9. Lagarkov AN, Kissel VN (2004) Near-perfect imaging in a focusing system based on a left-handed-material plate. *Phys Rev Lett* 92:077401
10. Aydin K, Bulu I, Ozbay E (2007) Subwavelength resolution with a negative-index metamaterial superlens. *Appl Phys Lett* 90:254102
11. Liu ZW, Fang N, Yen TJ, Zhang X (2003) Rapid growth of evanescent wave by a silver superlens. *Appl Phys Lett* 83:5184–5186
12. Fang N, Lee H, Sun C, Zhang X (2005) Sub-diffraction-limited optical imaging with a silver superlens. *Science* 308:534–537
13. Melville DOS, Blaikie RJ (2005) Super-resolution imaging through a planar silver layer. *Opt Express* 13:2127–2134
14. Lee H, Xiong Y, Fang N, Srituravanich W, Durant S, Ambati M, Sun C, Zhang X (2005) Realization of optical superlens imaging below the diffraction limit. *New J Phys* 7:255
15. Taubner T, Korobkin D, Urzhumov Y, Shvets G, Hillenbrand R (2006) Near-field microscopy through a SiC superlens. *Science* 313:1595–1595
16. Shamonina E, Kalinin VA, Ringhofer KH, Solymar L (2001) Imaging, compression and Poynting vector streamlines for negative permittivity materials. *Electron Lett* 37:1243–1244
17. Ramakrishna SA, Pendry JB, Wiltshire MCK, Stewart WJ (2003) Imaging the near field. *J Mod Opt* 50:1419–1430
18. Wood B, Pendry JB, Tsai DP (2006) Directed subwavelength imaging using a layered metal-dielectric system. *Phys Rev B* 74:115116
19. de Ceglia D, Vincenti MA, Cappeddu MG, Centini M, Akozbek N, D’Orazio A, Haus JW, Bloemer MJ, Scalora M (2008) Tailoring metallodielectric structures for superresolution and superguiding applications in the visible and near-IR ranges. *Phys Rev A* 77:033848

20. Belov PA, Hao Y (2006) Subwavelength imaging at optical frequencies using a transmission device formed by a periodic layered metal-dielectric structure operating in the canalization regime. *Phys Rev B* 73:113110
21. Shalaev VM (2000) *Nonlinear optics of random media: fractal composites and metal-dielectric films*. Springer, Berlin
22. Cai WS, Genov DA, Shalaev VM (2005) Superlens based on metal-dielectric composites. *Phys Rev B* 72:193101
23. Palik ED (ed) (1997) *Handbook of optical constants of solids*. Academic, New York
24. Larkin IA, Stockman MI (2005) Imperfect perfect lens. *Nano Lett* 5:339–343
25. Melville DOS, Blaikie RJ, Wolf CR (2004) Submicron imaging with a planar silver lens. *Appl Phys Lett* 84:4403–4405
26. Ramakrishna SA, Pendry JB (2002) The asymmetric lossy near-perfect lens. *J Mod Opt* 49:1747–1762
27. Fang N, Zhang X (2003) Imaging properties of a metamaterial superlens. *Appl Phys Lett* 82:161–163
28. Genov DA, Sarychev AK, Shalaev VM (2003) Metal-dielectric composite filters with controlled spectral windows of transparency. *J Nonlinear Opt Phys Mater* 12:419–440
29. Born M, Wolf E (1999) *Principles of optics*. Cambridge University Press, Cambridge
30. Adrian FJ (1982) Charge-transfer effects in surface-enhanced Raman-scattering. *J Chem Phys* 77:5302–5314
31. Durant S, Liu ZW, Steele JA, Zhang X (2006) Theory of the transmission properties of an optical far-field superlens for imaging beyond the diffraction limit. *J Opt Soc Am B* 23:2383–2392
32. Liu ZW, Durant S, Lee H, Pikus Y, Fang N, Xiong Y, Sun C, Zhang X (2007) Far-field optical superlens. *Nano Lett* 7:403–408
33. Raether H (1988) *Surface plasmons*. Springer, Berlin
34. Ebbesen TW, Lezec HJ, Ghaemi HF, Thio T, Wolff PA (1998) Extraordinary optical transmission through sub-wavelength hole arrays. *Nature* 391:667–669
35. Lezec HJ, Degiron A, Devaux E, Linke RA, Martin-Moreno L, Garcia-Vidal FJ, Ebbesen TW (2002) Beaming light from a subwavelength aperture. *Science* 297:820–822
36. Xiong Y, Liu Z, Sun C, Zhang X (2007) Two-dimensional Imaging by far-field superlens at visible wavelengths. *Nano Lett* 7:3360–3365
37. Jacob Z, Alekseyev LV, Narimanov E (2006) Optical hyperlens: far-field imaging beyond the diffraction limit. *Opt Express* 14:8247–8256
38. Salandrino A, Engheta N (2006) Far-field subdiffraction optical microscopy using metamaterial crystals: theory and simulations. *Phys Rev B* 74:075103
39. Liu ZW, Lee H, Xiong Y, Sun C, Zhang X (2007) Far-field optical hyperlens magnifying sub-diffraction-limited objects. *Science* 315:1686–1686
40. Jacob Z, Alekseyev LV, Narimanov E (2007) Semiclassical theory of the hyperlens. *J Opt Soc Am A* 24:A54–A61
41. Smolyaninov II, Hung YJ, Davis CC (2007) Magnifying superlens in the visible frequency range. *Science* 315:1699–1701
42. Kildishev AV, Chettiar UK, Jacob Z, Shalaev VM, Narimanov EE (2009) Materializing a binary hyperlens design. *Appl Phys Lett* 94:071102
43. Kildishev AV, Narimanov EE (2007) Impedance-matched hyperlens. *Opt Lett* 32:3432–3434
44. Narimanov EE, Shalaev VM (2007) Beyond diffraction. *Nature* 447:266–267
45. Shalaev VM (2008) Transforming light. *Science* 322:384–386
46. Kildishev AV, Shalaev VM (2008) Engineering space for light via transformation optics. *Opt Lett* 33:43–45
47. Kawata S, Ono A, Verma P (2008) Subwavelength colour imaging with a metallic nanolens. *Nat Photonics* 2:438–442
48. Shvets G, Trendafilov S, Pendry JB, Sarychev A (2007) Guiding, focusing, and sensing on the subwavelength scale using metallic wire arrays. *Phys Rev Lett* 99:053903

49. Huang FM, Zheludev N, Chen YF, de Abajo FJG (2007) Focusing of light by a nanohole array. *Appl Phys Lett* 90:091119
50. Huang FM, Chen Y, de Abajo FJG, Zheludev NI (2007) Optical super-resolution through super-oscillations. *J Opt A Pure Appl Opt* 9:S285–S288
51. Huang FM, Kao TS, Fedotov VA, Chen YF, Zheludev NI (2008) Nanohole array as a lens. *Nano Lett* 8:2469–2472

Chapter 9

Transformation Optics and Electromagnetic Cloak of Invisibility

9.1 Invisibility and Transformation Optics: An Overview

This chapter elaborates on the possibility and approach of using metamaterials to achieve the ultimate optical illusion – invisibility. Invisibility is a longtime dream that may date back to the very beginning of human civilization. The concept of being unseen and hence undetectable has appeared numerous times in myths, legends, folklore and fiction as well as occurring in modern works such as movies, TV series and video games. For example, in the Greek mythology, the hero Perseus (son of Zeus) killed and beheaded Medusa (one of the Gorgons) when equipped with a helmet of invisibility. Also during the ancient Greek period, Plato described in his great work *The Republic* the ring of Gyges which could allow its owner to be invisible at will. This is one of the literary sources of many popular and similar subsequent stories, including the well-known book series and movie trilogy *The Lord of the Rings*.

All these stories, though fascinating to people for generations, have little to do with the physics of real life. In fact, nature and technology contain a number of cases where the phenomenon of invisibility is demonstrated to some extent. In order to proceed with our discussion of the range of schemes to obtain the desired invisibility effect, we first clarify what the word “invisibility” really implies. Literally, invisibility represents the state of an object staying in plain view of an observer without being seen. In the real world, the phenomena of being invisible may be grouped into a few categories, which we briefly mention next. An otherwise visible object can stay indiscernible from the surrounding environment due to similarities in colors or patterns. This is usually referred to as camouflage and is prevalent in the natural colorings of many animals. Another method of being undetectable is to prevent information about the object from reaching detectors (like radar). This is usually accomplished by using absorptive surfaces along with special shapes and materials, all intended to reduce the cross-section of the object against particular sources. This is the idea behind various stealth techniques. The ultimate version of invisibility is to make an object reflect no light and absorb no energy. That is, the object is given the same scattering properties as those of a vacuum. This last method of invisibility is the eventual goal of cloaking devices with electromagnetic metamaterials.

Camouflage can be classified into two types based on its adaptability in real time. Static camouflage exists universally among wild animals resulting from evolutionary pressure over generations. Many species exhibit colors or patterns that are similar to their surroundings, which allow to avoid predators or to sneak up on prey. This idea has been adopted by humans for many years for various purposes, especially in battledress. Active camouflage, which refers to the ability of an object to blend into its environment adaptively, allows concealment from visual observation in real time. Nature's famous examples are chameleons, which are able to change their skin color for various purposes such as camouflage, communication, and temperature control. A more convincing case of active camouflage in nature is observed in some species of octopi that can perfectly blend into their background by actively changing various skin properties including color, shape and texture. Man-made active camouflage effects have also been demonstrated using a camera-plus-projector scheme developed in the Tachi group at the University of Tokyo [1]. Their prototype camouflage system uses a camera placed behind an object to be hidden to record background images. Then, the recorded real-time background scene is processed by a computer and then projected onto the masked object. In this way, a see-through effect is achieved and an illusory transparency is obtained for the object.

Stealth technology, also known as low observability technology, is in a sense invisibility because it acts to prevent information about an object from returning to a detector such as a radar station. This field covers a range of techniques that render military vehicles less detectable. Generally speaking, stealth technology can refer to any technique that minimizes the visibility of objects to various observation schemes including radar, infrared or other detection methods. Because radar is today's primary detection method for military aircraft, the term "stealth technology" is usually used for a combination of schemes to suppress radar returns from aircraft. The overall objective of stealth technology is to minimize the reflection cross-section of the object. The techniques that have been adopted for this goal include the use of radar-absorbing coatings to reduce the reflectance, flat surfaces and sharp edges to reflect radar signals away from the detector, a non-metallic airframe to increase radar transparency, and so on. Noticeable examples of stealth aircraft include the F-117 Nighthawk and the B-2 Spirit bomber from the United States Air Force.

It is interesting to note that neither active camouflage nor stealth technology can provide the ideal effect of invisibility. A perfectly invisible device should exhibit the same scattering property as that of a vacuum. In other words, the device together with the object to be hidden should reflect no light and cast no shadow. Neither the illusionary see-through effect in the computer-mediated camouflage nor the reduced radar cross-section in stealth technology can offer the ultimate apparatus of invisibility. Fortunately, artificially structured metamaterials have enabled unprecedented flexibility in manipulating electromagnetic waves and producing new functionalities, and have brought the ancient dream one step closer to reality. During the last few years, increasing attention has been focused on creating an electromagnetic cloak of invisibility based on various schemes, including anomalous localized resonance [2-4], dipolar scattering cancellation [5, 6], tunneling light transmittance [7], sensors and active sources [8], and coordinate transformation [9, 10].

The transformation approach, which generalized a similar idea for conductivity cloaking [11, 12], has triggered enormous interest because the proposed device is supposed to render a macroscopic object invisible, and the design is not sensitive to the object that is being masked. In other words, cloaks based on transformation optics bear remarkable similarities to the mythological cloaks: a closed surface is created which renders arbitrary objects within its interior invisible to detection. The objective of this chapter is to discuss the principles of such devices and possible designs for cloaking at optical frequencies.

We emphasize that cloaking is only one topic within the broad context of transformation optics, which allows scientists to control the path of light in an unprecedented manner [13]. By creating complicated spatial distributions of the electric permittivity and magnetic permeability, we can curve optical space and mold the flow of light in many unusual ways. With transformation designs, we can create a hypothetical space with desired topological properties – a situation that looks quite similar to the curved time-space in the general relativity.

It is somewhat surprising to learn that the relationship between light propagation and effective space-time geometries was considered almost a century ago, for example, in early papers by Tamm [14, 15]. The basics of transformation optics are built on the fundamental results developed by Dolin [16], Post [17] and Lax–Nelson [18]. In his work, Dolin not only realized that Maxwell’s equations appear to be form-invariant under a space-deforming transformation, but also demonstrated deeper physical insight. He conceived a spherical inhomogeneity with a specific set of anisotropic permeability and permittivity tensors such that an incident plane wave can pass through the inhomogeneity without distortions – exactly the idea behind today’s transformation-based electromagnetic cloak. Unfortunately, these important early studies were not fully appreciated and were almost forgotten. Only recently has the field of transformation optics been reestablished [9, 10, 19–21].

Because of the form-invariance of Maxwell’s equations under coordinate transformations, we can design a functional device following an objective-oriented strategy. First, we apply a form-invariant transformation to Maxwell’s equations to distort and tailor real space in a desired manner in accordance with the required functionality. Second, the permittivity and permeability tensors needed to achieve the real space distortion are determined from coordinate transformations, and a usually inhomogeneous and anisotropic medium is specified. Finally, realistic design and fabrication constraints for the required material properties are incorporated to eventually realize the device. Note that the obtained material parameters from the second step are typically very complicated and are hard to synthesize using naturally occurring materials and conventional technologies. This is the major reason that the transformation approach has gained popularity only during the recent prosperity of metamaterial research.

Additionally, we should not underestimate the difficulty in achieving the specific material properties for any functional devices based on transformation optics. As of early 2009, various transformation-based devices have been proposed including an invisibility cloak, a magnifying far-field superlens [22], a beam shifter and splitter [23], a light beam rotator [24] and a planar focusing antenna [25], among others. However, most of the more interesting devices already proposed stop at the

second step discussed above and remain as only conceptual designs, with two notable exception being the experimental demonstrations of electromagnetic cloaks at microwave frequencies [26,27]. This an indication that metamaterial research is still in its infancy, and there is a large amount of work to be done before we can fully direct the electromagnetic fields in artificial structures at will.

9.2 Cloaking by Coordinate Transformation

At the root of transformation optics is the mathematical form-invariance of Maxwell's equations describing the interrelationships among fields, sources and materials. Let us first write down the standard differential form of the equations in a Cartesian coordinate system:

$$\begin{aligned}
 \nabla \cdot (\varepsilon \vec{E}) &= \rho \\
 \nabla \cdot (\mu \vec{H}) &= 0 \\
 \nabla \times \vec{E} &= -\mu \frac{\partial \vec{H}}{\partial t} \\
 \nabla \times \vec{H} &= \varepsilon \frac{\partial \vec{E}}{\partial t} + \vec{J}
 \end{aligned} \tag{9.1}$$

Here we avoid using the electric displacement field \vec{D} and the magnetic flux density \vec{B} to simplify the discussion. All notations in the equations follow the usual interpretation. The current density \vec{J} and the charge density ρ represent the sources of the system, and the permittivity ε and permeability μ are 3×3 tensors in the general case.

For an arbitrary coordinate transformation from the original Cartesian coordinate x to a new coordinate x' , the coordinate change can be described using the Jacobian matrix G consisting of all first-order partial derivatives $g_{ij} = \partial x'_i / \partial x_j$ (we avoided the standard notation J for the Jacobian to avoid possible confusion with the current density). Form-invariance implies an amazing property for Maxwell's equations: the form of Maxwell's equations in the new (primed) coordinate remains exactly the same as (9.1) as long as the set of transformations is applied to all the variables in the following manner [9,20]:

$$\varepsilon' = \frac{G \varepsilon G^T}{|G|}; \quad \mu' = \frac{G \mu G^T}{|G|}, \tag{9.2}$$

for materials properties, and

$$\vec{E}' = (G^T)^{-1} \vec{E}; \quad \vec{H}' = (G^T)^{-1} \vec{H} \tag{9.3}$$

for electromagnetic fields.

If free current and charges exist in the system, \vec{J} and ρ should also be renormalized as follows:

$$\vec{J}' = \frac{G\vec{J}}{|G|}; \rho' = \frac{\rho}{|G|} \quad (9.4)$$

where G^T and $|G|$ represent the transpose and determinant of the Jacobian matrix, respectively.

After all these transformations of variables as well as replacing the nabla symbol ∇ by its counterpart ∇' for the new system, the Maxwell's equations in the x' coordinate become identical to the Cartesian form given in (9.1). The proof of transformation-invariance is a bit involved and is out of the scope of this chapter. The interested reader may consult the related literature directly [20]. Note that the material properties (i.e., the permittivity and permeability tensors) for the new coordinate can also be obtained based on other methods of derivation, for example, starting from the Minkowski form of Maxwell's equations [28] or using the transformations of contra-variant tensors similar to the tools in general relativity [29].

To help readers obtain a better understanding of the basic concepts and implementation procedure of transformation optics, let us consider a simple example and show step-by-step procedures to obtain the required material parameters based on a specific desired functionality. Starting from a cylindrical region $r' \leq b$ in a cylindrical coordinate system (r', θ', z') , we try to transform the axis of the cylinder $r' = 0$ into a hollow region of $r \leq a$ in the new coordinates (r, θ, z) , as shown in Fig. 9.1. That is, we compress the region $r' \leq b$ in the old system into a concentric cylindrical shell of $a \leq r \leq b$ in the new coordinate system. Please note that from now on, we associate the prime symbol with the original system, while using the non-primed system for the new one. The reason why we make this change is because we will

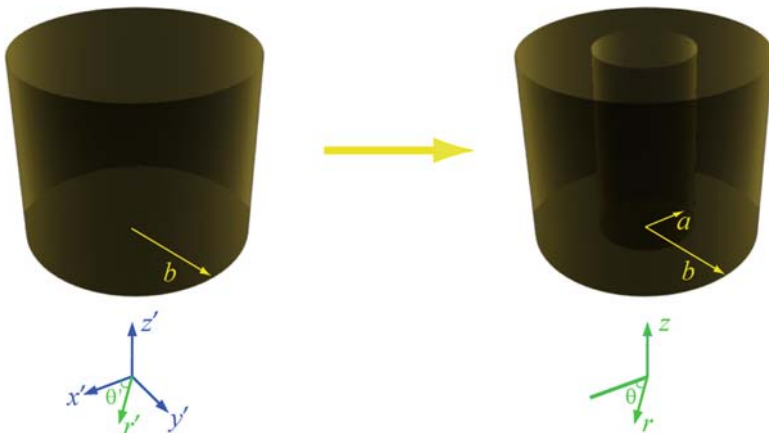


Fig. 9.1 The coordinate transformation that compress a cylindrical region of $r' \leq b$ in the old coordinate system (r', θ', z') into a concentric cylindrical shell of $a \leq r \leq b$ in the new coordinate system (r, θ, z)

discuss the properties and parameters for the new coordinate extensively throughout the rest of this chapter, so it is good to avoid superfluous prime symbols in the text and equations.

The simplest way to complete the spatial transformation in Fig. 9.1 is the following linear function:

$$r = (1 - a/b)r' + a \quad (9.5)$$

while the other two coordinates (θ , z) are left unchanged. With the given form of the transformation function, we can calculate the transformation coefficients

$$g_{ij} = \sum_l (\partial x_l / \partial q_i) (\partial x_l / \partial q_j) \quad (9.6)$$

from a Cartesian mesh ($x' = r' \cos \theta'$; $y' = r' \sin \theta'$; z') to the transformed system (r , θ , z).

The calculation of the transformation coefficients is much simpler than in a general case because the medium (free space) in the old coordinates is isotropic and homogeneous, and the Jacobian matrix is purely diagonal. The elements of the transformation matrix are:

$$\begin{aligned} h_r = \sqrt{g_{rr}} &= \left[\left(\frac{\partial x'}{\partial r} \right)^2 + \left(\frac{\partial y'}{\partial r} \right)^2 \right]^{1/2} = \left[\left(\frac{\partial x'}{\partial r'} \frac{\partial r'}{\partial r} \right)^2 + \left(\frac{\partial y'}{\partial r'} \frac{\partial r'}{\partial r} \right)^2 \right]^{1/2} \\ &= \frac{b}{b-a} \end{aligned} \quad (9.7a)$$

$$\begin{aligned} h_\theta = \sqrt{g_{\theta\theta}} &= \left[\left(\frac{\partial x'}{r \partial \theta} \right)^2 + \left(\frac{\partial y'}{r \partial \theta} \right)^2 \right]^{1/2} = \frac{1}{r} \left[\left(\frac{\partial x'}{\partial \theta'} \right)^2 + \left(\frac{\partial y'}{\partial \theta'} \right)^2 \right]^{1/2} \\ &= \frac{b}{b-a} \cdot \frac{r-a}{r} \end{aligned} \quad (9.7b)$$

$$h_z = \sqrt{g_{zz}} = \left[\left(\frac{\partial z'}{\partial z} \right)^2 \right]^{1/2} = 1 \quad (9.7c)$$

Based on these elements in the transformation matrix, we obtain the following permittivity and permeability components for the concentric cylindrical shell in the new coordinate system ($a \leq r \leq b$):

$$\varepsilon_r = \mu_r = \frac{h_\theta h_z}{h_r} = \frac{r-a}{r} \quad (9.8a)$$

$$\varepsilon_\theta = \mu_\theta = \frac{h_r h_z}{h_\theta} = \frac{r}{r-a} \quad (9.8b)$$

$$\varepsilon_z = \mu_z = \frac{h_r h_\theta}{h_z} = \left(\frac{b}{b-a} \right)^2 \cdot \frac{r-a}{r} \quad (9.8c)$$

The material parameters as functions of the radius r in the transformed coordinate are plotted in Fig. 9.2 for a representative case. During numerical simulations and

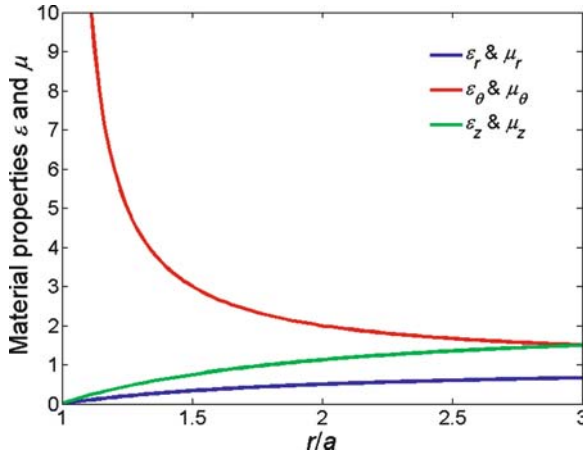


Fig. 9.2 The required material properties as functions of the radius r in order to complete the spatial transformation in Fig. 9.1 based on the linear transformation in (9.5). A shape factor of $a/b = 1/3$ is used in this example

experimental realizations, material parameters in Cartesian coordinates are sometimes required. The tensor components of permittivity in the (x, y, z) coordinate system are related to those in the cylindrical system (r, θ, z) as follows [30]:

$$\varepsilon_{xx} = \varepsilon_r \cos^2 \theta + \varepsilon_\theta \sin^2 \theta \quad (9.9a)$$

$$\varepsilon_{xy} = \varepsilon_{yx} = (\varepsilon_r - \varepsilon_\theta) \sin \theta \cos \theta \quad (9.9b)$$

$$\varepsilon_{yy} = \varepsilon_r \sin^2 \theta + \varepsilon_\theta \cos^2 \theta \quad (9.9c)$$

and the permeability components can be obtained following the same rule.

We should stress a few important features of the material properties in the new coordinate system. First, because there is nothing but a vacuum in the old coordinate system in our example, the tensors for the material in the new system are only dependent on the Jacobian of the transformation itself. Secondly, the permittivity and permeability tensors for the new coordinate system are identical because both tensors follow exactly the same transformations according to (9.2). Obviously, if the old system contains a uniform background permittivity of ε_b , all components of the permittivity tensor in the new system should be multiplied by this value. Most importantly, although the space prior to the transformation is merely a vacuum, the material for the new coordinate system is neither homogeneous nor isotropic. Actually, all components of the permittivity and permeability tensors are strong functions of r , and some extreme values occur like the infinite value of ε_θ and μ_θ at $r = a$ required by the transformations. The inhomogeneity and anisotropy in the transformed parameters are very general features in transformation optics, and they emphasize once again the basic pursuit of metamaterial research – the realization of material properties not observed in their constituent materials and are not found in nature. Devices and functionalities in transformation optics, after some basic mathematics, come down to a matter of metamaterial research.

The above example is not just a toy exercise. In fact, with this seemingly trivial example, we present one of the most important devices with transformation optics – an electromagnetic cloak in cylindrical coordinates. The inner cylindrical region in the new system is transformed from a volume-less line in uniform Cartesian coordinates; therefore no electromagnetic radiation can enter into the inner cylindrical space in the transformed system. Consequently, we can conceal an arbitrary object in the hollow region, and an external observer is unable to detect it electromagnetically. In short, it is a cloak of invisibility.

Using a similar technique, we can also create cloaking devices of other shapes such as a spherical cloak [9]. In this case, we need to open a hollow region of $r < a$ inside a spherical space of radius b in the original coordinates (r', θ', ϕ') . Like the linear transformation used in the cylindrical example, we use the same coordinate change $r = (1 - a/b)r' + a$ for r while keep θ and ϕ unchanged. The Jacobian matrix for this transformation and the rules in (9.2) require the following values for the permittivity and permeability components within the cloaking shell $a < r < b$:

$$\varepsilon_r = \mu_r = \frac{b}{b-a} \left(\frac{r-a}{r} \right)^2 \quad (9.10a)$$

$$\varepsilon_\theta = \mu_\theta = \frac{b}{b-a} \quad (9.10b)$$

$$\varepsilon_\phi = \mu_\phi = \frac{b}{b-a} \quad (9.10c)$$

For both the cylindrical and the spherical cloaking devices, the material properties outside the external surface at $r = b$ remain identical to those before the coordinate transformation. In our examples, the external material is vacuum. Inside the cloaked region $r < a$, the permittivity and permeability are free to assume any values because they do not give any contribution to the overall scattering properties of the system. As a result, an arbitrary object can be hidden inside the cloaked region (as long as the size fits), and the electromagnetic scattering of the whole system including the annulus-shaped cloak and any object inside it is identical to the scattering properties of vacuum. This intriguing feature sets the transformation-based cloaking device apart from other schemes proposed for invisibility [2–8], which usually rely on a priori knowledge of the object to be concealed.

Now let us briefly address the uniqueness theorem of electromagnetic scattering, which touches on the fundamental possibility of a perfect cloak of invisibility. We argued above that the scattering properties of the whole cloaking system are identical to that of a vacuum. Such a claim, however, seems to conflict with the uniqueness of the inverse scattering problem, which indicates that any given electromagnetic field distribution would uniquely determine the boundary conditions [31, 32]. In fact, the uniqueness theorem of scattering applies only to isotropic media, while the material properties of cloaking devices are necessarily inhomogeneous and anisotropic [26]. Therefore, it is theoretically allowed that two distinct systems, one a vacuum and the other a cloak, share the same non-scattering properties.

The ray trajectories inside a spherical cloak with material parameters given in (9.10) are illustrated in Fig. 9.3 (from [9]). The incident plane wave enters the

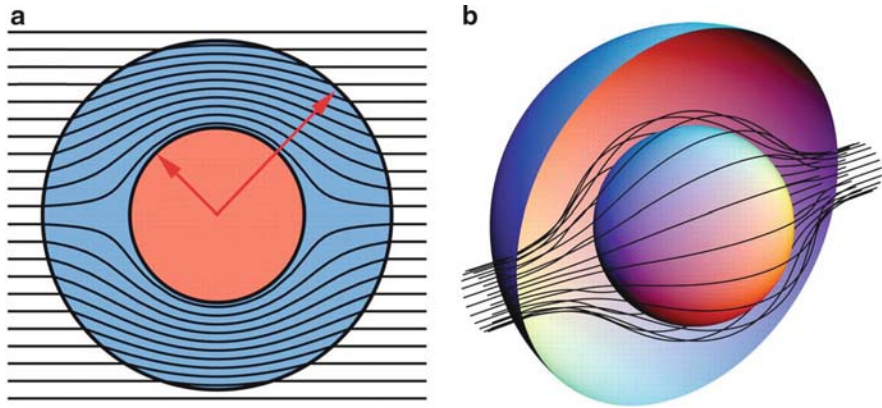


Fig. 9.3 The wave trajectories of a spherical cloaking system with material properties specified in (9.10). (a) A two-dimensional cross sectional view; (b) a three-dimensional view. Reprinted from [9] with permission from AAAS

concentric shell and flows smoothly around the cloaked region due to the specific gradient in the ε and μ components of the cloaking shell. After the inner sphere, the wave distortion is fully recovered and eventually exits the system as plane wave again. The fields outside the cloaking device contain no information about the whole system including anything hidden inside the cloaked region. Hence, electromagnetically, the device is completely invisible and undetectable to an external observer.

It is worth noting that the concept of using a gradient in the material properties to control the light path is not a new invention. There is actually an example of (partial) invisibility in nature due to a gradient in the refractive index of air. Above the surface of a desert radiated by the scorching sun, the refractive index of the hot and rarefied air right above the desert surface is smaller than that of the comparatively cooler air away from the ground. As a result, light rays from above may bend away from the sand surface before reaching the eyes of a desert traveler. Thus, the gradient in the refractive index of the air explains the cause of the inferior mirage occurring in deserts, which create illusive images of lakes (actually, the image of blue sky) and forests that deceive travelers. Moreover, there is an “invisible” region below and in front of our observer because, when he looks in that direction, he actually receives light rays from above and in front of him.

9.3 Towards Experimental Demonstrations

With all these fascinating features of electromagnetic cloaks based on transformation optics, one natural question arises: how can we really build such a cloak of invisibility? From an application point of view, the construction of an electromagnetic cloak implies that we need to elaborate realistic structures and materials to

fulfill the set of parameters corresponding to any types of cloak, like the properties required by (9.8) or (9.10). Although recent studies on electromagnetic metamaterials have provided unprecedented control over the material properties, it is still quite challenging, if not impossible, to exactly fulfill the material parameters governed by a particular form of the coordinate transformation. Taking the cylindrical cloak as an example, we see from Fig. 9.2 that continuous variations in the anisotropic parameters of both ε and μ are required within the concentric region. As detailed in Chap. 2, it is challenging to achieve any effective magnetic response at frequencies of gigahertz and above, let alone the well-controlled magnetic permeability distributed in a particular fashion. Furthermore, although magnetic responses at microwave or optical frequencies have been demonstrated using artificial “meta-atoms” like split-ring resonators, coupled nanowires or paired nanostrips, controlling all the components of the permeability tensor simultaneously in an anisotropic metamaterial is probably beyond the capability of current metamaterial research. Additionally, there are singularities in some parameters of the constitutive material of the cloak; for example, the infinite values of ε_θ and μ_θ at the inner boundary $r = a$ of a cylindrical cloak are singularities. Such extreme values along with the rapid changes in the material parameters are hardly realistic.

To ease the harsh requirements in the anisotropic spatial variations of the constitutive parameters, we can consider a cloaking device that will work for only a particular state of polarization. Let us again use the cylindrical cloak as an example. The desired material properties with the ε and μ tensors given in (9.8) imply complicated distributions of all components of both tensors. Such parameters, when fulfilled perfectly, would provide cloaking performance for any external incident field with arbitrary propagation direction and an arbitrary polarization state. For the standard incident polarizations (TE and TM), the requirement in (9.8) can be relaxed such that only three of the six components are relevant. For example, with TE polarization (electric field polarized parallel to cylinder axis), only ε_z , μ_r and μ_θ enter into Maxwell’s equations. Moreover, the parameters can be further simplified to form reduced parameters which are more realistic for practical applications. Since the trajectory of the waves is determined by the dispersion relation, and, therefore, by the cross-product components of the ε and μ tensors instead of the two tensors individually, the cloaking operation is sustained as long as $n_\theta = \sqrt{\varepsilon_z \mu_r}$ and $n_r = \sqrt{\varepsilon_z \mu_\theta}$ are kept the same as those determined by the values in (9.8). A rigorous proof of the last claim is available in Ref. [26] and the supporting materials therein.

Following the guidelines for the simplification of the constitutive parameters given above, we can force the angular component μ_θ of the permeability tensor in (9.8) to be unity and obtain the following material properties for TE incident wave polarization [26]:

$$\mu_r = \left(\frac{r-a}{r}\right)^2; \mu_\theta = 1; \varepsilon_z = \left(\frac{b}{b-a}\right)^2 \quad (9.11)$$

Equation (9.11) shows that the simplification procedure results in a set of reduced parameters that allow for a permeability gradient only along the radial direction. No

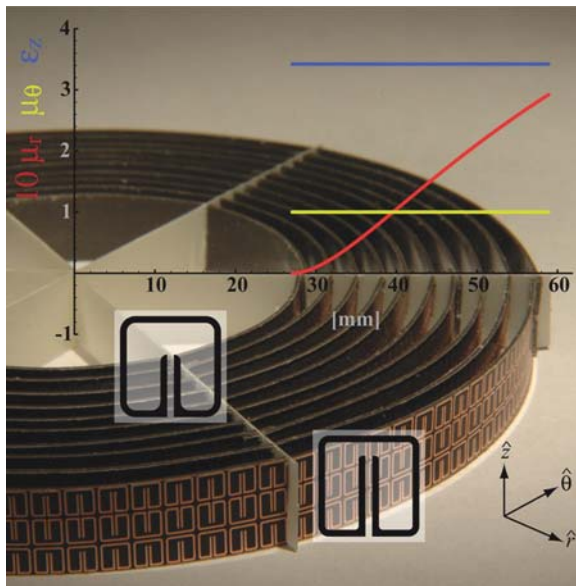


Fig. 9.4 Structure of the cylindrical cloaking device at a microwave frequency along with plot of the material properties μ_r , μ_θ and ε_z that are implemented. Reprinted from [26] with permission from AAAS

magnetic response is necessary for the azimuthal permeability component, and the permittivity along the vertical direction ε_z is a constant that is larger than one.

Now that we have simplified the material specifications, the next step is to construct a metamaterial with specific dimensions, unit cells, and constituent materials to obtain spatial variations in the material parameters as necessitated by (9.11). In the first experimental demonstration of a cylindrical cloak at microwave frequencies [26], the device was made up of ten concentric dielectric cylinders filled with copper split-ring resonators, as shown in Fig. 9.4. The SRRs are placed in the $\theta-z$ plane, so they exhibit a magnetic resonance within a predesigned frequency range when there is a magnetic flux component along the radial direction. The strength of the magnetic response and the value of the effective radial permeability μ_r are determined by the geometry and density of the unit cells. Therefore, the magnetic permeability μ_r can be tuned by varying the dimensions of the SRRs, and the required gradient in μ_r in (9.11) can be achieved. During the design, all the geometrical parameters of SRRs, including the curvature at the corners of each loop, must be adjusted very carefully to realize quasi-independent control of both μ_r and ε_z . Such fine control enables a constant value of ε_z while tuning the value of μ_r from 0 at the inner layer to $(1 - a/b)^2$ at the outer surface of the cylindrical cloak. As for the azimuthal permeability μ_θ , since the SRRs exhibit no effective magnetic response with in-plane magnetic flux, μ_θ remains at the value of 1 throughout the device. The three constitutive parameters are also plotted in Fig. 9.4. (from [26]).

The operating frequency of the device in Fig. 9.4 is 8.5 GHz, which corresponds to a free-space wavelength of 3.5 cm. The edge length of each SRR is 3 mm, which is less than 1/10 of the free-space wavelength. Hence the structure is indeed a metamaterial device. In order to evaluate the degree to which the structure approximates a cloak at the targeted microwave frequency, the cylindrical device is placed in a parallel plate waveguide comprising two conducting plates separated by the height of the cloak, which is roughly one half of the wavelength inside the cloaking material. In this case the propagating properties of the electromagnetic wave can mimic that of a plane wave incident upon a two dimensional cylindrical cloak extended infinitely along the direction of its axis. The apparatus in Ref. [26] used to test the cloak design was able to perform field maps, so both the amplitude and the phase of the electric field inside the planar waveguide were measured as polarized microwaves were directed toward the device. In the experiment, the electric field patterns were measured with a conducting cylinder placed inside the cloaked region, and these fields were compared against the case of a bare, unshielded copper cylinder. The result is shown in Fig. 9.5 (from [26]). With a bare metal cylinder as the scatterer (Fig. 9.5a), the incident waves were scattered, and the wave front after the object is substantially distorted, which represents the shadow of the object. When the object is surrounded by the cloaking shell (Fig. 9.5b), the perturbation of the microwaves by the system is alleviated. The result, although not a perfect demonstration of invisibility, confirmed the feasibility of creating a cloaking device using metamaterials, and it verified the bending and recovery of waves due to a gradient in the material properties. In addition, the device significantly suppressed both the backward and forward scattering of the incident waves, which is a clear indication of the cloaking capability. This demonstration accomplished by engineers at Duke University was the first experimental validation of electromagnetic cloaking; it has drawn enormous media interest and was named one of the top ten breakthroughs of 2006 [33].

Within our discussion of the realization of an electromagnetic cloak, let us briefly address the issue of operational bandwidth, which is of both theoretical value and practical interest. In the equations up to this point in this chapter, the frequency

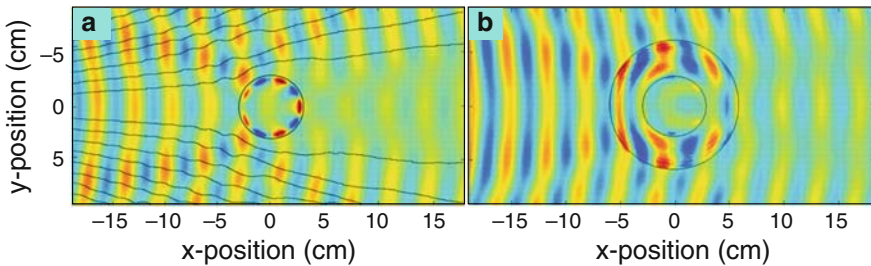


Fig. 9.5 Snapshots of time-dependent, steady-state electric-field patterns in an electromagnetic cloak design. (a) Experimental measurement the field pattern with an unshielded copper cylinder. (b) Experimental measurement of the copper cylinder surrounded by the cloaking device. The stream lines in (a) indicates the direction of power flow. Reprinted from [26] with permission from AAAS

dependence of the material parameters is not taken into account. The bandwidth of a transformation-based cloaking device is determined by the frequency range over which the material properties in (9.8), (9.10) or (9.11) are exactly satisfied. Unfortunately, the curved trajectory of light within the cloak implies a refractive index n of less than 1 in order to satisfy the minimal optical path requirement of Fermat's principle, but any metamaterial with $n < 1$ must be dispersive to fulfill causality. In other words, since the phase velocity in the cloaking material is larger than the speed of light, dispersion is necessary to avoid a superluminal group velocity, which is strictly forbidden except for the case of strong anomalous dispersion where substantial loss occurs. In addition, theoretical analysis shows that the anisotropic cloaking parameters required by a given transformation can be precisely fulfilled only for a single frequency value [34]. Therefore any shell-type cloak design can work only over a very narrow frequency range. It is also revealed that there might be a solution for this fundamental bandwidth constraint based on a multiple, "cascaded" cloaks designed for different wavelengths [35], using a complicated combination of techniques including dispersion control, dynamic transformation and active medium. In Sect. 9.7, we will discuss several alternative schemes for the realization of broadband, low-loss cloaks operating at optical frequencies.

9.4 Non-magnetic Optical Cloak

The experimental demonstration of the microwave cloak confirmed the feasibility of cloaking devices using the transformation approach. However, the design used in Ref. [26] cannot be implemented for an optical cloak, which is certainly of particular interest because optical frequencies are where the word "invisibility" is conventionally defined. The reported microwave cloak in Ref. [26] used a set of simplified parameters specified in (9.11), and the required gradient in the radial permeability was achieved by varying the dimensions of a series of SRRs. As for optical wavelength range, it is a known fact that there are intrinsic limits to the scaling of SRR size in order to exhibit a magnetic response in the visible spectrum [36, 37]. Replacing the SRRs with other optical magnetic structures like paired nano-rods [38] or nano-strips [39] is also a very challenging approach because magnetism based on such resonant plasmonic structures is usually associated with a high loss factor, which is detrimental to the performance of cloaking devices.

The requirement of optical magnetism can be avoided if we consider just a particular polarization of incidence. In contrast to the design of a microwave cloak with TE polarization as shown in the previous section, we focus on TM incidence with the magnetic field polarized along the z axis of a cylindrical system [40], as shown in Fig. 9.6a. In this case only μ_z , ε_r and ε_θ must satisfy the requirements in (9.8), and the dispersion relations inside the cloak remain unaffected as long as the products of $\mu_z\varepsilon_r$ and $\mu_z\varepsilon_\theta$ are kept the same as those determined by the values in (9.8). It is worth noting that under TM illumination only one component of μ is of interest, which allows us to completely remove the need for any optical magnetism. In (9.8)

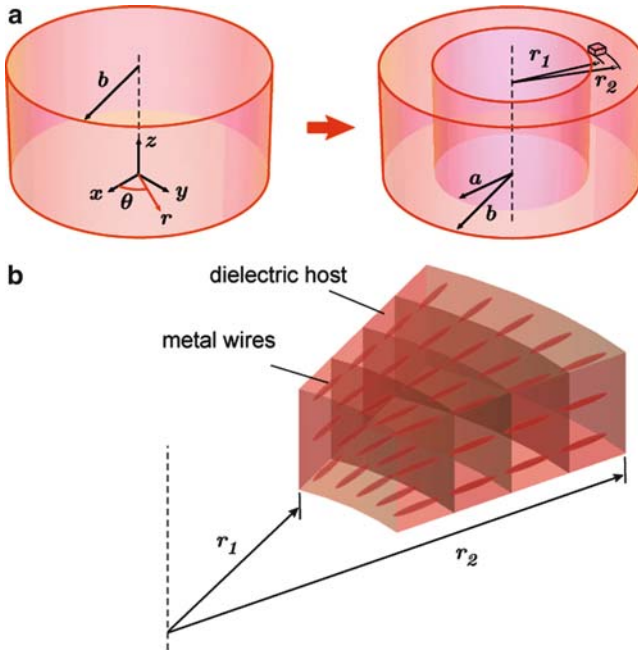


Fig. 9.6 Coordinate transformation and structure of the designed non-magnetic optical cloak. (a) The coordinate transformation that compresses a cylindrical region $r < b$ into a concentric cylindrical shell $a < r < b$. There is no variation along the z direction. (b) A small fraction of the cylindrical cloak

we multiply ε_r and ε_θ by the value of μ_z and obtain the following reduced set of cloak parameters:

$$\mu_z = 1, \quad \varepsilon_\theta = \left(\frac{b}{b-a}\right)^2, \quad \varepsilon_r = \left(\frac{b}{b-a}\right)^2 \left(\frac{r-a}{r}\right)^2. \quad (9.12)$$

Compared to the cloak with ideal properties as shown in (9.8), the reduced parameters in (9.12) provide the same wave trajectory. The only adverse effect of using the reduced set is the non-zero reflection due to the impedance mismatch at the outer boundary. The ideal parameters in (9.8) result in a perfectly-matched impedance of $Z = \sqrt{\mu_z/\varepsilon_\theta} = 1$ at $r = b$, while the reduced set in (9.11) produces an impedance at the outer boundary of $Z = 1 - R_{ab}$, where $R_{ab} = a/b$ denotes the ratio between the inner and outer radii. Therefore, the level of power reflection due to reduced parameters can be estimated as $|(1 - Z)/(1 + Z)|^2 = [R_{ab}/(2 - R_{ab})]^2$.

The non-magnetic nature of the system as indicated in (9.12) removes the most challenging issue of the design. The azimuthal permittivity ε_θ is a constant with a magnitude larger than 1, which can be easily achieved in conventional dielectrics. The key to the implementation is to construct the cylindrical shell with the desired radial distribution of ε_r varying from 0 at the inner boundary of the cloak ($r = a$)

to 1 at the outer surface ($r = b$). The required distribution of ε_r in the design can be realized by using metal wires of subwavelength size in the radial direction embedded in a dielectric material, as shown in Fig. 9.6b. The aspect ratio of the metal wires, defined by the ratio of the length to the radius of the wire, is denoted by α . The spatial positions of the wires don't have to be periodic and can be random. Also, for large cloaks, the wires can be broken into smaller pieces that are smaller in size than the wavelength.

The shape-dependent electromagnetic response of a subwavelength particle such as the metal wire in Fig. 9.6b can be characterized by the Lorentz depolarization factor L and the screening parameter, as given in (2.40) and (2.43). Note that a long wire with large aspect ratio α along the electric field results in a small depolarization factor and a large screening factor, which indicates strong interactions between the field and the wires. For a composite cloak with metal wires as inclusions in a dielectric, the electromagnetic properties are well-described by “shape-dependent” effective-medium theory (EMT) as discussed in Sect. 2.4. The effective permittivity ε_{eff} for a composite material comprising metal particles with permittivity ε_m , a volume filling factor f and screening factor κ , along with a dielectric component with permittivity ε_d and a filling factor $1 - f$, is given by (2.42) with the solution:

$$\varepsilon_{eff} = \frac{1}{2\kappa} \left\{ \bar{\varepsilon} \pm \sqrt{\bar{\varepsilon}^2 + 4\kappa\varepsilon_m\varepsilon_d} \right\} \quad (9.13)$$

where $\bar{\varepsilon} = [(\kappa + 1)f - 1]\varepsilon_m + [\kappa - (\kappa + 1)f]\varepsilon_d$, and the sign in (9.13) should be chosen such that $\varepsilon_{eff}' > 0$.

The benefit of using metal wires in a composite cloak is that the radial permittivity ε_r determined by (9.13) may exhibit a positive value less than 1 with minimal imaginary part. For the structure in Fig. 9.6b, the filling fraction in (9.13) for calculating ε_r is $f(r) = f_a \cdot (a/r)$, with f_a being the filling fraction of metal at the inner surface of the cloak. The azimuthal permittivity ε_θ inside the cloak is essentially the same as that of the dielectric because the response of the wires to the angular electrical field E_θ oriented normal to the wires is small and at low metal filling factors it can be neglected.

The reduced set of cloak parameters in (9.12) requires a smooth variation of the radial permittivity from 0 to 1 as r changes from a to b . For optimal performance, $\varepsilon_{eff,r}$ should exactly follow the function described in (9.12) such that

$$\varepsilon_{eff,r}(f_a \cdot a/r) = [b/(b - a)]^2 [(r - a)/r]^2. \quad (9.14)$$

In a practical design, $\varepsilon_{eff,r}$ is allowed to have some discrepancy from the optimal value inside the cloak. The most important points are at the inner and outer surfaces of the cloak, where (9.14) should be satisfied exactly. This ensures the desired wave trajectory at $r = b$ and the minimum leakage energy at $r = a$.

To determine all of the parameters of the design shown in Fig. 9.6b, we define two filling fraction functions $f_0(\lambda, \alpha)$ and $f_1(\lambda, \alpha)$ such that for given constituent composite materials and a wire aspect ratio of α , the effective radial permittivity is

$$\begin{cases} \varepsilon_{eff,r}(\lambda, f_0(\lambda, \alpha)) = 0 \\ \varepsilon_{eff,r}(\lambda, f_1(\lambda, \alpha)) = 1 \end{cases} \quad (9.15)$$

Combining (9.14) and (9.15), at the operational wavelength λ we obtain

$$\begin{cases} f_0(\lambda, \alpha) = f_a \\ f_1(\lambda, \alpha) = f_a \cdot a/b \end{cases} \quad (9.16)$$

Hence we can express the shape factor R_{ab} as

$$R_{ab} = a/b = f_1(\lambda, \alpha)/f_0(\lambda, \alpha). \quad (9.17)$$

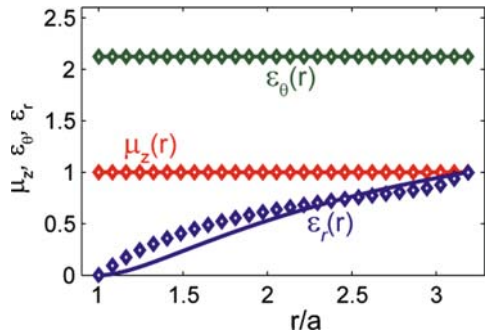
Using (9.17) with the expression for ε_θ in (9.12), we obtain the operating condition of the cloak:

$$\varepsilon_\theta(\lambda) = \left(\frac{f_0(\lambda, \alpha)}{f_0(\lambda, \alpha) - f_1(\lambda, \alpha)} \right)^2. \quad (9.18)$$

For practical applications, it is important to design a cloaking device operating at a pre-set operational wavelength λ_{op} . For this purpose the design process is as follows. First we choose materials for the metal wires and the surrounding dielectric. Second, we calculate the values of f_0 and f_1 as functions of the aspect ratio α at λ_{op} using the EMT model in (9.13). The required aspect ratio for λ_{op} is the one that satisfies (9.18). Then, the geometrical factors of the cloak, including R_{ab} and f_a , can be determined based on (9.16) and (9.17). Note that the same design works for all similar cylindrical cloaks with the same shape factor R_{ab} .

As a practical example, we have designed an optical cloak operating at the wavelength of 632.8 nm (He–Ne laser) and consisting of silver and silica. Equations (9.13), (9.15) and (9.18) together yield the desired aspect ratio $\alpha = 10.7$, and the filling fractions at the two boundaries are $f_a = 0.125$ and $f_b = 0.039$, respectively. Then with (9.16) and (9.17) we find the shape factor of the cylindrical cloak to be $R_{ab} = 0.314$. The effective parameters of μ_z , ε_r and ε_θ from this design together with the exact set of reduced parameters determined by (9.12) are shown in Fig. 9.7. We can see that μ_z and ε_θ perfectly match the theoretical

Fig. 9.7 Material parameters ε_r , ε_θ and μ_z of the proposed cloak operating at $\lambda = 632.8$ nm. The *solid lines* represent the exact set of reduced parameters determined by (9.12). The *diamond markers* show the material properties of the designed metal wire composite cloak with parameters obtained from (9.13) to (9.18)



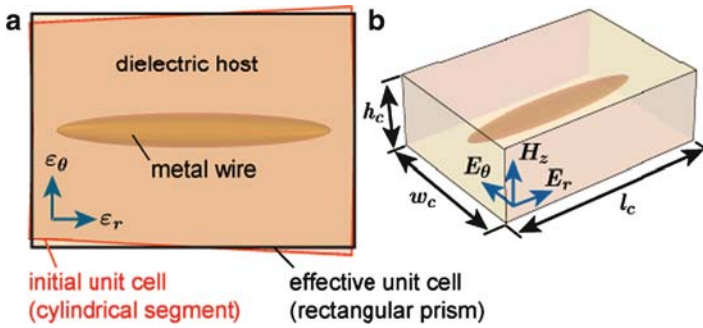


Fig. 9.8 Unit cell for full-wave finite-element simulations of effective parameters. (a) The actual unit cell (cylindrical sector) encapsulating a spheroidal silver wire is substituted by a cell made of a right rectangular prism. (b) The geometry of the 3D rectangular unit cell. In simulations h_c and l_c are fixed, while w_c changes in proportion to the radius of each layer

requirements throughout the cylindrical cloak. The radial permittivity ϵ_r fits the values required by (9.12) exactly at the two boundaries of the cloak, and follows the overall tendency very well inside the cloak.

To validate if the required distribution of permittivity could be achieved using prolate spheroidal silver nanowires embedded in a silica tube, we determine the effective anisotropic permittivity of a unit cell with sub-wavelength dimensions. We start with a homogenization method, where the actual unit cells (cylindrical sectors) with different electromagnetic surroundings are substituted by cells made of right rectangular prisms, as shown in Fig. 9.8. The full-wave finite-element (FE) numerical analysis confirms that the range of desired ϵ_r and ϵ_θ fits rather well with those predicted by EMT. The FE modelling also shows that the dependence of ϵ_r and ϵ_θ can match exactly those required by (9.12) through additional adjustment of the aspect ratio and the volume fraction of the nanowires in each layer. As for the loss feature, the FE simulations show that the radial permittivity ϵ_r has an imaginary part of about 0.1 throughout the cloak. Although this is a very small value for metal-dielectric metamaterials, it may still weaken the cloaking effect. It is possible to compensate the loss by using a gain medium as already proposed for applications of perfect tunnelling transmittance [7] and lossless negative-index materials [41].

To illustrate the performance of the proposed non-magnetic optical cloak with a design corresponding to Fig. 9.6 at $\lambda_{op} = 632.8$ nm, we performed field mapping simulations using a commercial FE package (COMSOL Multiphysics). The object hidden inside the cloak is an ideal metallic cylinder with radius $r = a$. The simulation model consisted of the cylindrical cloak identical to the one shown in Fig. 9.6 with TM polarized waves. The simulation domain also consisted of PML layers at all the boundaries to absorb the outgoing waves. The simulated results of magnetic field distribution around the cloaked object together with the power flow lines are illustrated in Fig. 9.9. We note that the size of the cloak is more than six times the operational wavelength, while the simulated area is more than 20 times the wavelength. Figure 9.9a shows the field distribution around the metal cylinder surrounded by the designed cloak with parameters given by the diamond markers in

Fig. 9.9 Finite-element simulations of the magnetic field mapping around the cloaked object with TM illumination at $\lambda = 632.8$ nm. (a) The object is inside the designed metal wire composite cloak with parameters given by the diamond markers in Fig. 9.7. (b) The object is surrounded by vacuum without the cloak

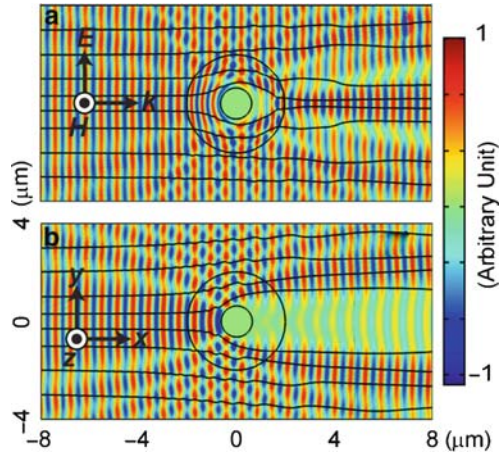


Fig. 9.7. With the cloak (Fig. 9.9a) the wave fronts flow around the cloaked region with remarkably small perturbation, while without the cloak (Fig. 9.9b) the waves around the object are severely distorted and an evident shadow is cast behind the cylinder. In the designed system with $R_{ab} = 0.314$, the estimated power reflection is about 4% when one uses the reduced set of parameters given by (9.12). This is a low level of reflection, and the small value is consistent with what we observe in simulations. Thus, our simulations clearly show the capability of reducing the scattering from the object hidden inside the cloaked region.

In this section we have demonstrated a design of an optical cloak based on coordinate transformation. The non-magnetic nature of our design eases the pain of constructing gradient magnetic metamaterials in three-dimensional space, and therefore paves the way for the realization of cloaking devices at optical frequencies. The proposed design can be generalized to cloaks with other metal structures, such as chains of metal nanoparticles or thin continuous or semi-continuous metal strips. It can be also adopted for other than the optical spectral ranges, including the infrared and the microwave. We note that the achievable invisibility with the proposed cloak is not perfect due to impedance mismatch associated with the reduced material specifications and the inevitable loss in a metal-dielectric structure. However, we believe that even rudimentary designs and implementations of an optical cloak are of great potential interest and bring us one step closer to the ultimate optical illusion of invisibility.

9.5 Cloaking with High-Order Transformations

As we have described in the previous two sections, in an electromagnetic cloak based on a transformation approach, reduced sets of material properties are generally favored due to their easier implementation in reality, although a seemingly

inevitable drawback of undesired scattering exists in such cloaks [26]. The major detrimental effect of using the non-simplified parameters as compared to the perfect set is the non-zero scattering due to impedance mismatch at the outer surface of the cloaking system. In this section we suggest using high-order transformations to create smooth moduli at the outer boundary of the cloak, therefore completely eliminating the detrimental scattering within the limit of geometric optics [42].

Again, let us consider a coordinate transformation where a cylindrical region $r' \leq b$ is compressed into a concentric cylindrical shell $a \leq r \leq b$, as shown in Fig. 9.1. Mathematically, there are countless ways to perform the spatial transformation. In most reported literature on this topic [9, 26, 30, 40], a linear transformation function in the form of (9.5) is used for this purpose. This linear transformation, although straightforward and intuitive, prohibits any flexible control of the associated moduli. As a result, impedance mismatching and undesired scattering are inevitable for cloaks using any form of reduced parameters, including the demonstrated microwave cloak in Ref. [26] for TE incidence and the designed optical cloak in Ref. [40] for TM polarization.

This scenario, however, can be dramatically changed when using a high-order transformation instead of the linear one. We may conceive any possible transformation function $r = g(r')$ from (r', θ', z') to (r, θ, z) in order to compress the cylindrical region $r' \leq b$ into a concentric shell. We allow several flexible variables in the expression of $g(r')$ for further adjustments as detailed later. With the given form of the transformation, we calculate the Jacobian matrix for this coordinate change, and based on the techniques described in Refs. [9, 28], the permittivity and permeability tensors can be determined as well:

$$\begin{aligned}\varepsilon_r &= \mu_r = (r'/r) \partial g(r') / \partial r'; & \varepsilon_\theta &= \mu_\theta = 1/\varepsilon_r; \\ \varepsilon_z &= \mu_z = (r'/r) [\partial g(r') / \partial r']^{-1}.\end{aligned}\quad (9.19)$$

For the linear transformation, the material parameters in (9.19) reduce to the simple forms given in Refs. [26, 30]. Note that for a closed-form expression of the parameters in (r, θ, z) space, all r' in (9.19) should be replaced by $r' = g^{-1}(r)$. From the expressions in above we can see that the impedance at the outer boundary is perfectly matched, that is, $\sqrt{\mu_\theta/\varepsilon_z}\Big|_{r=b} = \sqrt{\mu_z/\varepsilon_\theta}\Big|_{r=b} = 1$, which is an important feature of an ideal cloak.

From the material properties of an exact cloak, the corresponding reduced parameters can be obtained [26, 40]. As shown in the previous section, a non-magnetic cloak is of particular interest at optical frequencies due to the absence of optical magnetism in nature. We focus on TM incidence with the magnetic field polarized along the z axis. In this case only μ_z , ε_r and ε_θ enter into Maxwell's equations. To simplify the ε and μ tensors while maintaining the wave trajectory inside the cylindrical shell, in (9.19) we multiply ε_r and ε_θ by μ_z and obtain the following reduced set of non-magnetic cloak parameters:

$$\varepsilon_r = (r'/r)^2; \quad \varepsilon_\theta = [\partial g(r') / \partial r']^{-2}; \quad \mu_z = 1; \quad (9.20)$$

Similarly, for the TE polarization, the required parameters for a general transformation are:

$$\mu_r = (r'/r)^2 [\partial g(r')/\partial r']^2; \mu_\theta = 1; \varepsilon_z = [\partial g(r')/\partial r']^{-2} \quad (9.21)$$

From (9.20) we calculate the impedance at the outer boundary:

$$Z|_{r=b} = \sqrt{\mu_z/\varepsilon_\theta}|_{r=b} = \partial g(r')/\partial r'. \quad (9.22)$$

And the impedance for the TE mode has the same form as (9.22). In the rest part of this section we will focus on the TE mode, but we should keep in mind that the approach below applies to both TM and TE cases.

By setting it equal to unity, we can fix the function $g(r')$ together with all the material properties, and a non-magnetic cloak with minimized scattering is achieved. The perfectly matched impedance also indicates $(\partial r/\partial r')|_{r=b} = 1$. This smooth modulus at the outer surface removes the discontinuity and minimizes the scattering after the high-order transformation.

Following the implementation guidance described above, we consider a quadratic transformation function with one flexible parameter p :

$$r = g(r') = [1 - a/b + p(r' - b)]r' + a. \quad (9.23)$$

We see that the boundary confinements $g(0) = a$ and $g(b) = b$ are fulfilled. By setting $Z|_{r=b} = 1$, we fix the flexible variable $p = a/b^2$ and obtain the following optimal transformation:

$$r = g(r') = [(a/b)(r'/b - 2) + 1]r' + a. \quad (9.24)$$

All non-magnetic material properties can be determined consequently using (9.20). To make sure that the transformation is monotonic, we require a shape factor $a/b < 0.5$.

As an example, Fig. 9.10 shows the anisotropic material properties of two non-magnetic cylindrical cloaks with $p = a/b^2$ (optimal quadratic transformation) and $p = 0$ (linear transformation) respectively. The shape factor in this example is $a/b = 0.31$. In the optimal quadratic case, all three material parameters ε_r , ε_θ and μ_z are equal to unity at the outer boundary $r = b$, which perfectly matches the surrounding vacuum parameters.

To compare the performance of the non-magnetic cloaks with different transformation methods, we conduct field-mapping simulations using the finite-element package COMSOL Multiphysics. The cloaking systems are examined at $\lambda = 632.8$ nm with the same geometry as that in Fig. 9.10. The object hidden inside the cloaks is an ideal metallic cylinder with a radius the same as that of the inner surface. In Fig. 9.11, under four circumstances we plot the magnitudes of the normalized scattered field. The scattered field from the object itself is shown in Fig. 9.11a. The strong forward scattering at the right-hand side corresponds to the

Fig. 9.10 Anisotropic material parameters ε_r , ε_θ of two non-magnetic cloaks with $p = a/b^2$ (optimal quadratic transformation, *solid lines*) and $p = 0$ (linear transformation, *dashed lines*). μ_z equals unity in both cases. The shape factor (a/b) in this example is 0.31 and the diameter ($2b$) is $4\ \mu\text{m}$. Reprinted with permission from [42]. Copyright (2007), American Institute of Physics

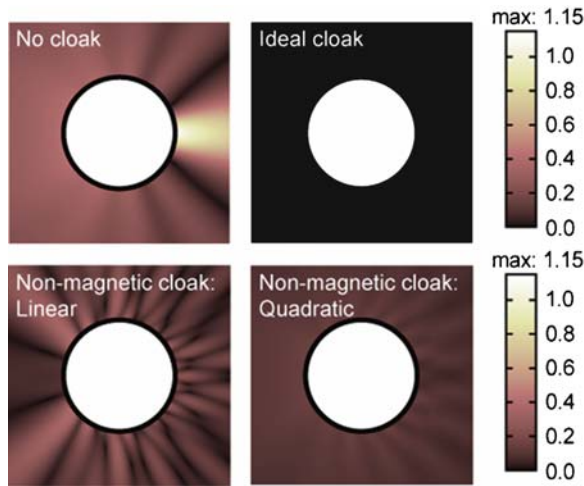
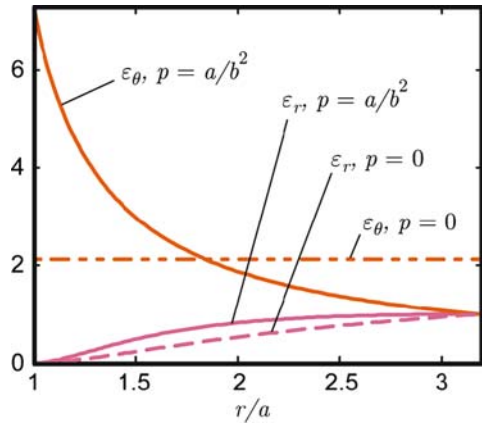


Fig. 9.11 Full-wave field-mapping simulations of the magnitudes of normalized scattered field for a metal cylinder inside (a) a vacuum without any cloak; (b) an ideal linear cloak; (c) the linear non-magnetic cloak with $p = 0$ and (d) the optimal quadratic cloak with $p = a/b^2$. Reprinted with permission from [42]. Copyright (2007), American Institute of Physics

shadow cast behind the object. The scattered field outside an ideal cloak is illustrated in Fig. 9.11b, which is essentially zero in magnitude. The results of non-magnetic cloaks for both the linear transformation and the optimal quadratic case are illustrated in Fig. 9.11c and d, respectively. The linear case exhibits an evident scattering pattern from the outer boundary of the system because of the impedance mismatch. On the other hand, the quadratic transformation function results in negligible scattering from the cloaking system. The figure of merit for cloaking (defined as the ratio of the scattering cross-sections without and with the cloak) is about 10 for the considered quadratic cloak, and it increases towards infinity with the size of the cloaking system.

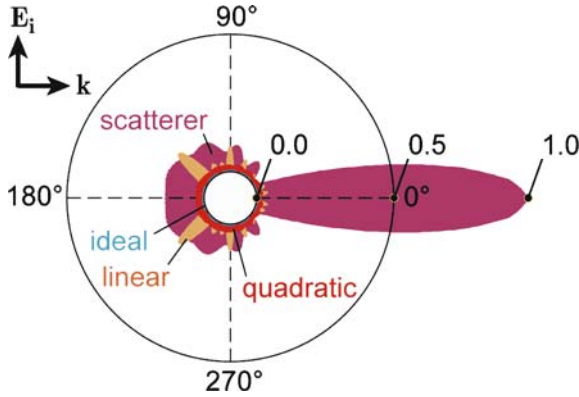


Fig. 9.12 The scattering patterns from the four cases shown in Fig. 9.11. *Purple*: a metal cylinder (scatterer) with no cloak; *blue*: the cylinder with the ideal cloak; *orange*: the cylinder with a linear non-magnetic cloak; *red*: the cylinder with an optimal quadratic non-magnetic cloak. Reprinted with permission from [42]. Copyright (2007), American Institute of Physics

To clearly illustrate the scattering and directivity properties of different cloaking systems, in Fig. 9.12 we plot the scattering radiation patterns corresponding to the four cases of Fig. 9.11. The curves in Fig. 9.12 show the energy flow in the radial direction normalized by the maximum value in the non-cloaked case at a boundary outside the outer surface of the cloaks. In the ideal cloaking system, the scattering energy flow is zero, which is indicated by the solid inner circle in Fig. 9.12. The linear cloak with reduced parameters gives rise to a noticeable and strongly directional scattering pattern. In the non-magnetic quadratic cloak, the overall scattering is much less significant. The peak value of the radial Poynting vector in the quadratic cloak is more than six times smaller than that of its linear counterpart. Moreover, the directivity in the scattering pattern is substantially suppressed as compared to the linear cloak case, which is an important feature of a quasi-ideal cloak.

To summarize this section, we proposed an electromagnetic cloak using high-order transformation to create smooth rather than discontinuous moduli at the outer interface. By this approach, the undesired scattering is completely eliminated within the limit of geometric optics, even for cloaks using non-magnetic materials to simplify the implementation. We applied this scheme to the non-magnetic cylindrical cloak and demonstrated that the scattered field is reduced by almost an order of magnitude in a cloak with optimal quadratic transformation comparing to that with the usual linear compression.

9.6 Designs for High-Order Optical Cloaking

The electromagnetic cloaks based on high-order transformations [42], as discussed in the previous section, may provide not only better cloaking performance, but also more flexibility in determining the properties of constitutive materials. In this

section, we present two novel designs for optical cloaking based on high-order transformations for TM and TE polarizations, respectively. These designs are possible for visible and infrared wavelengths [43].

From an application point of view, the design of an electromagnetic cloak is meant to elaborate realistic structures and materials which fulfill the set of required parameters corresponding to any cloaking systems. The reported experimental demonstration of a microwave cloak in Ref. [26] presented a structure where (9.11) was satisfied, and the proposed non-magnetic optical cloak in Ref. [40] corresponded to the case described by (9.12). One common feature shared in the two systems is that both works utilize designs based on a standard linear transformation $r = g(r') = (1 - a/b)r' + a$. In sharp contrast to the previous work, the purpose of this section is to present realistic designs based on more general high-order transformations. In particular, for the TM polarization, we propose a non-magnetic cloak design compatible with mature fabrication techniques such as direct deposition and direct etching; for TE incidence, we present a structure that allows for a radial gradient in the magnetic permeability while avoiding the use of plasmonic metallic units in the optical range.

First we focus on the non-magnetic cloak in the TM mode with parameters given in (9.20). In this case, the design of cloak is essentially to produce the required gradient in ε_r and ε_θ using readily available materials. Apparently, a cloak cannot consist of only a single-constituent material, because a spatial variation in material properties is critical to building a cloak. To start the design, we first examine the overall flexibility we can achieve in the effective permittivity of a general two-phase composite medium. When an external field interacts with a composite consisting of two elements with permittivity of ε_1 and ε_2 respectively, minimal screening occurs when all internal boundaries between the two constituents are parallel to the electric field, and maximal screening happens when all boundaries aligned perpendicular to the field. As we have discussed in Chap. 4, these two extremes are possible in an alternating layered structure, provided that the thickness of each layer is much less than the wavelength of incidence [44]. In this case the two extreme values of the effective permittivity can be approximated as

$$\varepsilon_{\parallel} = f\varepsilon_1 + (1 - f)\varepsilon_2; \varepsilon_{\perp} = \varepsilon_1\varepsilon_2/(f\varepsilon_2 + (1 - f)\varepsilon_1) \quad (9.25)$$

where f and $1 - f$ denote the volume fractions of components 1 and 2, and the subscripts \parallel and \perp indicate the cases with electric field polarized parallel and perpendicular to the interfaces of the layers, respectively.

The two extrema in (9.25), namely the Wiener bounds to permittivity, set the absolute bound on all possible values of the effective permittivity of a two-phase composite [45, 46]. In realistic composites, more strict limits, for example those from the spectral representation developed by Bergman and Milton [47, 48], might apply in addition to the Wiener bounds, but (9.25) nonetheless provides a straightforward way to evaluate the accessible permittivity in a composite with given constituent materials. The Wiener bounds can be illustrated on a complex ε -plane with the real and imaginary parts of ε being the x and y axis, respectively, as we

have shown in Fig. 4.2. In this plane, the low-screening bound in (9.25) corresponds to a straight line between ε_1 and ε_2 , and the high-screening bound in (9.25) defines an arc which is part of the circle determined by the three points ε_1 , ε_2 and the origin.

The required material properties for the cloak in (9.20) indicates that, for a non-magnetic cylindrical cloak with any transformation function, ε_r varies from 0 at the inner boundary of the cloak ($r = a$) to 1 at the outer surface ($r = b$), while ε_θ is a function of r with varying positive value, except for the linear transformation case where $\partial g(r')/\partial r'$ is a constant. Now we can evaluate the possibility of fulfilling the required parameters in (9.20) based on alternating metal-dielectric slices whose properties are estimated by (9.25). With phase 1 being a metal ($\varepsilon_1 = \varepsilon_m < 0$) and phase 2 representing a dielectric ($\varepsilon_2 = \varepsilon_d > 0$), the desired material properties of the cloak are only possible when the slices are within the $r-z$ plane of the cylindrical coordinates. In this case ε_r and ε_θ correspond to ε_{\parallel} and ε_{\perp} in (9.25), respectively. This scenario is illustrated in Fig. 9.13. The thick solid and dashed lines represent the two Wiener bounds $\varepsilon_{\parallel}(f)$ and $\varepsilon_{\perp}(f)$ respectively. The constituent materials used for the calculation are silver and silica at a green light wavelength of 532 nm. The pair of points on the bounds with the same filling fraction are connected with a straight line for clarification purposes. When ε_r changes between 0 and 1, the value of ε_θ varies accordingly as shown by the arrow between the two thin dashed lines. Therefore, the construction of a non-magnetic cloak requires that the relationship between the two quantities ε_{\parallel} and ε_{\perp} (as functions of f) within the range shown in Fig. 9.13 fits the material properties given in (9.20) for a particular transformation function $r = g(r')$. Another attractive feature of the proposed scheme is the

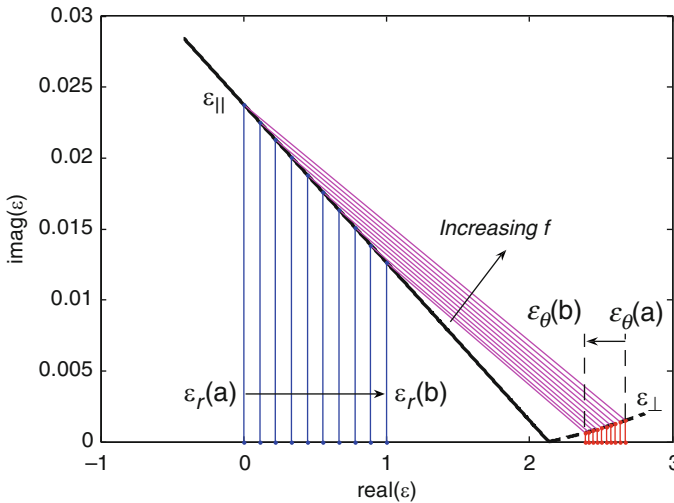
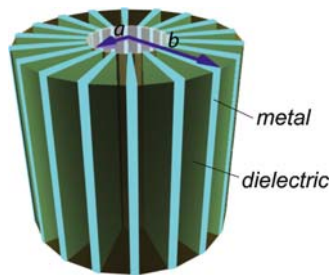


Fig. 9.13 The principle of constructing a non-magnetic cloak in the TM mode with high-order transformations. The *thick solid* and *dashed lines* represent the two Wiener bounds $\varepsilon_{\parallel}(f)$ and $\varepsilon_{\perp}(f)$, respectively. Basic material properties for this calculation: $\varepsilon_1 = \varepsilon_{Ag} = -10.6 + 0.14i$ and $\varepsilon_2 = \varepsilon_{SiO_2} = 2.13$ at $\lambda = 532$ nm. Reprinted with permission from [43]. Copyright (2008) OSA

Fig. 9.14 Schematic of a cylindrical non-magnetic cloak with high-order transformations for TM polarization. Reprinted with permission from [43]. Copyright (2008) OSA



minimal loss factor. As shown in Fig. 9.13, the loss feature described by the imaginary part of the effective permittivity is on the order of 0.01, much smaller than that of a pure metal or any resonant metal-dielectric structures. A schematic of the proposed structure consisting of interlaced metal and dielectric slices is illustrated in Fig. 9.14.

Mathematically, for a preset operational wavelength we seek a transformation together with the cylindrical shape factor a/b that fulfills the following equation:

$$\varepsilon_m \varepsilon_d \left(\frac{\partial g(r')}{\partial r'} \right)^2 + \left(\frac{r'}{g(r')} \right)^2 - (\varepsilon_m + \varepsilon_d) = 0 \quad (9.26)$$

And

$$g(0) = a; g(b) = b; \partial g(r')/\partial r' > 0 \quad (9.27)$$

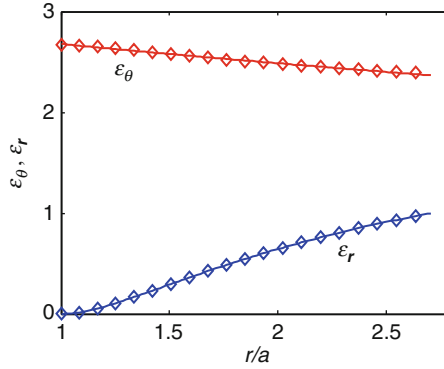
There does not exist an exact analytical solution to the equations above. However, we may use polynomial functions to approach a possible solution. More specifically, a quadratic function in the following form of (9.23) can serve as a good candidate for an approximate solution to (9.26). Such a transformation automatically satisfies the boundary and monotonicity requirements in (9.27), and it is possible to fulfill (9.26) with minimal deviation when a proper shape factor is chosen. In Table 9.1 we provide transformations, materials and geometries for non-magnetic cloaks designed for several important frequency lines across the visible range including 488 nm (Ar-ion laser), 532 nm (Nd:YAG laser), 589.3 nm (sodium D-line), and 632.8 nm (He-Ne laser). In the calculations, the permittivity of silver is taken from well accepted experimental data [49], and the dielectric constant of silica is from the tabulated data in Ref. [50]. Note that the same design and transformation work for all similar cylindrical cloaks with the same shape factor a/b . When the approximate quadratic function is fixed for a given wavelength, the filling fraction function $f(r)$ is determined by the following equation:

$$f(r) = \frac{\text{Re}(\varepsilon_d) - (g^{-1}(r)/r)^2}{\text{Re}(\varepsilon_d - \varepsilon_m)} \quad (9.28)$$

As an example, in Fig. 9.15 we show the anisotropic material properties of a non-magnetic cloak corresponding to the $\lambda = 532$ nm case in Table 9.1. Our calculation shows that with the approximate quadratic transformation, the effective parameters

Table 9.1 Approximate quadratic transformations and materials for constructing a cloak with alternating slices

λ	ε_l	ε_2	$p \times (b^2/a)$	a/b
488 nm	$\varepsilon_{Ag} = -8.15 + 0.11i$	$\varepsilon_{SiO_2} = 2.14$	0.0662	0.389
532 nm	$\varepsilon_{Ag} = -10.6 + 0.14i$	$\varepsilon_{SiO_2} = 2.13$	0.0517	0.370
589.3 nm	$\varepsilon_{Ag} = -14.2 + 0.19i$	$\varepsilon_{SiO_2} = 2.13$	0.0397	0.354
632.8 nm	$\varepsilon_{Ag} = -17.1 + 0.24i$	$\varepsilon_{SiO_2} = 2.12$	0.0333	0.347
11.3 μm	$\varepsilon_{SiC} = -7.1 + 0.40i$	$\varepsilon_{BaF_2} = 1.93$	0.0869	0.356

**Fig. 9.15** Anisotropic material parameters ε_r and ε_θ of a non-magnetic cloak made of silver-silica alternating slices corresponding to the third row ($\lambda = 532$ nm) in Table 9.1. The *solid lines* represent the exact parameters determined by (9.20), and the *diamond markers* show the parameters on the Wiener's bounds given by (9.25). Reprinted with permission from [43]. Copyright (2008) OSA

ε_r and ε_θ obtained with the Wiener bounds in (9.25) fit with the exact parameters required for this transformation by (9.20) remarkably well, with the average deviation of less than 0.5%.

Compared to the previously designed cloak in Ref. [40] which requires thin metal needles embedded in a dielectric host following a pre-designed distribution, the fabrication feasibility of the newly proposed design is obvious because such vertical wall-like structures are compatible with mature fabrication techniques like direct deposition and direct etching.

In the next part of the section, we focus on constructing a cylindrical cloak for TE mode working within the mid-infrared frequency range with a gradient in the magnetic permeability, as requested by (9.21). An electromagnetic cloak operating at mid-infrared is of great military and civilian interests, because this wavelength range corresponds to the thermal radiation band from human bodies. For this purpose there could be several different approaches which all involve silicon carbide, an important media for metamaterial research in mid-infrared. SiC is a polaritonic material with its phonon resonance band falling into the spectral range centered at around 12.5 μm (800 cm^{-1}), which introduces a sharp Lorentz behavior in its electric permittivity. The dielectric function of SiC at mid-infrared is well described with the model in (5.4). On the high-frequency side, the dielectric function is strongly

negative, which makes its optical response similar to that of metals and has been utilized in applications like a mid-infrared superlens [51, 52]. At frequencies lower than the resonance frequency, the permittivity can be strongly positive, which makes SiC an attractive candidate for producing high-permittivity Mie resonators at the mid-infrared wavelength range [53].

SiC structures can be used to build mid-infrared cloaking devices in different styles. For example, we may consider using the needle-based structure detailed in Ref. [40] for the TM mode, where needles made of a low-loss negative- ε polaritonic material like SiC or TiO₂ are embedded in an IR transparent dielectric like ZnS. The non-magnetic cloak using alternating slices structure as we have shown in this section provides a more realistic design. With SiC as the negative- ε material and BaF₂ as the positive- ε slices with material properties given in Ref. [50], we can find the appropriate transformation function and shape factor that fulfills the material property requirements at a preset wavelength. The result for $\lambda = 11.3 \mu\text{m}$ (CO₂ laser range) is shown in the last row of Table 9.1.

Now we consider a cylindrical cloak for the TE mode with the required material properties given in (9.21), which indicates that a gradient in the magnetic permeability along the radial direction is necessary. To be more specific, μ_r varies from 0 at the inner boundary ($r = a$) to $[\partial g(r')/\partial r']^2$ at the outer surface ($r = b$), while the required ε_z changes accordingly following the function $[\partial g(r')/\partial r']^{-2}$. The magnetic requirement may be accomplished using metal elements like split-ring resonators, coupled nanostrips or nanowires. However, such plasmonic structures inevitably exhibit a high loss, which is detrimental to the cloaking performance. A SiC based structure provides an all-dielectric route to a magnetic cloak for the TE mode due to the Mie resonance in a subwavelength SiC unit.

Meta-magnetic responses and a negative index of refraction in structures made from high-permittivity materials have been studied extensively in recently years [53–57]. Magnetic resonance in a rod-shaped high-permittivity particle can be excited by different polarizations of the external field with respect to the rod axis. When a strong magnetic resonance and an effective permeability substantially distinct from 1 are desired, the rod should to be aligned parallel to the electric field to assure the maximum possible interaction between the rod and the external field. In our design of a cylindrical cloak for the TE mode, the desired radial permeability has values of less than (but close to) 1, and resonance behavior in the effective permittivity ε_z should be avoided for a minimal loss. Therefore, with the electrical field polarized along the z axis of the cylindrical system, we arrange the SiC rods along the r axis and form an array in the $\theta - z$ plane. The proposed structure is depicted in Fig. 9.16, where arrays of SiC wires along the radial direction are placed between the two surfaces of the cylindrical cloak.

The effective permeability of the system can be estimated as follows using the approach in Ref. [54]:

$$\mu_r = \frac{2}{kL_1^2} \frac{L_1 J_1(kL_1) - t J_1(kt) + a_0 t H_1^{(1)}(kt) - a_0 L_1 H_1^{(1)}(kL_1) + c_0 t J_1(nkt)/n}{J_0(kL_2/2) - a_0 H_0^{(1)}(kL_2/2)} \quad (9.29)$$

Fig. 9.16 Schematic of a cylindrical non-magnetic cloak with high-order transformations for TE polarization. Reprinted with permission from [43]. Copyright (2008) OSA

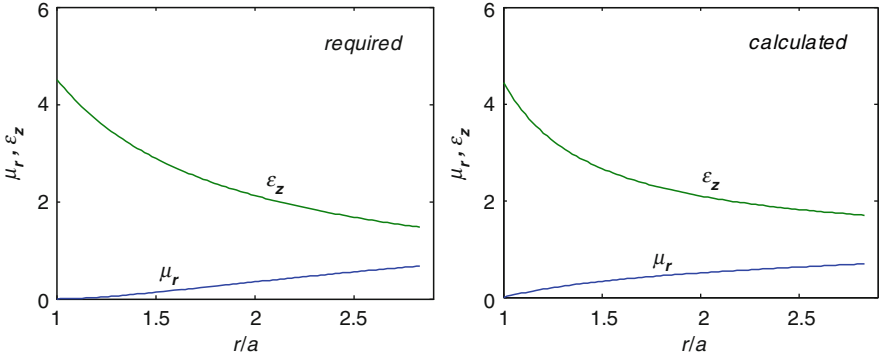
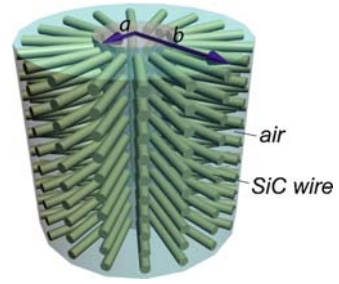


Fig. 9.17 The required and the calculated effective parameters μ_r and ε_z for a cylindrical TE cloak with SiC wire arrays for $\lambda = 13.5 \mu\text{m}$. Reprinted with permission from [43]. Copyright (2008) OSA

where h and φ represent the periodicities along the z and θ directions respectively, t denotes the radius of each wire, $n = \sqrt{\varepsilon_{\text{SiC}}}$ is the refractive index, $k = 2\pi/\lambda_0$ denotes the wave vector, $L_1 = \sqrt{hr\varphi/\pi}$ and $L_2 = (h + r\varphi)/2$ represent the two effective unit sizes based on area and perimeter estimations respectively.

$a_0 = [nJ_0(nkt)J_1(kt) - J_0(kt)J_1(nkt)] / [nJ_0(nkt)H_1^{(1)}(kt) - H_0^{(1)}(kt)J_1(nkt)]$ and $c_0 = [J_0(kt) - a_0H_0^{(1)}(kt)] / J_0(nkt)$ are the scattering coefficients, and the Bessel functions in the equation follow the standard notations. The permittivity along the z direction is well approximated using Maxwell–Garnett method [54]. In the design we choose the appropriate transformation, geometry and operational wavelength such that the calculated effective parameters μ_r and ε_z follow what is required by (9.21) with tolerable deviations. In Fig. 9.17 we plot the required and the calculated μ_r and ε_z for a TE cloak at $\lambda = 13.5 \mu\text{m}$. The parameters used for this calculation are $a = 15 \mu\text{m}$, $a/b = 0.35$, $t = 1.2 \mu\text{m}$, $h = 2.8 \mu\text{m}$, $\varphi = 10.6^\circ$, and the p coefficient in the quadratic transformation is $0.5a/b^2$. We observe very good agreement between the required values and the calculated ones based on analytical formulae, and the imaginary part in the effective permeability is less than 0.06. This computation verifies the feasibility of the proposed cloaking system based on SiC wire arrays for the TE polarization.

To summarize this section, using high-order transformations we proposed two novel designs of optical cloaks for TM and TE polarizations. This critical development builds upon our previous work on the design of a non-magnetic cloak and the suggestion of using high-order transformations to produce more flexible cloaking systems. The realistic structures and models discussed in the section may lead to a practical path towards realizing actual cloaking devices at optical wavelengths.

9.7 Alternative Approaches for Optical Cloaking

In all of the preceding sections of this chapter we focused on the “standard” method for optical cloaking, where a volume with a closed surface in free space is converted into a hollow shell sharing the same outer boundary. In this method, the resultant constitutive materials for such cloaking devices are necessarily anisotropic and dispersive. In this section we present a few alternative approaches for cloaking at optical frequencies with appealing features such as broadband operation, isotropy and low loss.

The first alternative scheme to be discussed is the “invisibility carpet” initiated by Li and Pendry [58]. In contrast to the cylindrical or spherical cloaks where the cloaked region is compressed into a non-scattering line or point, the transformation for carpet cloaking is designed such that a curved, conducting surface is converted into a flat surface, eliminating the distortion of light from the deformed mirror as well as anything underneath it. This scenario is illustrated in Fig. 9.18, where the cloak is rectangular in shape with a portion of its bottom curved inwards to produce a hidden region. Therefore, the cloaking device hides the curved carpet along with any object hiding under it by giving the region the appearance of a flat, reflecting surface. The spatial transformation occurs between the bottom-curved rectangular region in the actual system and a regular rectangle in a virtual space, as depicted by the grey areas in Fig. 9.18.

Although the proposed invisibility carpet does not seem to be an ideal cloaking device as it fails to offer a “see-through” effect against the background of a free space, it does possess distinct advantages over the standard cloaking systems discussed in the previous sections. Unlike the cylindrical or spherical cloaks where the required permittivity and permeability distribution necessarily exhibits singular values at their inner boundaries, the constitutive parameters for an invisibility carpet are much more modest, avoiding all extreme values. Furthermore, since the transformation function for the desired spatial conversion is not unique, the coordinate transformation can be purposely tailored in such a way that the anisotropy of the cloak material is substantially suppressed, with a residual anisotropy factor (defined as the ratio between the effective refractive index along orthogonal directions) of usually no more than a few percent away from unity. This is achieved by the minimization of the Modified-Liao functional with slipping boundary conditions [59], as detailed in Ref. [58]. The cloaking carpet with quasi-isotropic parameters corresponds to the case of a spatial transformation with conformal mapping, meaning

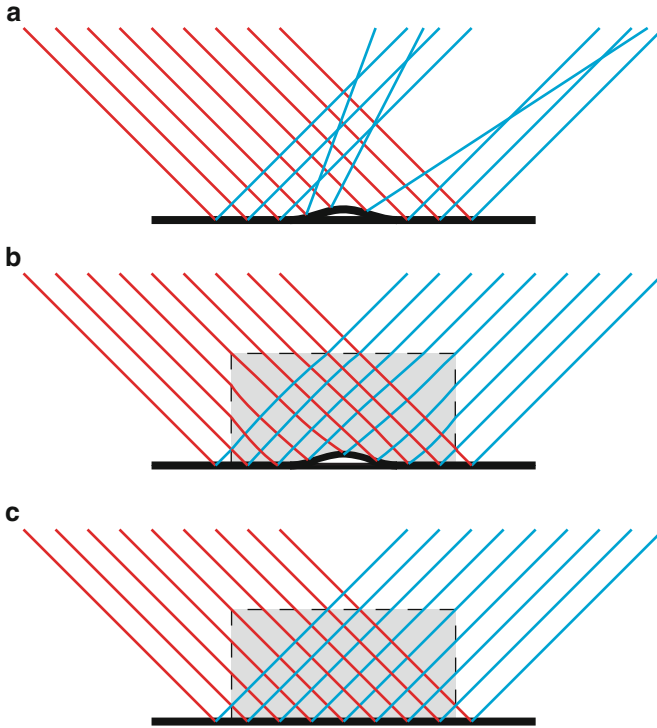


Fig. 9.18 Schematic of the invisibility carpet. (a) Light scattered from a bump on a planar reflecting surface. (b) Light scattered from the deformed mirror shielded by an invisibility carpet. Note that all rays outside the *rectangular box* are identical to those of a plane wave incident upon a planar reflector. (c) Ray tracing of a plane wave directly impinging on a perfect reflecting plane. The *red* and *blue* rays represent the incident and scattered light rays, respectively. The *solid black line* indicates conducting planes, and the *gray color* denotes regions where coordinate transformation is applied

that pairs of grid lines intersecting at 90° are preserved during the transformation. One example of the material parameters for a quasi-isotropic rectangular carpet is illustrated in Fig. 9.19 [58]. This surface plot shows the magnitude of the normalized effective permittivity $\epsilon_{eff}/\epsilon_{ref}$ in the device, with ϵ_{ref} representing the background permittivity ($\epsilon_{ref} = 1$ if the device is placed in free space against a conductive plane). The permeability is unity throughout the region, so the effective index of refraction is simply the square root of ϵ_{eff} . The anisotropy factor is about 1.04 – a value that can be neglected without inducing sizable deviations, and the magnitude of ϵ_{eff} ranges between 0.68 and 1.96.

The material properties of the invisibility carpet in Fig. 9.19 implies several appealing features for experimental realizations of such a device. First of all, the quasi-conformal mapping gives rise to square-shaped transformed cells, which result in extremely low anisotropy in the cloaking material. By neglecting the trivial anisotropy in the constitutive materials in the design, we can avoid the use of

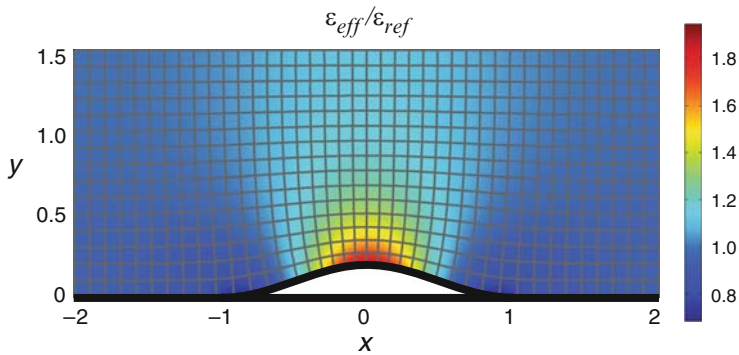


Fig. 9.19 Two-dimensional spatial distribution of the normalized effective permittivity in a carpet-cloaking device. Quasi-conformal mapping is used, as indicated by the *gray-colored grid lines*. The *solid black lines* represent perfect conducting planes. Reprinted with permission from [58]. Copyright (2008) by the American Physical Society

particles with complicated shapes. Secondly, the range of the required dielectric function is very modest and without singularities. Moreover, if the device is operated against a dielectric background with $\epsilon_{ref} > 1$, the required effective permittivity will rise accordingly. For example, the range of ϵ_{eff} becomes 1.2–3.5 if the invisible carpet in the previous example is immersed in water ($n_{ref} = 1.33$). Such a span of effective permittivity is within the reach of usual dielectric materials. Consequently, an all-dielectric invisibility carpet brings hope for two of the most desirable features in a general cloaking system – low-loss and broadband operation.

The experimental realization of the invisibility carpet, also referred to as a ground-plane cloak, was first reported by a Duke University research group at microwave frequencies [27]. In this demonstration, nonresonant metamaterial elements with controlled, subwavelength geometries are used to construct the rectangular-shaped carpet, and the measured field mapping shows that the distortion of waves from a perturbation on a conducting plane is effectively mitigated with the help of the ground-plane cloak. The broadband operational range of the device was also confirmed in the experiment. In principle, the same design is effectively scalable towards operation at optical frequencies, although the delicate manipulation of metal-dielectric meta-atoms at deeply subwavelength scales might be too challenging when it comes to the optical range.

Soon after the realization of the microwave ground-plane cloak, optical carpet cloaking was demonstrated simultaneously by two independent groups [60, 61]. In both devices, a refractive index profile similar to that in Fig. 9.19 is achieved by “tuning” the filling fraction of silicon in a two-dimensional film. This can be realized in a silicon slab either by drilling holes via focused ion beam milling [60], or by plasma etching with a patterned mask [61]. Note that the sizes and separations of the voids or pillars in the silicon film must be substantially smaller than the operational wavelength of the devices, so that the effective-medium approach works. The densities of nanofabricated holes or pillars are carefully engineered in order

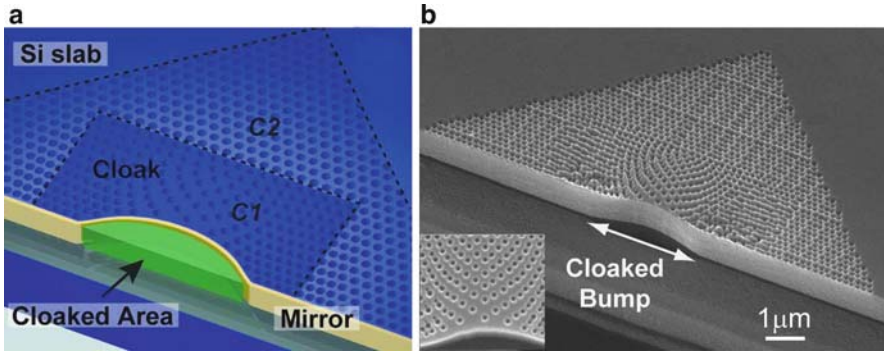


Fig. 9.20 An all-dielectric invisibility carpet working at the near-infrared wavelength range. (a) The design of the silicon-based device with different regions marked; (b) SEM image of the fabricated carpet cloak. The *inset* is a zoomed view of the central region of the device. Reprinted from [60] by permission from Macmillan Publishers Ltd: Nat Mater, copyright (2009). Courtesy of X. Zhang

to yield the desired two-dimensional profile of the effective index of refraction. As an example, the design and SEM image of the carpet cloak reported by the Berkeley group are shown in Fig. 9.20 [60]. In both experiments, the waveguide mode reflected from the deformed mirror is shown to be largely collimated, resembling that of an incoming beam that is directly incident upon a flat surface without any deformation. These carpet cloaking devices are all-dielectric without any resonant or strongly dispersive elements involved, so they are nearly lossless and broadband. These features are also confirmed in the two experiments. The two silicon-based invisibility carpets work around a near-infrared wavelength of $1.6 \mu\text{m}$, beyond silicon's interband absorption wavelength. Moving the operational wavelength to the visible range may require other constitutive materials, and more demanding fabrication techniques are probably necessary as the wavelength itself shrinks further to the submicron regime.

There is yet another scheme to achieve low-loss, broadband optical cloaking with isotropic constitutive materials. Smolyaninov and coauthors suggest that the anisotropic material parameters required in transformation-based devices can be emulated by specially designed, tapered waveguides [62]. When this general principle is applied to optical cloaking, broadband electromagnetic cloaking can be demonstrated in a nice and simple way. The experimental realization in Ref. [62] utilizes a configuration that is identical to the classic geometry of the Newton rings observation, and the tapered waveguide is formed within the gap between a gold-coated convex lens and a planar metal surface. A schematic view of the experimental setup is shown in Fig. 9.21. In this structure, there exists a cutoff radius on the order of tens of microns for the allowed waveguide modes, and no photon launched into the waveguide can reach an area within the cutoff radius from the point of contact between the two gold-coated surfaces. More interestingly, light beams directly incident at the cutoff region generate no shadow – a characteristic feature of invisibility cloaks. The cloaked area spans a region about 100 times larger than the operational

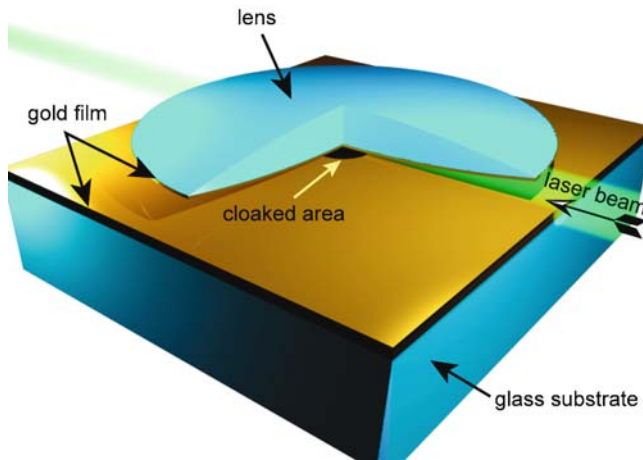


Fig. 9.21 A schematic view of the experimental realization of optical cloaking by tapered waveguides. One-quarter of the gold-coated convex lens is removed in the figure to show the interior details

wavelength. The experiment in Ref. [62] is conducted using visible light of different wavelengths, and the direct “see-through” effect is obtained against the background of free space. Such features are not readily available in carpet cloaking devices. Moreover, it’s interesting to note that the geometry in the cloaking experiment using a tapered waveguide in Ref. [62] is similar to another broadband invisibility approach proposed in Ref. [63], which is based on transformation optics of a curved, non-Euclidean space such as the surface of a virtual sphere.

Cloaking at optical frequencies can also be demonstrated in a purely two-dimensional surface with surface plasmon polaritons [64]. In this work, the distribution of the radial component of permittivity in a nonmagnetic cylindrical cloak as indicated by (9.12) is approximated by tuning the effective refractive index as perceived by plasmon waves. The scenario is analogous to the hyperlens discussed in Sect. 8.5, where the anisotropic distribution of the effective parameters in a cylindrical coordinate system can be fulfilled for either light waves or surface plasmons. Some basic characteristics of an electromagnetic cloak, including reduced visibility and the flow of energy around the cloaked region, were partially verified in the experimented in Ref. [64].

9.8 Concluding Remarks on Transformation Optics

As discussed in this chapter, one of the most exciting applications of transformation optics is an electromagnetic cloak that can bend light around itself, similar to the flow of water around a stone, making invisible both the cloak and an object hidden inside. By excluding light from a certain area of space and bending the light around the space, one can make an object in that area invisible (see Fig. 9.22a).

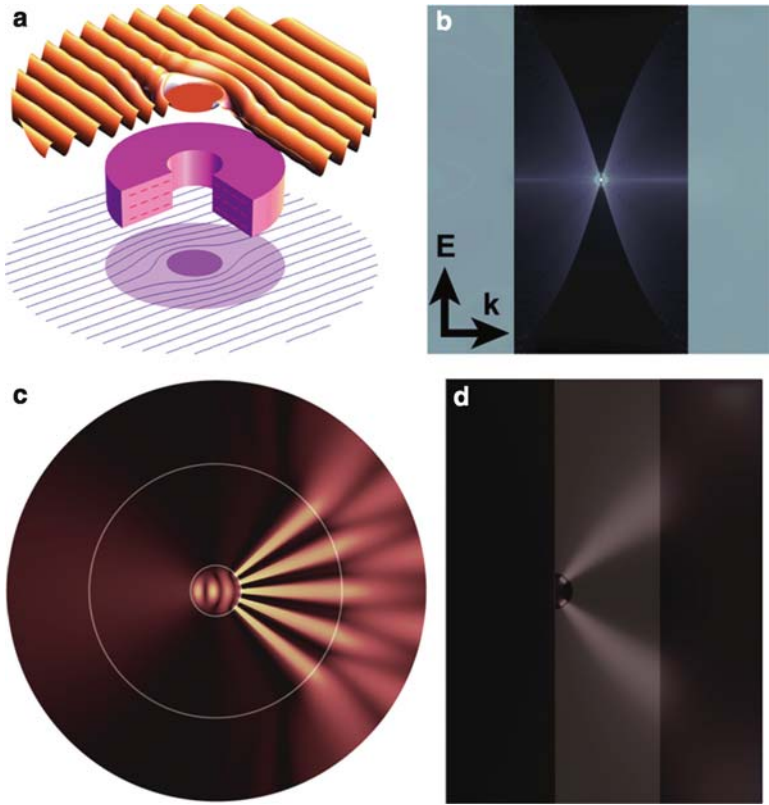


Fig. 9.22 Examples of transformation-based devices. (a) Optical cloaking; (b) light concentrator; (c) impedance-matched hyperlens; (d) planar hyperlens. (b) and (d) reprinted with permission from [22]. Copyright (2008) OSA. (c) Reprinted with permission from [65]. Copyright (2007) OSA

However, as mentioned in the beginning of this chapter, practical applications of transformation optics go far beyond just cloaking. Theory allows the control of light in an extreme and ultimate manner by providing a general recipe for obtaining complex spatial distributions of anisotropic permittivity and permeability. Using these distributions, a “curvilinear” optical space is molded, thereby creating the channel for the desired flow of light. The core challenge here is to approximate the required ideal optical space by manufacturable nanostructured metamaterials, with minimal loss of the required functionality, and thereby move from the theoretical description to actual prototypes.

One can, for example, not only exclude light from some region, as in a cloak, but also do the opposite and concentrate light within a certain area of the space. In such a concentrator, light could be collected from all directions onto an arbitrarily small spot, leading to extremely high intensities [22] (see Fig. 9.22b). The light concentrator may enable applications such as omni-directional solar light collection and field-enhanced sensing.

Transformation optics can also enable an impedance-matched hyperlens (see Fig. 9.22c) which does not reflect and therefore represents a highly efficient imaging device with sub-wavelength resolution [65]. Moreover, transformation optics can make possible a planar hyperlens [22] (see Fig. 9.22d), which could be one of most exciting and promising metamaterials application to date (see also Chap. 8). Such a planar magnifying hyperlens could revolutionize the field of optical imaging.

Transformation optics enabled by metamaterials transforms the science of light and opens up many exciting applications that often go beyond what we could imagine until very recently. The field of transformation optics, which is enabled by metamaterials, has inspired a fresh look to be taken at the very foundations of optics [13]. Analogous to general relativity, where time and space are curved, transformation optics shows that the space for light can also be bent in an almost arbitrary way. The ability to design and engineer optical space provides the possibility of controlling the flow of light with nanometer spatial precision. Thus, general relativity may find practical use in a number of novel optical devices based on transformation optics, guiding how, using metamaterials, the space for light can be curved in a pre-designed and well-controlled way.

Generally, light propagates so that the optical path, which is given by the product of the physical length and the refractive index, is minimized (has an extremum, strictly speaking). Thus, by creating a complex distribution for the refractive index n , the geometrical path that minimizes the optical path can be curved in an almost arbitrarily complex way. One might think that such molding of a light path is possible only in the limit of geometrical optics, which implies a scale much larger than the wavelength. However, we saw in this chapter that provided the basic optical parameters of materials, ϵ and μ , are transformed appropriately, and because of the generic invariance of Maxwell's equations, transformation optics makes it possible to mold and control light on all scales, from macroscopic sizes down to the deeply subwavelength scale. Thus by creating a desired distribution of ϵ and μ , and thus a distribution of refractive index n , one can "curve" the space for light in a nearly arbitrary way, making it possible to propagate light not only in the backward direction (when n is negative) but also along nearly any curved line. As a result, a myriad of fascinating devices are achievable using transformation optics and metamaterials.

References

1. Tachi S (2003) Telexistence and retro-reflective projection technology (RPT). Proceedings of the 5th Virtual Reality International Conference (VRIC2003), Laval Virtual, France
2. Nicorovici NA, McPhedran RC, Milton GW (1994) Optical and dielectric-properties of partially resonant composites. *Phys Rev B* 49:8479–8482
3. Milton GW, Nicorovici NAP (2006) On the cloaking effects associated with anomalous localized resonance. *Proc R Soc Lond Ser A* 462:3027–3059
4. Nicorovici NAP, Milton GW, McPhedran RC, Botten LC (2007) Quasistatic cloaking of two-dimensional polarizable discrete systems by anomalous resonance. *Opt Express* 15:6314–6323
5. Kerker M (1975) Invisible bodies. *J Opt Soc Am* 65:376–379

6. Alu A, Engheta N (2005) Achieving transparency with plasmonic and metamaterial coatings. *Phys Rev E* 72:016623
7. Garcia de Abajo FJ, Gomez-Santos G, Blanco LA, Borisov AG, Shabanov SV (2005) Tunneling mechanism of light transmission through metallic films. *Phys Rev Lett* 95:067403
8. Miller DAB (2006) On perfect cloaking. *Opt Express* 14:12457–12466
9. Pendry JB, Schurig D, Smith DR (2006) Controlling electromagnetic fields. *Science* 312:1780–1782
10. Leonhardt U (2006) Optical conformal mapping. *Science* 312:1777–1780
11. Greenleaf A, Lassas M, Uhlmann G (2003) Anisotropic conductivities that cannot be detected by EIT. *Physiol Meas* 24:413–419
12. Benveniste Y, Miloh T (1999) Neutral inhomogeneities in conduction phenomena. *J Mech Phys Solids* 47:1873–1892
13. Shalaev VM (2008) Transforming light. *Science* 322:384–386
14. Tamm IE (1924) Electrodynamics of an anisotropic medium in the special theory of relativity. *J Russ Phys Chem Soc* 56:248
15. Tamm IE (1925) Crystal-optics of the theory of relativity pertinent to the geometry of a bi-quadratic form. *J Russ Phys Chem Soc* 57:1
16. Dolin LS (1961) On a possibility of comparing three-dimensional electromagnetic systems with inhomogeneous filling. *Izv Vyssh Uchebn Zaved Radiofiz* 4:964–967
17. Post EJ (1962) Formal structure of electromagnetics: general covariance and electromagnetics. Interscience, New York
18. Lax M, Nelson DF (1976) Maxwell equations in material form. *Phys Rev B* 13:1777–1784
19. Chew WC, Weedon WH (1994) A 3D perfectly matched medium from modified Maxwell's equations with stretched coordinates. *Microw Opt Technol Lett* 7:599–604
20. Ward AJ, Pendry JB (1996) Refraction and geometry in Maxwell's equations. *J Mod Opt* 43:773–793
21. Milton GW, Briane M, Willis JR (2006) On cloaking for elasticity and physical equations with a transformation invariant form. *New J Phys* 8:248
22. Kildishev AV, Shalaev VM (2008) Engineering space for light via transformation optics. *Opt Lett* 33:43–45
23. Rahm M, Cummer SA, Schurig D, Pendry JB, Smith DR (2008) Optical design of reflectionless complex media by finite embedded coordinate transformations. *Phys Rev Lett* 1:063903
24. Chen HY, Chan CT (2007) Transformation media that rotate electromagnetic fields. *Appl Phys Lett* 90:241105
25. Kong FM, Wu BII, Kong JA, Huangfu JT, Xi S, Chen HS (2007) Planar focusing antenna design by using coordinate transformation technology. *Appl Phys Lett* 91:253509
26. Schurig D, Mock JJ, Justice BJ, Cummer SA, Pendry JB, Starr AF, Smith DR (2006) Metamaterial electromagnetic cloak at microwave frequencies. *Science* 314:977–980
27. Liu R, Ji C, Mock JJ, Chin JY, Cui TJ, Smith DR (2009) Broadband ground-plane cloak. *Science* 323:366–369
28. Schurig D, Pendry JB, Smith DR (2006) Calculation of material properties and ray tracing in transformation media. *Opt Express* 14:9794–9804
29. Leonhardt U, Philbin TG (2006) General relativity in electrical engineering. *New J Phys* 8:247
30. Cummer SA, Popa BI, Schurig D, Smith DR, Pendry J (2006) Full-wave simulations of electromagnetic cloaking structures. *Phys Rev E* 74:036621
31. Nachman AI (1988) Reconstructions from boundary measurements. *Ann Math* 128:531–576
32. Wolf E, Habashy T (1993) Invisible bodies and uniqueness of the inverse scattering problem. *J Mod Opt* 40:785–792
33. (2006) Breakthrough of the year – the runners-up. *Science* 314:1850–1855
34. Chen HY, Liang ZX, Yao PJ, Jiang XY, Ma HR, Chan CT (2007) Extending the bandwidth of electromagnetic cloaks. *Phys Rev B* 76:241104
35. Kildishev AV, Cai W, Chettiar UK, Shalaev VM (2008) Transformation optics: approaching broadband electromagnetic cloaking. *New J Phys* 10:115029
36. Zhou J, Koschny T, Kafesaki M, Economou EN, Pendry JB, Soukoulis CM (2005) Saturation of the magnetic response of split-ring resonators at optical frequencies. *Phys Rev Lett* 95:223902

37. Klein MW, Enkrich C, Wegener M, Soukoulis CM, Linden S (2006) Single-slit split-ring resonators at optical frequencies: limits of size scaling. *Opt Lett* 31:1259–1261
38. Podolskiy VA, Sarychev AK, Shalaev VM (2002) Plasmon modes in metal nanowires and left-handed materials. *J Nonlinear Opt Phys Mater* 11:65–74
39. Kildishev AV, Cai WS, Chettiar UK, Yuan HK, Sarychev AK, Drachev VP, Shalaev VM (2006) Negative refractive index in optics of metal-dielectric composites. *J Opt Soc Am B* 23:423–433
40. Cai WS, Chettiar UK, Kildishev AV, Shalaev VM (2007) Optical cloaking with metamaterials. *Nat Photonics* 1:224–227
41. Klar TA, Kildishev AV, Drachev VP, Shalaev VM (2006) Negative-index metamaterials: going optical. *IEEE J Sel Top Quantum Electron* 12:1106–1115
42. Cai WS, Chettiar UK, Kildishev AV, Shalaev VM, Milton GW (2007) Nonmagnetic cloak with minimized scattering. *Appl Phys Lett* 91:111105
43. Cai WS, Chettiar UK, Kildishev AV, Shalaev VM (2008) Designs for optical cloaking with high-order transformations. *Opt Express* 16:5444–5452
44. Aspnes DE (1982) Optical-properties of thin-films. *Thin Solid Films* 89:249–262
45. Wiener O (1912) Die Theorie des Mischkorpers für das Feld der stationären Stromung. *Abh Math-Phys Klasse Königlich Sachsische Des Wiss* 32:509–604
46. Aspnes DE (1982) Bounds on allowed values of the effective dielectric function of 2-component composites at finite frequencies. *Phys Rev B* 25:1358–1361
47. Bergman DJ (1980) Exactly solvable microscopic geometries and rigorous bounds for the complex dielectric-constant of a 2-component composite-material. *Phys Rev Lett* 44:1285–1287
48. Milton GW (1980) Bounds on the complex dielectric-constant of a composite-material. *Appl Phys Lett* 37:300–302
49. Johnson PB, Christy RW (1972) Optical-constants of noble-metals. *Phys Rev B* 6:4370–4379
50. Palik ED (ed) (1997) Handbook of optical constants of solids. Academic, New York
51. Korobkin D, Urzhumov Y, Shvets G (2006) Enhanced near-field resolution in midinfrared using metamaterials. *J Opt Soc Am B* 23:468–478
52. Taubner T, Korobkin D, Urzhumov Y, Shvets G, Hillenbrand R (2006) Near-field microscopy through a SiC superlens. *Science* 313:1595
53. Schuller JA, Zia R, Taubner T, Brongersma ML (2007) Dielectric metamaterials based on electric and magnetic resonances of silicon carbide particles. *Phys Rev Lett* 99:107401
54. O'Brien S, Pendry JB (2002) Photonic band-gap effects and magnetic activity in dielectric composites. *J Phys Condens Matter* 14:4035–4044
55. Huang KC, Povinelli ML, Joannopoulos JD (2004) Negative effective permeability in polaritonic photonic crystals. *Appl Phys Lett* 85:543–545
56. Wheeler MS, Aitchison JS, Mojahedi M (2005) Three-dimensional array of dielectric spheres with an isotropic negative permeability at infrared frequencies. *Phys Rev B* 72:193103
57. Peng L, Ran LX, Chen HS, Zhang HF, Kong JA, Grzegorzczuk TM (2007) Experimental observation of left-handed behavior in an array of standard dielectric resonators. *Phys Rev Lett* 98:157403
58. Li JS, Pendry JB (2008) Hiding under the carpet: a new strategy for cloaking. *Phys Rev Lett* 101:203901
59. Knupp PM, Steinberg S (1993) Fundamentals of grid generation. CRC Press, Boca Raton, FL
60. Valentine J, Li J, Zentgraf T, Bartal G, Zhang X (2009) An optical cloak made of dielectrics. *Nat Mater* 8:568–571
61. Gabrielli LH, Cardenas J, Poitras CB, Lipson M (2009) Silicon nanostructure cloak operating at optical frequencies. *Nat Photonics* 3:461–463
62. Smolyaninov II, Smolyaninova VN, Kildishev AV, Shalaev VM (2009) Anisotropic metamaterials emulated by tapered waveguides: application to optical cloaking. *Phys Rev Lett* 102:213901
63. Leonhardt U, Tyc T (2009) Broadband invisibility by non-euclidean cloaking. *Science* 323:110–112
64. Smolyaninov II, Hung YJ, Davis CC (2008) Two-dimensional metamaterial structure exhibiting reduced visibility at 500 nm. *Opt Lett* 33:1342–1344
65. Kildishev AV, Narimanov EE (2007) Impedance-matched hyperlens. *Opt Lett* 32:3432–3434

Index

A

Abbe diffraction limit, 137
Absorption coefficient, 18, 19, 24, 31
Ampère's law, 66
Anderson localization, 72
Anisotropic materials
 highly anisotropic material, 102, 118
Anti-resonance, 55, 88
Artificial dielectrics, 59–60, 65
Atomic force microscope (AFM), 47, 87

B

Babinet principle, 112
Backward phase-matching, 131
Band gap
 in dielectrics, 12–14, 16
 in photonic crystals, 117, 125
 in semiconductors, 12, 13
Beer's law, 18
Bianisotropic materials, 3
Birefringence, 19, 50, 118
Bistability, 125, 126
Block-elimination (BE) method, 146
Bound electrons, 12, 21–23
Bruggeman geometry, 26, 27, 33

C

Camouflage, 159, 160
Causality, 6, 32, 53, 103, 171
Cavity model, 93, 94
Chiral materials, 102, 120
Chirality, 117, 120
Clausius–Mossotti relation, 27, 29, 34
Clusters, 33, 71, 72
Complex permittivity plane, 63
Conformal mapping, 187–189

Constitutive relations, 14, 15, 20, 29, 52
Coordinate systems
 Cartesian, 162–166
 cylindrical, 163–165
 spherical, 161, 166, 167
Coordinate transformation, 161–168, 172, 177, 188
Critical wavelength, 13, 14

D

Damping constant, 16, 18, 20, 21, 24, 31, 65, 67, 69, 70
Depolarization factor, 35
Depolarization field, 28
Designs for optical cloaking
 high-order, 180–187
 non-magnetic, 171–176, 182–187
Dielectric constant, 8, 13, 16, 25, 29, 30, 32, 63, 64, 70, 89, 96, 142, 183
Dielectric function, 15–18, 20–24,
Diffraction limit, 40, 42, 138, 139, 149, 150, 152, 154
Diffraction threshold, 92
Dipole moment
 electric, 29, 79,
 magnetic, 79
Direct laser writing (DLW), 45, 46
Dispersion curve, 119, 151, 153
Dispersion relation, 117, 118, 168, 171
Double-negative materials, 102
Drude model, 21, 23, 24, 30, 32, 65, 70, 94, 142, 143

E

Effective parameters
 conductivity, 34, 68, 70
 damping constant, 16, 18, 20, 21, 24, 31, 65, 67, 69, 70

- dielectric function, 15–18, 20–24, 26, 29, 30, 32, 65, 66, 69, 70, 97, 98, 114, 184
 - electron density, 66, 68, 69, 84
 - electron mass, 66, 69
 - mean free path, 21, 24
 - permeability, 6–8, 14, 51, 52, 77, 79–81, 83, 85, 89, 95–98, 101, 105–109, 112, 113, 116, 117, 123, 124, 161, 164–166, 168, 169, 177, 181, 184–188, 192
 - permittivity, 6–8, 13, 14, 16, 18–20, 24, 27, 29, 30, 32, 33, 36, 51, 52, 60–65, 67–71, 89, 93, 94, 96–98, 106–108, 113, 114, 117–119, 124, 140–147, 161–163, 165, 166, 172, 173, 175, 177, 181, 183–185, 187–189, 191, 192
 - plasma frequency, 21, 60, 65–70, 77, 84
 - refractive index, 6, 8, 14, 15, 18, 19, 23, 24, 43, 44, 51–54, 60, 72, 94, 103, 104, 107–109, 111, 112, 116–118, 120, 127, 128, 137, 138, 151, 167, 171, 186, 187, 189, 191, 193
 - Effective medium theory (EMT)
 - d*-dimensional, 34
 - shape-dependent, 35, 36, 63, 173
 - Electric displacement, 14, 16, 87, 88, 114, 162
 - Electric field, 7, 11, 12, 14–20, 23, 27, 28, 35, 61, 62, 64, 65, 70, 73, 77, 82, 83, 87, 108, 124, 168, 170, 173, 181, 185
 - Electric flux density, 61
 - Electric permittivity, 51, 96, 97, 107, 118, 143, 161
 - Electric susceptibility, 14, 19, 29
 - Electromagnetic cloak
 - broadband, 190
 - carpet, 187–191
 - cylindrical, 163–166, 168–172, 174, 177, 178, 180, 182–187, 191
 - ground-plane, 189
 - non-magnetic, 171–187
 - spherical, 161, 166, 167, 187
 - Electromagnetic response
 - electric, 29, 60, 65, 71, 106, 107, 124, 128, 140
 - magnetic, 78–85, 88, 89, 95, 96, 105–108, 118, 124, 153, 168, 169, 171, 173, 185
 - Electron gas, 20, 21
 - Electron mean free path, 21
 - Electron transition, 16, 17, 89
 - Electron-beam lithography, 40, 81, 86, 87, 107, 109
 - Electronic structure, 11–13
 - Ellipsometry, 51–53
 - Energy bands
 - conduction band, 12, 13
 - forbidden band, 12, 13
 - valence band, 12, 13
 - Equivalent circuit model, 80, 84
 - Evanescence waves, 117, 137–141, 149, 151, 154
- F**
- Fermi level, 11, 20
 - Fermi velocity, 21
 - Figure of merit (FOM)
 - for cloaking, 179
 - for negative-index materials, 113, 116
 - Filling factor/filling fraction, 30–34, 60, 61, 63, 64, 70–72, 142–146, 173, 174, 182, 183, 189
 - Finite-difference time-domain method (FDTD), 110
 - Finite-element method, 56
 - Fishnet structure, 41, 43, 110–116, 125
 - Focused-ion beam (FIB) milling, 40
 - Form-invariance of Maxwell's equations, 161
 - Four-wave mixing, 73, 125, 126
 - Fourier transform infrared spectroscopy (FTIR), 49
 - Free electrons, 20–22, 24, 66–68
 - Fresnel equations, 15
- H**
- Harmonic generation, 73, 124
 - Helmholtz–Drude model, 15
 - High-permittivity materials, 185
 - Hyperlens
 - cylindrical, 152
 - impedance-matched, 192, 193
 - planar, 192, 193
 - tapered waveguide, 190, 191
- I**
- Impedance, 52, 53, 109, 113, 139, 147, 153, 172, 176–179, 192, 193
 - Inhomogeneity scale, 3, 26
 - Interband transitions, 21–23, 89
 - Interference lithography (IL), 42
 - Invisibility, 159–193
 - Isofrequency curves, 118, 151

J

Jacobian matrix, 163, 164, 177

K

Kinetic inductance, 84

Kramers–Kronig relations, 133

L

Lattice constant, 65, 68, 70, 97

Left-handed materials, 102–103

Lenz's law, 66, 79

Light concentrator, 192

Lorentz line shape, 16

Lorentz local field, 27–29

Lorentz model, 20, 27, 107

Lorentz sphere, 27, 28

Lorentz–Lorenz equation, 27

Loss-compensation, 133

M

Macroscopic effective parameters, 5–8,

Magnetic field, 7, 66–68, 78–85, 87, 88, 96,
97, 108, 109, 114, 124, 141, 171,
175–177

Magnetic flux density, 6

Magnetic moment, 80, 82, 87, 88

Magnetic permeability, 51, 98, 105, 108, 112,
161, 168, 169, 181, 184

Magnetic susceptibility, 14

Magnetolectric coefficients, 7

Manley–Rowe relations, 126

Maxwell–Garnett geometry, 26, 27

Maxwell–Garnett theory (MGT), 30–34

Maxwell's equations, 5, 6, 8, 14, 61, 81, 101,
103, 161–163, 168, 177, 193

Meta-atoms, 3, 11, 19, 25, 39, 42, 43, 45, 54,
71, 78, 79, 85, 88, 116, 168, 189

Metal-dielectric composites

layered/stratified, 60–64, 119, 141, 151

periodic array of metallic wires, 64–71

random, 26, 71, 73, 148

Metal-insulator phase transition, 30

Metal-insulator-metals waveguides, 102

Mie resonances, 96, 185

Mixing rules, 25–36

Modulation transfer function (MTF), 145

N

Nanoimprint lithography (NIL), 42,

Nanorods

array, 109

coupled/paired, 89, 108, 109

Nanostrips

array, 78

coupled/paired, 78, 86–93, 95, 114, 168,
185

Near-field scanning optical microscopy
(NSOM), 149

Near-field superlens (NFSL)

operational condition, 141

tunable, 142, 143, 145, 148, 149

Negative permeability, 77, 89, 113

Negative permittivity, 70, 107, 113, 140

Negative refraction, 107, 117–120, 133

Negative-index materials (NIMs)

double-negative, 102, 113, 114, 116

microwave, 106, 107, 120, 139,

optical, 107, 108, 112, 119, 120, 133

single-negative, 113, 114, 116

Non-magnetic materials, 7, 178, 180

Nonlinear electric susceptibility, 126

Nonlinear optics, 26, 123–134

Nonlinear polarization, 127

Nonlinear surface waves, 125

O

Optical Kerr medium, 124

Optical anisotropy, 19

Optical magnetism, 77–78, 89, 95, 140, 171

Optical parametric amplifications, 126,
131–134

Optical transfer function (OTF), 145

P

Parameter space, 7, 8

Percolation threshold, 33–35, 71–73

Perfect conductor, 68, 70, 107

Perfect lens, 102, 137–140, 145, 149

Perfect metal, 90

Phase anisotropy, 50, 51, 110

Phase measurement, 50, 51, 110, 111

Phase-matching

phase-matching condition, 128, 129, 131

phase mismatch, 129, 131

Photolithography, 39, 40, 42, 43

Photon energy, 13, 20

Photonic crystals, 45, 46, 117, 118

Plasma frequency

surface plasmon, 31, 140, 150

volume, 21

Plasmonics, 25

Polaritonic material, 97

Polarizability, 29, 30, 34, 79

Polarization density, 14, 16, 20

Polarization interferometry, 50, 109
 Poynting vector, 102–104, 107, 118, 125, 128,
 129, 139, 151, 180
 Propagating waves, 8, 138, 139, 145, 149–151,
 153

R

Reduced cloak parameters, 172, 173
 Reflectance, 6, 47, 48, 106, 160
 Reflection
 coefficient, 24, 52, 53
 spectrum, 48, 49, 84, 90, 92
 Refractive index, 14, 15, 18, 19, 23, 24, 43,
 44, 51–54, 60, 92, 94, 101–104,
 106–109, 111, 112, 116–118, 120,
 127, 128, 137, 138, 151, 167, 171,
 186–189, 191, 193
 Relative permeability, 14
 Relative permittivity, 8, 14, 29
 Resonance
 electric, 17, 55, 87, 88, 91, 113, 114, 124
 magnetic, 43, 55, 78, 80–91, 93–98, 105,
 108, 109, 113, 114, 116, 169, 185
 phonon, 16, 97, 140, 184
 plasmon/plasmonic, 30, 72, 107, 109, 113,
 114, 125, 154
 polaritonic, 98
 Retrieval of effective parameters
 retrieval process, 52–55
 retrieved effective parameters, 55, 83, 114
 Reversed Phenomena in negative-index
 materials
 Cerenkov radiation, 104, 105
 Doppler effect, 104
 Goos–Hänchen shift, 104, 105
 Snell law, 45, 104, 106, 116, 119
 Rodded medium, 60, 64–66, 70

S

Scanning electron microscope (SEM), 43, 45,
 47, 87, 112, 114–116, 150, 190
 Scattering radiation patterns, 180
 Screening parameter, 35, 173
 Second-harmonic generation (SHG), 126–131
 Self-assembly, 46, 47
 Self-inductance, 66, 68, 84
 Self-organization, 46, 47
 Sellmeier formula, 18, 32
 Semicontinuous metal films, 34, 71–73
 Silver-wire lens, 154
 Snell's law, 45, 104, 106, 116, 119

Solitons, 125
 Spatial dispersion, 71
 Spectral representation, 36, 181
 Spectrophotometers, 48, 49, 109
 Split-ring resonators (SRRs)
 double, 78–81, 85
 planar, 41, 43, 84, 85, 124
 scaling breakdown, 84
 single, 79, 82–84
 Stealth techniques, 159
 Sub-diffraction-limited resolution, 149, 152
 Sub-wavelength resolution, 138, 145, 149, 193
 Subwavelength imaging, 5, 119, 154
 Super resolution, 117, 137–155
 Super-oscillation, 154
 Superlens
 far-field, 149–151
 near-field, 140–147
 tunable near-field, 142, 143, 145, 148, 149
 Surface plasmon, 30, 31, 72, 107, 119, 125,
 140, 150, 153, 191
 Surface-enhanced Raman scattering (SERS),
 148

T

Third-harmonic generation (THG), 124, 125
 Transformation function
 high-order, 176–180, 182, 183, 186, 187
 linear, 165, 166, 177–179, 181–182
 quadratic, 178–180, 183, 184, 186
 Transformation matrix, 164
 Transformation optics, 89, 153, 159–193
 Transmission
 coefficient, 53, 145
 spectrum, 92
 Transmittance, 47, 109, 111, 125, 175
 Transverse wavevectors, 117, 137, 145, 146,
 151
 Two-photon-photopolymerization (TPP), 45

V

Vector potential, 66, 67
 Veselago lens, 139

W

Wave vector surface, 118
 Wiener bounds, 63, 64, 181, 182, 184
 Wire grid/wire medium/wire mesh, 60, 64–71
 Wood's anomaly, 92